

**NASA Contractor Report 4127**

**Solar Generation and  
Storage of O<sub>2</sub>(a<sup>1</sup>Δ<sub>g</sub>)**

**Allen J. Twarowski, Phan Dao,  
and Lisa A. Good**

**CONTRACT NAS1-17988  
MARCH 1988**

**(NASA-CR-4127) SOLAR GENERATION AND STORAGE  
OF O<sub>2</sub> (a 1 DELTA g) Final Report, 12 Mar.  
1985 - 12 Mar. 1987 (KMS Fusion) 160 p**

**CSCL 202**

**N88-21431**

**Unclass**

**H1/3s G124861**



**NASA Contractor Report 4127**

# **Solar Generation and Storage of O<sub>2</sub>(a<sup>1</sup>Δ<sub>g</sub>)**

**Allen J. Twarowski, Phan Dao,  
and Lisa A. Good  
*KMS Fusion, Inc.*  
*Ann Arbor, Michigan***

**Prepared for  
Langley Research Center  
under Contract NAS1-17988**



**National Aeronautics  
and Space Administration**

**Scientific and Technical  
Information Division**

**1988**

## TABLE OF CONTENTS

Chapter 1. INTRODUCTION.....	1
1.1 Program Goals.....	1
1.2 Tasks - Dye Sensitized Singlet Oxygen Generation.....	2
1.3 Outline of Chapters.....	5
1.4 References.....	5
Chapter 2. SURFACE SUPPORTED ISOLATED DYE MOLECULE STUDIES.....	6
2.1 Introduction.....	6
2.2 Experimental.....	7
2.2.1 Sample preparation.....	7
2.2.2 Data collection for porphin samples.....	9
2.2.3 Data collection for acriflavine studies.....	11
2.2.4 Oxygen addition.....	11
2.3 Results.....	13
2.3.1 NaCl substrate - porphins.....	13
2.3.2 Silica gel substrate - ZnTPP.....	21
2.3.3 Silica gel - acriflavine.....	27
2.3.4 Polymer substrate - porphins.....	30
2.4 Discussion.....	55
2.5 References.....	59
Chapter 3. TRIPLET EXCITON KINETICS.....	61
3.1 Introduction.....	61
3.2 Triplet Exciton Decay in Single Crystal Films.....	62
3.2.1 Experimental.....	62
3.2.2 Decay kinetics.....	63
3.2.3 Decay and absorption length.....	69
3.3 Triplet Exciton Decay in Polycrystalline Film.....	72
3.3.1 Experimental.....	72
3.3.2 Triplet density.....	74
3.3.3 Results and discussions.....	76
3.4 Conclusions.....	81
Appendix A: Decay kinetics in solid dyes.....	82
Case 1: Low fluences and/or later times.....	83
Case 2: High fluences and early times.....	83
Case 3: General cases.....	84
Appendix B: Absorption measurements with a pyroelectric calorimeter.....	84
Experimental.....	85
Calibration.....	88
3.5 References.....	92

Chapter 4. THERMAL MEASUREMENT OF TRIPLET DECAY.....	94
4.1 Introduction.....	94
4.2 Theory of Photothermal Deflection.....	94
4.2.1 Deflection vs. triplet decay.....	94
4.2.2 $\Phi_{\max}$ and triplet decay.....	99
4.3 Experimental Considerations in Photothermal Deflection Technique.....	100
4.3.1 Deflection measurements.....	105
4.3.2 Noise analysis.....	108
4.3.3 Sensitivity: signal vs. displacement.....	110
4.4 Photothermal Deflection: Testing and Evaluation.....	112
4.4.1 Test experiments.....	112
4.4.2 Photothermal deflection vs. phosphorescence.....	114
4.4.3 Evaluation of PD technique.....	119
4.5 Thin Film Pyroelectric Detection.....	121
4.5.1 Principles of operation.....	123
4.5.2 Experimental.....	127
4.5.3 Results of tests.....	129
4.6 Conclusions.....	131
4.7 References and Notes.....	133
Chapter 5. CONVERSION OF 2PVN TO ENDOPEROXIDE.....	136
5.1 Introduction.....	136
5.2 Experimental.....	136
5.3 Results.....	136
5.4 Discussion.....	143
Chapter 6. EXECUTIVE SUMMARY.....	149
6.1 Transfer of energy from isolated dye molecules.....	149
6.2 The photophysics of excitons in dye solids.....	152
6.3 A system which combines singlet oxygen generation and storage.....	153
6.4 Directions of future work.....	154

## LIST OF FIGURES

<b>Figure</b>	<b>Page</b>
1.1 Molecular structure of 2 PVN and 2 PVNE.	3
2.1 (a) NMR spectrum of purified acriflavine. (b) NMR spectrum of crude acriflavine.	8
2.2 Experimental apparatus for collection of porphin phosphorescence data.	10
2.3 Experimental apparatus for collection of acriflavine phosphorescence data.	12
2.4 ZnTPP on NaCl - phosphorescence decay. Oxygen pressure = 0 Torr, ■; 0.11 Torr, ◆. Least squares fit, -.	15
2.5 PdTPP on NaCl - phosphorescence decay. Oxygen pressure = 0 Torr, ■; 1.0 Torr, ◆. Least squares fit, -.	16
2.6 PtTPP on NaCl - phosphorescence decay. Oxygen pressure = 0 Torr, ■; 21 Torr, ◆. Least squares fit, -.	17
2.7 ZnTPP on NaCl - quenching of phosphorescence by oxygen. Data, ■; least squares fit, -.	18
2.8 PdTPP on NaCl - quenching of phosphorescence by oxygen. Data, ■; least squares fit, -.	19
2.9 PtTPP on NaCl - quenching of phosphorescence by oxygen. Data, ■; least squares fit, -.	20
2.10 ZnTPP on silica gel - phosphorescence decay. Oxygen pressure = 0 Torr, ■; 0.001 Torr, ◆; 0.01 Torr, ▲. Least squares fit, -.	22
2.11 ZnTPP on silica gel - phosphorescence decay as a function of temperature. Temperature = 25 C, ■; 91 C, . Least squares fit, -.	24
2.12 ZnTPP on silica gel - quenching of phosphorescence by oxygen. Temperature = 25 C. Data, ■; curve fit (see text), -.	25
2.13 ZnTPP on silica gel - quenching of phosphorescence by oxygen. Temperature = 60 C. Data, ■; curve fit (see text), -.	28
2.14 Acriflavine on silica gel - phosphorescence decay. Data, dotted line; biexponential curve fit, -.	29
2.15 Acriflavine on silica gel - $k_s$ versus oxygen pressure.	31

Figure		Page
2.16	Acriflavine on silica gel - $I_s$ versus oxygen pressure.	32
2.17	Acriflavine on silica gel - $k_f$ versus oxygen pressure.	33
2.18	Acriflavine on silica gel - $I_f$ versus oxygen pressure.	34
2.19	ZnTPP on nylon - phosphorescence decay. Oxygen pressure = 0 Torr, ■; 4.5 Torr, ▲. Least squares fit, -.	36
2.20	ZnTPP on poly(methylmethacrylate) - phosphorescence decay. Oxygen pressure = 0 Torr, ■; 0.13 Torr, ◆. Least squares fit, -.	37
2.21	ZnTPP on poly(styrene) - phosphorescence decay. Oxygen pressure = 0 Torr, ■; 0.08 Torr, ◆. Least squares fit, -.	38
2.22	ZnTPP on cellulose - phosphorescence decay. Oxygen pressure = 0 Torr, ■. Least squares fit, -.	39
2.23	ZnTPP on 2PVN - phosphorescence decay. Oxygen pressure = 0 Torr, ■; 0.06 Torr, ◆. Least squares fit, -.	40
2.24	ZnTPP on nylon - quenching of phosphorescence by oxygen. Data, ■; least squares fit, -.	42
2.25	ZnTPP on poly(methylmethacrylate) - quenching of phosphorescence by oxygen. Data, ■; least squares fit, -.	43
2.26	ZnTPP on poly(styrene) - quenching of phosphorescence by oxygen. Data, ■; least squares fit, -.	44
2.27	ZnTPP on cellulose - quenching of phosphorescence by oxygen. Data, ■; least squares fit, -.	45
2.28	ZnTPP on 2PVN - quenching of phosphorescence by oxygen. Data, ■; least squares fit, -.	46
2.29	PdTPP on nylon - phosphorescence decay. Oxygen pressure = 0 Torr, ■; 90 Torr, ◆. Least squares fit, -.	48
2.30	PtTPP on nylon - phosphorescence decay. Oxygen pressure = 0 Torr, ■; 100 Torr, ◆. Least squares fit, -.	49
2.31	PdTPP on nylon - quenching of phosphorescence by oxygen. Data, ■; least squares fit, -.	50
2.32	PtTPP on nylon - quenching of phosphorescence by oxygen. Data, ■; least squares fit, -.	51

Figure	Page
2.33 ZnTPP on nylon - temperature dependence of phosphorescence quenching by oxygen. Temperature = -3 C, ■; 25 C, ◆; 65 C, ▲. Least squares fit, -.	53
2.34 ZnTPP on nylon - temperature dependence of quenching rate constant. Data, ■; least squares fit, -.	54
3.1 Time-resolved Delayed Fluorescence of crystal films. The thickness is ca. 350 microns, and the crystal is freshly grown. The excitation wavelength is 570 nm and the emission is measured at 620 nm. The fluences used are $8 \times 10^{13}$ photons $\text{cm}^{-2} \text{ pulse}^{-1}$ in the lower trace and $5 \times 10^{14}$ photons $\text{cm}^{-2} \text{ pulse}^{-1}$ in the upper trace. Note that of the two decays, the upper shows a lesser contribution of bimolecular decay.	64
3.2 Fluence dependence of DF emission. The DF signals are extrapolated to time zero to give the initial emissions which are then plotted against laser fluence in a log-log plot. The linear and quadratic dependences on fluence are shown as solid lines.	65
3.3 DF decay in semilogarithmic plot. The fluence is $8 \times 10^{14}$ photons $\text{cm}^{-2} \text{ pulse}^{-1}$ , and the absorption coefficient is $30 \text{ cm}^{-1}$ (wavelength = 570 nm). The decay is faster than unimolecular for times smaller than 10 $\mu\text{sec}$ .	66
3.4 DF decay and bimolecular kinetics. The fluence is $8.0 \times 10^{14}$ photons $\text{cm}^{-2} \text{ pulse}^{-1}$ , and the absorption coefficient is $30 \text{ cm}^{-1}$ (wavelength = 570 nm). $(DF)^{-1/2}$ is plotted against time to show the second order kinetics behavior. The linear portion of the curve for small times (< 10 $\mu\text{sec}$ ) is indicative of the dominant bimolecular decay path. From the slope and y-intercept one can determine the T-T decay rate constant to be $1.1 \times 10^{-11} \text{ cm}^{-3} \text{ s}^{-1}$ .	68
3.5 DF decay vs. optical penetration depth. The crystal film is ca. 250 nm thick, and the excitation wavelength is changed to vary the penetration depth up to 400 nm. For the farthest point to the left, the excitation wavelength is 490 nm, and the absorption length is lower-bounded by 0.4 $\mu\text{m}$ but not known. Note the sharp decrease in unimolecular lifetime for thicknesses less than 5 $\mu\text{m}$ .	71
3.6 Absorption spectrum of a thin sublimed tetracene film. The 0-0 component of the first singlet transition at 517 nm is split into peaks at 505 and 520 nm.	73
3.7 Absorbance vs. film thickness. Pulsed used for absorption measurements. The amount of heat generated in the tetracene sublimed film upon pulsed excitation is plotted against thickness. The pyroelectric signal is calibrated according to Appendix B.	75

Figure	Page
3.8 DF decay of tetracene polycrystalline film. The excitation pulse is shorter than 10 nsec and set at 478 nm. The emission is recorded at 600 nm.	77
3.9 DF at 50 nsec after laser excitation. The excitation wavelength is 478 nm, and the emission is recorded at 600 nm. The curvature at high fluences is due to increasing bimolecular decay contribution.	78
3.10 Fluence dependence of DF at fixed times. $DF^{-\frac{1}{2}}$ is plotted against 1/Fluence as a function of time. The linearity is predicted by the model developed in Appendix A (see equations A.9 and A.10).	79
3.11 Unimolecular decay. Slope of plots similar to Fig. 3.3.5 (taken at various time) is plotted as a function of time in a semilogarithmic scale.	80
3.12 Schematic of pyroelectric calorimeter. The 1 x 1 in. square of PVDF (part B) is connected to signal lead via copper foil tabs (parts A and C).	86
3.13 Pyroelectric signal. The signal is obtained with a $1 \times 10^{-4}$ J/pulse which is incident on a spin-coated dye film which absorbs strongly at the laser wavelength (optical density of ca. 4). The maximum is attained in less than 10 $\mu$ sec, and the slow decay shows a time constant of 100 msec.	87
3.14 Response of pyroelectric calorimeter. The maxima of pyroelectric signals are displayed as a function of incident laser energy.	89
3.15 Absorption and reflection of the air/dye/metal layer.	90
4.1 Collinear photothermal deflection.	96
4.2 Experimental set-up	101
4.3 Probe beam. The HeNe probe is focused on the dye film with a 200 mm fl lens.	102
4.4 Illumination of position detector.	103
4.5 Deflection signal as a function of the pump probe overlap. The lower trace is the PD signal measured as the position of the probe is varied relative to the pumped spot. The upper trace is the PD signal integrated over the pump probe displacement. The integrated signal agrees with the intensity profile of the pump beam.	104
4.6 Bi-cell output vs. displacement of probe.	107

Figure	Page
4.7 Material dependence of deflection signal. PD signal measured with 5000 Å of acridine orange deposited on fused silica (A), pyrex (B) and lucite (C). For each substrate, the pump beam position was optimized for maximum PD signal.	113
4.8 Comparison of PD signal and phosphorescence. In this case, the PD signal is, at any given time, proportional to the excited state number density and is expected to follow the phosphorescence signal.	116
4.9 Time-resolved PD and phosphorescence signals on semi-logarithmic scale.	117
4.10 Lifetime of excitation as a function of dye concentration.	118
4.11 Lifetime of excitation as a function of glycerine temperature (viscosity).	120
4.12 Thin-film ferroelectric detector.	125
4.13 Ferroelectric signal. Time scale: 10 $\mu$ sec/div.	128
4.14 Comparison of ferroelectric and phosphorescence signal.	129
4.15 Response time of thin film ferroelectric detector.	132
5.1 Absorption spectrum of 2PVN showing a) the decrease in absorbance of the 294 nm band upon irradiation of the ZnTPP/2PVN film with light b) the increase in absorbance in the same absorption band with heating of polymer at 80° C for 15 min.	138
5.2 The fraction of naphthalene units converted to endo-peroxide as a function of the number of absorbed photons. 0, 2PVN film 0.1 mole per cent ZnTPP. ●, 2PVN film with 1.0 mole per cent ZnTPP.	139
5.3 The fraction of naphthalene units converted to endo-peroxide as a function of the number of absorbed photons. 0, 2PVN film 0.1 mole per cent PdTPP. ●, 2PVN film with 1.0 mole per cent PdTPP.	140
5.4 The fraction of naphthalene units converted to endo-peroxide as a function of the number of absorbed photons. 0, 2PVN film 0.1 mole per cent PtTPP. ●, 2PVN film with 1.0 mole per cent PtTPP.	141
5.5 The fraction of naphthalene units converted to endo-peroxide as a function of the number of photons absorbed by ZnTPP; ●, uncorrected data. ■, corrected data (see text).	142

Figure	Page
5.6      The quantum yield of endoperoxide formation as a function of the fraction of naphthalenes converted to endoperoxide. ZnTPP data; 0, $\Delta$ -0.1 mole per cent ZnTPP, ●, $\blacktriangle$ -1.0 mole per cent ZnTPP.	144
5.7      The quantum yield of endoperoxide formation as a function of the fraction of naphthalenes converted to endoperoxide. PdTPP data; 0-0.1 mole per cent PdTPP, ●-1.0 mole per cent PdTPP.	145
5.8      The quantum yield of endoperoxide formation as a function of the fraction of naphthalenes converted to endoperoxide. PtTPP data; 0-0.1 mole per cent PtTPP, ●-1.0 mole per cent PtTPP.	146

## PREFACE

This report describes the results of work performed at KMS Fusion under NASA contract NAS1-17988. The technical effort was performed by Dr. Phan Dao, Ms. Lisa Good and Dr. Allen Twarowski (Principal Investigator). Primary responsibility for the technical work of this contract is reflected by the authorship of the chapters of this report. Chapters 3 and 4 which report work on exciton photophysics in organic crystalline solids were written by Dr. Dao. Chapters 2 and 5 which report work on the kinetics of energy transfer from surface supported dye molecules to molecular oxygen were written by Dr. Twarowski who also wrote the introductory chapter (Chapter 1) and the executive summary (Chapter 6). Ms. Good performed many of the technical tasks in all of the areas of investigation as well as taking responsibility for editing this report.

## CHAPTER 1: INTRODUCTION

### 1.1 Program Goals

The ultimate goal of this program is the development of an iodine laser capable of space based operation. The initial concept for this laser includes the following features.

1. Solar energy is collected using organic dye molecules. An order of 100 nm can absorb a large fraction of the incident solar radiation which has wavelength within the absorption band of the dye. Since many dye molecules have a fairly broad absorption feature in the visible (e.g. 50 - 100 nm), only a few films of different dyes would be needed to absorb a large fraction of the incident solar radiation. Assuming that only one-photon absorption will be of practical importance in these systems, the upper limit on energy collection efficiency is about 0.82, which is the fraction of solar energy available in the solar spectrum with wavelength shorter than 1300 nm. (Since the singlet delta state of oxygen lies an amount of energy corresponding to 1300 nm above the oxygen ground state, at temperatures close to 25 C only a photon with wavelength shorter than 1300 nm has enough energy to excite molecular oxygen to this state upon energy transfer from the dye film.) Even if 82 per cent of the incident solar radiation could be collected by dye films, inefficiencies in the utilization of this energy will be present. For most dye systems, the absorption of a photon with wavelength  $\lambda$  will only lead to excitation of one oxygen molecule. Thus an energy defect of  $hc(1/\lambda - 1/1300 \text{ nm})$  will be realized. At 650 nm already one half of the collected energy appears as heat. However, even with these considerations, an efficiency of over 10 per cent should be possible using only dyes absorbing in the visible.
2. Excited dye molecules formed by absorption of solar radiation within a dye layer must transfer their energy to dye molecules on the surface of the dye film so that ultimately this energy can be delivered to gaseous ground state oxygen. In a crystalline environment, electronic excitation energy may travel freely throughout the lattice. This mobile excitation is termed an exciton. In a molecular crystal bound together only weakly by van der Waal's forces, the exciton is strongly localized on the molecules that form the crystal. It can be thought to hop from molecule to molecule rather than as being delocalized over many molecular sites of the crystal. In most organic dye molecules, the lowest electronic state has a singlet spin configuration which can be easily populated by absorption of radiation. Triplet spin states can be populated from excited singlet states via radiationless transitions and usually have a much longer lifetime (0.001 to 1 second) than the excited singlet states (lifetime usually less than  $10^{-7}$  seconds) allowing more time for the excitation to migrate to the crystal surface. If the surface of the dye crystal layer is doped with dye molecules which have lower triplet state energy, the exciton can become trapped at these surface sites. The exciton trapping sites are envisioned to be purposely created on the dye film surface by deposition of a sub-monolayer of selected dye molecules. Energy transfer to gas phase oxygen is then presumed to occur when an oxygen molecule collides with the excited surface dye molecule.

3. The singlet delta oxygen molecule which is formed by energy transfer from surface sites on the dye film can be used directly to fuel an oxygen-iodine laser. However, it is possible that the oxygen gas may not be enriched enough in singlet oxygen to pump a laser - 15 per cent of the oxygen gas must be excited to the singlet delta state to reach threshold in an oxygen-iodine laser operating at room temperature. The electronically excited singlet delta oxygen can be stored and concentrated from the bulk oxygen gas by selectively reacting the singlet delta oxygen with an aromatic hydrocarbon to produce an endoperoxide. Some naphthalene compounds with aliphatic groups attached to the 1 and 4 positions on the naphthalene ring form stable 1,4-endoperoxides. Figure 1.1 shows the molecular structure of a polymeric naphthalene derivative, 1,4-dimethyl-2-poly(vinyl-naphthalene) or 2PVN, which was prepared and studied at KMS Fusion. Also shown in this figure is the reaction of 2 PVN with singlet delta oxygen to form the endoperoxide, 1,4-dimethyl-2-poly(vinylnaphthalene-1,4-endoperoxide) or 2PVNE.

4. The endoperoxide formation reaction is reversible. Singlet delta oxygen and the parent naphthalene compound can be fully recovered upon heating the solid. The solid endoperoxide can be stored for extended periods of time (weeks at room temperature) allowing this material to be formed in the solar generator section of the laser and physically transported to a different region for thermolysis.

5. Singlet delta oxygen released by thermolysis of the endoperoxide material can be directed into a laser gain region where it can be mixed with iodine vapor. The singlet oxygen both causes the dissociation of molecular iodine and transfers energy to atomic iodine from which energy can be extracted through a coherent stimulated emission process.

The last step has been extensively investigated and is considered the most well understood step in the solar powered laser scheme. Step 4, the release of singlet delta oxygen into the gas phase upon thermolysis of 2PVNE has been demonstrated at KMS Fusion. It was found that the singlet oxygen yield from thermolysis of 2PVNE films is reasonably large at submicron polymeric endoperoxide film thicknesses. Recently, singlet delta oxygen generation in a gas phase system upon thermolysis of a volatile endoperoxide also has been demonstrated at KMS Fusion. However, not enough research has yet been done on the volatile endoperoxide to quantify the singlet oxygen yield.

The first step listed above for the solar powered laser scheme is trivial. That dyes can be deposited in thin films and that these films absorb a large fraction of the incident radiation which has wavelengths within the absorption bands of the dye film has been known for some time.

Steps 2 and 3 were identified as the processes most poorly understood and most in need of investigation. The work funded under this contract attempted to answer key issues associated with steps 2 and 3 allowing evaluation of the entire solar pumped laser scheme.

## 1.2 Tasks - Dye Sensitized Singlet Oxygen Generation

Step 2, the transport of electronic excitation in a molecular crystal to surface trapping sites and the subsequent transfer of that energy to a gas phase oxygen molecule, is the most ambitious and complex of the steps in the laser scheme and it is this process which dominated our experimental efforts in the phase 2 SBIR contract. The transport of electronic excita-

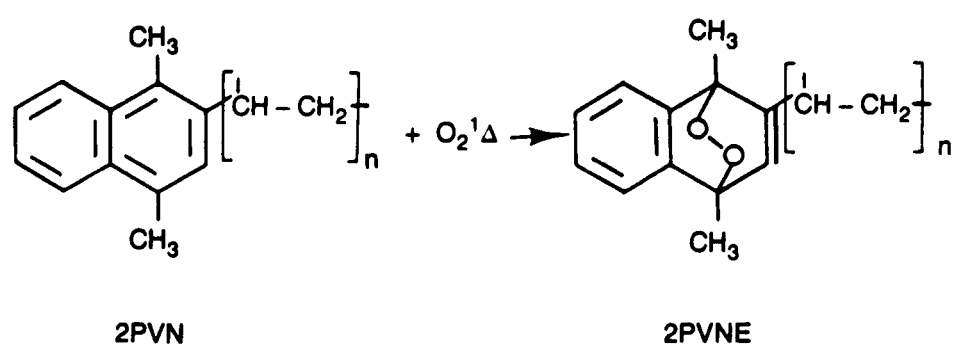


**Figure 1.1** Molecular structure of 2 PVN and 2 PVNE.

tion in thin dye films via exciton diffusion, the trapping of this excitation at specially deposited surface energy trapping sites, and the final transfer of energy from the surface energy trapping sites to gas phase oxygen is a complex process which has yet to be demonstrated. The photophysics of exciton behavior in single crystals of some aromatic hydrocarbons has been extensively studied, however other than for a few of these molecular solids little work has been reported for single crystals of dyes or polycrystalline dye films. Initial expectations of how the energy transfer process might work were based on results of investigations reported in the literature for single crystal anthracene and tetracene.

Our model of energy transfer in polycrystalline dye films was described in detail in the proposal for this contract work and will be only briefly discussed here. Absorption of a photon by a molecule of the crystalline dye film promotes the molecule from its ground state to a singlet excited state. This excitation can hop from molecule to molecule, but the singlet exciton thus formed is short lived and is expected to intersystem cross to a triplet exciton quickly. The triplet exciton diffuses throughout the crystal fairly rapidly. Its range is determined by the hopping velocity and the exciton's lifetime. The triplet exciton lifetime is determined by competition among several processes. The exciton can become trapped at a molecular crystal site which has a lower triplet state energy than the bulk triplet exciton energy band. This energy trapping site could be a molecular impurity or a crystal imperfection site. The triplet exciton can transfer its energy to a reaction center, an example being charge pair formation if the electronic band gap is lower in energy than the triplet excitation or if impurity molecules present in the crystal lattice or at surface sites can transfer charge to a triplet crystal molecule. All of the exciton destruction processes mentioned so far are dependent on only the first power of the triplet exciton density and so will result in an exponential dependence of the triplet density on time after creation.

An exciton destruction process which has been found to be of great importance in the anthracene singlet crystals is triplet-triplet annihilation. The T-T annihilation process is second order in triplet density and with a biexcitonic rate constant of  $4 \times 10^{-11} \text{ cm}^3/\text{s}$  the lifetime of a triplet exciton is shortened to less than a microsecond for triplet exciton densities of greater than  $3 \times 10^{16} \text{ cm}^{-3}$ . The deposition of molecules on the crystal surface with triplet energy lower than the bulk crystalline triplet exciton offers two advantages over crystals with clean surfaces. Triplet excitons are immobilized at these surface sites and effectively removed from the crystal bulk lowering the triplet exciton density and thereby increasing the exciton lifetime. The increased lifetime in turn allows the triplet excitons more opportunity to find a surface trapping site. Once immobilized at a surface trapping site, the triplet exciton is exposed to collisions of gas phase molecules and its lifetime is expected to be limited by the rate of energy transfer to colliding oxygen molecules.

The kinetics of triplet exciton decay and of energy transfer from crystalline surface sites to gas phase oxygen have not been reported for most dye molecules. The primary mission of the research effort reported here is the collection of a database of kinetic rate constants associated with triplet exciton decay in polycrystalline dye materials and with energy transfer from electronically excited dye molecules supported

on a substrate surface to gas phase oxygen. With this data an efficient solar powered generator hopefully can be designed and its operational conditions defined.

### **1.3 Outline of Chapters**

The rate of transfer of energy from surface supported dye molecules to gas phase oxygen was studied by measuring the rate of phosphorescence quenching of dye molecules when exposed to gaseous oxygen. While phosphorescence quenching of dye molecules by oxygen need not involve energy transfer to oxygen, nevertheless, singlet oxygen has been shown to be formed in this dye triplet state quenching process for many systems, and it is presumed in our studies that phosphorescence quenching is a valid measure of the energy transfer rate. Phosphorescence quenching of dye molecules on three types of supporting surfaces was studied. In chapter 2 our results of these studies are reported.

The kinetics of the decay of electronic excitation in crystalline dye materials can be investigated by a number of different methods. The only method reported in the literature relies on the production of fluorescing excited singlet states upon triplet-triplet exciton annihilation.<sup>1</sup> The time dependence of delayed fluorescence is recorded and the kinetics of triplet exciton decay are recovered from this data. In chapter 3 the results of delayed fluorescence measurements of tetracene single crystals and polycrystalline films are reported. These studies provide insight into the problems which can be expected with the use of polycrystalline films as well as providing a basis for comparison with thermal detection techniques.

Unfortunately the delayed fluorescence technique is not universally applicable to all dye solids most of which do not show delayed fluorescence upon excitation. We have undertaken the development of a thermal detection method which would be applicable to the investigation of electronic excitation decay in all dye solids (presuming that the fluorescence quantum yield in the solid is not too large - let's say less than 0.99). In chapter 4 work leading to the development of two thermal detection techniques is reported.

In chapter 5 work demonstrating the direct conversion of dye doped 2PVN to its endoperoxide, 2PVNE, upon illumination in the absorption band of the dye dopant is reported. This new approach has succeeded in essentially combining steps 1 to 3 of the program goals into one fairly efficient step. Finally, in chapter 6 the implications of our results for the feasibility of developing a solar powered laser are discussed.

### **1.4 References**

1. J. B. Birks, "Photophysics of Aromatic Molecules," (Wiley-Interscience, NY, 1970), Chap. 11.

## CHAPTER 2: SURFACE SUPPORTED ISOLATED DYE MOLECULE STUDIES

### 2.1 Introduction

The rate at which energy can be transferred from a dye molecule adsorbed on the surface of an organic crystal to an oxygen molecule which collides with it from the gas phase will depend on the temperature and partial pressure of oxygen as well as the probability of energy transfer per collision. The latter quantity is intrinsic to the dye molecule and is the parameter which was sought in our studies of dye molecules supported on various solid substrates. Three categories of substrate were investigated; silica gel, NaCl crystals and polymers. All of these substrates provide, in varying degrees, a high surface area allowing the study of a large population of excited dye molecules while still insuring that the molecules are sufficiently separated from each other so that energy migration among molecules does not dominate the photokinetics of the system. However, all three types of substrate behave differently.

The silica gel substrate has been commonly employed for luminescence quenching studies. Kautsky first reported quenching of acriflavine luminescence by oxygen when this dye was adsorbed to silica gel.<sup>1</sup> He also demonstrated that quenching of acriflavine luminescence produced an excited oxygen molecule which he speculated was a low lying electronic state of molecular oxygen. It was not until the 1960's that the excited state of oxygen was identified as the singlet delta state.<sup>2</sup>

Several research groups have reported the fabrication of heterogeneous singlet oxygen generators using a dye sensitizer supported on silica gel.<sup>3-8</sup> The efficiency of these generators is not reported; however, in cases where enough information is provided, the efficiency can be estimated and is always low. Originally we supposed that the low efficiency of these systems could be attributed to the fact that the dye molecules were present on the silica gel surface in low density and therefore the total fraction of incident light absorbed was very low. The silica gel substrate could nevertheless serve as a dye substrate for measuring the kinetics of energy transfer from triplet dye molecule to gas phase oxygen. This point of view has proved to be somewhat in error. As shown below, it now appears that quenching of dye luminescence on silica gel involves oxygen adsorbed to the silica gel surface rather than gas phase oxygen.

In an effort to find a substrate surface which is passive (it only supports the dye molecule but does not interact with the dye, except through weak van der Waal's forces, or adsorb oxygen) we investigated dye deposited on a nylon mesh used in industry as a filtering material. The quenching behavior of dye molecules on this high surface area substrate was consistent with expectations of a collisional quenching model. However, further research has convinced us that during the process of depositing the dye on the nylon surface, much of the dye becomes embedded in the nylon polymer. Quenching takes place when dissolved oxygen diffuses through the polymer to the excited dye molecule. While the nylon mesh studies did not provide the information which we were seeking, they motivated the study of endoperoxide formation in dye doped 2PVN. These studies opened up a new direction for the efficient sensitized production and trapping of singlet delta oxygen and will be reported in Chapter 5.

Finally, dyes deposited on NaCl crystals were examined. The choice of this substrate material was motivated by the lack of success experienced with the nylon substrate. The NaCl crystal is not permeable to organic solvents and the ionic lattice structure of the crystal does not provide a good environment for a large neutral organic dye molecule, so that deposition of a dye on NaCl from an organic solvent will not likely lead to incorporation of the dye molecule in the interior of the NaCl crystal. Our quenching data support the supposition that the dye remains on the NaCl surface and is quenched by collisions of gas phase oxygen with the dye molecule.

## 2.2 Experimental

### 2.2.1 Sample preparation

Zinc 5,10,15,20-tetraphenyl-21H,23H-porphine (ZnTPP), palladium 5,10,15,20-tetraphenyl-21H,23H-porphine (PdTPP) and platinum 5,10,15,20-tetraphenyl-21H,23H-porphine (PtTPP) were purchased from Porphyrin Products, Ogden, Utah, and used as received. Acriflavine was purchased from Kodak and purified chromatographically. NMR analysis of the purified product identified it as the acriflavine dye while NMR spectrum of the crude acriflavine (see Figure 2.1) was strikingly different. However no difference in the luminescence quenching behavior was found between crude dye and purified acriflavine. Chambers and Kearns have reported the luminescence and absorption spectra of acriflavine as well as several other dyes.<sup>9</sup> These workers report that their results were also not influenced by the apparent purity of the dyes they investigated.

Kodak Chromagram (catalog number 13179) silica gel sheets were cut into 2.5 cm square pieces and uniformly wetted with 0.04 ml of a  $1 \times 10^{-5}$  M solution of dye in either acetone or methylene chloride delivering 4 nanomoles of dye to the substrate. After solvent evaporation the substrate was mounted to a quartz plate with Scotch double stick tape. The quartz plate in turn was mounted in a brass holder and placed in a sample chamber which was evacuated with a turbopump to  $10^{-5}$  Torr base pressure. A liquid feedthrough permitted the quartz plate to be heated or cooled. A copper-constantan thermocouple was attached to the brass holder and its temperature was read with an Omega Model 660 temperature monitor. The sample was heated to 60-100 C in vacuum for approximately one hour to hasten outgassing of solvent and excessive adsorbed water. When an ultimate pressure of  $1 \times 10^{-5}$  Torr at room temperature was achieved the sample was considered to be prepared for data collection. With this preparation the sample gave reproducible quenching results over a several day period if kept under vacuum.

Porphin dye was deposited on NaCl crystals (commercially available superfine crystals-without sodium iodide addition) by wetting 5 grams of salt crystals with a chloroform solution of 5 nmoles of the porphin. The solvent was evaporated under vacuum while vigorously shaking the slurry of salt crystals and porphin solution. Upon inspection under a microscope the cubic salt crystals were found to be roughly 0.02 cm edge dimension. Using this number and the reported density of NaCl of 2.2 gm/cm<sup>3</sup>, the dye surface coverage of the salt crystals was calculated to be about 4 per cent.

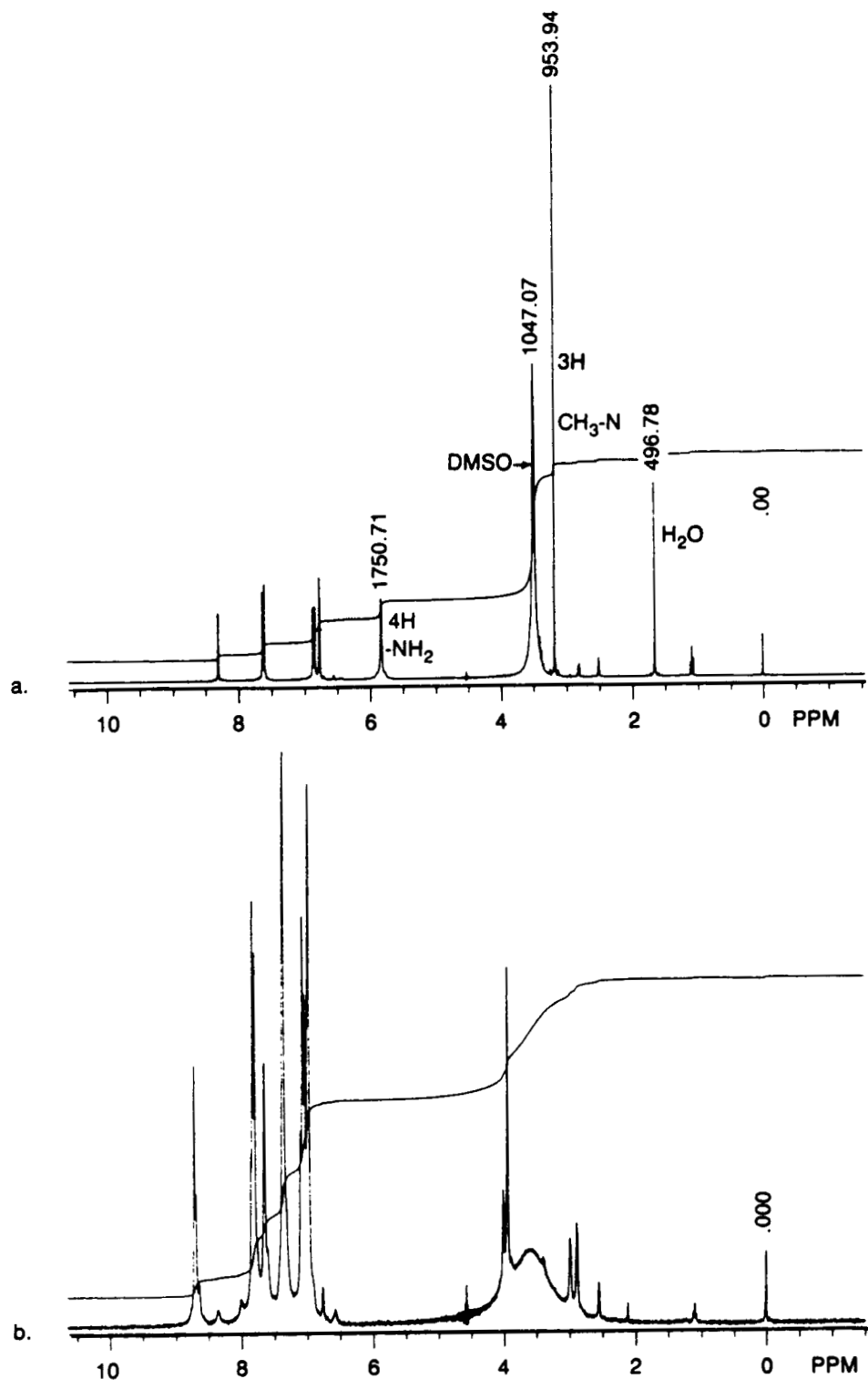


**Figure 2.1** (a) NMR spectrum of purified acriflavine.  
(b) NMR spectrum of crude acriflavine.

Twenty micron hydrophobic nylon mesh sheets were obtained from Micron Separations (catalog number N22SH315F5) and cut into 2.5 cm square pieces. The nylon mesh was uniformly wetted with 0.08 ml of a  $5 \times 10^{-5}$  M solution of dye in acetone or methylene chloride. After solvent evaporation the nylon mesh was attached to a quartz plate with Scotch double stick tape and mounted as described previously for the silica gel samples.

Polymer films which included embedded dye molecules were prepared by dissolving the dye and the polymer in a common solvent and spin coating or dip coating a quartz plate with the solution. The polymer coated quartz plate was mounted in the sample chamber as described above. Dye-doped poly(methyl methacrylate) [Scientific Polymer Products, catalog number 037B], poly(styrene) [Aldrich, MW 22000] and 1,4-dimethyl-2-poly(vinyl naphthalene) films were prepared in this manner. 2PVN was synthesized at KMS from the monomer supplied by Professor A.P. Schaap of Wayne State University.

Kodak cellulose sheets (catalog number 13255) were cut into 2.5 cm square pieces and treated with dye solution as described for the silica gel studies.

### 2.2.2 Data collection for porphin samples

The experimental apparatus used for the porphin data collection is illustrated in Figure 2.2. Excitation of the porphin samples was accomplished with 551 nm light from a Molelectron DL200 dye laser pumped by a Molelectron UV200 nitrogen laser. Roughly 1-10 microjoules of light energy per laser pulse was incident on an area of approximately 0.25  $\text{cm}^2$ . Phosphorescence from the porphin sample was viewed at a right angle to the excitation pulse and imaged on the photocathode of a cooled Hamamatsu R316-02 photomultiplier tube with an f2 lens. A Corion LG-697 long wavelength pass filter with a cutoff wavelength of 697 nm was inserted between the collection lens and the photomultiplier. The photomultiplier tube was connected to a Hamamatsu C1230 photon counter which was externally gated as follows. A beam splitter directed a small fraction of the dye laser output to a photodiode which was used as a zero time marker and trigger for most of the electronics. Delay generator 1, triggered by the photodiode, provided the start command for the photon counter. The output of this delay generator also provided the trigger for delay generator 2 which supplied a stop command to the photon counter. In this configuration the count window did not vary when the start command was delayed. The intrinsic delay built into the photon counter circuitry is reported to be 6 microseconds by the manufacturer. The delay between the start and stop command was set for a period of time at least five decay constants long.

For phosphorescence lifetime studies the start command to the photon counter was delayed beyond the intrinsic 6 microsecond delay. The actual delay between the laser pulse and the start command was viewed on a LeCroy 9400 digital oscilloscope. An AT&T 6300 computer recorded the photon counter output signal after arrival of each stop command at the photon counter and also recorded a value proportional to laser energy. The energy in the laser pulse was monitored with a Laser Precision Rk 3230 Energy Meter viewing a small fraction of the laser light split off from the main beam. The output signal from this device

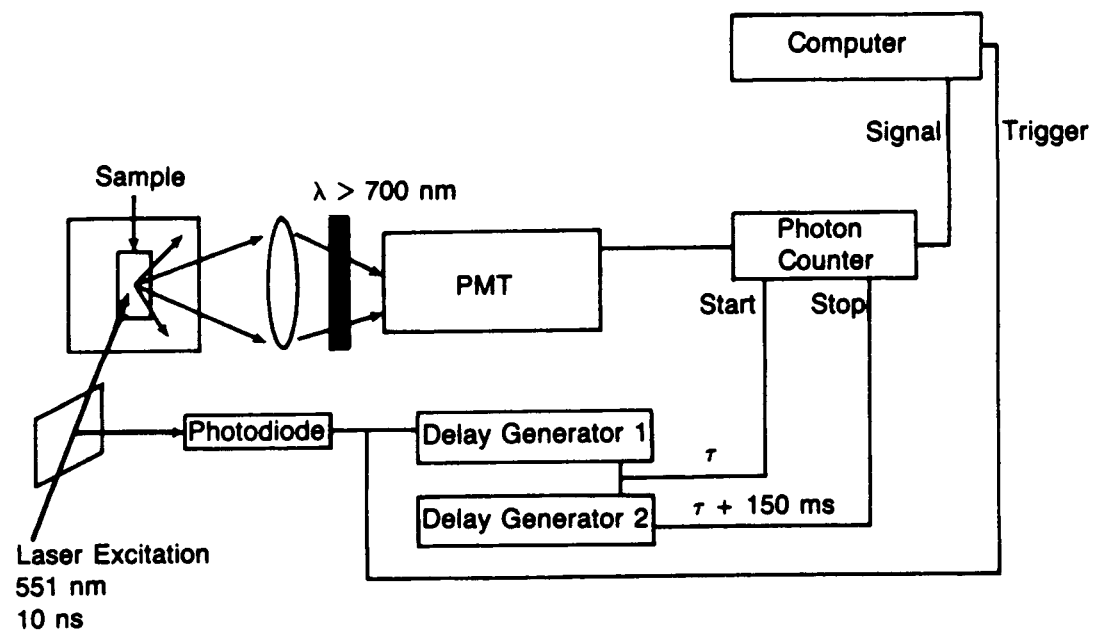


**Figure 2.2** Experimental apparatus for collection of porphin phosphorescence data.

decayed substantially during the photon counting interval so a sample and hold circuit was employed to maintain the peak value of the laser energy signal until it could be sampled by the computer. The signal from the photon counter was normalized for laser energy in software on a shot for shot basis. A typical phosphorescence measurement was the average of 20-100 laser pulses. Data acquisition and analysis were performed in software using the ASYST program from MacMillan software company.

### 2.2.3 Data collection for acriflavine studies

The experimental apparatus used for collection of acriflavine luminescence data is illustrated in Figure 2.3. Acriflavine coated silica gel samples were excited with the 455 nm line from a Coherent Innova 90-6 argon ion laser. A Uniblitz shutter (A.W. Vincent Assoc., Inc., Rochester, NY) was used to gate an 8 milliwatt pulse of the 455 nm laser beam to the sample for 10 ms illuminating approximately 1 cm<sup>2</sup> of the sample. The sample chamber configuration was identical with that used for the porphin experiments except a Corion S25-600 interference filter with a center wavelength of 600 nm replaced the 697 nm cutoff filter between the sample and the gallium arsenide photomultiplier tube.

Luminescence data was acquired using an AT&T 6300 computer but the handling of the photon counter signal differed from that described for the porphin experiments. The photon counter received a start command every 4 ms and a stop command 1 ms after the start command. This procedure effectively strobed the photon counter at 250 Hz with a 25 per cent duty cycle. A custom built pulse generator based on a 555 timer integrated circuit provided the strobe signals. When the shutter closed after the 10 ms excitation period, the computer was instructed to start acquiring data from the photon counter for a period of several seconds. Thus a collection of data points representing the time profile of the luminescence decay was acquired. This set of data consisted of the photon counter signal integrated for 1 ms spaced every 4 ms along the luminescence decay curve. Acquisition and analysis of the luminescence data was performed using the ASYST program from MacMillan software company.

### 2.2.4 Oxygen addition

The quenching of dye phosphorescence by molecular oxygen was studied as a function of the partial pressure of oxygen in the sample chamber. Oxygen was metered into the sample chamber through a needle valve and the total pressure of the sample chamber was monitored with a Leybold-Heraeus Combivac IT 230 ionization gauge controller and an IE-20 nude ionization gauge in the range of pressures of 10<sup>-5</sup> Torr to 0.01 Torr. Above 0.01 Torr, a 10 Torr Baratron capacitance manometer was used. When a NaCl sample or a doped polymer sample was present in the sample chamber, the partial pressure of oxygen was established under static conditions. The sample chamber was isolated from the turbopump and a quantity of oxygen sufficient to achieve the desired pressure was metered into the chamber. For these studies the oxygen partial pressure was always much larger than the base pressure achieved in the sample chamber and was stable to within a few per cent for the duration of the

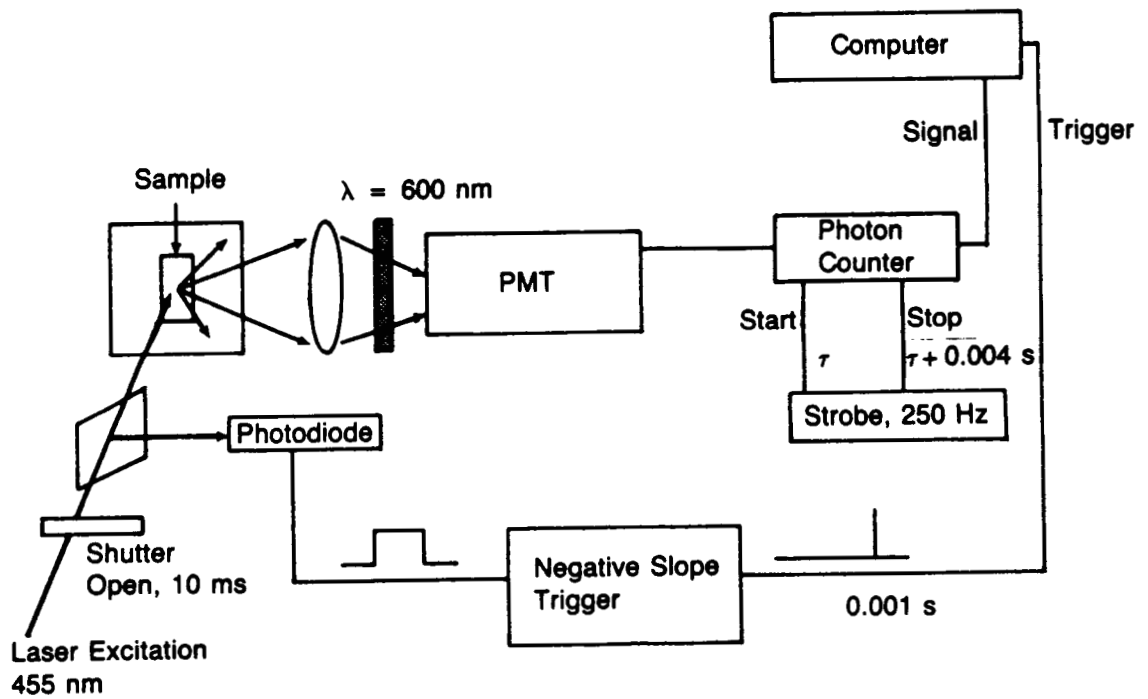


**Figure 2.3** Experimental apparatus for collection of acriflavine phosphorescence data.

data collection period. When a silica gel sample was being investigated, the partial pressure of oxygen in the sample chamber was established under dynamic pumping conditions. Oxygen gas was continuously injected into the chamber through a gas control valve while the chamber was being evacuated by the turbopump. The partial pressure of oxygen in these experiments was controlled by the flow rate of oxygen gas into the sample chamber.

The sample chamber and associated vacuum plumbing was constructed from a combination of stainless steel fittings with KF (Leybold-Heraeus) and Conflat (Varian) flanges. In high vacuum systems, the ultimate pressure which is achieved is determined by the rate of outgassing of water molecules from the walls of the vacuum chamber.<sup>10</sup> Mass spectrometric analysis of vacuum systems similar to the one used in these studies has confirmed that the residual gas in our vacuum chambers consists almost entirely of water vapor. We have assumed throughout our analysis of results that the partial pressure of water vapor in the sample chamber is equal to the base pressure achieved (approximately  $10^{-5}$  Torr) before the flow of oxygen is turned on.

In the following presentation of experimental results an oxygen partial pressure which is stated to be 0 Torr refers to a sample chamber under high vacuum ( $10^{-5}$  Torr). Under these conditions the partial pressure of oxygen is less than  $10^{-6}$  Torr.

The luminescence studies of ZnTPP coated on NaCl were complicated by a background luminescence observed with uncoated NaCl. The origin of this luminescence is believed to be impurities in the NaCl; however, no attempt was made to verify this conjecture. The luminescence from an uncoated sample was recorded under the same conditions of time delay and oxygen partial pressure used in the ZnTPP phosphorescence study and subtracted from the porphin phosphorescence signal. The magnitude of this correction varied from approximately 10 per cent of the total signal magnitude to as high as 50 per cent at combined conditions of high oxygen pressure and long time delay.

## 2.3 Results

### 2.3.1 NaCl substrate - porphins

Phosphorescence quenching of ZnTPP coated on NaCl was observed after a few millitorr of oxygen was admitted to the sample chamber. Phosphorescence quenching of the PdTPP and PtTPP samples was not observed until higher oxygen pressures were present in the sample chamber. The rate constant, k, for decay of phosphorescence was measured as a function of oxygen pressure employing the following procedure. The start command to the photon counter was delayed by a variable amount with respect to the laser pulse resulting in an integrated photon counter signal,  $S(\tau)$ , which varies with delay time,  $\tau$ , as

$$S(\tau) = \int_{\tau}^{\infty} Be^{-kt} dt = \frac{B}{k} e^{-k\tau} \quad (2.1)$$

Here  $B$  is proportional to the initial population of photoexcited triplet state dye molecules. A plot of the natural logarithm of  $S$  as a function of delay time should give a straight line with a slope equal to  $-k$ .

With the sample chamber under high vacuum the phosphorescence decay rate was measured at 28 C. Figure 2.4 shows the phosphorescence decay plot of ZnTPP. A least squares fit to the data gives a decay rate constant of  $72.2 \text{ s}^{-1}$  under high vacuum conditions. When oxygen is admitted to the sample chamber the phosphorescence rate constant increases as Figure 2.4 demonstrates. The decay rate constant more than triples when the oxygen pressure is changed from 0 to 0.11 Torr. This is a dramatic change clearly establishing the dynamic nature of phosphorescence quenching of ZnTPP by oxygen when this molecule is adsorbed on NaCl crystals. We hypothesize that quenching of ZnTPP phosphorescence is a result of collisions of gas phase oxygen molecules with ZnTPP molecules adsorbed on the NaCl surface. This explanation is consistent with the dynamic quenching (increase in the phosphorescence decay rate constant) which is observed. Both PdTPP and PtTPP behave in similar fashion. The phosphorescence lifetimes of these dyes are shorter than ZnTPP but dynamic quenching by oxygen is still observed.

Figures 2.5 and 2.6 show the phosphorescence decay plots for PdTPP and PtTPP respectively with and without the addition of oxygen to the sample chamber. The phosphorescence decay rate constant for PdTPP and PtTPP is measured to be  $1230 \text{ s}^{-1}$  and  $1.03 \times 10^4 \text{ s}^{-1}$ , respectively. The increase in decay constant from ZnTPP to PdTPP to PtTPP is attributed to increased spin-orbit coupling of the triplet emitting state with the singlet ground state caused by an increase in atomic number of the central metal atom.

A collisional quenching mechanism predicts that the integrated phosphorescence signal measured with zero delay time should vary inversely with oxygen pressure,  $P$ , (Stern-Volmer kinetics) as follows,

$$\frac{1}{S(\tau=0)} = \frac{k_T}{B} + \frac{kq}{B} P \quad (2.2)$$

where  $k$  has been written as

$$k = k_T + kq P \quad (2.3)$$

Here  $k_T$  is the triplet decay constant measured in the absence of quencher (e.g.  $72.2 \text{ s}^{-1}$  for ZnTPP on NaCl) and  $kq$  is the bimolecular rate constant for collisional quenching. From Eq. (2.2) a plot of the reciprocal of  $S(\tau=0)$  versus oxygen pressure should give a straight line. Figures 2.7-2.9 show the data for oxygen quenching of ZnTPP, PdTPP and PtTPP phosphorescence at room temperature plotted in this manner. The linear fit is reasonably good and provides evidence for the collisional quenching model. The quenching rate constant can be easily calculated by multiplying the ratio of the slope to y-intercept by the triplet decay rate constant,  $k_T$ . At 28 C the bimolecular rate constant for

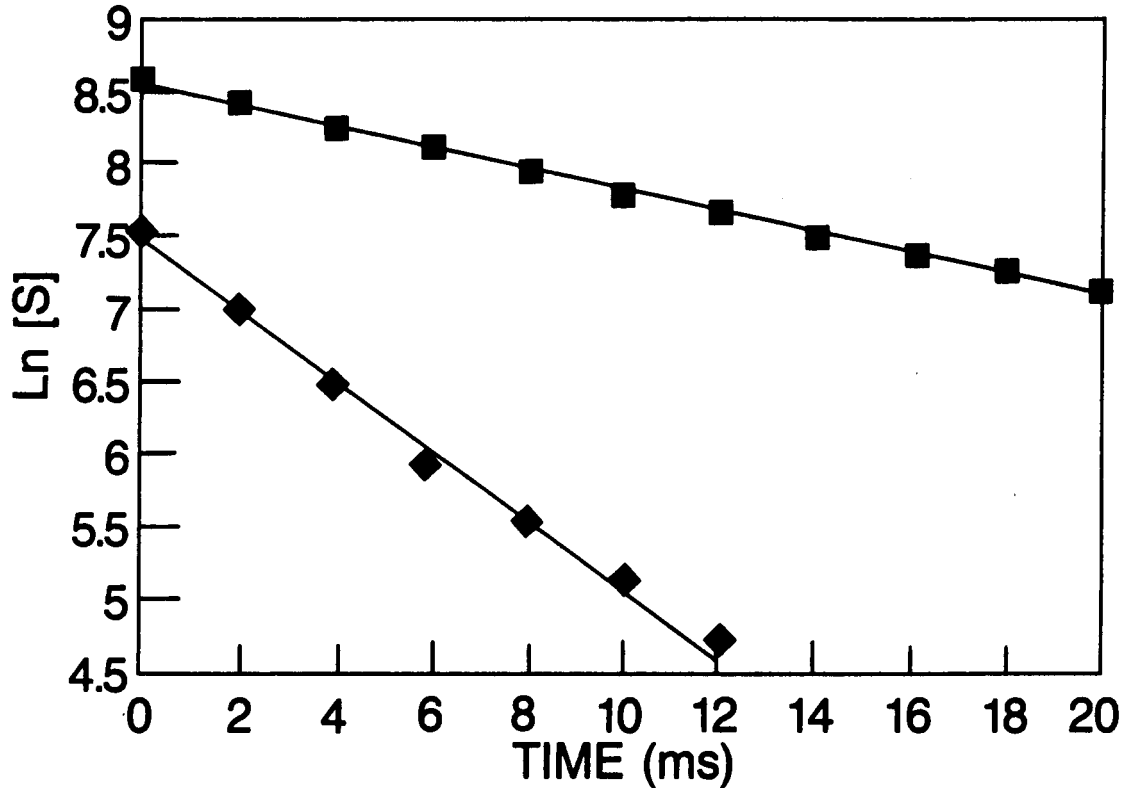


Figure 2.4 ZnTPP on NaCl - phosphorescence decay. Oxygen pressure = 0 Torr,  $\blacklozenge$ ; 0.11 Torr,  $\blacksquare$ . Least squares fit, -.

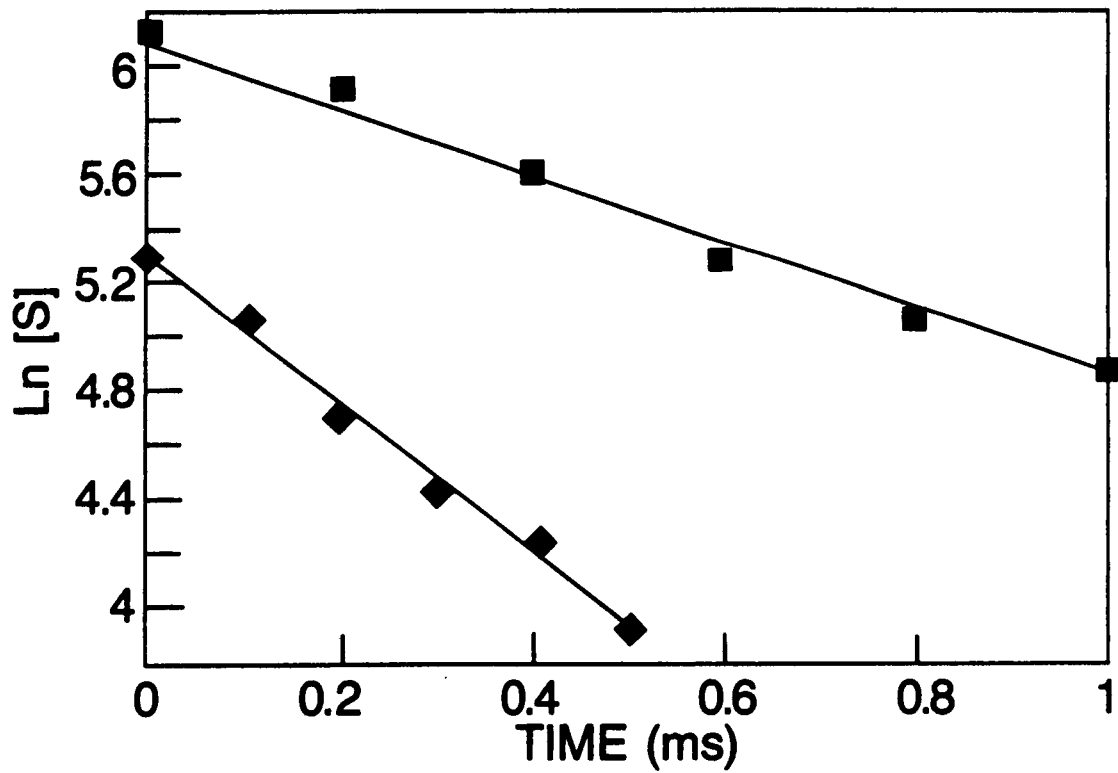


Figure 2.5 PtTPP on NaCl - phosphorescence decay. Oxygen pressure = 0 Torr, ■; 1.0 Torr, ♦. Least squares fit, -.

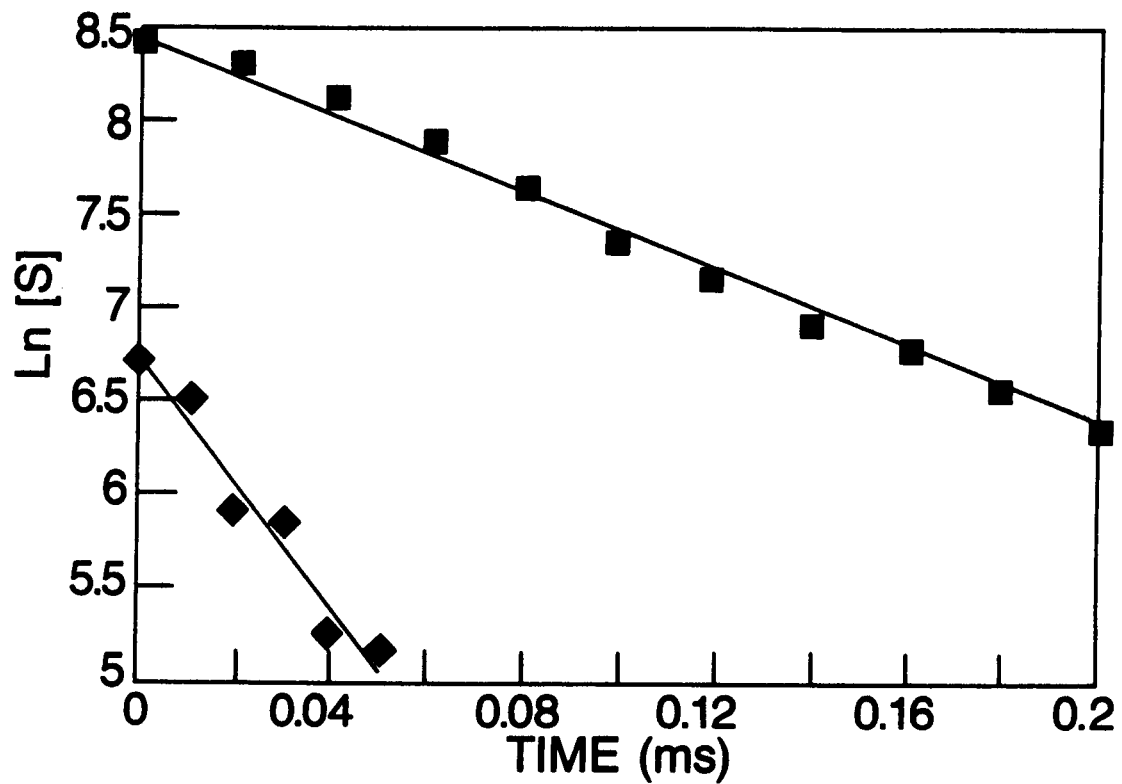


Figure 2.6 PtTPP on NaCl - phosphorescence decay. Oxygen pressure = 0 Torr,  $\blacksquare$ ; 21 Torr,  $\blacklozenge$ . Least squares fit, -.

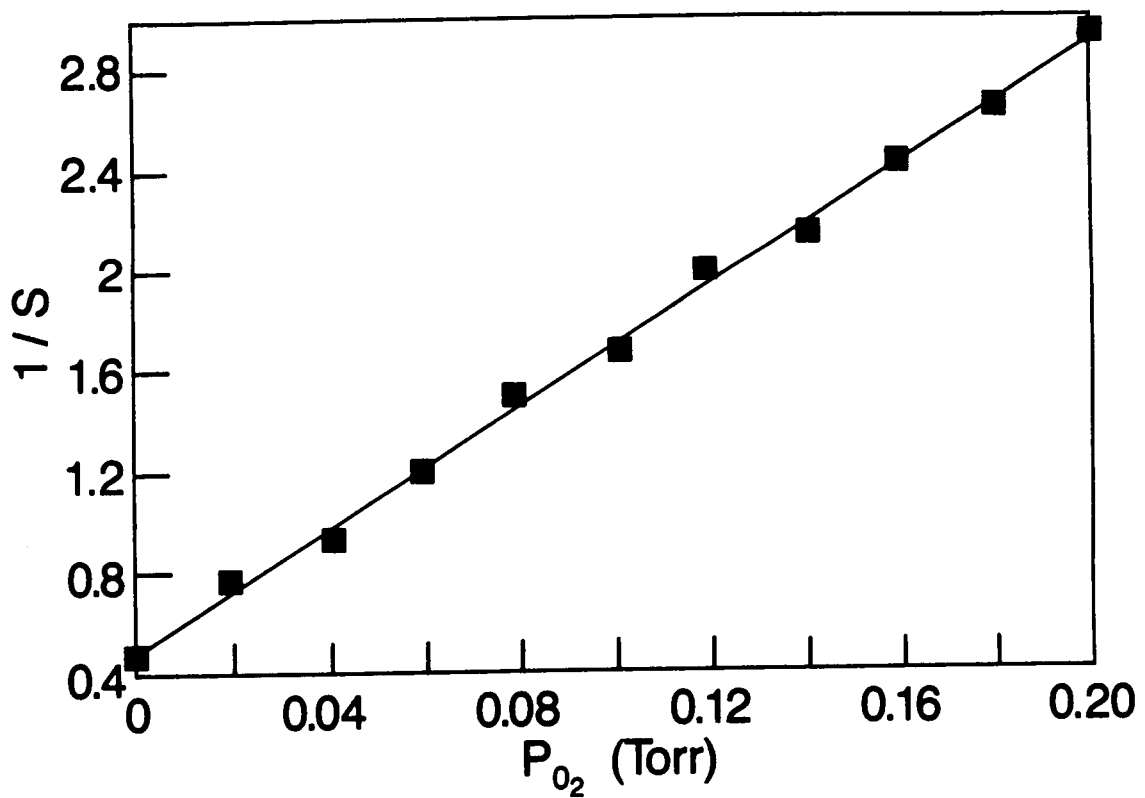


Figure 2.7 ZnTPP on NaCl - quenching of phosphorescence by oxygen. Data, ■; least squares fit, -.

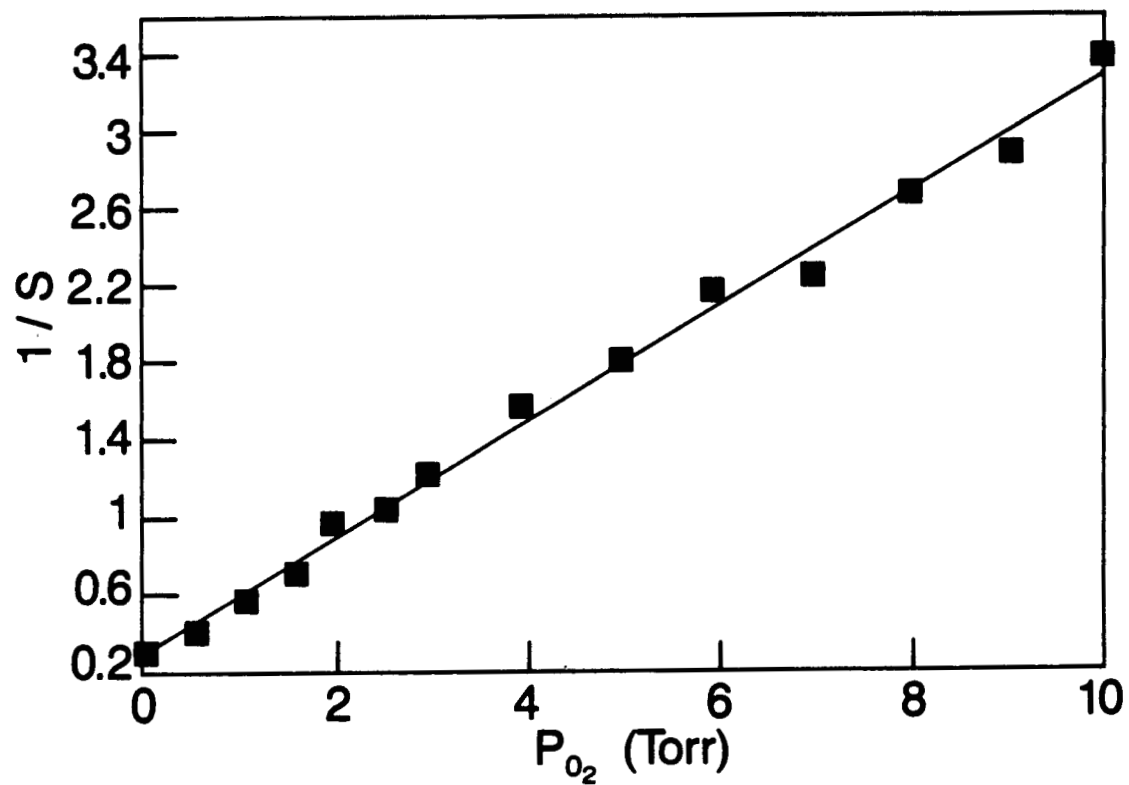
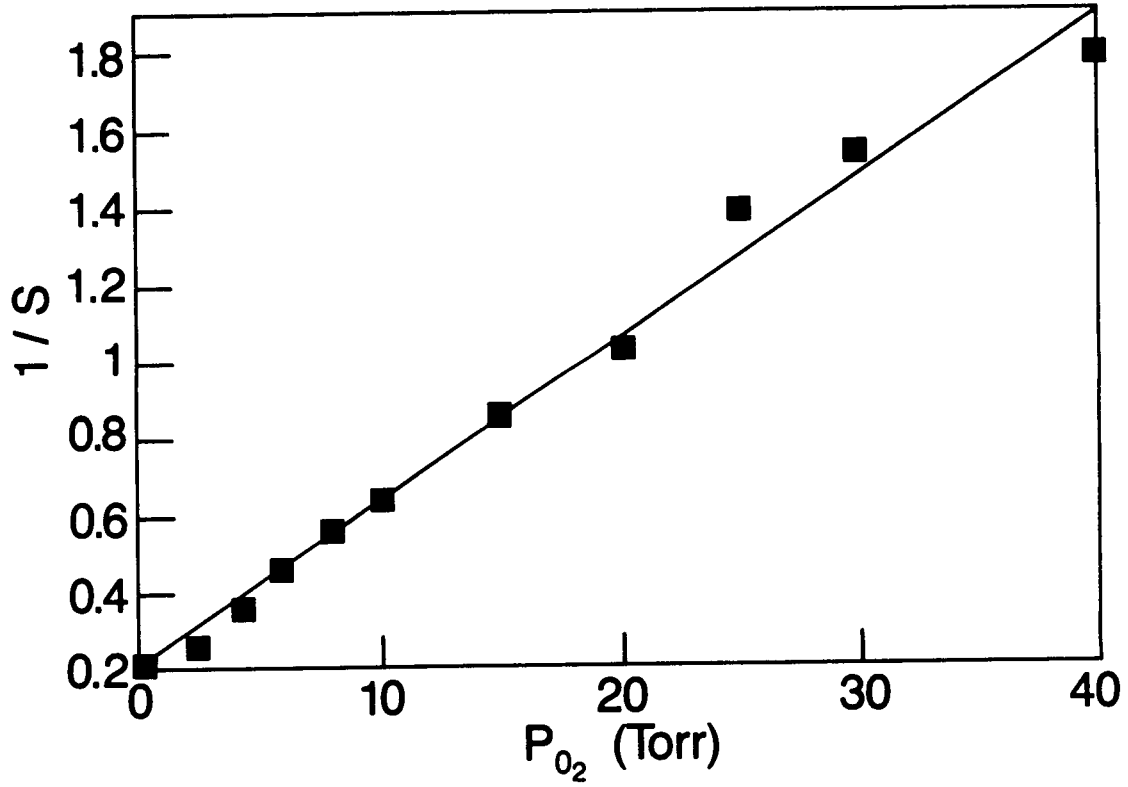


Figure 2.8 PdTPP on NaCl - quenching of phosphorescence by oxygen. Data, ■; least squares fit, -.



**Figure 2.9** PtTPP on NaCl - quenching of phosphorescence by oxygen. Data, ■; least squares fit, -.

quenching of phosphorescence by oxygen is determined to be  $1100 \text{ Torr}^{-1} \text{ s}^{-1}$ ,  $1310 \text{ Torr}^{-1} \text{ s}^{-1}$ , and  $1910 \text{ Torr}^{-1} \text{ s}^{-1}$  for ZnTPP, PdTPP and PtTPP respectively.

The temperature dependence of the quenching rate constant was studied for only one of the porphin molecules-PdTPP. The phosphorescence decay rate constant was measured at 59 C in the absence of oxygen and its value of  $1200 \text{ s}^{-1}$  is equal to the room temperature value to within the experimental uncertainty of the measurement, estimated to be about 5 per cent. The bimolecular rate constant for quenching of PdTPP luminescence by oxygen was determined to be  $911 \text{ Torr}^{-1} \text{ s}^{-1}$  at 59 C.

### 2.3.2 Silica gel substrate - ZnTPP

The quenching of the phosphorescence of ZnTPP adsorbed on silica gel occurs at markedly lower oxygen pressure in comparison with ZnTPP adsorbed on NaCl. At only 0.001 Torr of oxygen the phosphorescence yield has dropped by more than a third of its original value. Another striking difference between the two substrates is noted in the time dependence of the decay rate constant, k, with an increase in oxygen partial pressure. Figure 2.10 shows a plot of the natural logarithm of the integrated phosphorescence signal as a function of delay time,  $\tau$ . At high oxygen pressure (here only 0.01 Torr), the phosphorescence decay signal is determined by more than one rate constant. These phosphorescence decay curves were fit for a biexponential decay and the calculated curve fits are displayed in Figure 2.10 along with the data. The two phosphorescence decay rate constants obtained from the biexponential curve fit, termed the slow and fast component, are listed in Table 1 for 0, 0.001 and 0.01 Torr of oxygen. The slow rate constant does not change with oxygen pressure within the precision of our measurements; however, its value is a factor of two less than the rate constant for the decay of ZnTPP phosphorescence on NaCl. The fast rate constant is more difficult to accurately determine from the curve fits, but it is substantially larger than the slow decay constant. While the origin of the fast component is uncertain, the slow component is probably monomeric ZnTPP and it is this component which has been examined in detail in subsequent experiments.

**Table 1. Rate constants and pre-exponential factors for phosphorescence decay of ZnTPP on silica gel at 25 C.**

Pressure O <sub>2</sub> (Torr)	Slow component k <sub>T</sub> (s <sup>-1</sup> )	B/k <sub>T</sub> (s)	Fast component k <sub>T</sub> (s <sup>-1</sup> )	B/k <sub>T</sub> (s)
0	36	1300	-----	-----
0.001	38	560	160	280
0.01	37	140	250	270

The phosphorescence decay was also investigated at several different temperatures spanning the range of 25 C to 91 C. The data for

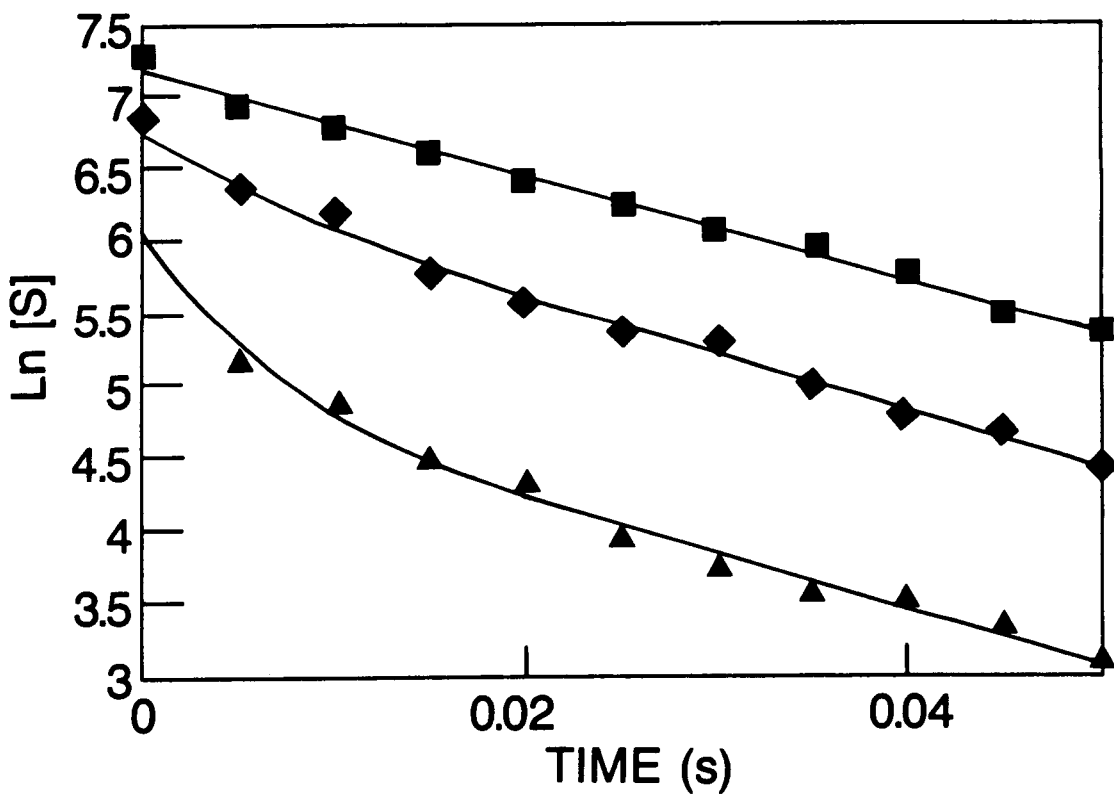


Figure 2.10 ZnTPP on silica gel - phosphorescence decay. Oxygen pressure = 0 Torr, ■; 0.001 Torr, ♦; 0.01 Torr, ▲.  
Least squares fit, -.

the extreme case of 91°C is shown in Figure 2.11. Even at this elevated temperature, a significant change from room temperature in the time dependence of the phosphorescence decay is not observed. The phosphorescence decay plots for all five of the temperatures at which data were obtained are adequately fit with a single exponential decay and give a decay constant of  $36.5 \pm 1.2 \text{ s}^{-1}$ .

The quenching of ZnTPP phosphorescence was measured as a function of gas phase oxygen pressure and these results are shown in Figure 2.12 together with the results of model calculations. The integrated phosphorescence signal was recorded as a function of oxygen pressure as was done when the NaCl substrate was studied; however, for the silica gel studies, the start of the photon collection period was delayed by 10 ms in order to minimize the influence of the fast component which can contribute significantly to the integrated signal at higher oxygen pressure. For a two component decay, the phosphorescence signal integrated from  $t = 10 \text{ ms}$  to infinity is given by the sum of two exponentials each with the form shown in Eq. 2.1. With a delay of 10 ms the fast component is attenuated by approximately a factor of five relative to the slow component. With this delay the slow component remains the dominant component contributing to the integrated phosphorescence signal in the pressure range of 0 to 0.01 Torr. The ordinate of the graph shown in Figure 2.12 is the fraction of triplet molecules (slow decay component predominantly) which are quenched [ $1 - S(P)/S(P=0)$ ]. This quantity is more easily compared with model calculations described below.

The lack of a change in the magnitude of the slow decay component of ZnTPP phosphorescence over a pressure range in which the pre-exponential factor,  $B/k$ , changes by an order of magnitude (see Table 1) is evidence of static quenching. Oxygen is apparently affecting the initial triplet population (proportional to  $B$ ) but not the decay rate constant,  $k$ . This behavior can be understood if it is presumed that quenching occurs by action of oxygen adsorbed on the silica gel rather than by collisions of gas phase oxygen molecules with ZnTPP. If oxygen is strongly bound to silica gel, only those ZnTPP molecules which are very close to adsorbed oxygen when photoexcited will be quenched. ZnTPP molecules which do not have neighboring oxygen molecules at the time of photoexcitation will phosphoresce with very little probability of being quenched (assuming the mobility of both oxygen and of ZnTPP on the silica gel surface is low). As the oxygen pressure is increased, the fraction of the silica gel surface covered by adsorbed oxygen increases thus increasing the probability of ZnTPP phosphorescence quenching.

Phosphorescence quenching data were fit with a simple model of oxygen adsorption on silica gel. It is assumed that adsorption of oxygen to a quenching site can be described by a two component Langmuir adsorption isotherm,<sup>11</sup>

$$\Theta = bP/(1+bP+b'P') \quad (2.4)$$

where  $\Theta$  is the fraction of quenching sites occupied by oxygen,  $P$  is the partial pressure of oxygen,  $b$  is the Langmuir constant for oxygen and the prime after a symbol identifies a property or variable belonging

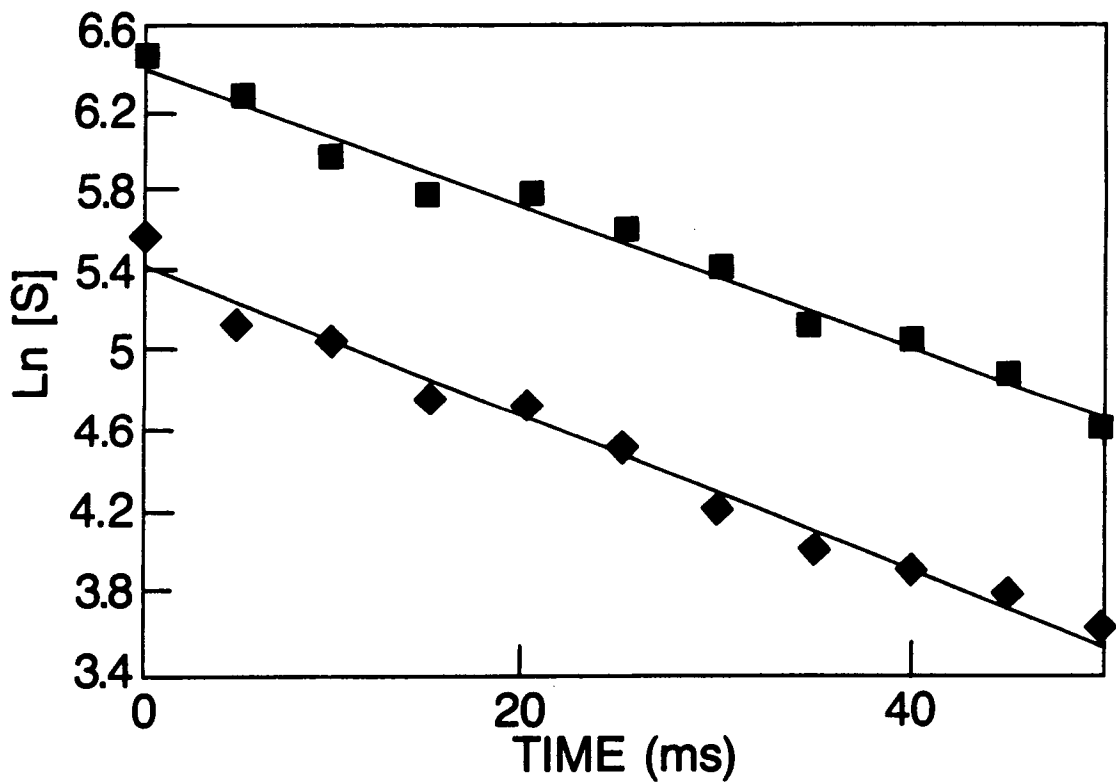
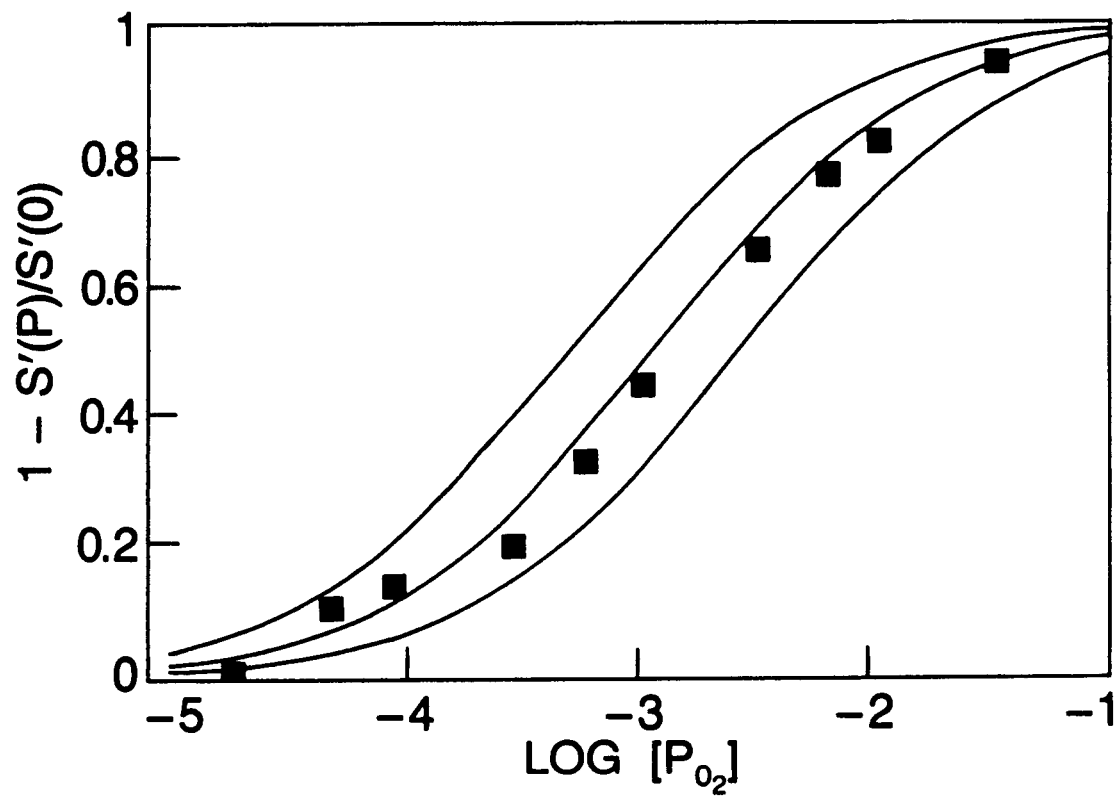


Figure 2.11 ZnTPP on silica gel - phosphorescence decay as a function of temperature. Temperature = 25 C, ■; 91 C, ◆. Least squares fit, -.



**Figure 2.12** ZnTPP on silica gel - quenching of phosphorescence by oxygen. Temperature = 25 C. Data, ■; curve fit (see text), -.

to water. Equation 2.4 can be simplified if  $b'P' \gg 1$ . Assuming the inequality is valid, the fraction of quenching sites occupied by oxygen can be written as

$$\theta = aP/(1+aP) \quad (2.5)$$

where  $a = b/b'P'$ . Using the expression for the Langmuir constant derived from gas kinetic theory, namely

$$b = \{A\tau_0/(2\pi mkT)^{1/2}\} \exp(-Q/RT) \quad (2.6)$$

the constant,  $a$ , in Eq. 2.5 is given by

$$a = (m'/m)^{1/2}(\tau_0/\tau_0') (A/A') (1/P') \exp[-(Q-Q')/RT] \quad (2.7)$$

Here  $m$  is the mass of the oxygen molecule,  $A$  is the cross sectional area of the adsorption site of oxygen, and  $\tau_0$  is the average residence time of oxygen at the adsorption site if the adsorption energy  $Q$  were zero. The other symbols have their usual meaning. The ratio of cross sectional areas and the ratio of residence times at zero adsorption energy are not expected to differ from unity by a substantial amount and were set equal to one in the model calculations. The partial pressure of water,  $P'$ , was taken to be equal to the base pressure of the sample chamber,  $1 \times 10^{-5}$  Torr at room temperature. The use of Eq. 2.5 is justified only if the inequality  $b'P' \gg 1$  is true. Using Eq. 2.6 for  $b'$  together with values of  $1 \times 10^{-19}$  m<sup>2</sup> for  $A'$ ,  $1 \times 10^{-12}$  s for  $\tau_0'$ , and  $1 \times 10^{-5}$  Torr for  $P'$ , the inequality in  $b'P'$  is transformed to an inequality in the adsorption energy of water,  $Q' > 65$  kJ/mole.

It is reasonable to expect the adsorption sites surrounding ZnTPP on silica gel to vary in adsorption energy for both water and oxygen. To obtain the fraction of quenching sites occupied at oxygen pressure  $P$ , the Langmuir fraction given by Eq. 2.5 must be multiplied by the energy distribution function,  $G(E)$  and integrated with respect to  $E = Q - Q'$  giving

$$F(P) = \int \theta(P, E) G(E) dE. \quad (2.8)$$

The function  $F(P)$  then is equated with the fraction of ZnTPP phosphorescence which is quenched by oxygen. A normalized Gaussian distribution was chosen for the weighting function,

$$G(E) = \{1/\sigma\sqrt{\pi}\} \exp[-(E-E_m)^2/\sigma^2] \quad (2.9)$$

characterized by the mean energy difference,  $E_m = (Q - Q')_m$ , and the half width,  $\sigma$ , both treated as adjustable parameters.  $E_m$  was varied in steps of 1 kJ/mole from 25 to -25 kJ/mole and  $\sigma$  was varied in steps of 0.5 kJ/mole from 0.5 to 20 kJ/mole. The sum of the variances between the model calculation and the experimental quenching fraction at pressure  $P$ ,  $1 - S(P)/S (P = 0)$ , was computed for each value of  $E_m$  and  $\sigma$  and was termed the deviation. The best fit was identified by the values of  $E_m$  and  $\sigma$  which resulted in a minimum deviation. For luminescence quenching data taken at 23 C, the minimum deviation was obtained for  $E_m = -11$  kJ/mole and  $\sigma = 4$  kJ/mole. The model calculation obtained with these fitting parameters is shown in Figure 2.12 as the center solid curve. The fit to the experimental data is reasonably good. The two outer curves in Figure 2.12 were obtained from model calculations in which  $E_m$  deviates from its optimal value by only 2 kJ/mole. These curves are clearly poor fits to the experimental data indicating that the calculation results are quite sensitive to the fitting parameter  $E_m$ .

The modified Langmuir adsorption model which was used to analyze the phosphorescence quenching of ZnTPP on a silica gel substrate predicts a temperature dependence for  $F(P)$  which enters the function through the energy term in a (Equation 2.7). The fraction of phosphorescence which is quenched at any fixed oxygen partial pressure should change with temperature. However, the adsorption energies of sites on silica gel are not expected to change until quite high temperatures are reached and chemical bonds of surface siloxyl groups are broken. Therefore the values of the fitting parameters,  $E_m$  and  $\sigma$ , which describe the site adsorption energy distribution are expected to remain unchanged as the temperature is increased. To test this behavior, phosphorescence quenching data were collected at 60 C, and the curve fitting routine was performed varying both  $E_m$  and  $\sigma$ . The pre-exponential of  $a$  was reduced by a factor of 2 because at 60 C the base pressure of the sample chamber rose to approximately twice its value at room temperature. Figure 2.13 shows the experimental data and the best curve fit which was obtained. The minimum variance occurred when  $E_m$  and  $\sigma$  assumed values identical with those found using the 23 C data.

### 2.3.3 Silica gel - acriflavine

The quenching of acriflavine supported on silica gel is of interest because this system have been studied for over half a century.<sup>1,12-19</sup> Even though the oxygen quenching of luminescence of this dye has been reported and discussed for some time, a thorough analysis of the results in the context of oxygen adsorption on the silica gel substrate has not been attempted. The results and analysis of the quenching of ZnTPP on silica gel by oxygen have been presented first because the photokinetics of acriflavine is somewhat more complicated than that of porphin.

At room temperature acriflavine emits both phosphorescence and delayed fluorescence derived from thermal repopulation of the first excited singlet state from the triplet. Figure 2.14 shows a graph of the natural logarithm of the photon counter signal,  $\$$ , (counts collected over a 1 ms time window), as a function of time after the excitation pulse. Since the photon counter signal for the acriflavine studies was obtained under conditions in which this signal was integrated for only 1 ms, a time much shorter than the luminescence

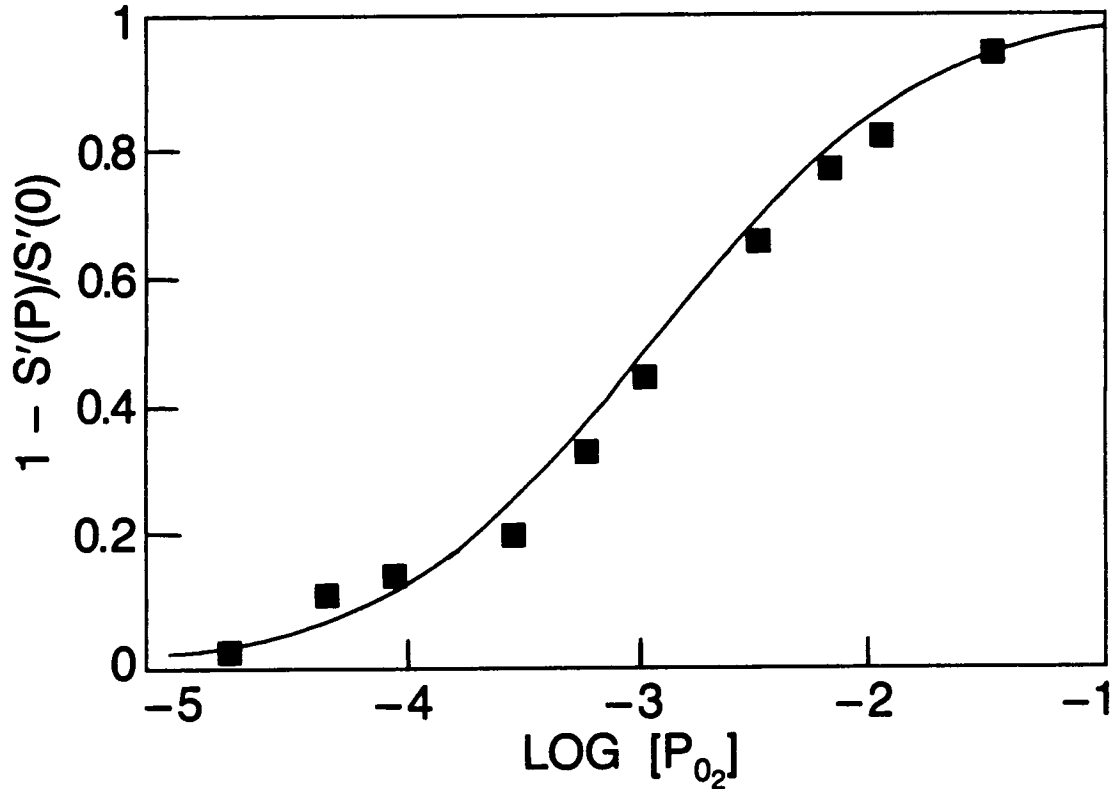
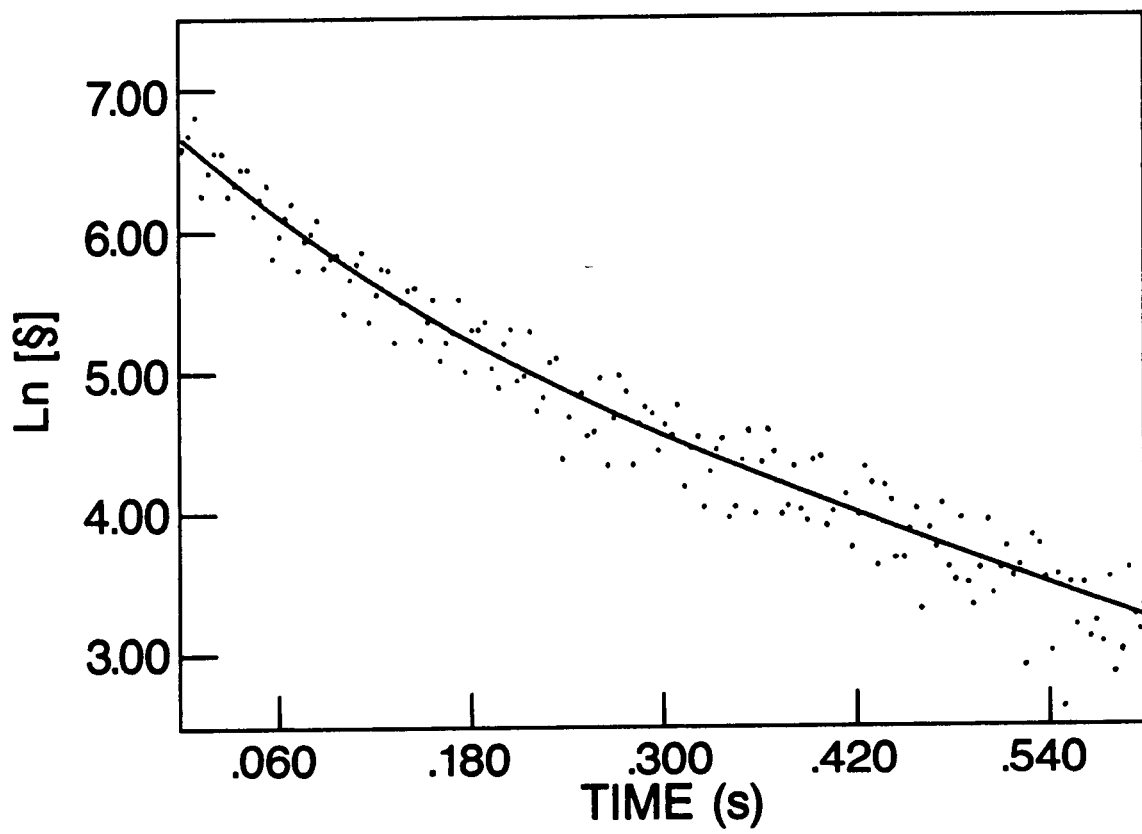


Figure 2.13 ZnTPP on silica gel - quenching of phosphorescence by oxygen. Temperature = 60 C. Data, ■; curve fit (see text), -.



**Figure 2.14** Acriflavine on silica gel - phosphorescence decay.  
Data, dotted line; biexponential curve fit, -.

lifetime, the ordinate of Figure 2.14 is proportional to the luminescence intensity rather than the intensity divided by the decay rate constant as was the case for the porphin experiments.

As clearly seen in Figure 2.14, the luminescence decay of acriflavine on silica gel is not well described by a single exponential even with the sample under high vacuum. A fit of the data to the sum of two exponentials matches the data much more closely. The biexponential curves were fitted to acriflavine luminescence data using a curve fitting routine available in the ASYST data analysis program and the solid curve in Figure 2.14 shows the result of this curve fitting effort. A biexponential luminescence decay has been previously reported by Rosenberg and Humphries<sup>19</sup> who assigned the slow component to monomeric acriflavine and the fast component to acriflavine dimers.

Figures 2.15-2.18 show the dependence of the slow decay constant,  $k_s$ , the fast decay constant,  $k_f$ , and the respective pre-exponentials,  $I_s$  and  $I_f$ , on the partial pressure of oxygen in the sample chamber. From the data presented in Figure 2.15 for the oxygen partial pressure dependence of  $k_s$ , it appears that the value of this rate constant increases as pressure is increased. Some dynamic quenching, possibly associated with the movement of oxygen on the silica gel surface, is observed. The change, however, is not large (less than  $1 \text{ s}^{-1}$  per decade of change in oxygen pressure is observed). In contrast to the change in the rate constant, the value of  $I_s$  changes dramatically as the partial pressure of oxygen is increased as is shown in Figure 2.16. A factor of two decrease in  $I_s$  occurs rather abruptly at  $10^{-5}$  Torr. As the oxygen pressure is increased further, a much more gradual change in the value of  $I_s$  is observed.

A change in the value of  $k_f$  as the oxygen pressure increases, shown in Figure 2.17, is more difficult to observe because of the scatter in the data. A small increase in  $k_f$  may occur as oxygen pressure is increased. The pre-exponential of the fast decaying component,  $I_f$ , shown in Figure 2.18, increases in value as oxygen pressure is increased up to a partial pressure of  $10^{-4}$  Torr. Above this pressure,  $I_f$  rapidly falls to less than a fourth of its initial value at  $10^{-2}$  Torr.

Because of the complexity of the emission behavior for acriflavine and the presence of a weak but sizable dynamic quenching, no attempt was made to fit the acriflavine data to the absorption model.

### 2.3.4 Polymer substrate - porphins

Initially it was thought that dye coated on nylon mesh by deposition from solution was adsorbed to surface sites on the nylon fibers. However, the luminescence quenching rates measured for this system are markedly smaller than that for dye deposited on NaCl. Furthermore, the magnitude of these quenching rates can be explained if it is assumed that the dye has become incorporated inside the nylon polymer solid. For this reason the results of porphin dyes deposited on nylon mesh are included in this section together with results for dye which is intentionally doped in poly(styrene), 2PVN and poly(methyl methacrylate). It is also believed that dye deposited on the cellulose substrate was incorporated inside the cellulose polymer structure and results obtained with this substrate material are also included in this section.

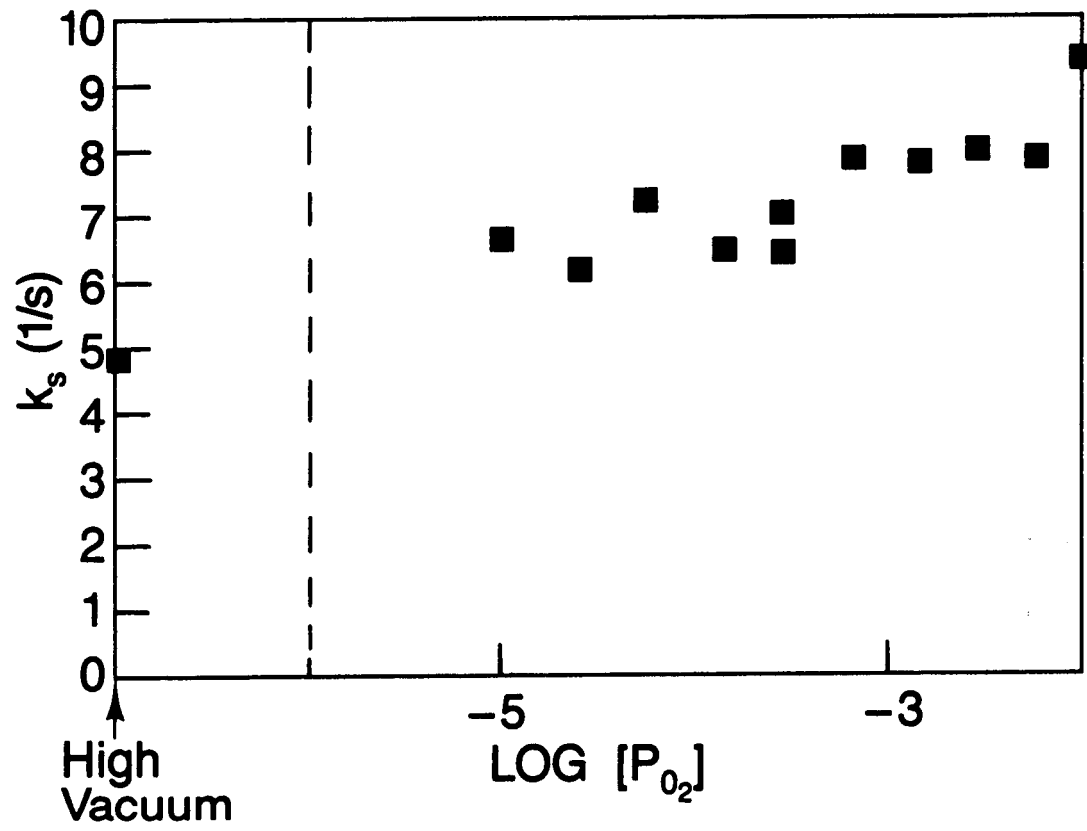


Figure 2.15 Acriflavine on silica gel -  $k_s$  versus oxygen pressure.

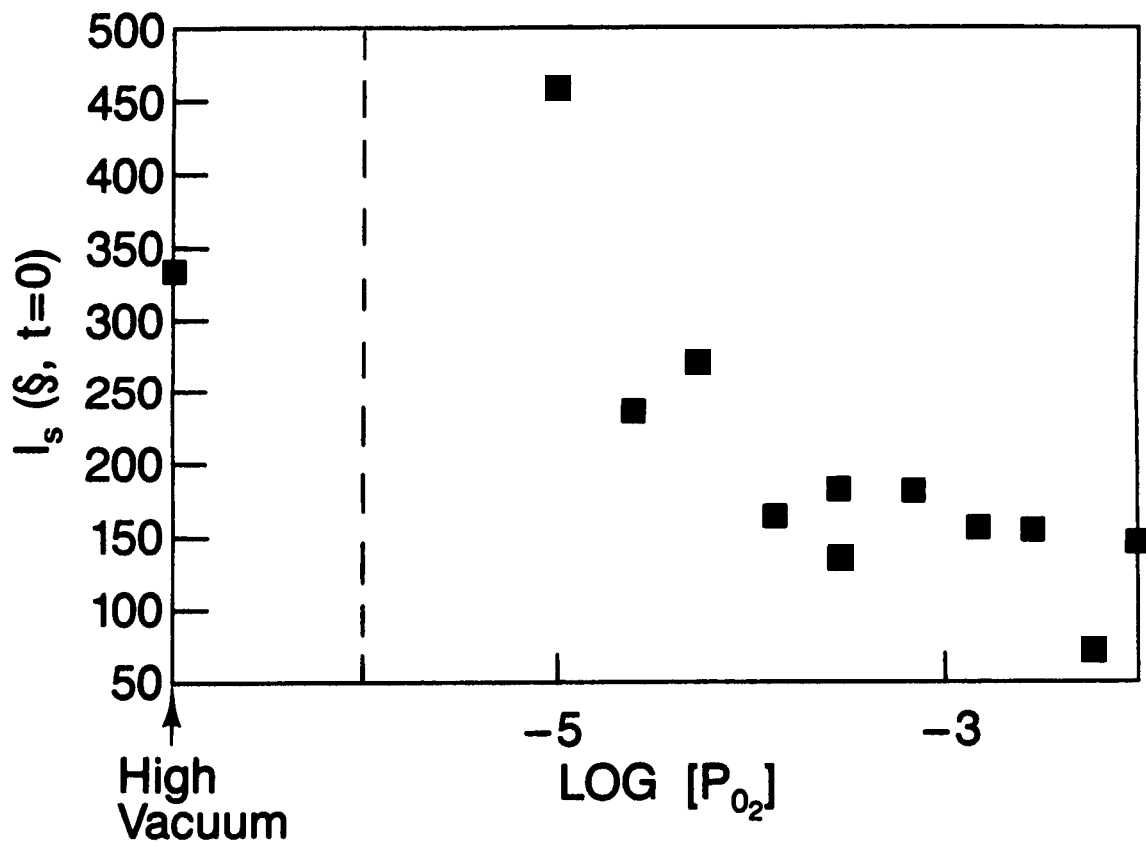


Figure 2.16 Acriflavine on silica gel -  $I_s$  versus oxygen pressure.

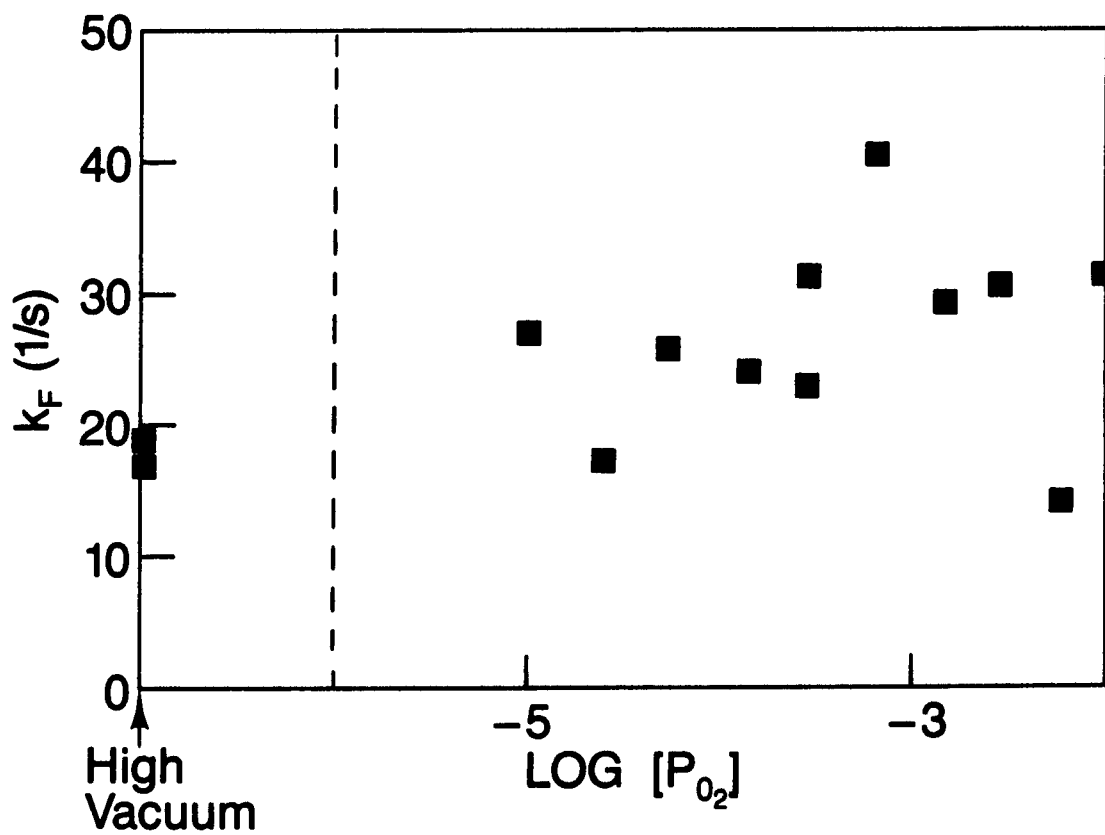


Figure 2.17 Acriflavine on silica gel -  $k_f$  versus oxygen pressure.

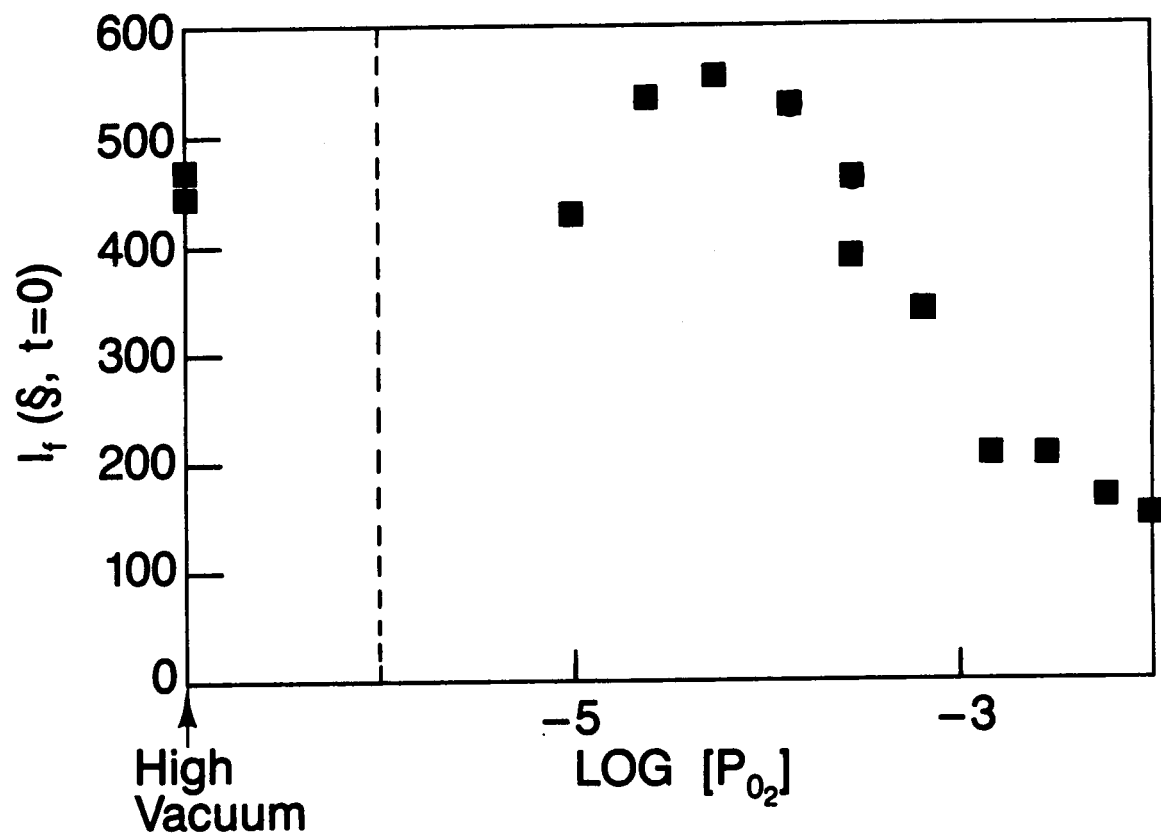


Figure 2.18 Acriflavine on silica gel -  $I_f$  versus oxygen pressure.

Several studies of dye luminescence quenching are reported in this section. First, data showing oxygen quenching of ZnTPP luminescence in various polymer substrates at room temperature are presented. Next, the rates of quenching by oxygen of a series of porphins (ZnTPP, PdTPP, and PtTPP) deposited on nylon, are compared. Finally, the temperature dependence of the quenching rate constant was also examined for one dye/polymer system, namely, ZnTPP on nylon.

The phosphorescence decay of ZnTPP embedded in various polymers was recorded with the sample under high vacuum. Figures 2.19-2.23 are the plots of the natural logarithm of the luminescence signal vs. delay time for ZnTPP doped nylon, poly-(methylmethacrylate), poly(styrene), cellulose and 2PVN. These figures also show the phosphorescence decay when the sample is exposed to oxygen. In all cases the phosphorescence quenching is observed to be dynamic. The phosphorescence decay constants in the absence of oxygen are listed in Table 2. The polymer substrates appear to group into two sets according to the magnitude of  $k_T$ . The three polymers which were soluble in chlorinated hydrocarbon solvents, poly(methylmethacrylate), poly(styrene) and 2PVN, all have a value of  $k_T$  close to  $15\text{ s}^{-1}$ . The other two polymers, nylon and cellulose, have a value for  $k_T$  twice as large, namely,  $32\text{ s}^{-1}$ .

Table 2. Permeability of oxygen in various polymers at 25 C.

Polymer	$k_T(\text{s}^{-1})$	Permeability ( $\text{cm}^{-1}\text{Torr}^{-1}\text{s}^{-1}$ )	
		This work	Literature (1)
2PVN	18	$6 \times 10^8$	----
Poly(styrene)	13	$2 \times 10^8$	$7 \times 10^8$
Poly(methyl methacrylate)	14	$1 \times 10^8$	$3 \times 10^8$ (2)
Nylon	33	$3 \times 10^7$ (3)	$1 \times 10^7$ (4)
Cellulose	32	$6 \times 10^5$	$6 \times 10^5$ (1)

(1) H. Yasuda and V. Stannett, "Permeability Coefficients", Handbook of Polymers, 2nd edition, editors J. Brandrup and E.H. Immergut, (Wiley, NY), 1975, p. III-229.

(2) Permeability value is for poly(ethylmethacrylate).

(3) Measured value is for nylon 66.

(4) Permeability value is for nylon 6.

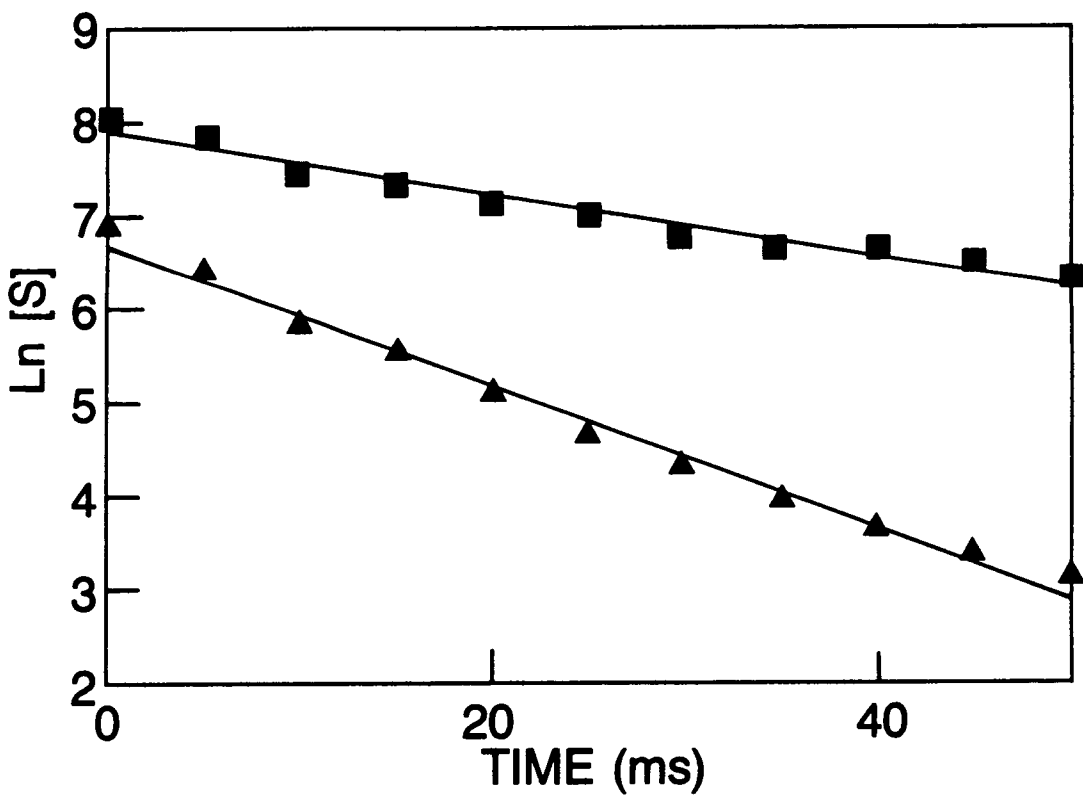


Figure 2.19 ZnTPP on nylon - phosphorescence decay. Oxygen pressure = 0 Torr, ▲; 4.5 Torr, ■. Least squares fit, -.

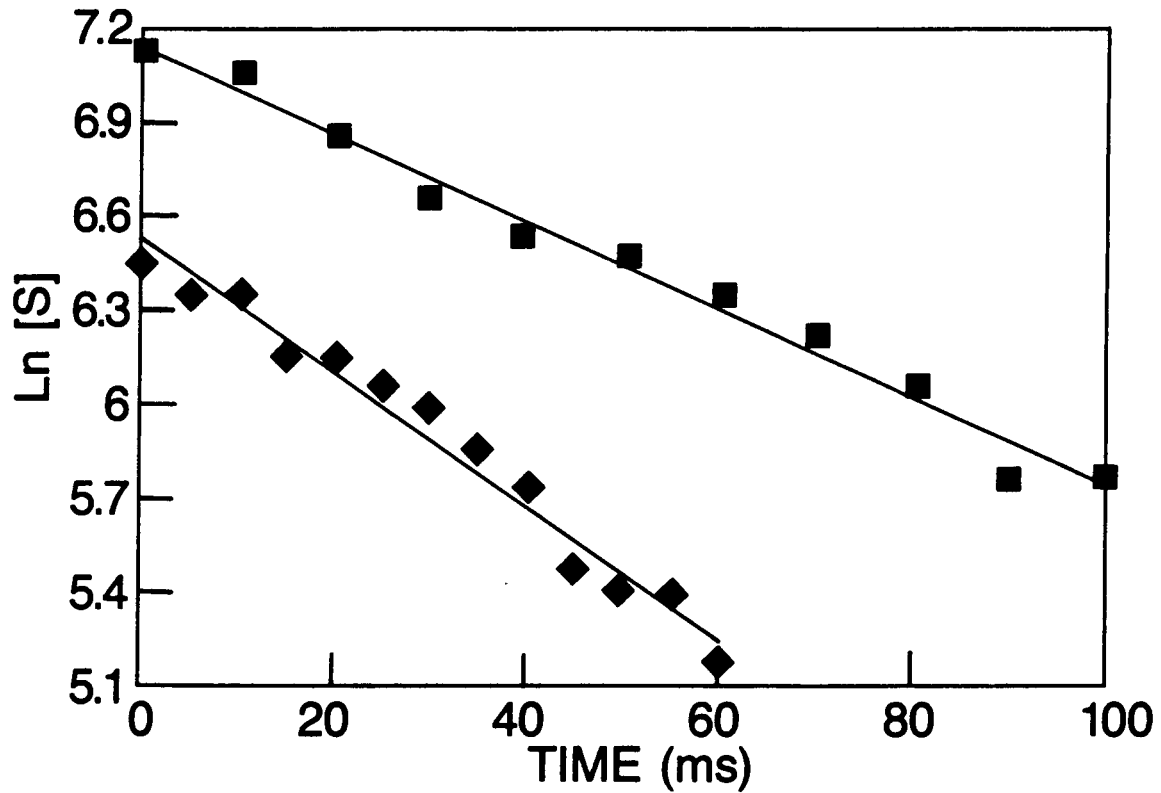


Figure 2.20 ZnTPP on poly(methylmethacrylate) - phosphorescence decay. Oxygen pressure = 0 Torr, ■; 0.13 Torr, ◆. Least squares fit, -.

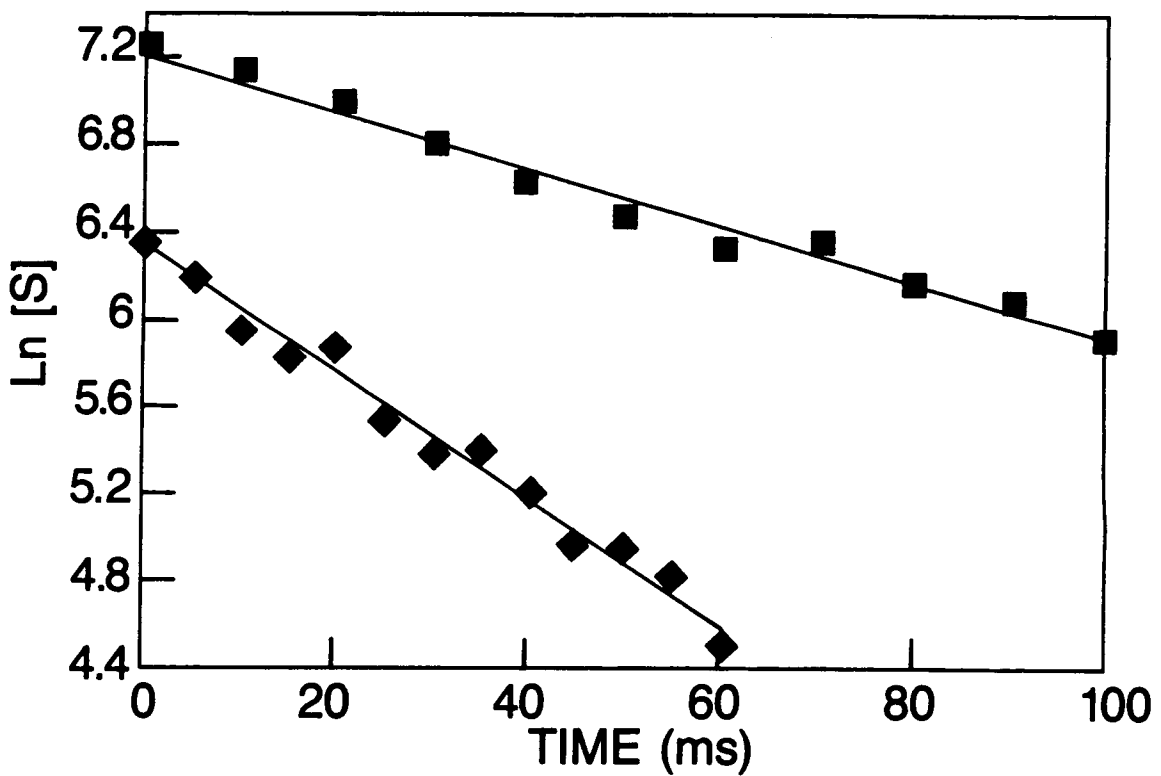


Figure 2.21 ZnTPP on poly(styrene) - phosphorescence decay.  
Oxygen pressure = 0 Torr, ■; 0.08 Torr, ♦. Least squares fit, -.

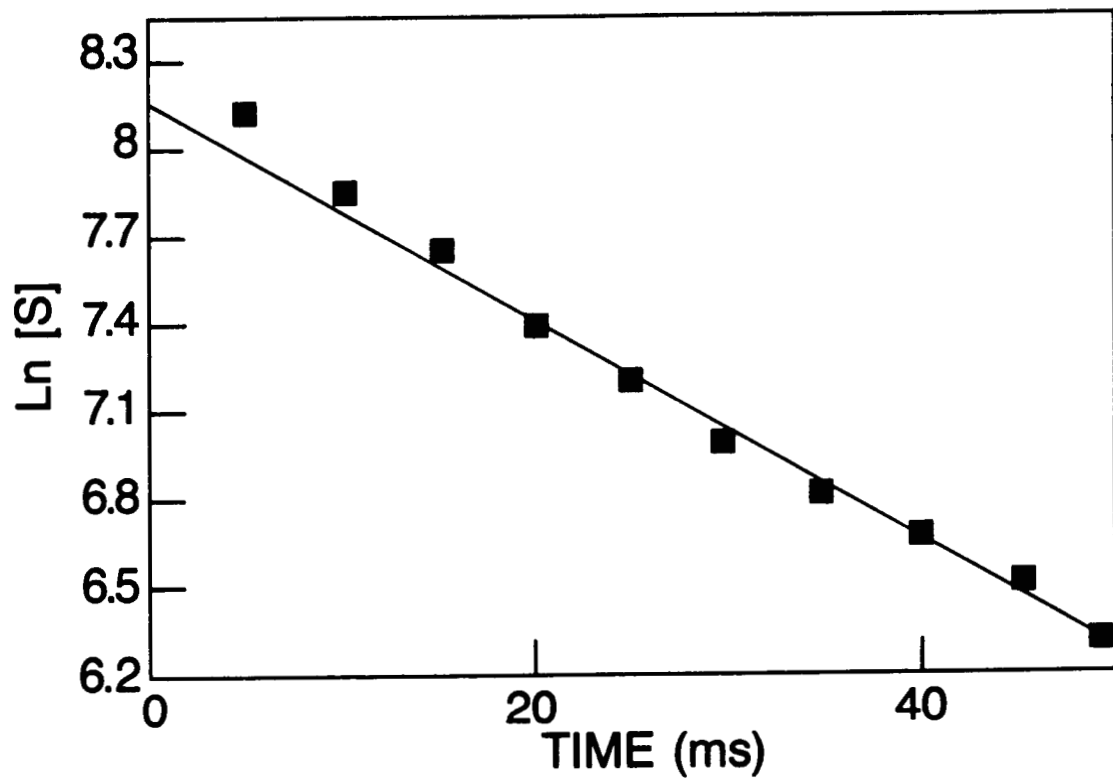


Figure 2.22 ZnTPP on cellulose - phosphorescence decay. Oxygen pressure = 0 Torr, ■. Least squares fit, -.

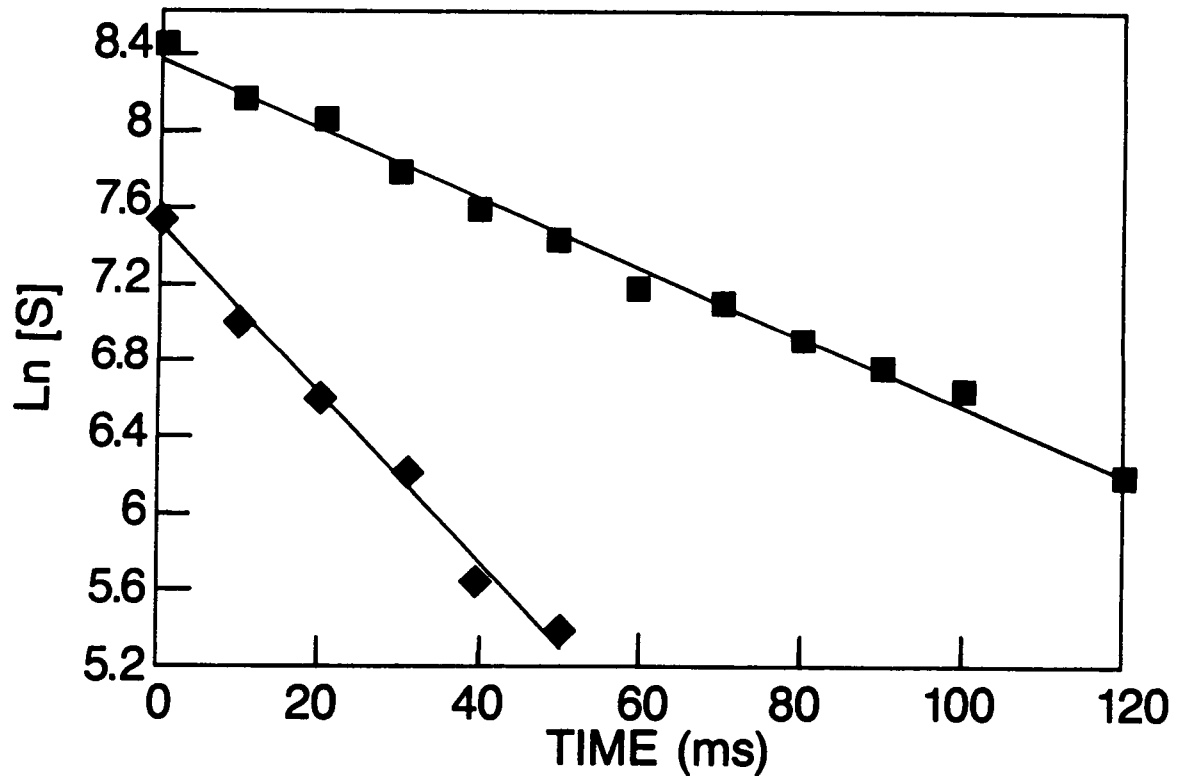


Figure 2.23 ZnTPP on 2PVN - phosphorescence decay. Oxygen pressure = 0 Torr, ■; 0.06 Torr, ◆. Least squares fit, -.

Figures 2.24-2.28 show plots of the phosphorescence signal as a function of the partial pressure of oxygen in the gas phase. The data are plotted as the reciprocal of the phosphorescence signal versus oxygen partial pressure with the expectation that the quenching mechanism is the same for all of the polymer substrates. A solution phase model for phosphorescence quenching adequately explains most of our data. Quenching is believed to occur when molecular oxygen dissolved in the polymer diffuses to an excited dye molecule. The integrated phosphorescence signal,  $S$ , is taken to be linearly proportional to the quantum yield for phosphorescence and as such can replace it in the Stern-Volmer expression now written as,

$$1/S = (k_T/B) + (kq/B)C \quad (2.10)$$

Here  $C$  is the concentration of oxygen dissolved in the polymer in moles/liter,  $k_T$  is the phosphorescence lifetime in the absence of oxygen,  $B$  is the proportionality constant which multiplies the quantum yield to give the phosphorescence signal, and  $kq$  is the quenching rate constant. For simplicity it is assumed that the concentration of oxygen does not vary throughout the polymer, otherwise  $C$  represents an average concentration.

The bimolecular rate constant,  $kq$ , appearing in Eq. 2.10 is given by

$$kq = 4\pi\alpha(D_d+D_0)(r_d+r_0) \quad (2.11)$$

where  $D_d$  is the diffusivity of the dye in the polymer,  $D_0$  is the diffusivity of oxygen in the polymer, and  $r_d$  and  $r_0$  are the effective radii of the dye molecule and of the oxygen molecule, respectively. The factor of 4 appearing in Eq. 2.11 is the probability that an encounter by an excited dye molecule with oxygen will lead to quenching of phosphorescence. Equation 2.11 can be simplified by assuming that the radius of the dye molecule is much larger than that of oxygen and the diffusivity of oxygen is much larger than that of the dye. With these assumptions Eq. 2.11 becomes approximately

$$kq = 4\pi\alpha(D_0)(r_d) \quad (2.12)$$

The concentration of oxygen in the polymer is considered to be a linear function of the partial pressure of oxygen in the gas phase: the proportionality constant which connects the concentration of oxygen in the polymer with the partial pressure of this gas is the solubility,  $X$ , (moles/liter-Torr).  $C$  can be replaced in Eq. 2.10 by  $XP$  where  $P$  is the partial pressure of oxygen in the gas phase. Making this substitution as well as using the expression for  $kq$  appearing in Eq. 2.12, one obtains

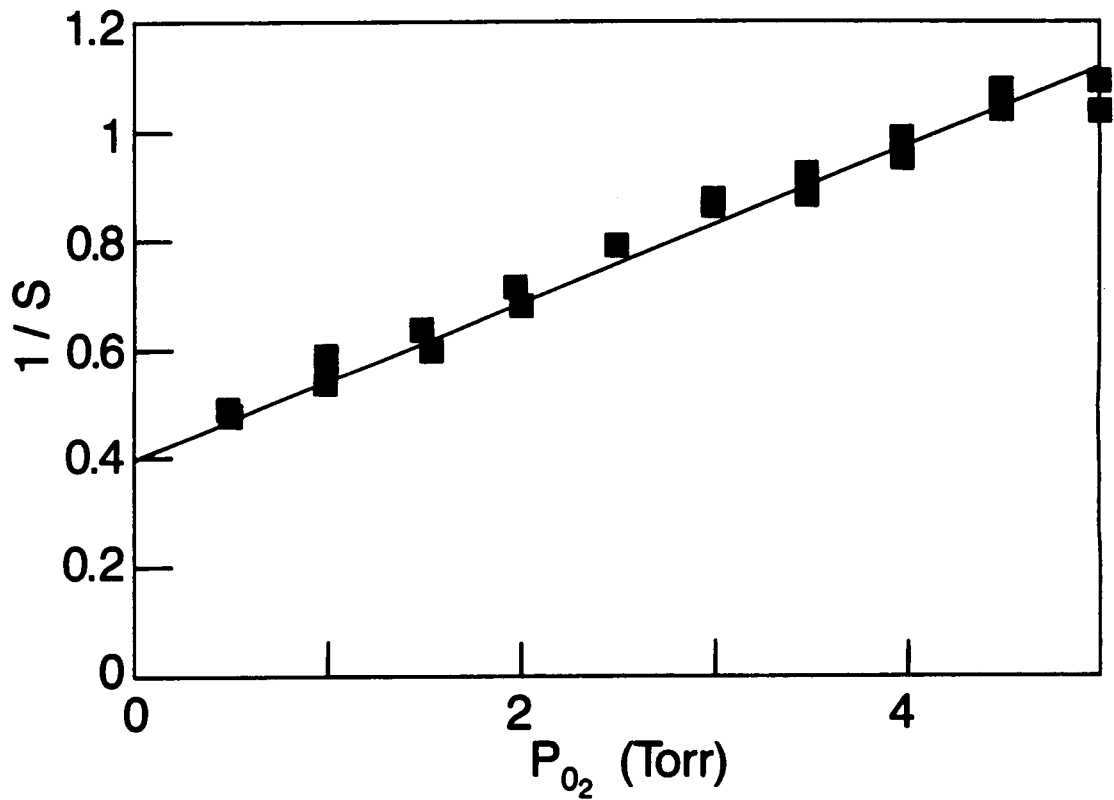


Figure 2.24 ZnTPP on nylon - quenching of phosphorescence by oxygen. Data, ■; least squares fit, -.

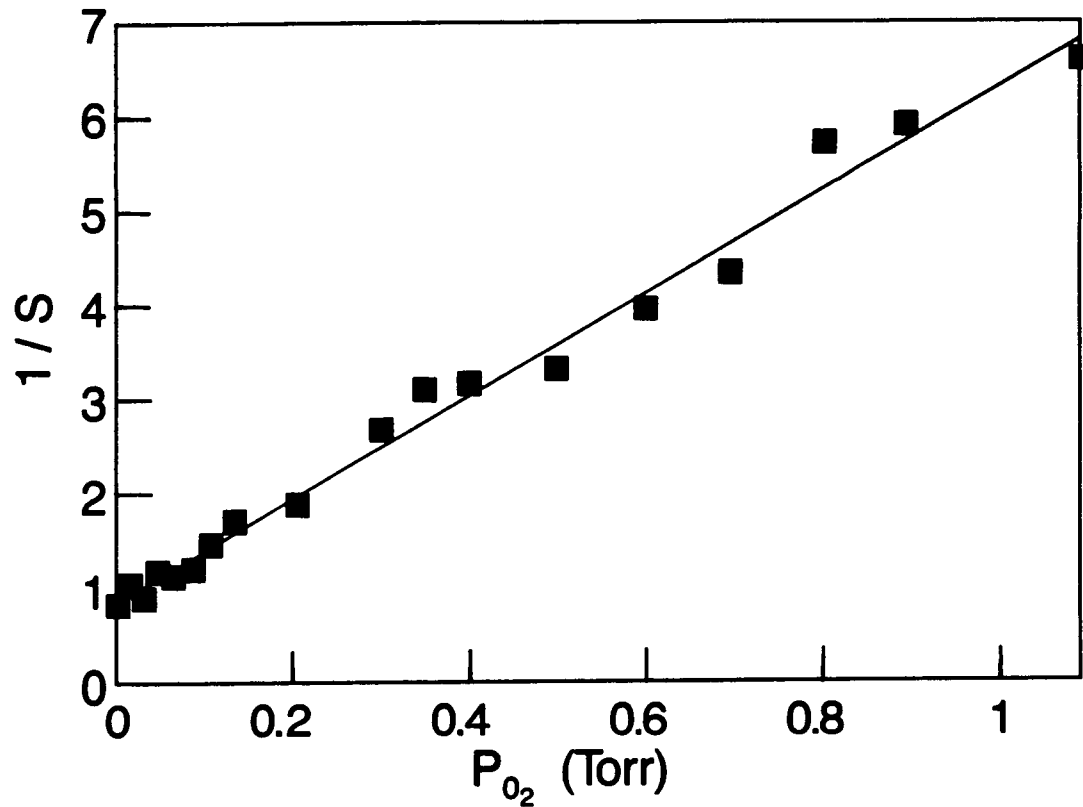


Figure 2.25 ZnTPP on poly(methylmethacrylate) - quenching of phosphorescence by oxygen. Data, ■; least squares fit, -.

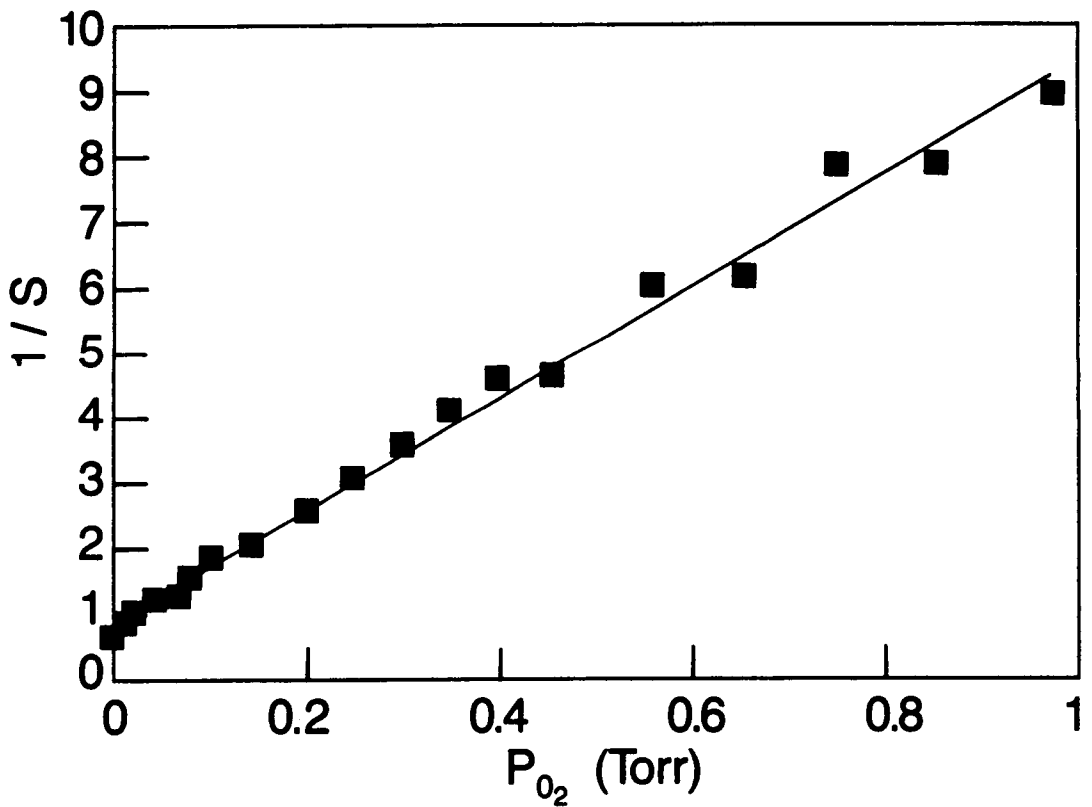


Figure 2.26 ZnTPP on poly(styrene) - quenching of phosphorescence by oxygen. Data, ■; least squares fit, -.

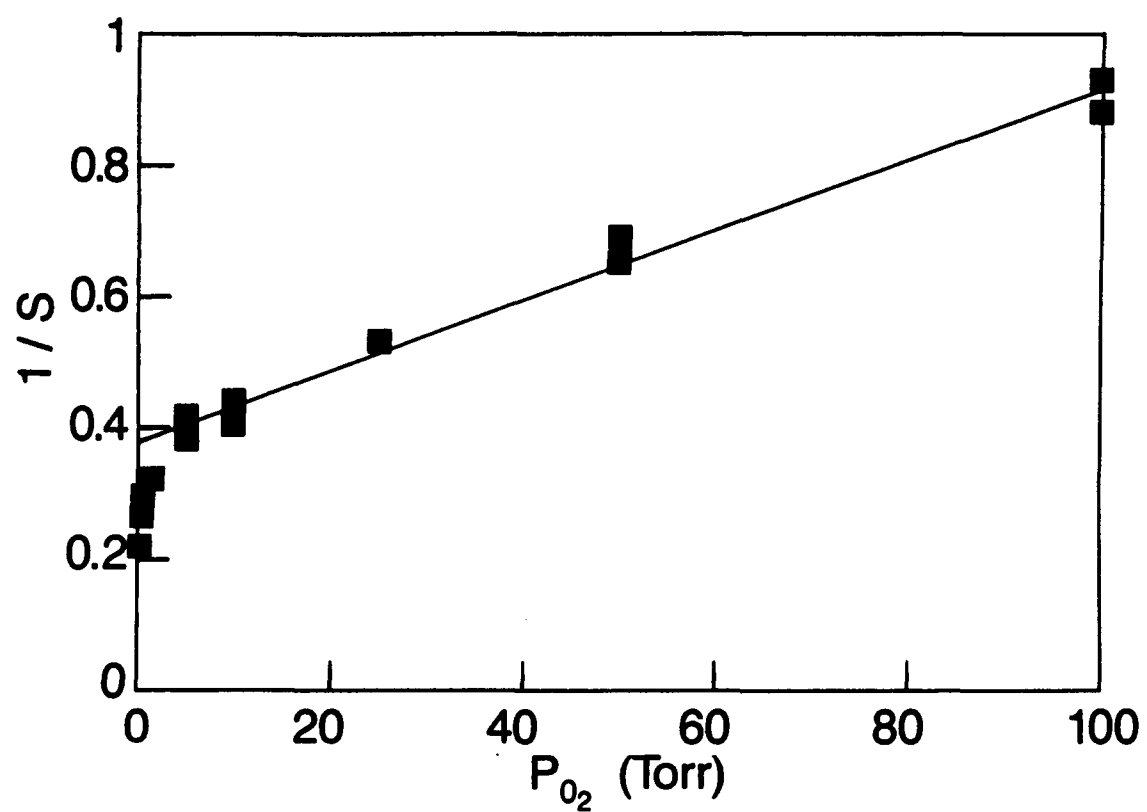


Figure 2.27 ZnTPP on cellulose - quenching of phosphorescence by oxygen. Data, ■; least squares fit, -.

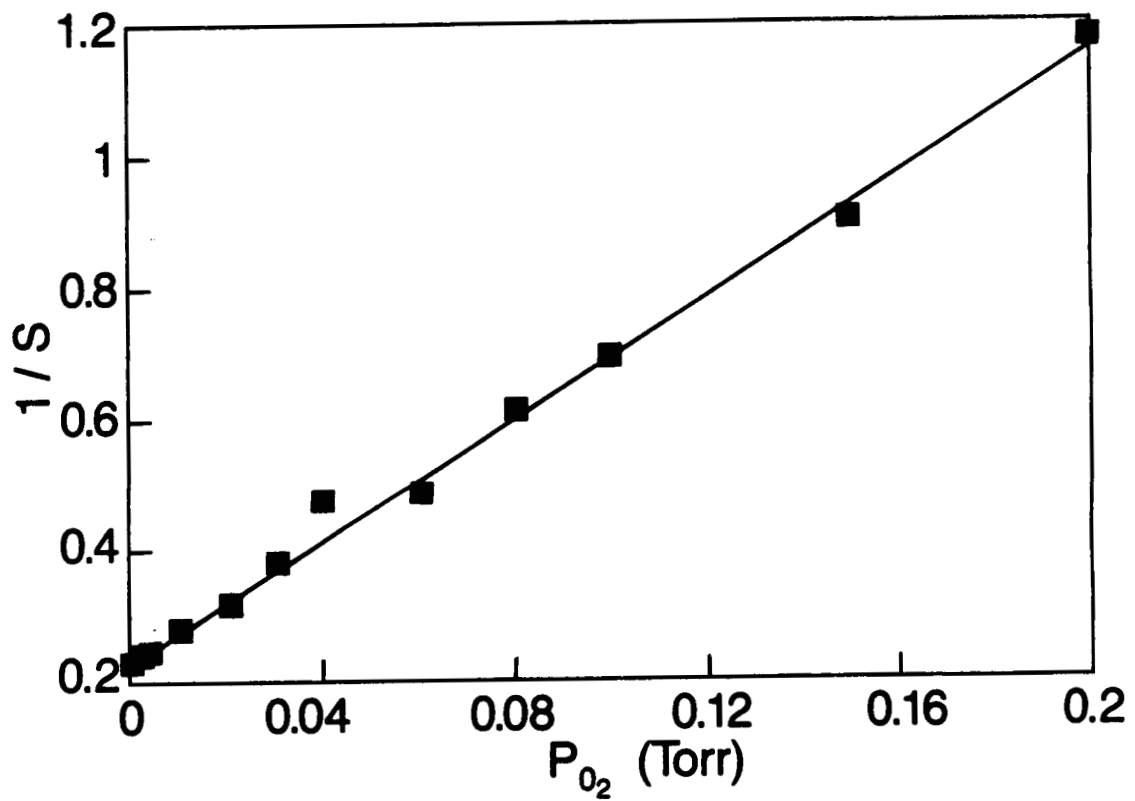


Figure 2.28 ZnTPP on 2PVN - quenching of phosphorescence by oxygen. Data, ■; least squares fit, -.

$$1/S = (k_T/B) + (4\pi\alpha D_0 rd/B)XP \quad (2.13)$$

A plot of the reciprocal of the integrated phosphorescence signal versus oxygen partial pressure should be linear, and the ratio of the slope to y-intercept multiplied by the luminescence rate constant at zero oxygen pressure,  $k_T$ , will give a number equal to  $4\pi\alpha D_0 rd X$ .

If the same dye is doped into several different polymers, the size of the dye molecule,  $rd$ , is not expected to change, leaving any observed variation in the apparent quenching rate constant in the product  $D_0X$  or possibly in  $\alpha$ , the quenching probability. This product is termed the permeability of the polymer for oxygen and has been measured for some polymers. Table 2 lists the values of the permeability calculated from the linear fits to the Stern-Volmer plots of Figures 2.23-2.27 assuming a dye radius of 0.5 nm and a probability factor,  $\alpha$ , of unity. For comparison, values of the permeability taken from the Handbook of Polymers are also listed in Table 2. Considering the crudeness of the model and the approximations necessary for estimates of the permeability, the agreement with literature permeability values is reasonably good.

The porphin series, ZnTPP, PdTPP and PtTPP, display an increasing probability of quenching by oxygen with increasing atomic number of the central metal ion when the dye is supported on a NaCl substrate. This photophysics of this porphin series was also studied on the nylon substrate and the results contrast significantly with the NaCl results.

Figures 2.19, 2.29, 2.30 show the phosphorescence decay of ZnTPP, PdTPP and PtTPP, respectively, under high vacuum and when exposed to oxygen. As already noted above for the ZnTPP molecule, the quenching of these three porphins by oxygen is dynamic. For the most part the quenching follows the Stern-Volmer analysis discussed above for the quenching of ZnTPP in various polymers. Figures 2.24, 2.31, 2.32 show the Stern-Volmer plots of the porphin series. The linear least squares fits shown in these figures give the data needed to calculate the quenching rate constant. The bimolecular rate constant values are listed in Table 3 along with the quenching rate constants of the porphins adsorbed to the NaCl substrate.

**Table 3. Rate constant for quenching of porphin phosphorescence by oxygen.**

Porphin	$k_q (s^{-1})$ Nylon	NaCl
ZnTPP	22	1100
PdTPP	22	1300
PtTPP	22	1900

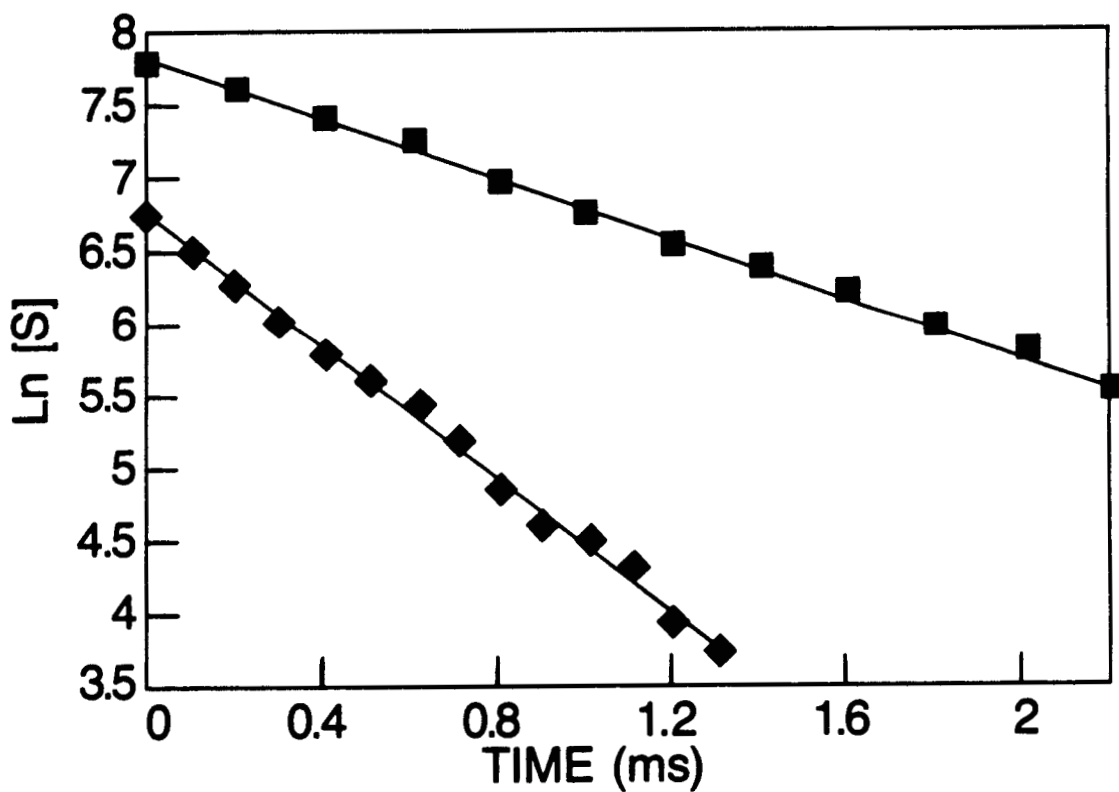


Figure 2.29 PdTPP on nylon - phosphorescence decay. Oxygen pressure = 0 Torr, □; 90 Torr, ◆. Least squares fit, -.

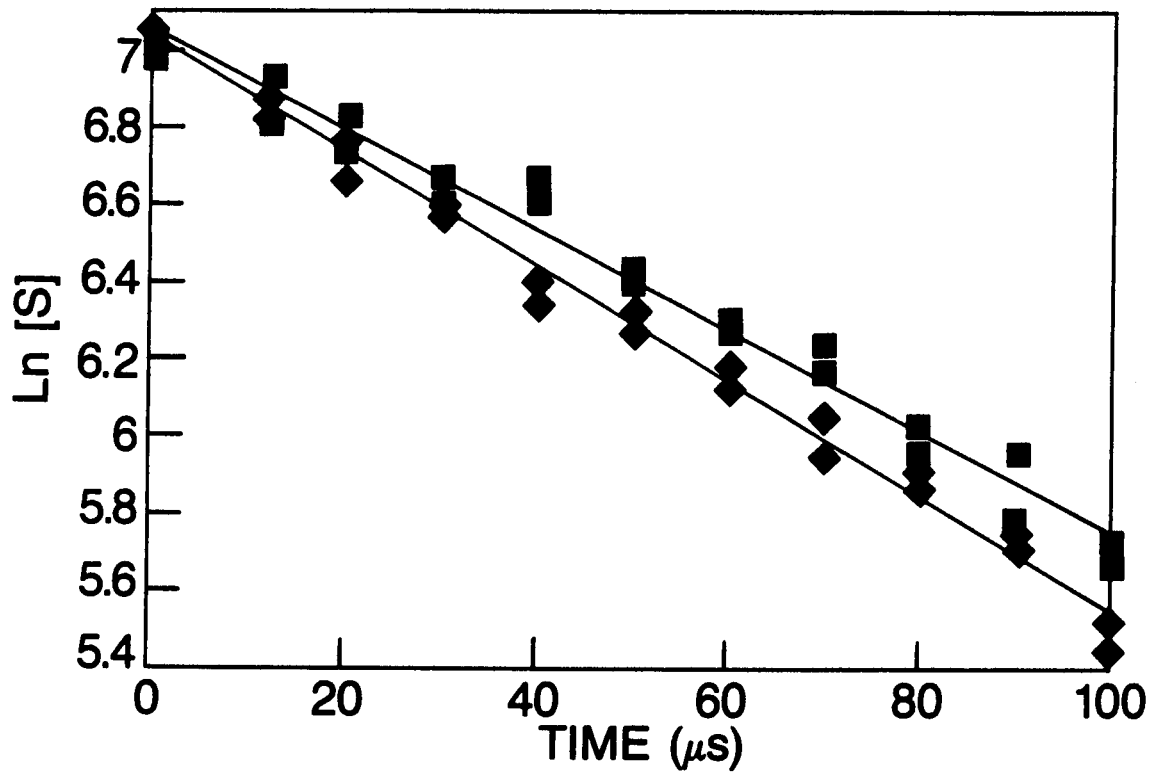


Figure 2.30 PtTPP on nylon - phosphorescence decay. Oxygen pressure = 0 Torr, ■; 100 Torr, ♦. Least squares fit, -.

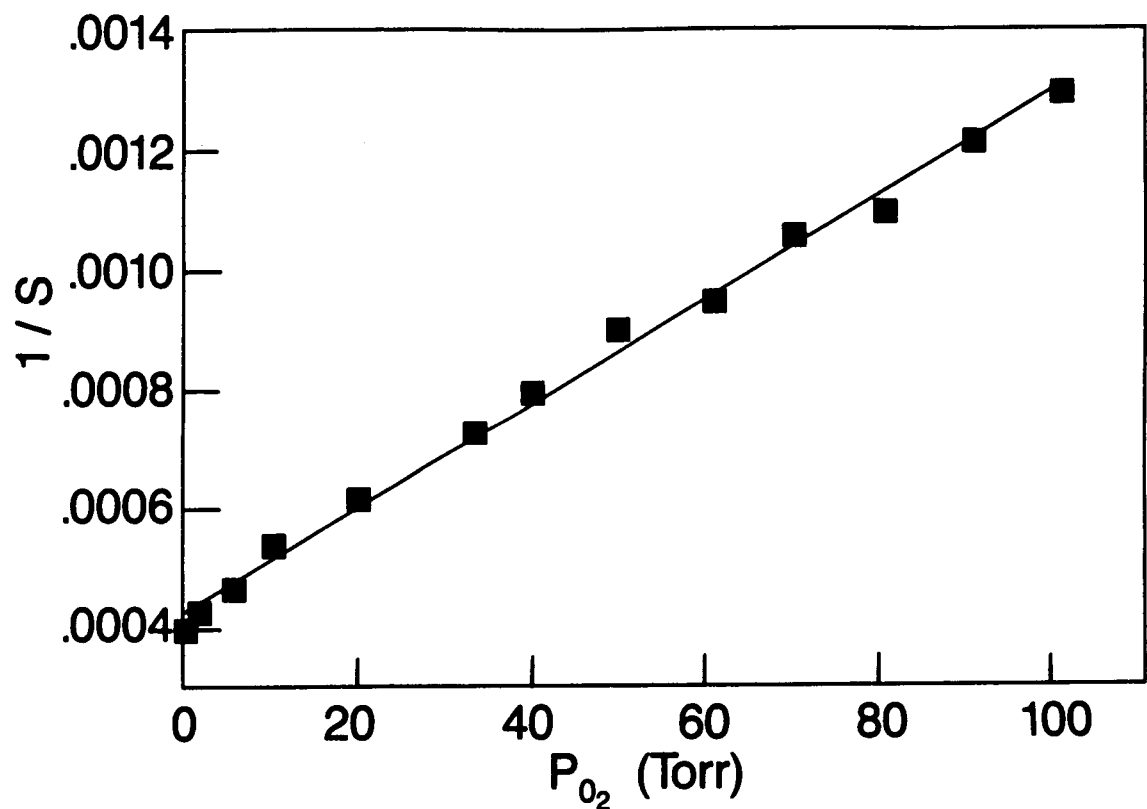


Figure 2.31 PdTPP on nylon - quenching of phosphorescence by oxygen. Data, ■; least squares fit, -.

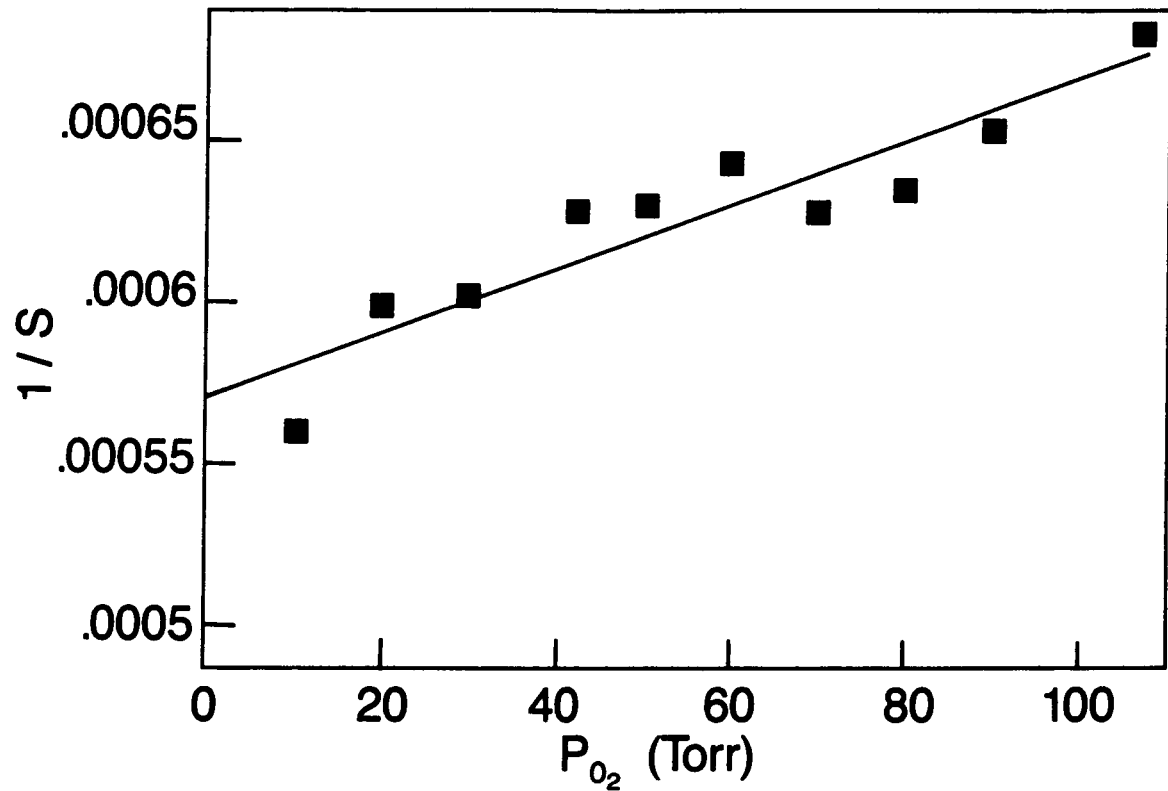


Figure 2.32 PtTPP on nylon - quenching of phosphorescence by oxygen. Data, ■; least squares fit, -.

The fitting of the data in Figure 2.32 requires explanation. Some deviation from perfect linearity is displayed at low oxygen partial pressure. This deviation may be caused by the presence of two different populations of porphin dye; one porphin dye population is embedded in the nylon polymer lattice as is assumed in our analysis and the other porphin molecules occupy surface sites on the nylon fibers. The latter population of porphins on the nylon surface will be more easily quenched (quenched at lower oxygen pressure) than the dissolved dye population and this will be observed as an initial rapid increase in the reciprocal phosphorescence signal (ordinate value in Figure 2.32) followed by a slower linear increase in  $1/S$ . Because of the deviation in linear behavior noted above, only data at pressures at or above 10 Torr were used in the fitting procedure (this leaves out only 1 point in our data set).

The quenching of nylon bound porphin phosphorescence by oxygen displays no apparent influence by the central metal ion in the porphyrin ring. This is in contrast with the results found for the NaCl substrate which showed a steady increase in quenching rate constant as the atomic number of the central metal ion was increased. A difference in the magnitude of  $k_q$  between the two substrates is even more pronounced. The quenching rate constant is roughly  $103 \text{ s}^{-1}$  on the NaCl substrate but only  $20 \text{ s}^{-1}$  on the nylon substrate. These differences between the two substrates are consistent with the models which were developed to explain the photokinetics of dye phosphorescence quenching by oxygen.

The quenching rate for porphin embedded in nylon is limited by the rate of diffusion of oxygen through the polymer to the dye molecules. Once the oxygen is brought within the "solvent cage" of the dye molecule, it experiences many collisions with the dye molecule and quenching is insured. Within this diffusion controlled model, the nature of the dye molecule is relatively unimportant and so it is not surprising that  $k_q$  does not show a significant modification when the central metal ion of the porphin is changed. In contrast, quenching of porphins adsorbed on the surface of NaCl crystals is not limited by the transport of molecular oxygen to the dye molecule. Rather, the strength of the molecular interaction apparently controls the extent of quenching and thus the magnitude of  $k_q$ .

The temperature dependence of the quenching by oxygen of ZnTPP deposited on nylon was studied and the Stern-Volmer plots of this data are shown in Figure 2.33. The slope of the plots of reciprocal integrated phosphorescence signal versus oxygen pressure is seen to increase with temperature while the y-intercept does not change greatly with temperature. This is expected if the decay constant at zero oxygen pressure and the quantum yield for triplet formation are independent of temperature but the bimolecular quenching rate constant varies with temperature. The quenching rate constant was calculated from the least squares fits to the Stern-Volmer plots such as those shown in Figure 2.33 and an Arrhenius plot of these values is shown in Figure 2.34. From the linear least squares fit to the Arrhenius plot, an activation energy of 19 kJ/mole is calculated. (The slope is equal to the negative of the activation energy,  $E_a$ , divided by  $R$ , the gas constant.) If the assumption that ZnTPP has become incorporated in the nylon polymer lattice is correct, this activation energy of 19 kJ/mole is probably a

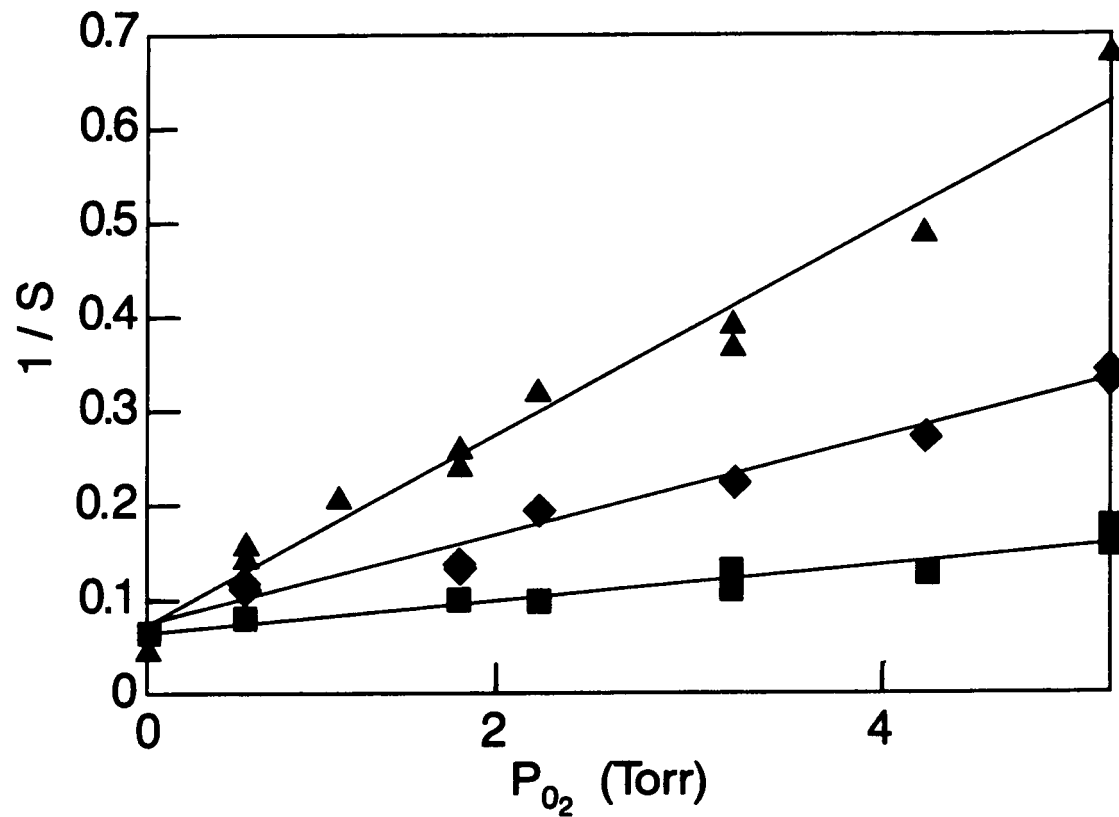


Figure 2.33 ZnTPP on nylon – temperature dependence of phosphorescence quenching by oxygen. Temperature =  $-3\text{ C}$ , ■;  $25\text{ C}$ , ♦;  $65\text{ C}$ , ▲. Least squares fit, -.

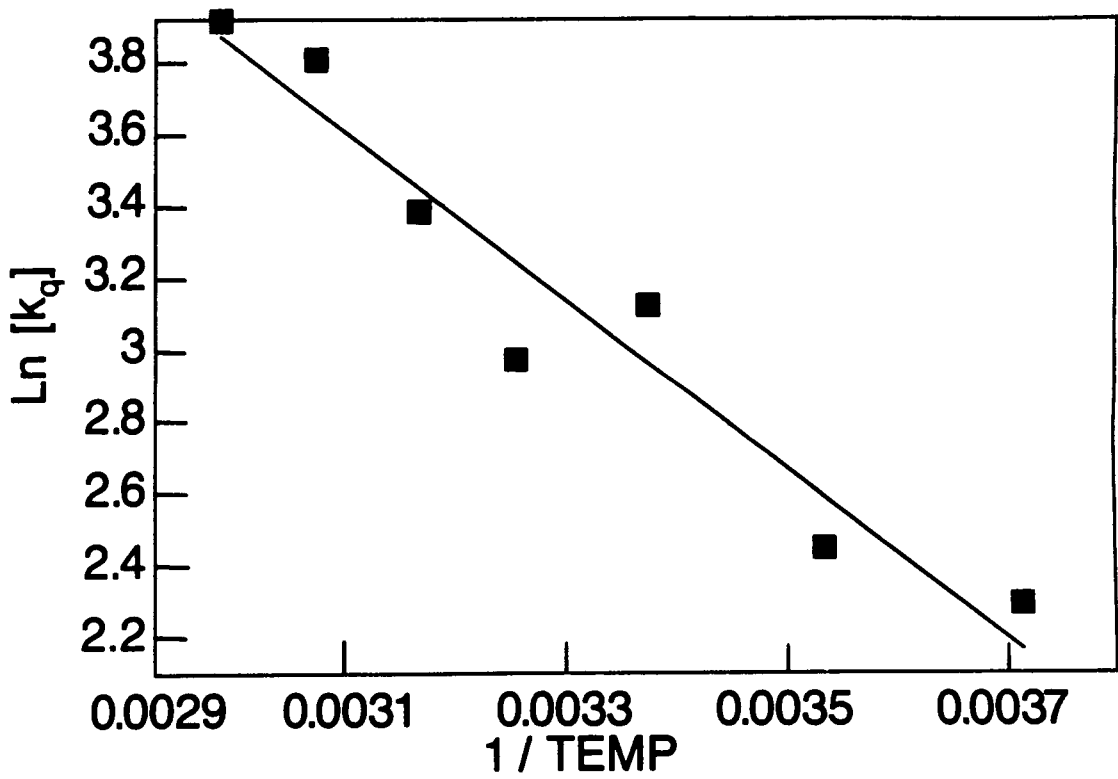


Figure 2.34 ZnTPP on nylon - temperature dependence of quenching rate constant. Data, ■; least squares fit, -.

measure of the temperature dependence of the product of the solubility and diffusivity of oxygen in nylon.

## 2.4 Discussion

The quenching by molecular oxygen of the phosphorescence of dye molecules adsorbed to a solid substrate is physically different for the three substrates reported above. On the NaCl substrate the quenching of dye phosphorescence is accompanied by an increase in the phosphorescence decay rate. The integrated phosphorescence signal obeys Stern-Volmer kinetics when the gas phase pressure of oxygen is chosen as the independent variable. We conclude from this behavior that dye molecules are quenched on this surface by collisions of gas phase oxygen with the dye molecules. Using a value of  $10^{-18} \text{ m}^2$  for the cross sectional area of the ZnTPP molecule, the number of collisions per second per Torr of oxygen experienced by this dye molecule is  $4 \times 10^6$ , calculated from gas kinetic theory. At room temperature the rate constant for phosphorescence quenching of a single ZnTPP molecule is  $1100 \text{ s}^{-1} \text{ Torr}^{-1}$  (from the least squares fit to the data presented in Figure 2.7). The probability of quenching per collision, given by the ratio of these numbers, is  $3 \times 10^{-4}$ .

The luminescence quenching of ZnTPP supported on NaCl crystals is consistent with a model which assumes that quenching occurs upon collision of gas phase oxygen with ZnTPP molecules located on the surface of the salt crystal. However, other quenching models are not necessarily excluded by our results. The quenching of ZnTPP phosphorescence when this dye is supported on a polymer substrate also shows a reasonably linear Stern-Volmer quenching behavior. However, the quenching constant of the polymer/dye system depends strongly on the polymer substrate and is much lower in value than the quenching rate constant measured for the same dye supported on NaCl. This difference is consistent with a model which presumes that the dye has become imbedded in the nylon solid and that luminescence quenching occurs upon diffusion of oxygen into the substrate. The ionic lattice of the NaCl substrate is much less likely to accommodate a large non-ionic molecule like ZnTPP and the assumption that the ZnTPP molecules reside on the surface of NaCl is probably correct. However, quenching of ZnTPP luminescence directly by collisions of gas phase oxygen rather than by absorbed oxygen has not been unequivocally proved by the results presented here.

Porphins embedded in polymers (intentionally or otherwise) are quenched by oxygen when this gas is admitted to a previously evacuated sample chamber. The extent of quenching increases with oxygen pressure and can be fit using Stern-Volmer kinetics with the sample chamber oxygen pressure as the independent variable. Deviations from a linear Stern-Volmer plot are noted for both nylon and cellulose substrates and will be discussed in more detail below. The apparent rate constant for the quenching of dye luminescence by oxygen is characteristic of the polymer substrate and is a number determined from the linear Stern-Volmer fit.

A solution phase quenching model is consistent with all of our observations for the quenching of polymer supported dyes and provides a means of comparing the apparent rate constant for quenching with data determined in other experiments. The dye molecules are presumed to be

incorporated in the polymer substrate. Dissolved oxygen diffuses throughout the polymer and upon encountering an excited dye molecule, quenches its luminescence. The apparent quenching rate constant is a product of a diffusion controlled reaction rate constant, a probability factor and a solubility coefficient. Further analysis shows that the apparent rate constant for luminescence quenching is proportional to the product of the oxygen diffusion coefficient and the solubility coefficient. This product is termed the permeability of the polymer for oxygen and has been measured by other methods and reported in the literature. Comparison of the permeabilities which are determined from the phosphorescence quenching data with literature values shows

1. The permeability values determined from phosphorescence quenching data are of the correct order of magnitude.
2. The ordering of permeability values which was determined from phosphorescence quenching data is the same ordering determined from literature values of this quantity.

Given the nature of the assumptions which enter our determination of the value of the permeability as derived from the apparent rate constant for quenching and the fact that it is not at all clear that polymers of the same molecular weight and branching structure are being compared, the agreement found between literature values of the permeability and our values is considered very satisfactory.

As mentioned above, the quenching of ZnTPP in nylon and in cellulose deviates from a linear Stern-Volmer behavior, more so for the data obtained using the cellulose substrate. In both cases, a linear fit to the high oxygen pressure data was used in obtaining a value for the apparent quenching rate constant. The increase in the apparent rate constant at low pressure is thought to be an artifact of the method of sample preparation. Dye becomes embedded in the polymer when a solution containing the dye molecules wets the polymer substrate and is allowed to evaporate. It is possible that some of the dye solution coats the substrate surface (particularly important for the high surface area cellulose substrate) and upon evaporation, a significant fraction of the dye molecules remain on the polymer surface. Because the apparent rate constant for quenching is larger for molecules which are bombarded by gas phase oxygen molecules (approximately  $1000 \text{ s}^{-1} \text{ Torr}^{-1}$ ) as compared with those quenched by polymer dissolved oxygen (approximately  $20 \text{ s}^{-1} \text{ Torr}^{-1}$ ), it is expected that the low pressure quenching data will reflect the former while the high pressure data are dominated by dissolved oxygen quenching.

Silica gel has been used extensively as a dye molecule support for the sensitized production of gas phase singlet delta oxygen. Our results are consistent with a model which assumes that ZnTPP phosphorescence is primarily quenched (presumably by energy transfer from ZnTPP to  $O_2$ ) by adsorbed oxygen and not by collisions of gas phase oxygen molecules with the dye molecule under the conditions of our study. It is expected that this mechanism for phosphorescence quenching of dye molecules by oxygen is general for dyes adsorbed on a silica gel surface. If so the production of gas phase singlet delta oxygen requires not only energy transfer from the dye molecule to adsorbed oxygen but also desorption of the excited oxygen. The latter step will compete with the quenching of singlet delta oxygen excitation by the silica gel surface.

The adsorption model which we have used to explain the quenching of porphin dye adsorbed to silica gel is a simple Langmuir adsorption isotherm modified in two respects. First the adsorption of oxygen to sites surrounding a ZnTPP molecule is considered to compete with water molecules. It is well known that water adsorbs to silica gel (it is used as a dessicant) and also that water vapor is the major gaseous component in high vacuum ( $10^{-4}$  to  $10^{-7}$  Torr) systems. The extent of adsorption of both water and oxygen to silica gel is determined by the adsorption energy of each molecule to sites on the silica gel surface.

A second modification is made to the Langmuir adsorption model which allows the adsorption energies to vary from site to site. A Gaussian distribution function in the difference in the energy of adsorption of oxygen and of water to silica gel is used to model the site to site variation. This distribution is characterized by two fitting parameters, the mean energy difference,  $E_m = (Q-Q')_m$ , and the distribution width  $\sigma$ . The first parameter, the mean energy difference, was found to be -11 kJ/mole from the fit to the ZnTPP phosphorescence quenching data. From the sign and magnitude of this energy difference it appears that water is bound more strongly than oxygen to the silica gel surface by 11 kJ/mole. A value of 4 kJ/mole was obtained for the second fitting parameter  $\sigma$ , the distribution half width, indicating a rather narrow distribution in site energies. The narrowness of the site energy distribution is not unreasonable if it is remembered that the independent variable in our distribution function is the difference in adsorption energy of oxygen and water to the same silica gel surface site. If the bonding of water at the adsorption sites is similar to the bonding of molecular oxygen then variations in bonding energy from site to site may be quite large but nevertheless result in a small variation in the difference in bonding energy between oxygen and water.

An assumption made in the adsorption model is that the adsorption energy of water on silica gel is greater than approximately 65 kJ/mole. This assumption together with the value of  $E_m$  places the adsorption energy of oxygen at greater than 54 kJ/mole. This is a large adsorption energy and may be thought to be an unrealistic consequence of the lower bound assumed for the adsorption energy of water (see the discussion following Eq. 2.4). However, if the adsorption energy of water were significantly less than 65 kJ/mole, most of the sites of silica gel would be unoccupied at a partial pressure of water of  $10^{-5}$  Torr. Under these conditions oxygen alone would populate the adsorption sites of silica gel. It is possible to fit the room temperature quenching data with a one component version of Eq. 2.3 (with  $b'$  set equal to zero); however, the adsorption energy of oxygen needed to fit the quenching data is 52 kJ/mole, still a large value. Furthermore, the temperature dependence predicted by this one component adsorption model is far different from that which is observed. If an adsorption model correctly accounts for the phosphorescence quenching of silica gel bound ZnTPP by oxygen then it appears that at least some sites on silica gel (those next to sites occupied by ZnTPP) have a strong affinity for oxygen.

If the rate constant for quenching of ZnTPP luminescence by gas phase oxygen is assumed to be independent of surface substrate, then the value of  $1100 \text{ Torr}^{-1} \text{ s}^{-1}$  measured using the NaCl substrate can be used to predict the change in luminescence decay rate for ZnTPP adsorbed to silica gel at any partial pressure of oxygen. The decay rate constant predicted for silica gel bound ZnTPP exposed to 0.01 Torr of oxygen is  $47 \text{ s}^{-1}$ , a 30 per cent increase over the rate constant measured under high vacuum. This 30 per cent increase in phosphorescence decay rate is not observed in our studies.

It is possible that the luminescence properties of ZnTPP are affected by the substrate surface as indeed is evidenced by the factor of two difference in phosphorescence decay constant between silica gel and NaCl. It may also be possible that the silica gel environment partially shelters the ZnTPP molecules from quenching by gas phase oxygen.

When oxygen quenches a large fraction of the luminescence of silica gel bound ZnTPP, a multiexponential time dependence of the luminescence decay is observed. The luminescence decay is adequately fit by a two component decay. The slowly decaying component of the luminescence signal is assumed to originate from monomeric ZnTPP adsorbed to silica gel. It was this component whose luminescence quenching behavior was selectively studied. Because the fast component is not observed for samples under high vacuum under the conditions of our experiment, the origin of this component remains uncertain. It is possible that the fast luminescence decay component can be attributed to ZnTPP adsorbed to special sites on silica gel which greatly affect the photophysical properties of the ZnTPP molecule, in this instance by providing an efficient path for nonradiative decay or by enhancing the triplet to singlet ground state coupling. Another possibility is that dimers or aggregates of ZnTPP are formed when this dye is adsorbed to silica gel and the fast decaying component which we see at relatively high oxygen partial pressure is due to these species. The biexponential luminescence decay from acriflavine adsorbed to silica gel has been explained in this manner.<sup>19</sup> Finally, the fast decaying component may be attributed to those molecules which have complexed with oxygen before they were excited. It remains a task of further investigation to determine the origin of this luminescence component.

Other workers have found evidence for mobility of large organic molecules on the surface of silica gel.<sup>20-21</sup> The lack of dynamic quenching of ZnTPP phosphorescence by adsorbed oxygen indicates that under the experimental conditions of this study the mobility of ZnTPP or oxygen on the silica gel surface can not be very large. Possibly the motion of both of these molecules on the silica gel surface is hindered by the occupation of surrounding sites by water molecules. Using the Langmuir equation and an adsorption energy of 70 kJ/mole for water, the fraction of adsorption sites on the silica gel surface which are occupied by water is calculated to be approximately 90 per cent. With an adsorption energy of this magnitude, the residence time of a water molecule at an adsorption site, given by  $\exp[-Q/RT]$ , is calculated to be longer than the phosphorescence lifetime of ZnTPP implying that once photoexcited, if ZnTPP does not find an oxygen molecule adsorbed next to it, the likelihood that it will be quenched by oxygen is not high. The acriflavine molecule adsorbed to silica gel shows, in our studies, a small change in its luminescence lifetime. Previous work with this same system failed to observe this change.<sup>19</sup> The much longer lifetime of the acriflavine triplet state (0.2 s) makes it a more sensitive indicator of dynamic quenching. However, it is worth noting that the acriflavine system is quite complicated and a full understanding of the quenching of this molecule on the silica gel surface is not yet possible.

## 2.5 References

1. H. Kautsky, A. Hirsch and W. Baumeister, "Energy Transformations on Boundary Surfaces. II. Photoluminescence of Fluorescent Dyes at Surfaces," *Ber. deut. Cehm. Ges.* 64, 2053 (1931).
2. D. R. Kearns and A. U. Khan, "Sensitized Photooxygenation Reactions and the Role of Singlet Oxygen," *Photochem. Photobiol.* 10, 193 (1969), and references therein.
3. R. C. Petterson, S. M. Kalbag and C. S. Irving, "Solid-phase Photochemical Singlet Oxygen Generator," *Ann. N.Y. Acad. Sci.* 171, 133 (1970)
4. J. R. Williams, G. Orton and L. R. Unger, "Preparation of Singlet Oxygen by Heterogeneous Photosensitization," *Tet. Lett.* 46, 4603 (1973)
5. R. Nilsson and D. R. Kearns, "Some Useful Heterogeneous Systems for Photosensitized Generation of Singlet Oxygen," *Photochem. Photobiol.* 19, 181 (1974)
6. W. C. Eisenberg, A. Snelson, R. Butler, J. Veltman and R. W. Murray, "Gas Phase Generation of Singlet Oxygen at Atmospheric Pressure," *Tet. Lett.* 22, 377, (1981)
7. W. C. Eisenberg, A. Snelson, J. Veltman and R. W. Murray, "Gas Phase Observation of the  $1.27-\mu\text{m}$  Emission of Singlet Delta Oxygen Generated at Atmospheric Pressure by Heterogeneous Photosensitization," *Tet. Lett.* 22, 1949 (1981)
8. W. R. Midden and S. Y. Wang, "Singlet Oxygen Generation for Solution Kinetics: Clean and Simple," *JACS* 195, 4129 (1983).
9. R. W. Chambers and D. R. Kearns, "Triplet States of Some Common Photosensitizing Dyes," *Photochem. Photobiol.* 10, 215 (1969).
10. J. F. O'Hanlon, "A User's Guide to Vacuum Technology," (Wiley-Interscience, NY), 1980, p. 280.
11. A. W. Adamson, "Physical Chemistry of Surfaces," 4th edition, (Wiley, NY, 1982), Chap. 16.
12. H. Kautsky and A. Hirsch, "Nachweis Geringster Sauerstoffmengen Durch Phosphoreszenztilgung," *Zeits. f. anorg. allgem. Chemie* 222, 126 (1935)
13. J. Franck and P. Pringsheim, "Phosphorescence of Adsorbed Trypaflavine and Its Quenching by Oxygen," *J. Chem. Phys.* 11, 21 (1943)
14. J. L. Rosenberg and D. J. Shombert, "The Reaction of Oxygen with Electronically Excited Acriflavine," *J. Am. Chem. Soc.* 82, 3257 (1960)
15. R. F. Weiner and H. H. Selinger, "Oxygen Quenching of Trypaflavine Luminescence," *Photochem. Photobiol.* 4, 1207 (1965)

16. Shunji Kato, "Studies on the Organic Phosphorescence. III. Quenching by Some Gases and Vapors," Bull. Chem. Soc. Japan 30, 34 (1957)
17. E. I. Grigor'ev, I. A. Myasnikov and V. I. Tsivenko, "Photosensitized Formation of Singlet Oxygen in Heterogeneous Dye-Solid-Gas Systems," Russ. J. Phys. Chem. 55, 1652 (1981)
18. E. I. Grigor'ev, I. A. Myasnikov and V. I. Tsivenko, "The Influence of the Nature of the Solid on the Photosensitized Formation of Singlet Oxygen in Support-Dye-Oxygen Systems," Russ. J. Phys. Chem. 56, 1059, 1599 (1982).
19. J. L. Rosenberg and F. S. Humphries, "Oxygen Quenching of Acriflavine Phosphorescence," J. Phys. Chem. 71, 330 (1967).
20. R. K. Bauer, R. Borenstein, P. deMayo, K. Okada, M. Rafalska, W. R. Ware and K. C. Wu, "Surface Photochemistry: Translational Motion of Organic Molecules Adsorbed on Silica Gel and Its Consequences," J. Am. Chem. Soc. 104, 4635 (1982)
21. P. de Mayo, L. V. Natarajan and W. R. Ware, ACS Symposium Series 278, "Organic Phototransformations in Nonhomogeneous Media," M. A. Foxe, Ed. (ACS, Washington, D.C., 1985), p. 1.

## CHAPTER 3: TRIPLET EXCITON KINETICS

### 3.1 Introduction

To evaluate the KMSF singlet oxygen generator it is crucial to know the efficiencies at which triplet excitons diffuse to surface sites and transfer energy to gas phase oxygen. The efficiency of the former process depends both on the diffusion of bulk triplets to surface trapping sites and the competition of all decay processes. To have efficient energy transfer to surface trapping sites the triplet observed lifetime must be longer than the time it takes excitons to migrate to the surface. In the case of the well understood tetracene crystals, even at moderate triplet exciton densities ( $10^{15} \text{ cm}^{-3}$ ), T-T (Triplet-Triplet) annihilation already limits the triplet observed lifetime to less than  $1 \times 10^{-4} \text{ s}$ . A unimolecular decay rate of  $100 \text{ s}^{-1}$  was measured in tetracene single crystals<sup>1</sup> and believed to be dependent on impurity levels as well as defect number density. With a decay rate this low bimolecular annihilation will be a dominant decay path for a wide range of triplet densities, as initially projected. The proposed system, however, uses polycrystalline films instead of single crystals. Polycrystalline dye films were proposed because they are readily prepared using either vacuum sublimation techniques (discussed later) or spin-coating techniques.

The main technical objectives of this experimental phase are (a) to verify excitonic energy transport in single crystals, (b) to observe excitonic energy diffusion in vacuum-deposited dye films and (c) to assess the role of various triplet decay paths in both materials.

The decay of triplet excitons proceeds via unimolecular and bimolecular processes. Bimolecular processes involve the collision of two excitons resulting in the disappearance of one triplet (annihilation) or disappearance of both with the creation of a singlet excited state (fusion). The most direct way to study triplet kinetics is to measure phosphorescence from the triplet. Unfortunately, the triplet to ground-state transition is forbidden, and much faster decay processes compete with phosphorescence making it difficult to observe in solid dyes. There are conceivably two other ways to monitor triplets: one relies on a fortuitous ability of certain dyes to emit delayed fluorescence (DF), as discussed below, and the other measures the total amount of heat generated by nonradiative decay of triplet excitons. Note that the ultimate product of any nonradiative excitonic decay is heat; therefore, decay of triplet excitons can be measured by monitoring heat. In this report, T-T decay rates of tetracene will be measured by monitoring delayed fluorescence, and thermal detectors which are capable of quantifying the heat generated in annihilation processes, will be investigated. Because heat is the universal by-product of any decay process, thermal detection is a more elegant technique and can be applied to any dye molecules: a description of the photothermal deflection technique<sup>2</sup> and the thin film pyroelectric technique and their discussions are in Chapter 4. The DF method is less universally applicable and relies on the fact that delayed fluorescence is observed in some aromatic hydro-

carbons (such as anthracene and tetracene) where the sum of two triplet energies is slightly higher than the singlet state.<sup>3,4</sup> In these dyes, two triplet excitons can fuse to give a singlet. Emission from the produced singlet state is called delayed fluorescence (DF). This Chapter reports the studies of tetracene films with DF.

### 3.2 Triplet Exciton Decay in Single Crystal Films

Tetracene was chosen as the first single crystal dye to investigate for several reasons: (a) Tetracene is one of the most studied molecular solids<sup>5</sup> and therefore provides a body of data which can be compared with our results; (b) excitonic energy transfer has been observed and well characterized for its crystals;<sup>6</sup> (c) tetracene can be prepared as a single crystal, polycrystalline films or amorphous films; and (d) its triplet density can be readily monitored by delayed fluorescence.

#### 3.2.1 Experimental

Sample preparation is important in any experiment employing single crystals. Tetracene was obtained from Aldrich and used as received. Crystals were grown from the vapor phase in a sealed glass container in the presence of 10 Torr of nitrogen. The dye is sublimed from the hot end of the container, where a temperature of 250 C was maintained, to the cold end, which was kept at room temperature over a period of 48 hours. Crystals as large as 4 mm<sup>2</sup> in surface area and 50-250 microns in thickness were deposited over a 48 hour period of time. When the crystal is exposed to air an oxidized layer develops on the tetracene surface;<sup>6</sup> therefore, measurements were taken with minimal exposure to minimize the growth of the oxidized layer. The crystals were mounted between glass plates prior to investigation.

Delayed fluorescence in tetracene crystals is induced by absorption of light from a pulsed dye laser (Molelectron DL-II pumped by a UV-12 nitrogen laser). The pulse duration, 5 nsec, is typically much smaller than the emission lifetimes. The laser wavelength was chosen so that tetracene crystals were optically thin to illumination. At 570 nm, the absorption depth is measured to be  $0.033 \pm 0.05$  cm in agreement with the results of Vaubel et al.<sup>7</sup> This value cannot be measured precisely with traditional transmission methods due to substantial reflectance of tetracene crystals. The emission is passed through a monochromator (I.S.A. H-20), a long wavelength pass optical filter and a neutral density filter before being imaged on a photomultiplier tube (PMT). The monochromator is set at 620 nm which corresponds to the singlet fluorescence. An S-20 PMT (Hamamatsu R928) is used as the detector. The photocurrent is recorded with a digital oscilloscope (LeCroy 9400). Signal averaging is done with the oscilloscope and data analysis is performed by an IBM XT personal computer.

It is well documented that singlet excitons in tetracene crystals undergo unimolecular fission into two triplets at room temperature.<sup>8</sup> This radiationless process is possible because in tetracene the sum of triplet energies is only 0.2 eV higher than the singlet energy. The spin-allowed process is fast and reduces the fluorescence lifetime to an observed value of  $145 \pm 50$  psec.<sup>9</sup> Unfortunately, it is difficult to measure phosphorescence at room temperature in tetracene crystals. As a consequence delayed fluorescence is used as a tool to monitor triplet

number density. Note that DF, in spite of being a bimolecular decay pathway, is only a negligible loss mechanism for triplets. In other words, it is assumed that triplet density is proportional to the square root of DF because of its fusion kinetics, but its effect on the decay of triplets is not considered.

Because fission of singlets is the dominant mechanism of triplet production, the triplet yield could be as high as 2. This yield is of importance to our study because of the following reason. The decay rate of the triplet exciton is a function of the triplet number density,  $n$ , if bimolecular kinetics is effective. The determination of the bimolecular rate,  $\gamma$ , is only possible with the knowledge of triplet density right after the pulsed illumination,  $n(0)$ . In this study  $n(0)$  is approximated by  $\eta cF$ , where  $\eta$  is the yield of producing a triplet as mentioned above,  $c$  the absorption coefficient and  $F$  the laser fluence. Kinetic information is obtained as shown next.

### 3.2.2 Decay kinetics

Figure 3.1 displays the photomultiplier signal obtained when the monochromator is set at 620 nm. The initial spike of the signal is attributed to prompt fluorescence and scattering, and the remaining tail to delayed fluorescence (DF). Prompt fluorescence and scattered light constitute the noise transient which occurs within the first 5 ns. The time resolution is limited by the oscilloscope sampling rate of  $1 \times 10^8$  s $^{-1}$  and the first 20 ns of the decay waveform are considered to be the mentioned noise transient. The slower signal is assigned to delayed fluorescence on the basis that its decay time constant is much longer than the laser pulse width, the detector response time and the observed time of the prompt fluorescence. Further analysis of the time evolution as well the quadratic laser fluence dependence also supports this assignment. The observed emission is spectrally broad (450-700 nm) and matches the fluorescence spectrum of tetracene. Since DF results from the fusion of two triplets, the initial delayed emission (at time close to laser occurrence) should vary as the square of laser fluence. Because of the prominent noise transient in the DF waveform at time zero, the  $DF(0)$  values are obtained by extrapolating the waveforms to zero time. Figure 3.2 shows DF signal at zero time as a function of laser fluence on a logarithmic scale. The upper solid line in Figure 3.2 shows the slope expected for a second order dependence on laser intensity and the lower line shows a corresponding first order dependence. The measured fluence dependence is clearly stronger than first order and matches a quadratic dependence.

Analysis of the time-resolved DF signal is required to determine the kinetic order and rate constants for triplet decay. Plotting the logarithm of the DF signal as a function of time, as shown in Figure 3.3, yields a curve which deviates significantly from linearity at times less than 10 microseconds. According to the treatment in Appendix A, first order decay would appear in Figure 3.3 as a linear curve. The observed nonlinearity in the DF decay time profile is indicative of a decay kinetics order higher than first in the initial time interval. Data can be analyzed to yield both first order and second order rate constants.

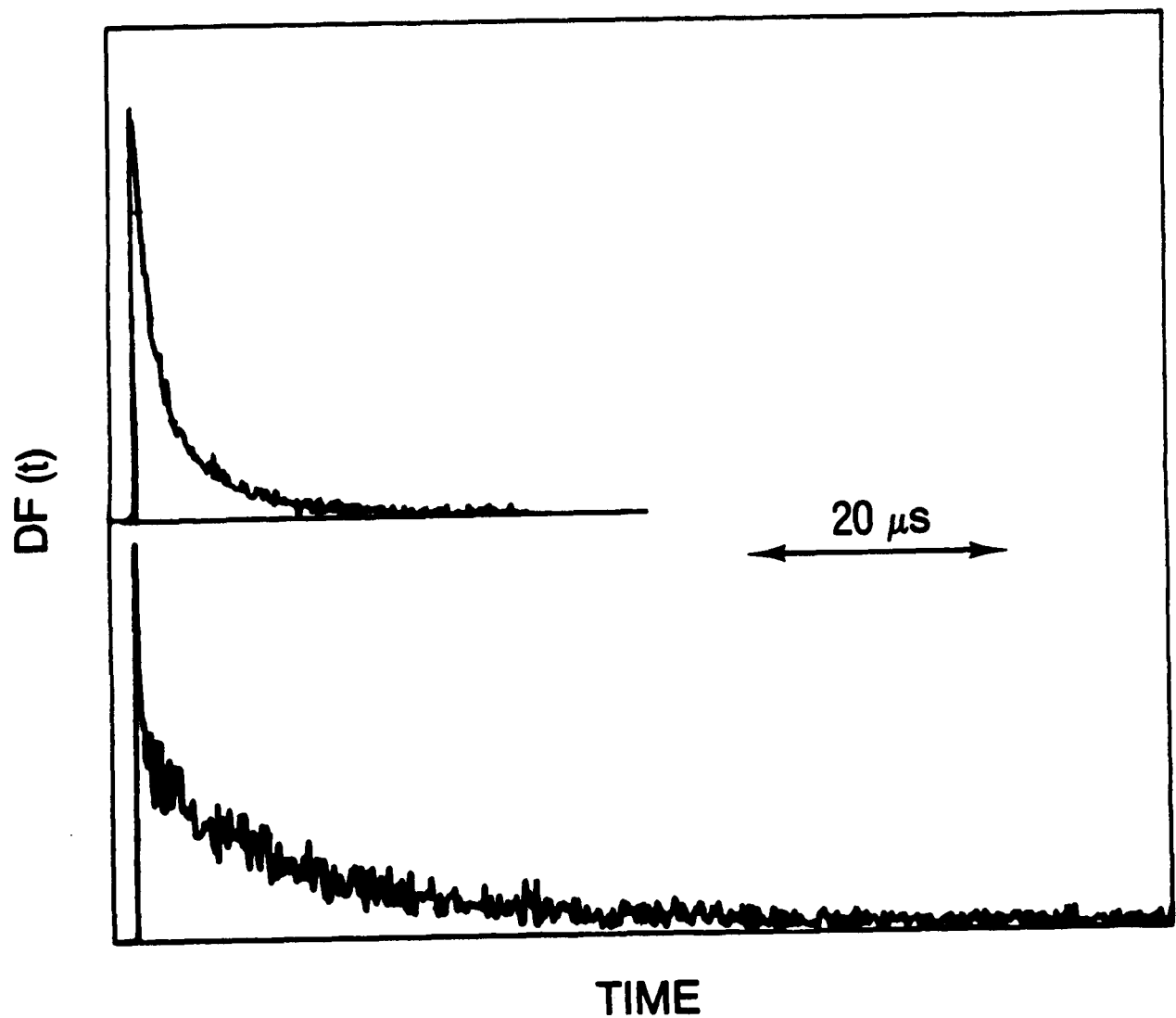


**Figure 3.1** Time-resolved Delayed Fluorescence of crystal films.

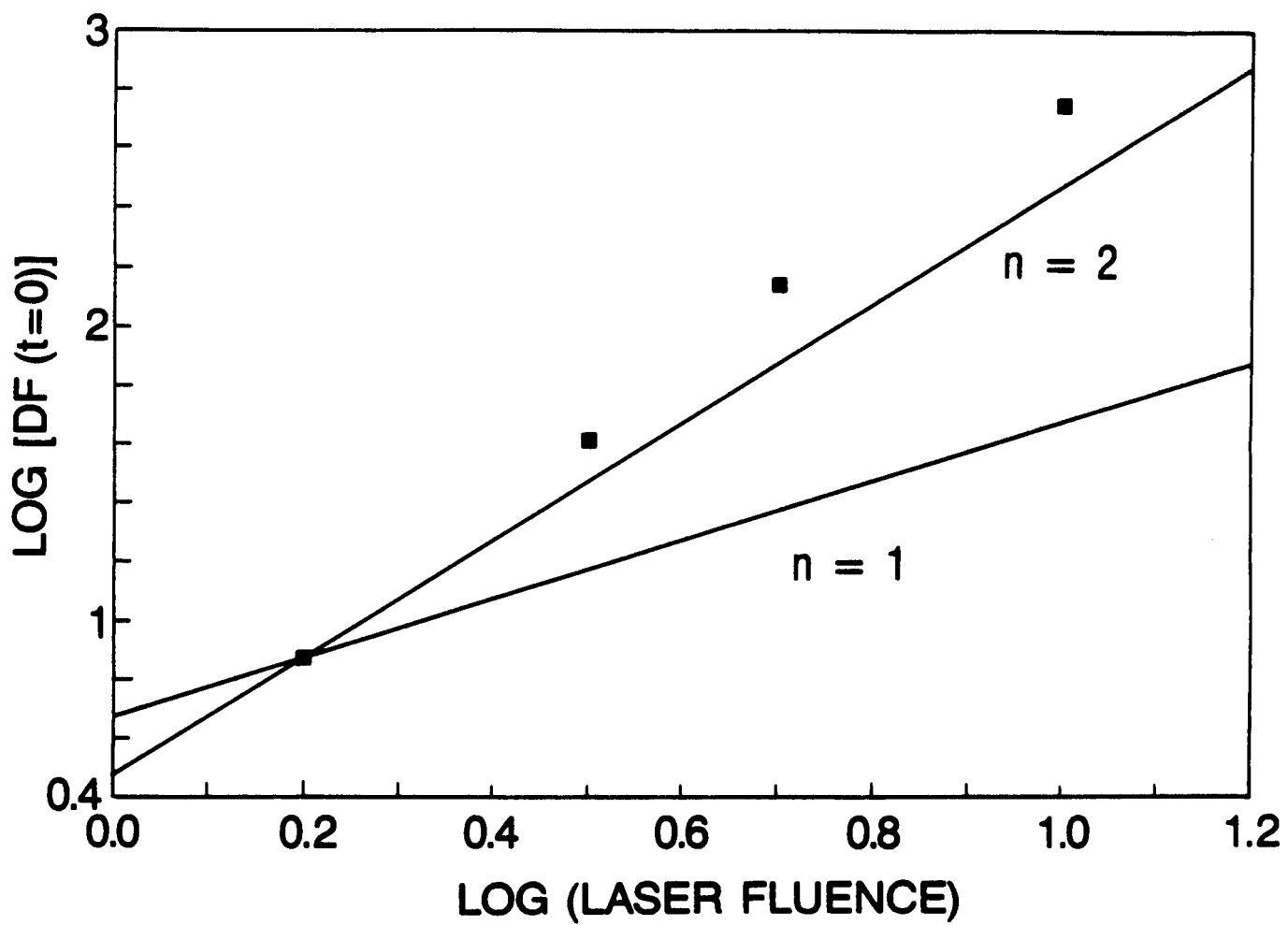
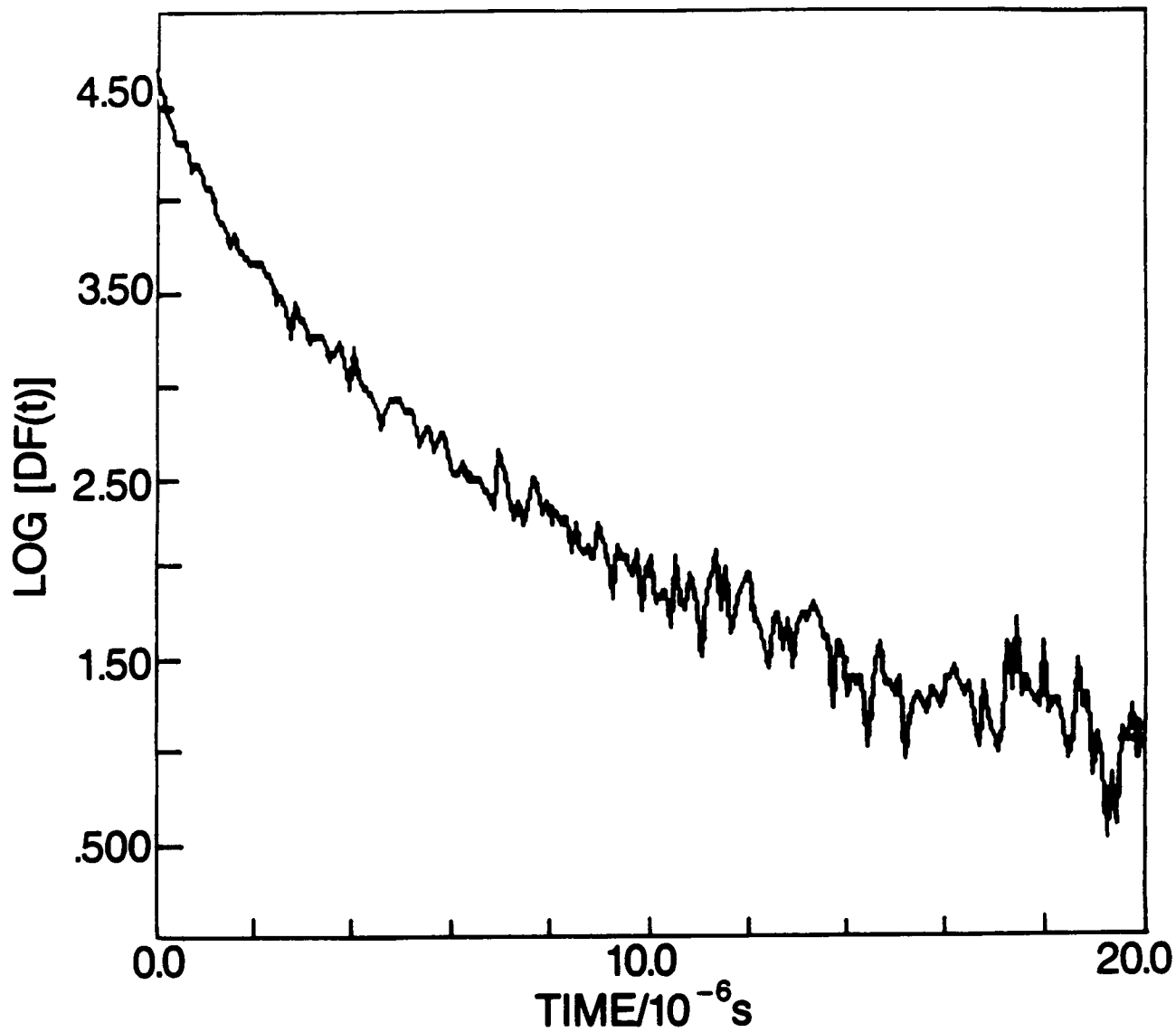


Figure 3.2 Fluence dependence of DF emission.



**Figure 3.3** DF decay in semilogarithmic plot. The fluence is  $8 \times 10^{14}$  photons  $\text{cm}^{-2}$  pulse $^{-1}$ , and the absorption coefficient is  $30 \text{ cm}^{-1}$  (wavelength = 570 nm).

It was shown in Appendix A that for  $\beta \gg \gamma n(0)$  and  $t \gg 1/\gamma n(0)$ , the decay of DF signal is typically exponential. Furthermore the decay rate of DF is twice the first order decay rate  $\beta$  of  $n$ . The factor of two between the mentioned decay rates results from the fact that DF is actually proportional to  $[n(t)]^2$ . Within the limits set by the low fluence and large time conditions which are mentioned above, Eq. (A.5) is valid.

$$DF(t) = A [n(0)]^2 e^{-2\beta t} \quad (A.5)$$

The unimolecular decay rate,  $\beta$ , can be extracted from plots similar to that shown in Figure 3.3 with the use of Eq. (A.5). The slope of the linear curve in the inset of Figure 3.3 is measured. In practice, the computer algorithm which calculates the slope automatically restricts the analysis to the time window in which linearity is observed. In these measurements, laser fluences are also kept low to make sure that more than 80 percent of the curve is analyzable. A unimolecular rate of  $1.2 \pm 0.2 \times 10^5 \text{ s}^{-1}$  is measured for fresh crystals.

At short times after the laser pulse both unimolecular and bimolecular processes have to be considered. In this regime, the time-resolved DF signal is given by Eq. (A.4) of Appendix A. Equation (A.4) is rewritten below in a slightly different form with the fluence dependence explicitly shown:

$$DF(t) = \frac{Ac^2 F^2 e^{-2\beta t}}{\left[ \frac{\gamma c F}{\beta} (1 - e^{-\beta t}) + 1 \right]^2} \quad (3.1)$$

The notation is as follows:  $A$  = geometrical constant depending on the emission collection efficiency;  $c$  = coefficient of absorption [ $\text{cm}^{-1}$ ];  $F$  = laser fluence [ photon  $\text{cm}^{-2} \text{ pulse}^{-1}$  ];  $\beta$  = unimolecular decay rate [ $\text{s}^{-1}$ ];  $\gamma$  = bimolecular rate [ $\text{cm}^{-3} \text{ s}^{-1}$ ] and  $t$  = time [s]. From Eq. 3.1 it is apparent that for  $cF\gamma \gg \beta$  and  $t < 1/\beta$ , the time dependence can be approximated by the following expression

$$DF(t) = A \left( \frac{1}{cF} + \gamma t \right)^{-2} \quad (3.2)$$

A plot of  $DF^{-1/2}$  against  $t$  should give a straight line. The resulting slope is  $\gamma A^{-1/2}$  and the y-intercept is  $A^{-1/2} c^{-1} F^{-1}$ . The bimolecular decay rate can be determined from this analysis.

To utilize Eq. (3.2),  $(DF)^{-1/2}$  was plotted against time as in Figure 3.4. Note that this particular plot will reveal any decay which depends quadratically on triplet density. The curve is quite linear for times less than 10 microseconds and typical for second order decay kinetics. The fact that second order decay is not observed in the later part of the waveform means that as triplet density decreases, the bimolecular decay will become less important than the unimolecular decay. These findings again confirm the concurrent effects of unimolecular and bimolecular decay rates.

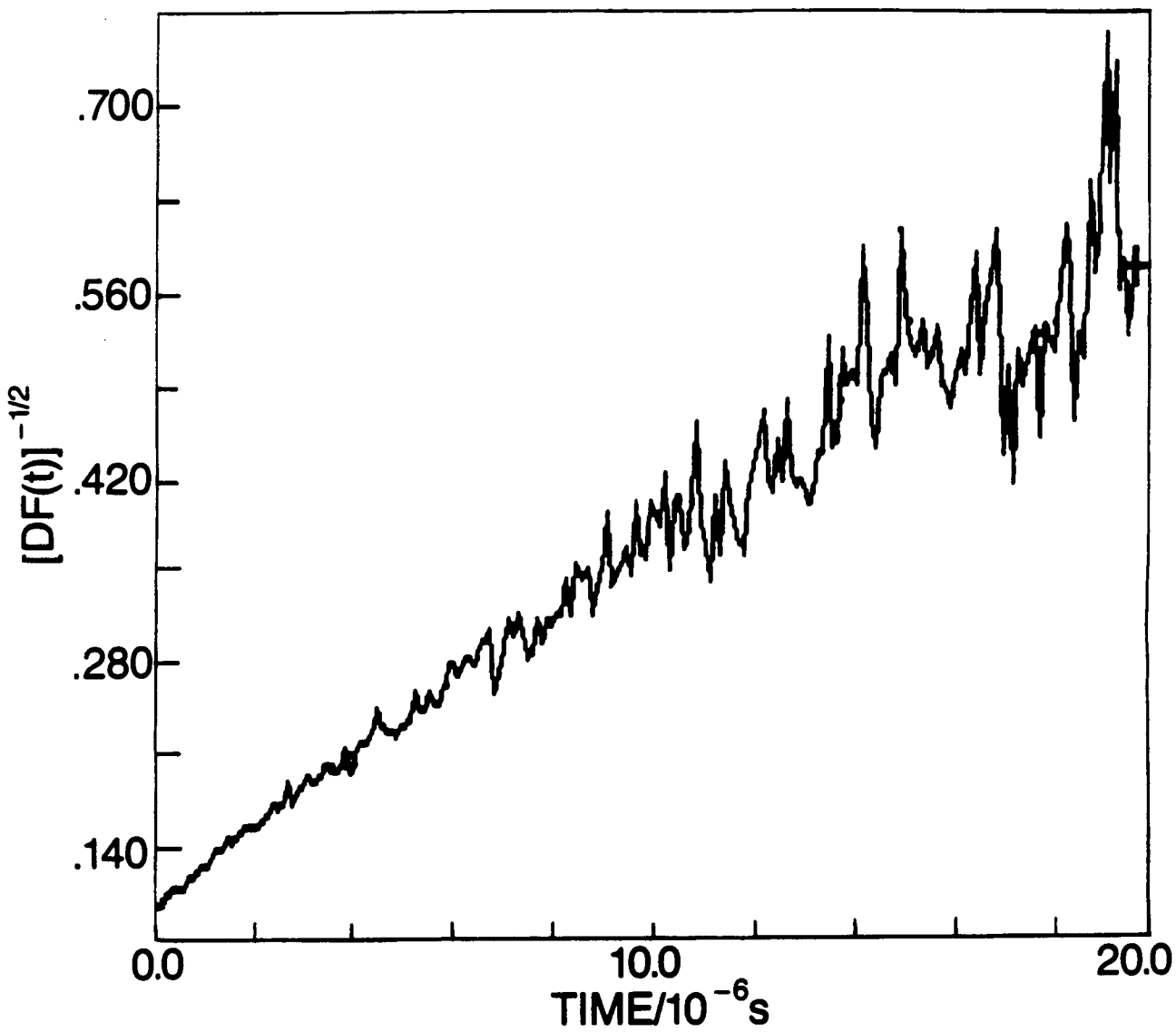


Figure 3.4 DF decay and bimolecular kinetics. The fluence is  $8.0 \times 10^{14}$  photons  $\text{cm}^{-2}$  pulse $^{-1}$ , and the absorption coefficient is  $30 \text{ cm}^{-1}$  (wavelength = 570 nm).

The bimolecular decay rate,  $\gamma$ , is calculated from the slope and y-intercept of plots similar to that shown in Figure 3.4. Note that the ratio (slope/y-int) is  $\gamma/\eta cF$  where  $\eta$  is the efficiency of producing triplet by absorption into the singlet state and assumed to be between 1 and 2. The denominator is the initial triplet number density whenever the duration of the excitation is shorter than all decay lifetimes. Our mode of excitation guarantees the validity of this approximation. Our measured absorbance at 570 nm agrees with measurements performed by Vaubel and Kallmann.<sup>7</sup> Using a measured value of  $30 \text{ cm}^{-1}$  as the absorption coefficient at the excitation wavelength, an annihilation rate of  $1.12 \times 10^{-11} \text{ cm}^3 \text{ sec}^{-1}$  is obtained. In the calculations, (a) the quantum yield of triplet formation is assumed to be unity, (b) it is assumed that, following a T-T annihilation, the probability of emission is small, (c) the effect of triplet diffusion in the radial direction is neglected, and (d) it is supposed that light is uniformly absorbed along the laser beam axis. The effect of lateral diffusion is to reduce the actual triplet density in the illuminated volume. If the optical density of the crystal is higher than 0.3, the triplet density at one surface of the crystal would be 50% higher than triplet density at the opposite end. In all measurements, optical densities are kept below 0.3 to minimize effect (d). Our measured rate of T-T annihilation is a factor of 4 lower than the value reported by Bouchriha et al.,  $4 \times 10^{-11} \text{ cm}^3 \text{ sec}^{-1}$ .<sup>10</sup> The largest discrepancy is probably introduced by the assumption that the triplet yield,  $\eta$ , is equal to 1.

These results show that triplets exist as mobile excitons in crystalline single crystals. From the engineering point of view however, single crystal films of practical dimensions are very hard to grow and difficult to handle. There is certainly a need for investigating more controllable systems such as sublimed thin films. Section 3.3 will address the excitonic decay in such a film.

### 3.2.3 Decay and absorption length

The performance of the proposed singlet delta oxygen generator was initially assessed with the assumption that the unimolecular decay rate will be of the order of  $100 \text{ s}^{-1}$  as measured by McGlynn et al.<sup>11</sup> in tetracene single crystals. The unimolecular deactivation of triplets in our tetracene single crystals, however, was measured to be three orders of magnitude higher ( $1.2 \times 10^5 \text{ sec}^{-1}$ ). This dramatic change needs to be addressed and considered in the system design. It is worth noting that the lifetime shortening can be caused by (a) triplet diffusion to a contaminated surface and subsequent annihilation, (b) annihilation at defects and impurity sites in the bulk and (c) energy transfer from surface sites to oxygen which can contribute to the depletion of triplets. Measurements show that triplet decay kinetics is a sensitive function of sample preparation, exposure to air and possibly film thickness. An order of magnitude increase in  $\beta$  (measured at 570 nm) is recorded as the crystal is exposed to air over a long period of time: from  $1.2 \times 10^5 \text{ s}^{-1}$  for a freshly grown crystal to  $1 \times 10^6 \text{ s}^{-1}$  for a 3 week old sample. This aging effect could result from a slow oxidation of the crystal bulk or from molecular oxygen which may have diffused over time into the bulk of the crystal.

The annihilation of triplet excitons at a tetracene crystal surface can contribute to a reduction of the observed triplet lifetime. Similar

observations have been reported in the literature. Faidysh and Zima<sup>12</sup> observed that the energy transfer in mixed anthracene-tetracene crystal films is a function of sample thickness, d. In these experiments, energy is transferred from anthracene (host) singlet excitons to tetracene (impurity sites) which fluoresces. The competition between exciton trapping at surface defects and tetracene sites was reported to be the cause of the decreased energy transfer at small crystal thickness. Birks<sup>13</sup> attributed the shortening of fluorescence lifetime in micron thick crystals to surface oxidation of anthracene. The observation is attributed to trapping of singlet excitons at the anthraquinone surface because the absorption of the latter is red-shifted with respect to anthracene. For tetracene crystals, exposure to air results in surface oxidation and formation of a tetraquinone layer which acts as a sink for singlet excitons.<sup>14</sup> Because the triplet energy of anthraquinone is ca. 0.9 eV higher than anthracene<sup>15</sup> and the same order could be true for tetracene, trapping of triplet excitons was not expected to occur.

To understand triplet decay in tetracene crystals, the dependence of the triplet lifetime on absorption depth was studied. As described earlier, the effect of interest is the possible quenching of triplets at the surface and the increase of  $\beta$  when surface quenching is deliberately promoted. The most straightforward experiment would be to measure DF of crystals of various thicknesses (e.g. 500 - 0.5 microns) upon a uniform absorption of the excitation beam. The preparation of crystal films with thicknesses varying over a wide range is close to impossible and such a scheme is hard to execute. For these reasons, an alternative experiment is done in which a tetracene crystal is excited with a pulsed laser whose wavelength is changed to control the depth of absorption. To enhance the effects, tetracene crystals are exposed to air for a period of 6-8 weeks to make sure that the oxidation has carried on to an advanced stage. The trapping probability of an exciton at the closest dye surface must be a function of its distance to that surface. By reducing the absorption depth of the dye film, one can effectively decrease the average distance of the induced triplet exciton to the illuminated surface. The crystal thickness is estimated, by measuring the crystal area and weight, to be about 50 microns. The wavelength is changed from 570 to 530 nm corresponding to an absorption length from 400 to 0.4 microns.<sup>7</sup> Figure 3.5 shows the unimolecular lifetime as a function of the absorption length. The lifetime decreases dramatically for an absorption depth of less than 5 microns. At 490 nm, where the absorption depth is probably  $\ll 10^{-4}$  cm but not known, the rate is  $2.3 \times 10^6 \text{ s}^{-1}$ . These results demonstrate the presence of triplet annihilation sites at the surface of tetracene. It is not certain whether or not these sites are the same species, namely tetraquinone, that quench singlet excitons in Vaubel and Baessler's experiments.<sup>14</sup> As mentioned earlier, from the energetic point of view, tetraquinone triplet energy is presumably higher than tetracene and trapping is unlikely. Other processes which result in the annihilation of the excitonic energy such as charge-transfer reaction are probably responsible for the reduced lifetimes.

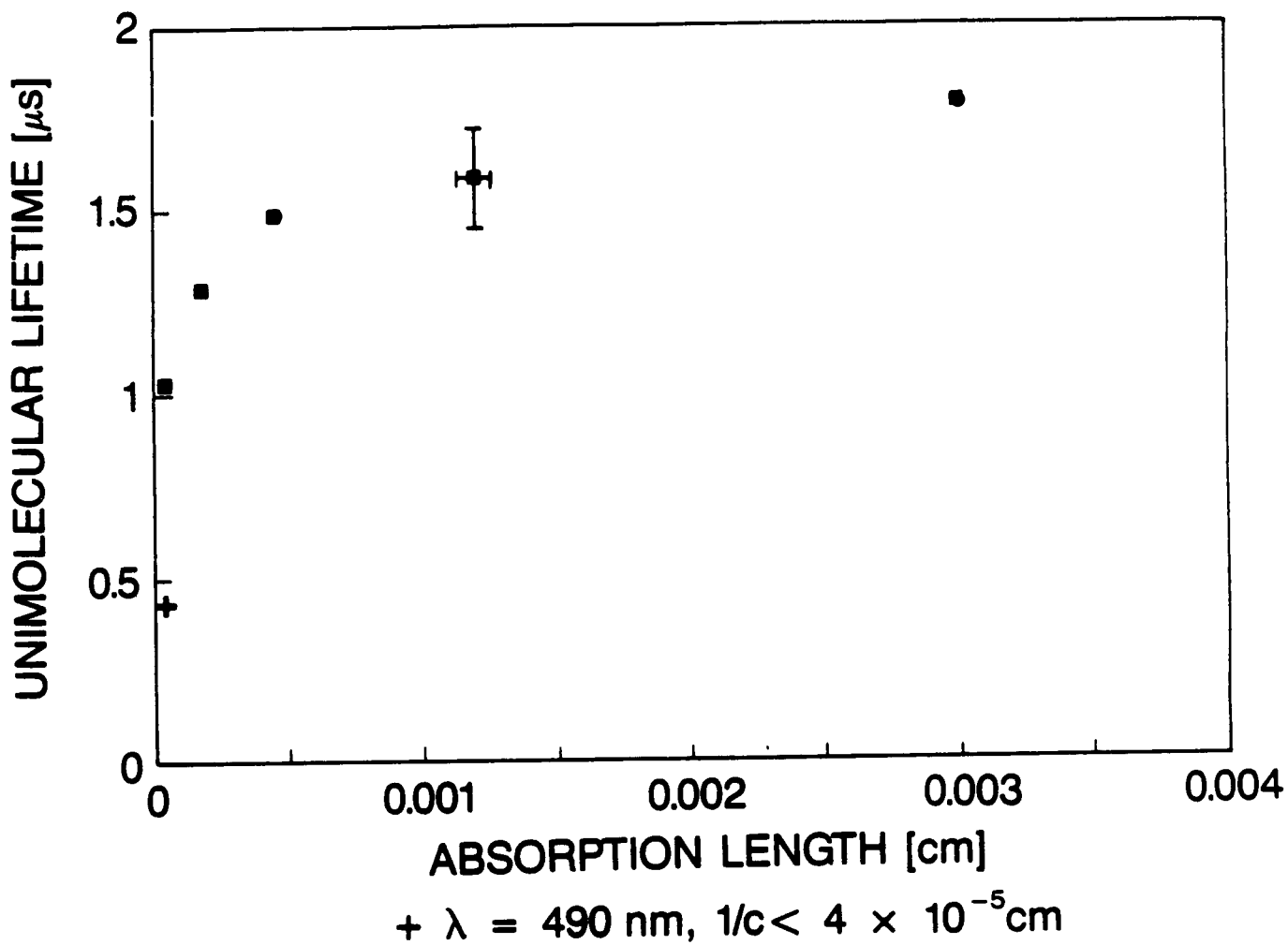


Figure 3.5 DF decay vs. optical penetration depth. The crystal film is ca. 250 nm thick, and the excitation wavelength is changed to vary the penetration depth up to 400 nm.

In conclusion, it was found that triplet excitons are present in single crystals of tetracene, and the bimolecular decay rate, which is within an order of magnitude of the literature values, was measured.

### 3.3 Triplet Exciton Decay in Polycrystalline Film

In light of the information attained in the previous study of tetracene crystals, it appears that (a) the method of preparing tetracene films might make a major difference as far as triplet decay is concerned and (b) the shortening of the unimolecular triplet lifetime can be a critical factor in the design of a thin film sensitizer. Because the films to be studied are now polycrystalline instead of single crystals, a large difference in decay rates is expected. The purpose of measuring decay rates of excited polycrystalline films is to demonstrate that these films can support excitonic transfer of energy, to measure the unimolecular and bimolecular decay rates and, using this data base, to determine the optimum conditions for energy transfer to surface trapping sites.

The purpose of studying polycrystalline films is to confirm that sublimed dye can be used in an O<sub>2</sub> singlet generator instead of single crystals. It is assumed that sublimed films can be made polycrystalline by controlling the conditions of deposition. There is evidence supporting that assumption. It is known that the crystalline structure of vacuum-deposited dye films, tetracene included, is controlled by regulating the temperature of the substrate onto which the dye is evaporated.<sup>16</sup> In general the warmer the substrate the more crystalline is the film. When the glass substrate is kept at room temperature (or warmer), evaporated films of perylene or coronene show sharp X-ray diffraction lines which indicate a well-oriented crystalline structure. Another indication of the crystalline structure is the Davydov splitting of the 0-0 component of the first singlet transition. The absorption spectrum of a 450 Å thick film of evaporated tetracene is measured in this study and shown in Figure 3.6. In the spectrum the Davydov splitting is present at about 520 nm. This splitting is mainly caused by molecular orientation and not from resonance coupling among randomly distributed molecules as shown by Maruyama et al.<sup>16</sup> They observed the disappearance of the splitting when the substrate is cooled down to liquid nitrogen temperatures prior to deposition, which results in the formation of amorphous films. Because evaporated films are polycrystalline, it is expected that they also support excitonic energy transfer in a similar way crystals do.

The study of exciton decay in sublimed dye films will be discussed next. Data analysis of DF will be different from what was previously described and for that reason another detailed explanation of the experimental procedure is given.

#### 3.3.1 Experimental

The optical setup is similar to the one discussed in 3.2. The delayed emission is induced by a pulsed dye laser (Molelectron DL-II pumped by a UV-12 nitrogen laser). The pulse duration, 5 nsec, is typically much smaller than the emission lifetimes. Tetracene, obtained from Aldrich, is purified by fractional sublimation. Purified dyes are

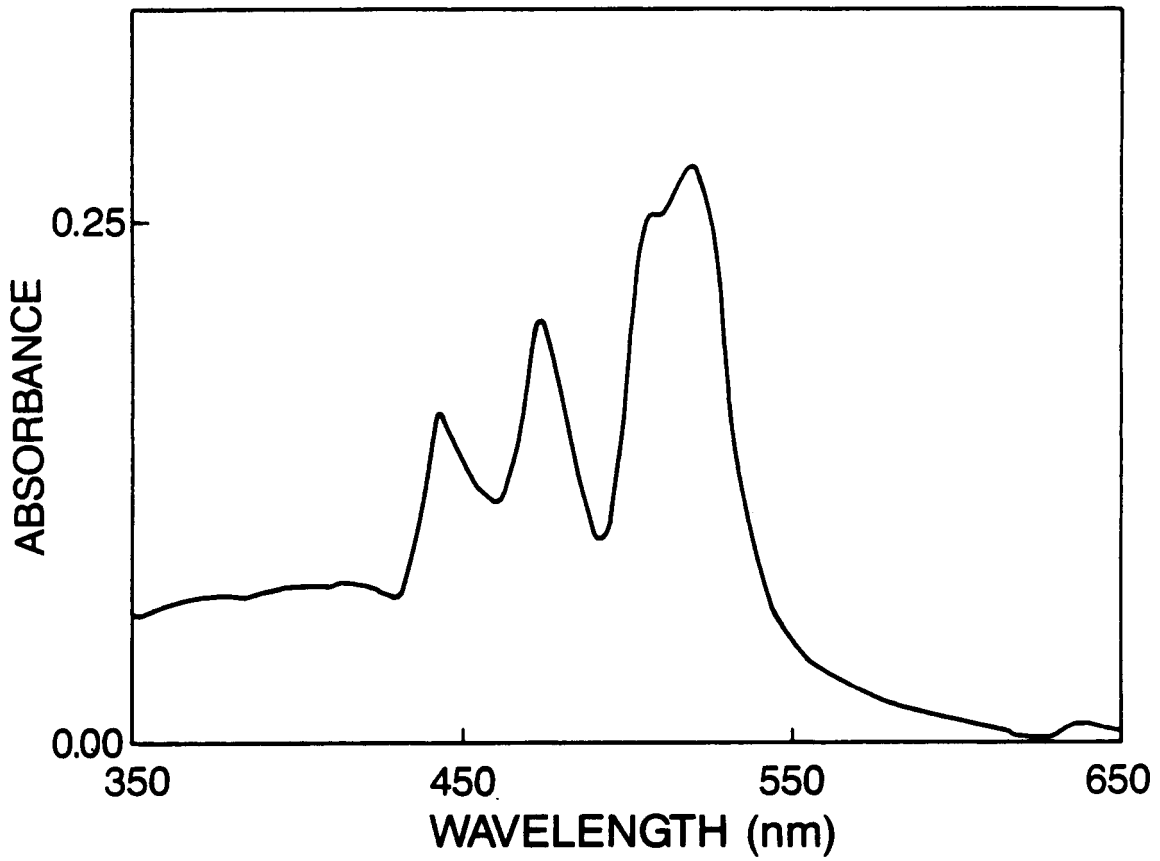


Figure 3.6 Absorption spectrum of a thin sublimed tetracene film.

then sublimed in high vacuum to deposit thin films in a vacuum coater (Edwards EM-100). Thin films are grown on glass or metallic substrates at room temperature by sublimation in vacuo ( $1 \times 10^{-5}$  Torr). The absorption coefficient of the film cannot be measured with traditional transmission methods because of the excessive scattering of tetracene polycrystalline films. As a consequence, pyroelectric absorption measurements, which are further discussed later, are required. The emission is dispersed by a monochromator (I.S.A. H-20), and long wavelength pass filters are used to further discriminate against scattered light. The monochromator is set at 560 nm which corresponds to tetracene singlet fluorescence. An S-20 photomultiplier (Hamamatsu R928) is used as the detector. The photocurrent is recorded with a digital oscilloscope (LeCroy 9400). Signal averaging and data analysis are done as described in Section 3.2.

### 3.3.2 Triplet density

To measure the bimolecular decay rate, it is necessary to know the triplet density,  $n$ , generated upon photoexcitation. Unfortunately, the photometric method does not give a direct measurement of  $n$ . The initial triplet number density will be approximated by the product  $\eta c f$ , where  $\eta$  is the singlet-triplet conversion efficiency,  $c$  the absorption length and  $F$  the laser fluence. In this study, the yield of forming triplet,  $\eta$ , is assumed to be 1 when light is absorbed into the singlet band. In polycrystalline solids where scattering is important, extinction of the incident light beam is comprised of absorption as well as scattering. Usual photometric instruments relying on transmission of light through the sample cannot distinguish absorption from scattering losses. In this experiment, the amount of heat generated in the film following excitation is measured by the laser pulse with a pyroelectric film (Kynar by Penwalt). With the supposition that emission yield is much less than unity and the conversion to thermal energy is proceeding with efficiency close to unity, the absorbance of the film is easily calculated from the calorimetric signal. The technique and the calibration scheme are described in Appendix B. The nature of the absorption measurement requires the dye film to be deposited on the aluminum side of the pyroelectric detector for the following reason. With a dye film, light can either transmit through the dye, scatter or reflect back. The total absorbance is not a simple function of the absorption length and dye thickness. Because of this difficulty, it is necessary for DF and absorption measurements to be performed on the same sample. In a typical experiment, dye films (< 1000 Å) are deposited directly on the pyroelectric film for delayed fluorescence as well as absorption measurements.

The laser wavelength is set at 478 nm where the p-band absorption of tetracene is maximum. Figure 3.7 shows absorption at 478 nm as a function of thickness. The displayed curve indicates that in a thick film, 50% of the maximum absorption occurs within the first 600 Å and using thicker films will result in a nonuniform initial triplet density. In the latter case triplet concentration at the illuminated surface is higher than in the bulk. Because the initial triplet density is used to ascertain the bimolecular decay rate, the experiment is best done with a more or less uniform initial triplet density and for this reason a film thinner than 1000 Å was chosen.

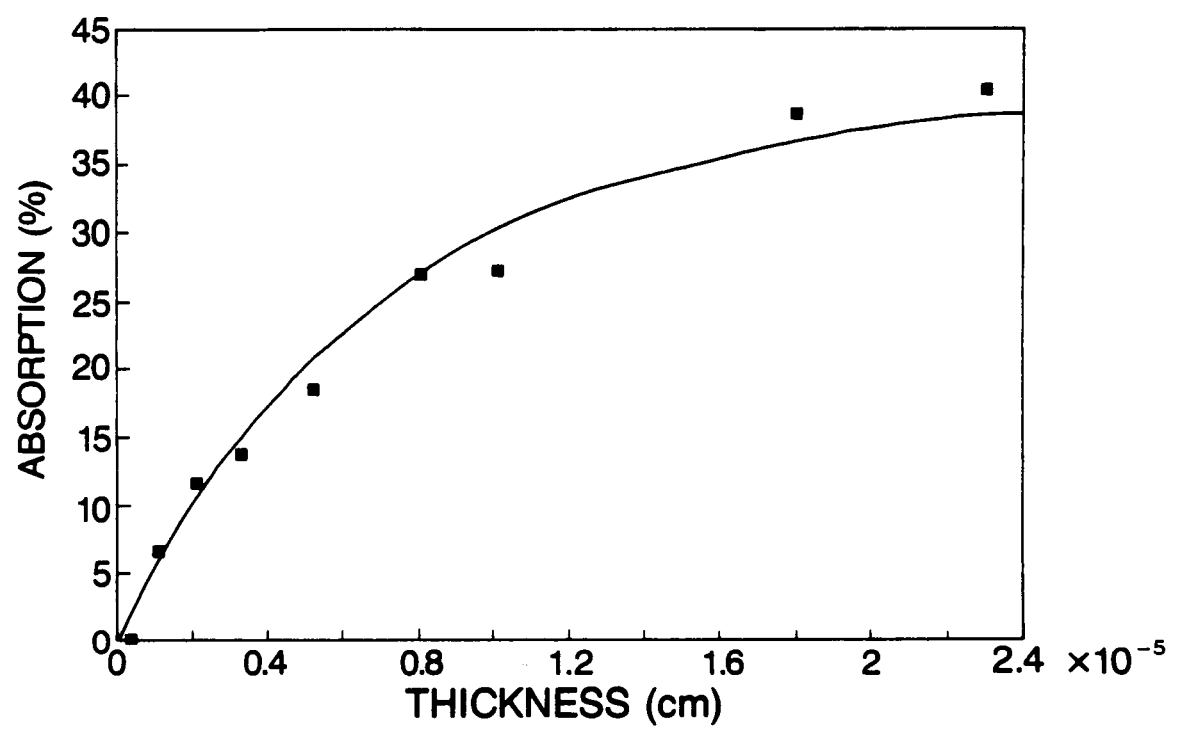


Figure 3.7 Absorbance vs. film thickness.

### 3.3.3 Results and discussions

Figure 3.8 shows the time-resolved emission recorded at 600 nm with the excitation at 478 nm. Because of the magnitude of the noise feature which is concurrent with the pulsed laser, the photomultiplier response is mildly saturated at time zero, but, for times greater than 20 nsec the response is observed to be linear. The DF signal decays with a time constant approximately two orders of magnitude smaller than the decay time constant measured in freshly grown single crystal films. The sampling interval of the digital oscilloscope (LeCroy 9400) is 10 nsec. Because of the reduced triplet lifetime, this time resolution is not fine enough for the time-resolved data to be analyzed the way it has been done with tetracene single crystals. Appendix A shows how the fluence dependence of a decay which is only coarsely time-resolved can be used in determining the decay kinetics. A fluence dependence study was conducted, and data were analyzed according to the results of Appendix A. The idea behind this method is to use the explicit dependence of DF on laser fluence and on time to determine the kinetic rates. In this study DF is recorded at fixed times (30 to 100 nsec) after the laser pulse, and its dependence on laser fluence is measured. Figure 3.9 shows DF against laser fluence [photon cm<sup>-2</sup> pulse<sup>-1</sup>]. It has been shown in Appendix A that for a predominantly unimolecular process, the DF signal is a single-exponent decay. When measured at a given time after the laser pulse, DF varies as the square of fluence (Eq. (A.6)). In Figure 3.9, the mentioned quadratic behavior is apparent only at laser fluences lower than  $3 \times 10^{13}$  photons cm<sup>-2</sup>. The deviation from quadratic dependence at high fluences is due to the contribution of bimolecular decay at high fluences and is evidence that the triplet decay is controlled by kinetics with order higher than 1. To determine the decay rate constants  $\beta$  and  $\gamma$ ,  $DF^{1/2}$  is plotted against 1/fluence as a function of time as in Figure 3.10. In Appendix A, it is shown that data points measured at the same time will fall on a straight line according to Eq. (A.7). The relation is verified for times from 30 to 100 nsec with respect to the laser pulse.

The unimolecular rate is determined with the analysis of Figure 3.10 and the use of Eq. (3.3) which is (A.9) in Appendix A.

$$\text{slope } (t) = e^{\beta t} A^{-1/2} c^{-1} \eta^{-1} \quad (3.3)$$

The slopes are those obtained in best fit lines similar to those shown in Figure 3.10 (at various times from 30 nsec to 100 nsec). In Figure 3.11 the logarithm of the slope is plotted against the time of measurement, and the slope of the resulting best fit line is equal to  $\beta$  according to Eq. (3.3). The linear fit in Figure 3.11 confirms Eq. (3.3) and gives a  $\beta$  of  $1.1 \times 10^7$  sec<sup>-1</sup> which shows two orders of magnitude increase with respect to the single crystal value measured earlier. The shortening of the unimolecular lifetime in polycrystalline films is worth some discussion. The microcrystalline structure of vacuum-deposited tetracene has been reported to be composed of large domains (width = 20 microns).<sup>17</sup> Because the film thickness (0.1 micron) is much smaller than the lateral dimension, it is expected that excitonic kinetics in these films will be similar to the single crystal

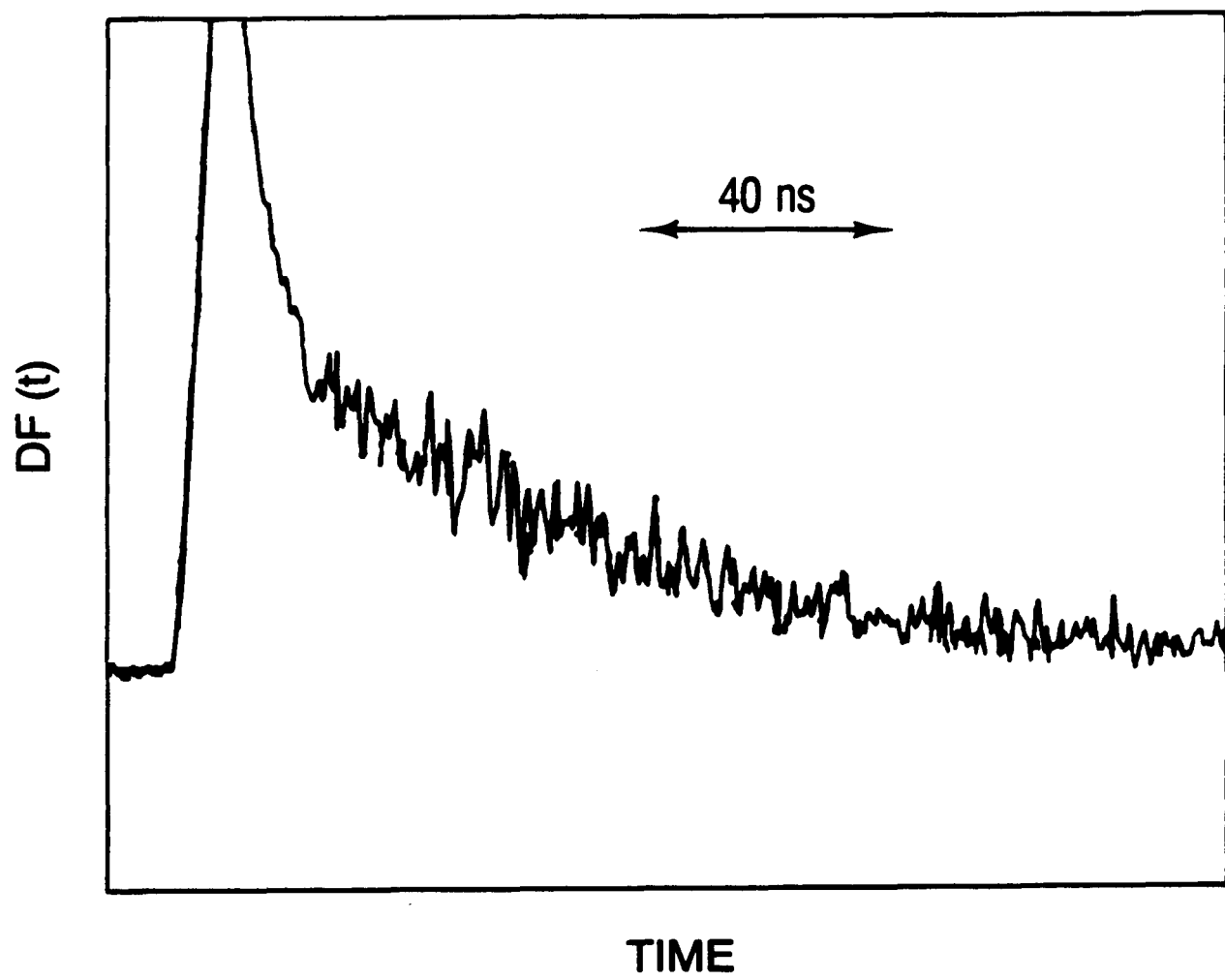


Figure 3.8 DF decay of tetracene polycrystalline film.

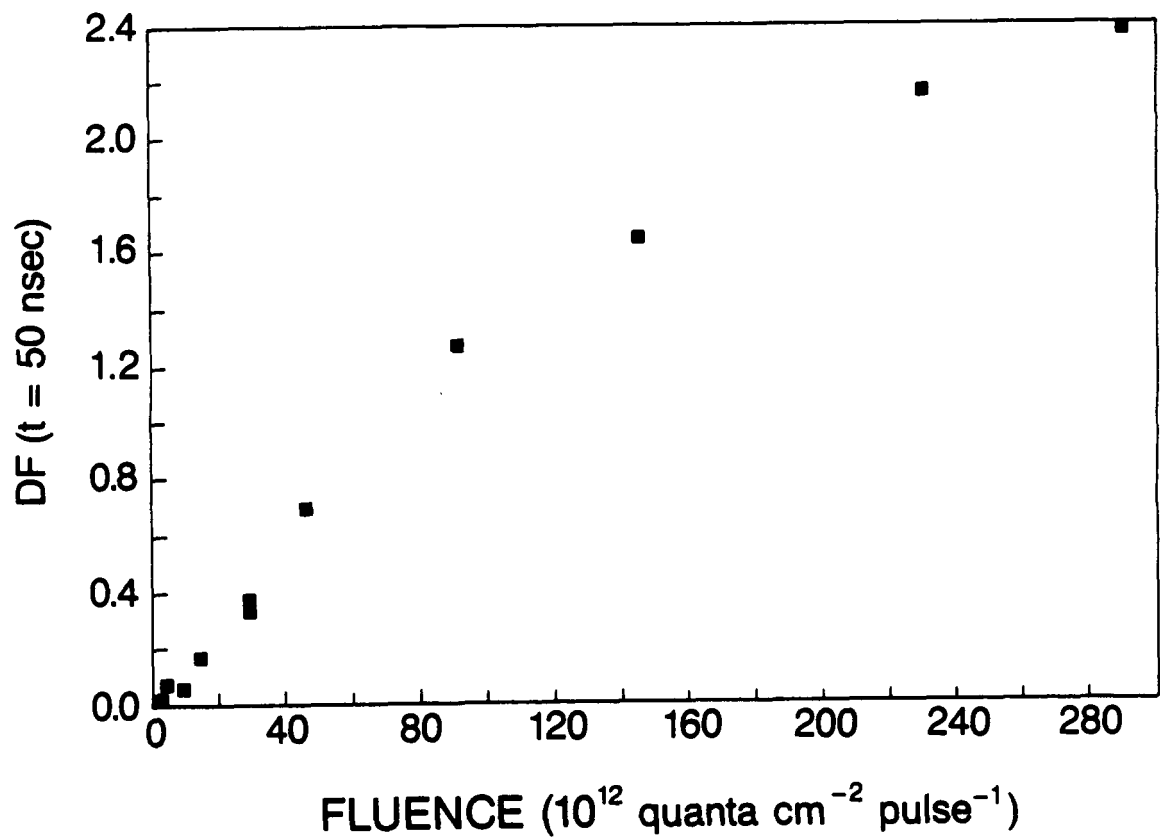


Figure 3.9 DF at 50 nsec after laser excitation. The excitation wavelength is 478 nm, and the emission is recorded at 600 nm.

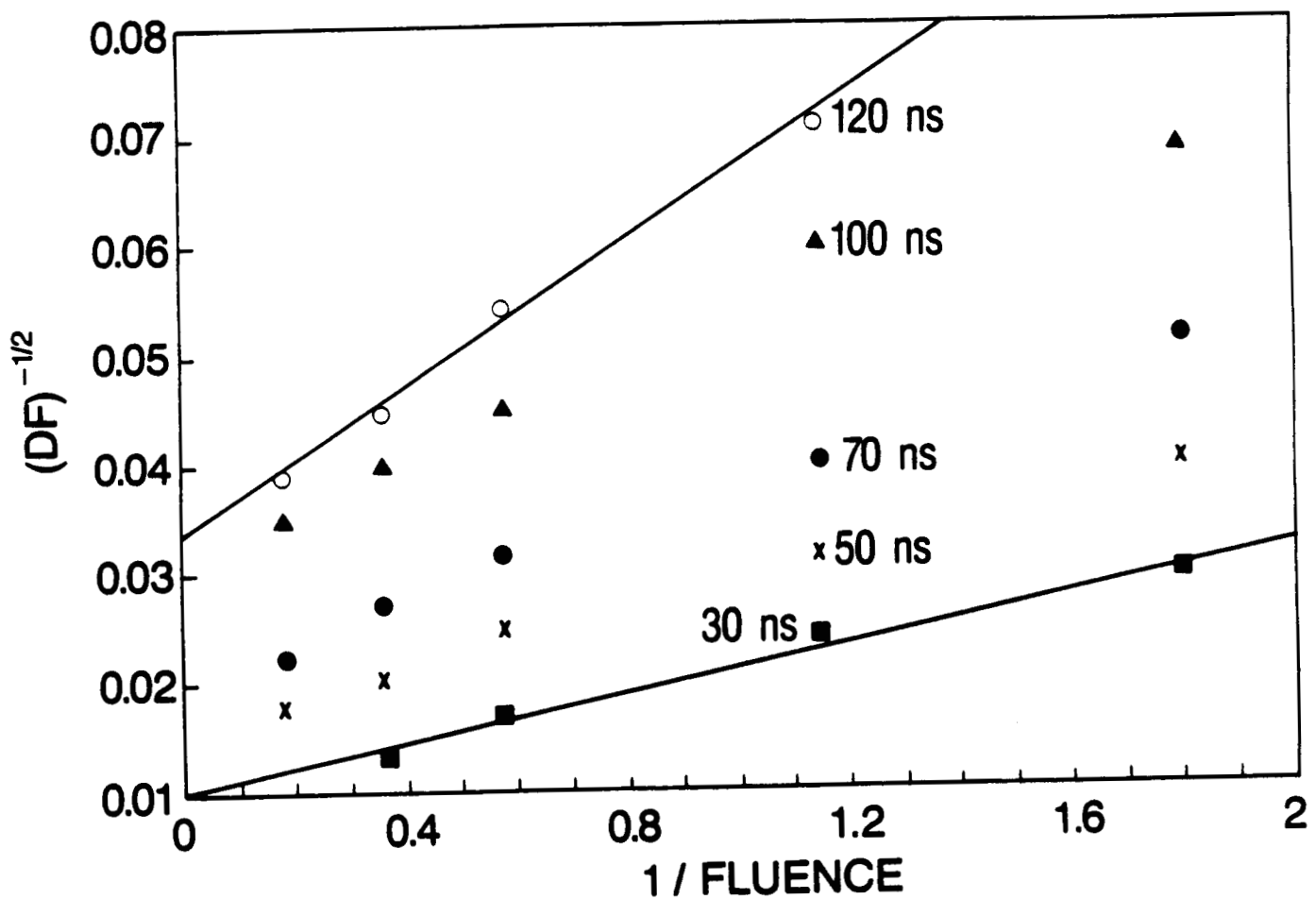


Figure 3.10 Fluence dependence of DF at fixed times.  $DF^{-1/2}$  is plotted against  $1/\text{Fluence}$  as a function of time.

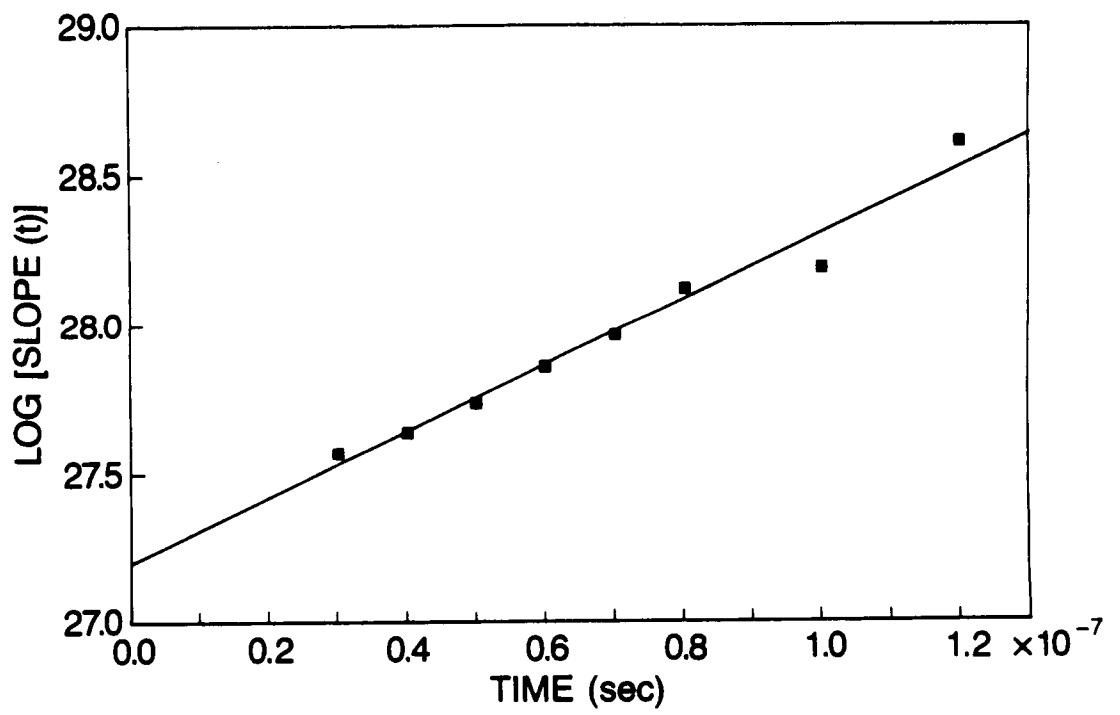


Figure 3.11 Unimolecular decay.

kinetics. The fact that  $\beta$  is two orders of magnitude higher in polycrystalline films than in single crystals is possibly due to the presence of more annihilation sites. Using a simple hopping model with a hopping frequency of  $1 \times 10^{10} \text{ s}^{-1}$ <sup>18</sup> and unity trapping efficiency, one calculates a triplet lifetime of  $10^{-7}$  sec for a 0.001 mol/mol trap concentration. There is reason to believe that impurity concentration is higher in vacuum-deposited films than in single crystal films: the slow process of crystallization in inert gas is by itself an effective purification process. To effectively deplete the triplet density, the annihilation sites do not have to be in the bulk. Tetraquinone, which was speculated to form at the surface, (discussed in Section 3.2) may play an important role in triplet annihilation. The formation of the latter is further facilitated by the higher density of defect sites in sublimed films and a possible diffusion of oxygen into the bulk.

The bimolecular rate comes from the knowledge of  $\beta$ , the y-intercept and slope of plots shown in Figure 3.10. It follows from the treatment in Appendix A (see Eq. (A.7)) that the ratio of y-intercept to slope is equal to

$$\frac{\text{Y-int}}{\text{Slope}} = \frac{\eta c \gamma}{\beta} \left( \frac{e^{\beta t} - 1}{e^{\beta t}} \right) \quad (3.4)$$

From the knowledge of  $\beta$ ,  $c$  and  $t$ , one can calculate the bimolecular rate constant;  $\eta \gamma = 1.5 \times 10^{-11} \text{ cm}^3 \text{ s}^{-1}$ . The uncertainty of  $\gamma$  is discussed next. The measured bimolecular rate is in fair agreement with single crystal results. If it is assumed that  $\eta=1$ , the T-T rate reported by Bouchriha et al.<sup>10</sup> would be a factor of 3 higher than the rate measured in polycrystalline films here, and a factor of 4 higher than the single crystal value. The quantum yield of producing triplets could be less than 1 or as high as 2. The yield would be small whenever radiationless decay of singlets is fast. The results here imply that the yield,  $\eta$ , is about 0.3 in the experiment. The value of  $\gamma$  in polycrystalline films, however, has to agree with the crystalline value to within the experimental error bar (20 percent). It is anticipated that the rate,  $\eta \gamma$ , measured with polycrystalline films would be smaller due to a faster singlet annihilation. The absence of that effect probably indicates that singlet annihilation is not any more likely in polycrystalline films than in crystalline films.

### 3.4 Conclusions

This chapter addresses the kinetics of triplets in thin films. The questions answered deal with the photophysics of dye films, and no attempt has been made to incorporate these issues with the technical feasibility of the prospect of an  $O_2^*$  generator. A summary of conclusions follows:

- (a) Time-resolved delayed fluorescence can be used to study triplet decay kinetics of tetracene crystals and sublimed polycrystalline films.
- (b) The measured bimolecular decay rate in tetracene crystals is within an order of magnitude of the literature value.

(c) The unimolecular decay in a freshly grown 50-micron-thick crystal at room temperature is three orders of magnitude faster than the accepted radiative decay rate. The observed  $\beta$  shows strong dependence on exposure to air and absorption depth.

(d) The unimolecular decay rate in polycrystalline films is two orders of magnitude higher than its crystalline counterpart.

(e) Bimolecular annihilation rates are measured for polycrystalline films and found to be comparable to the single crystal value (with the assumption that the estimate of initial triplet density used here is correct).

#### APPENDIX A: Decay kinetics in solid dyes

To properly interpret the delayed fluorescence (DF) data, a simple kinetic model describing the annihilation of triplet excitons is required. The model must have all the relevant parameters, namely unimolecular and bimolecular rate constants.

At room temperature, triplet excitons are essentially free except for trapping at bulk and surface sites. The number of triplet excitons per unit volume at time,  $t$ , is described by the following rate equation

$$\frac{dn}{dt} = -\beta n - \gamma n^2 \quad (A.1)$$

where  $\beta$  is the unimolecular decay rate and  $\gamma$  is the triplet-triplet ( $T-T$ ) annihilation rate. In (A.1) the triplet diffusion term is neglected. The triplet formation is not included because the time window of interest is the decay after the laser pulse, and in all cases, the laser duration is shorter than any relevant decay times. With  $n(0)$  being the triplet density at time zero (laser occurrence), the triplet density decays as follows:

$$n(t) = \frac{n(0)e^{-\beta t}}{\frac{\gamma n(0)}{\beta} (1-e^{-\beta t}) + 1} \quad (A.2)$$

For a laser beam having a flat intensity profile and operating in the optically thin regime,  $n$  is the constant in the illuminated volume. The optical density condition is less important for thin films because the longitudinal diffusion is fast (10 nsec for a 1000 Å thickness).

Delayed fluorescence was measured in this experiment. It should be noted that DF results from a fusion of two triplet excitons and fluorescence of the singlet, but because the total loss of triplet excitons via this mechanism is small compared to annihilation, one can always neglect its effect in Eq. (A.1). With these assumptions, the total delayed fluorescence can be expressed as

$$DF_{TOT}(t) = \frac{1}{2} f \gamma n^2(t) V \quad (A.3)$$

where  $V$  is the volume and  $f$  is the fraction of T-T annihilations which results in fluorescence. The DF signal at the detector can be written as

$$DF(t) = A n^2(t) = \frac{A [n(0)]^2 e^{-2\beta t}}{\left[ \frac{\gamma n(0)}{\beta} (1 - e^{-\beta t}) + 1 \right]^2} \quad (A.4)$$

with  $A$  being a factor combining the collection efficiency, excitation volume and  $f$ .

#### Case 1: Low fluences and/or later times

For measurements where  $\beta \gg \gamma n(0)$  or  $t \gg 1/n(0)$ , the decay of the triplet is typically unimolecular and the measured signal is exponential.

$$DF(t) = A [n(0)]^2 e^{-2\beta t} \quad (A.5)$$

With  $c$  being the absorption coefficient [ $\text{cm}^{-1}$ ],  $F$  the laser fluence [quanta  $\text{cm}^{-2}$  pulse $^{-1}$ ] and assuming unity triplet quantum yield the following is true:

$$DF(t) = A \eta^2 c^2 F^2 e^{-2\beta t} \quad (A.6)$$

It is apparent in (A.6) that plotting the logarithm of  $DF(t)$  against time will give a linear curve. The resulting slope is twice the unimolecular decay rate,  $\beta$ , and any deviation from linearity must occur at early times. The nonlinearity which might appear indicates that the bimolecular decay is comparable or more important than the first order process.

#### Case 2: High fluences and early times

From (A.4), one can write

$$[DF(t)]^{-\frac{1}{2}} = \frac{\gamma}{\beta A^{\frac{1}{2}}} (e^{-\beta t} - 1) + \frac{e^{\beta t}}{\eta c F A^{\frac{1}{2}}} \quad (A.7)$$

For times  $t$  such that  $t \ll 1/\beta$ , one can approximate

$$[DF(t)]^{-\frac{1}{2}} = \frac{\gamma t}{A^{\frac{1}{2}}} + \frac{1}{\eta c F A^{\frac{1}{2}}} \quad (A.8)$$

With the knowledge of  $c$  and  $F$ , (A.8) can be used to measure the T-T bimolecular decay rate. The nonlinearity of the plot will occur at times larger than  $1/\beta$  where only the unimolecular decay contributes.

### Case 3: General cases

For the general case, the decay as described in (A.4) and (A.7) can be rearranged to explicitly show how one can extract kinetics information from the fluence dependence study. The fixed delay time is a function of laser fluence. The quantity  $DF^{-1/2}$  is plotted against  $F^{-1}$  to yield linear curves. The slope and y-intercept of the curves are:

$$\text{slope} = e^{\beta t} A^{-\frac{1}{2}} c^{-1} \eta^{-1} \quad (A.9)$$

$$Y\text{-int} = \gamma \beta^{-1} A^{-\frac{1}{2}} (e^{\beta t} - 1) \quad (A.10)$$

The combination of (A.9) and (A.10) is then used to determine the kinetic rates.

It is necessary to rely on a fluence dependence study for kinetics information because the emission decay cannot be recorded with adequate time resolution. In the tetracene sublimed film, the decay is measurable for only approximately 200 nsec (20 data points with Lecroy 9400) and this is where the use of (A.9) and (A.10) becomes particularly valuable.

### APPENDIX B: Absorption measurements with a pyroelectric calorimeter

Laser calorimetry has been used for years to measure radiation absorption in both bulk and thin film solids. The fundamental quantity measured is the absorbance  $A$ , as defined by

$$A = \text{absorbed energy/incident light energy} \quad (B.1).$$

Traditional measurements of absorbance rely on optical transmission of the sample. In cases where the extinction coefficient has a considerable contribution from scattering, transmission methods will not give accurate measurements of absorbance. Because the purpose of the experiment is to measure the total absorbance of a given film thickness the effect of changing optical energy density in the vicinity of the interfaces is ignored.

#### Experimental:

Figure 3.12 shows the components of the pyroelectric detector. A 1.0 by 1.0 inch square of poly(vinylidenedifluoride) (PVDF purchased from Pennwalt as KYNAR S052N00) serves as the pyroelectric film. The

PVDF film has aluminum metallization: metal thickness = ca. 1000 Å. Signal and ground leads are attached to aluminum electrodes via copper foil tabs with conductive adhesive. The arrangement is such that most of the film is not in contact with the backing glass substrate and heat loss is minimized. The film to be measured is vacuum-deposited on the aluminum electrode. The measurement consists of illuminating the film at normal incidence with a pulsed laser (nitrogen-pumped dye laser) and recording the voltage across the electrodes. The electric signal is signal averaged and analyzed with a computer.

Thermal energy generated by absorption into the film raises the temperature of the PVDF film. The electrical response of the PVDF film is pyroelectric by nature and consequently tracks the temperature change rather than temperature itself. The total charge generated at the metal electrode is

$$Q = P \int_{\text{Area}} (T - T_0) dA \quad (\text{B.2})$$

where  $P$  is the pyroelectric coefficient,  $T_0$  the base temperature (=room temperature) and  $T$  the transient temperature.  $T$  rises to its maximum with the radiationless decay and/or thermal diffusion time constants (less than 100 nsec). It decays down to  $T_0$  with the time constant of the heat loss ( $= 100$  msec as shown in Figure 3.13) which is itself much smaller than the electrical time constant. The temperature change is related to laser fluences,  $I$ , as shown below:

$$T - T_0 = \frac{IdA}{(pc_p t + p_m c_{pm} t_m)} dA \quad (\text{B.3})$$

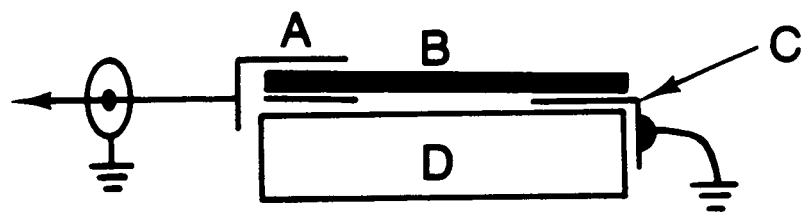
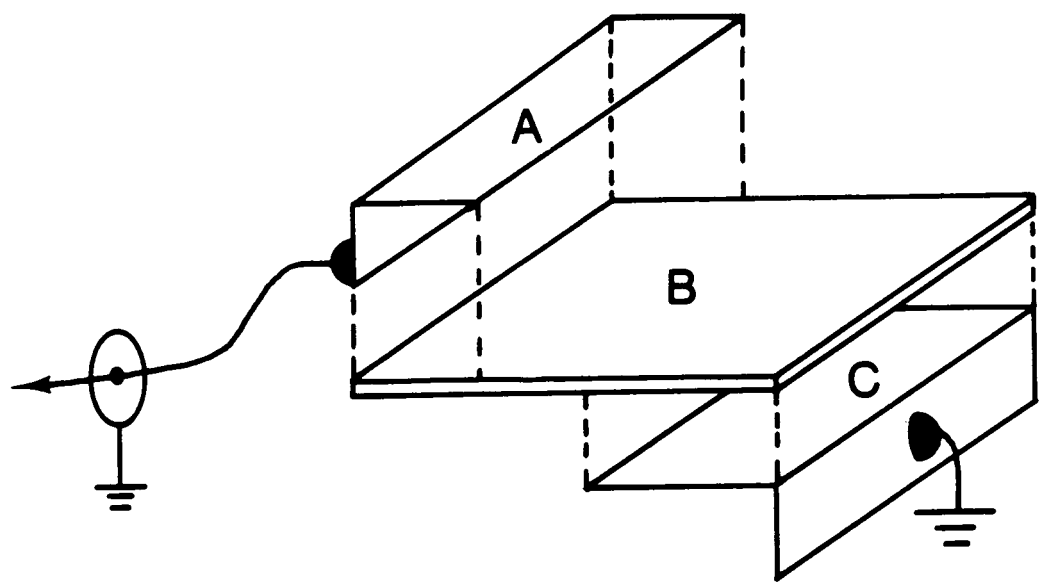
where  $p(p_m)$  = density of dye (of PVDF film)  
 $c_p(c_{pm})$  = specific heat of dye (of PVDF film)  
 $t(t_m)$  = dye thickness (PVDF thickness)

The charge and electrical signal are

$$Q = \frac{P E_{\text{laser}}}{(pc_p t + p_m c_{pm} t_m)} \quad (\text{B.4})$$

and

$$V = \frac{P E_{\text{laser}}}{(pc_p t + p_m c_{pm} t_m)} \left( \frac{t}{A\varepsilon} \right) \quad (\text{B.5})$$



**A,C : electrodes**  
**B : PVDF film**  
**D : glass plate**

**Figure 3.12 Schematic of pyroelectric calorimeter.**

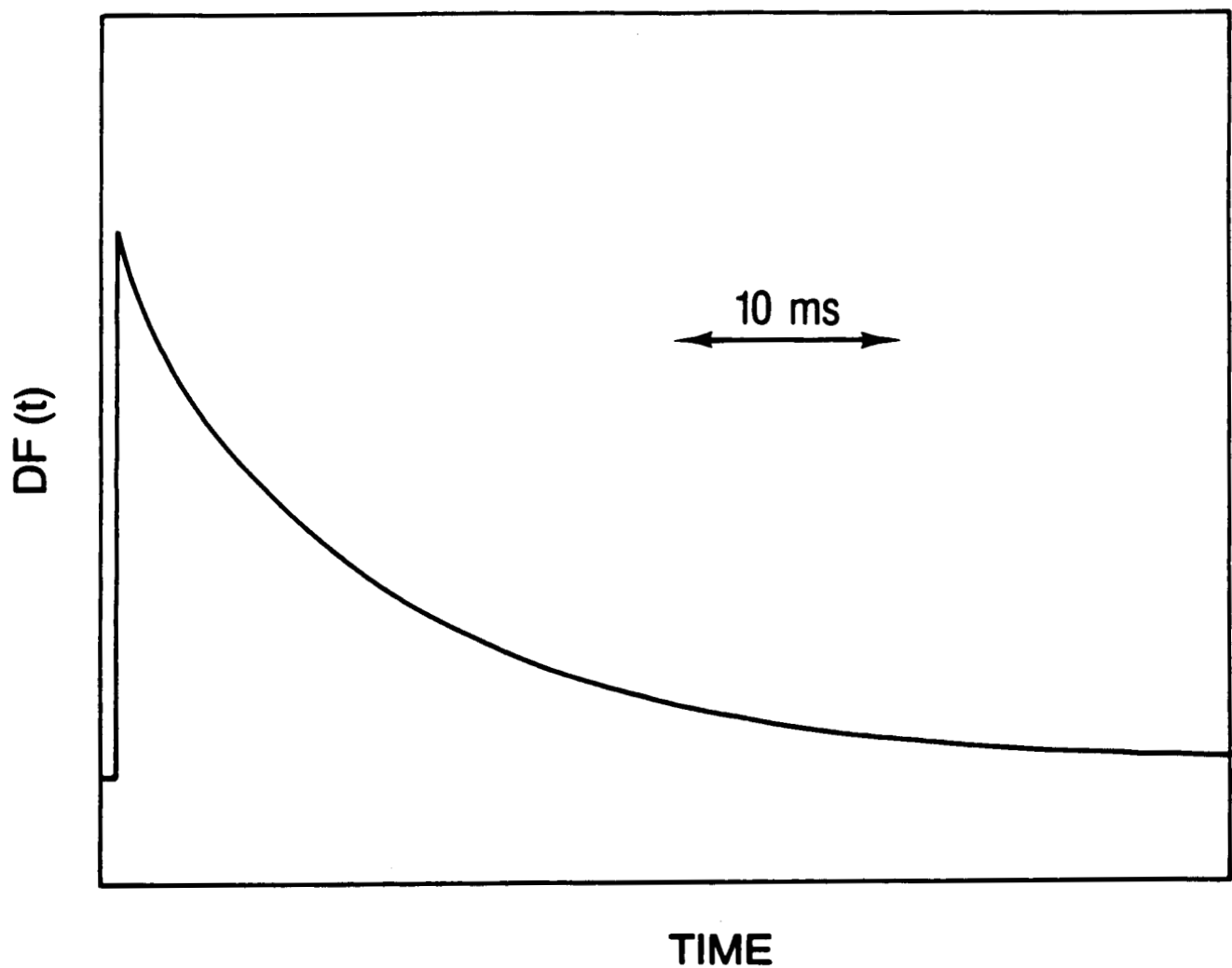


Figure 3.13 Pyroelectric signal.

where  $\epsilon$  is the PVDF dielectric constant and  $A$  the total film area. From Eq. (B.5) it is clear that the electric signal is proportional to the absorbed energy per laser shot,  $E_{\text{laser}}$ . Figure 3.14 displays the linearity of the detector response.

### Calibration:

To discuss the calibration scheme, it is crucial to elaborate on the actual measurement. Figure 3.15 describes the sequential absorption of the incident beam. The reflectance at the air-dye interface is  $R_1$  and the metal-dye interface  $R_2$ . The beam energy,  $I$ , at points A to D is given by

$$\begin{aligned} I_A &= (1-R_1) I_o \\ I_B &= (1-R_1)(1-S-A) I_o \\ I_C &= R_2 (1-R_1)(1-S-A) I_o \\ I_D &= R_2 (1-R_1)(1-S-A)^2 I_o \end{aligned} \quad (\text{B.6})$$

In Eq. (B.6),  $I_o$  is the incident energy,  $S$  the fraction of light scattered in one pass through the film and  $A$  the fraction of light absorbed. The amount of light absorbed (and the pyroelectric signal) is proportional to

$$\begin{aligned} E_{\text{laser}} &= (1-R_2)(1-R_1)(1-S-A)I_o + (1-R_1)A I_o \\ &\quad + (1-R_1)R_2(1-S-A)A I_o \end{aligned} \quad (\text{B.7})$$

For optically thick films the approximation:

$$E_{\text{laser}} = (1-R_1)A I_o \quad (\text{B.8})$$

is valid. For most cases,  $E_{\text{laser}}$  is a complicated function of the metal-dye reflectance,  $R_2$ . The calibration scheme assumes and requires that  $R_2$  is constant throughout the experiment. The calibrated signal is the one measured with a thick acriflavine film (thickness = 5000 Å which corresponds to a  $2.2 \times 10^{-7}$  mol cm<sup>-2</sup> surface density). Using the known absorption coefficient of acriflavine,  $2.1 \times 10^{-4}$  M<sup>-1</sup> cm<sup>-1</sup>,<sup>19</sup> one calculates the calibration film optical density to be 4.6. The air-dye reflectance is also reported<sup>19</sup> to be 0.87. The calibration signal therefore corresponds to an 87% absorption. The choice of the baseline signal is explained as follows: the first term of the right hand side of (B.7) is an absorption into the aluminum mirror and to accommodate for this effect, the signal of a very thin film (< 50 Å) is chosen to be

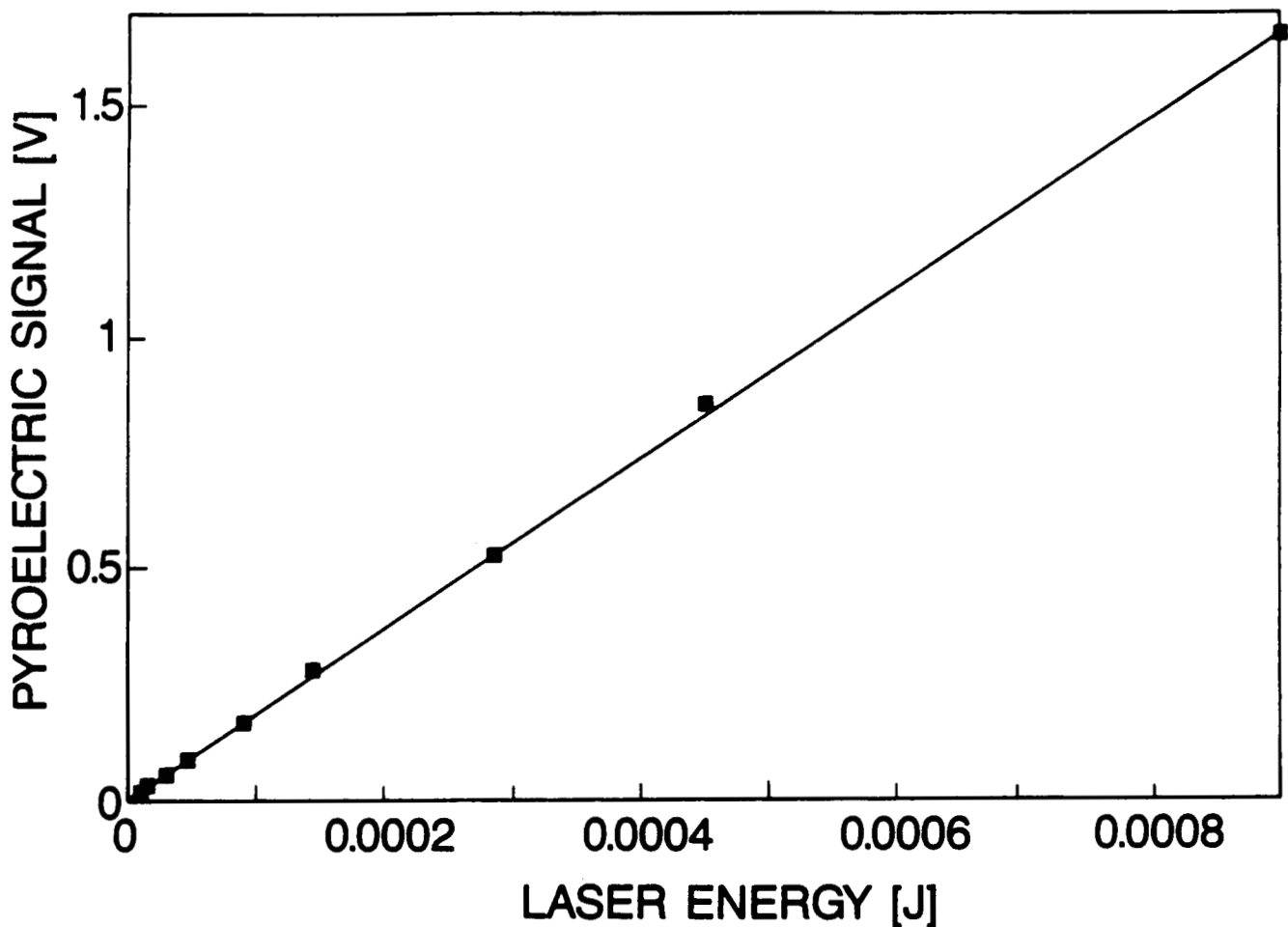


Figure 3.14 Response of pyroelectric calorimeter.

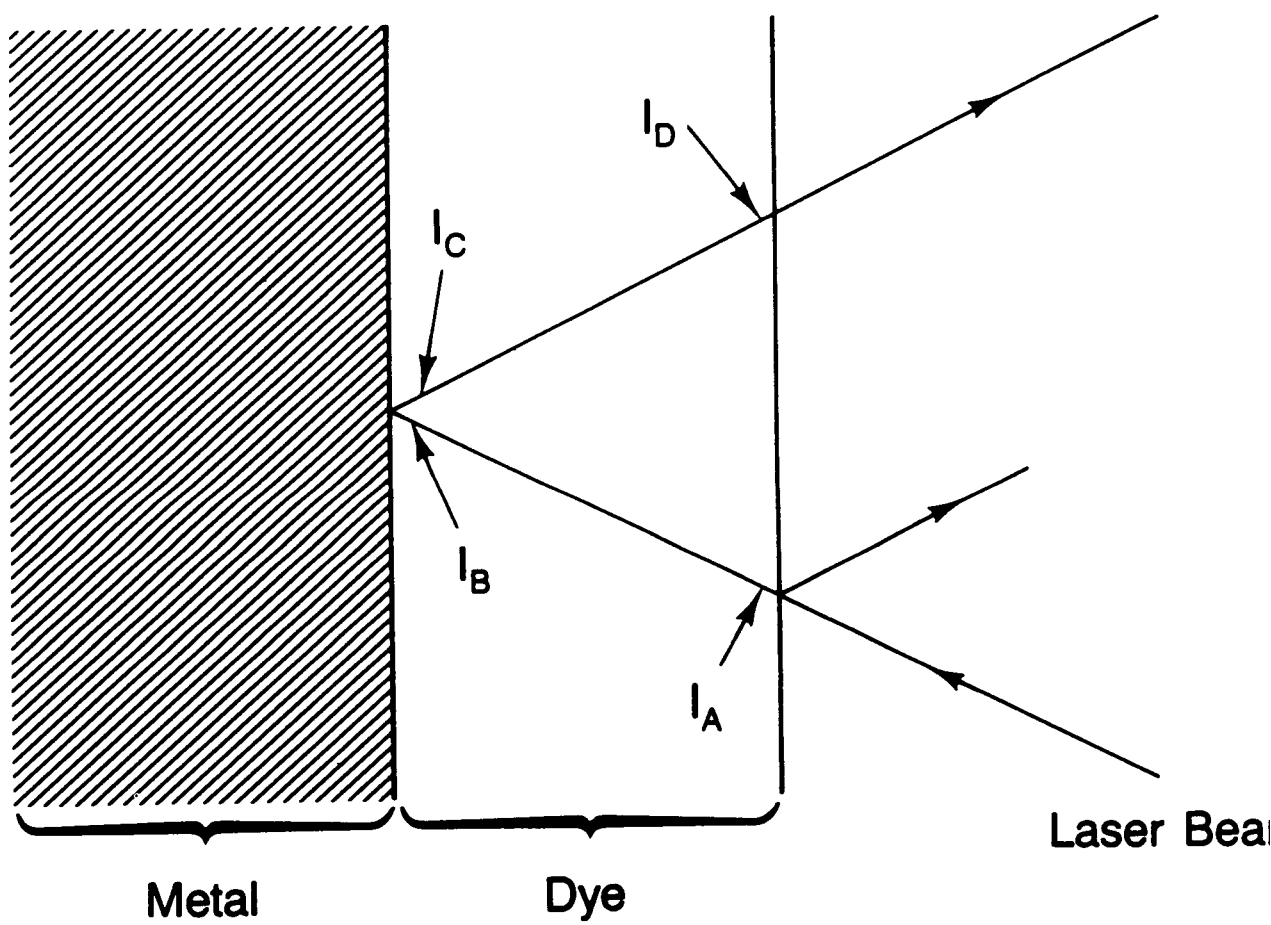


Figure 3.15 Absorption and reflection of the air/dye/metal layer.

the baseline level. Figure 3.7 shows the fraction of light energy absorbed as a function of tetracene film thickness with the excitation wavelength set at 478 nm.

### **3.5 References**

1. R. E. Kellogg and R. G. Bennett, "Radiationless Intermolecular Energy Transfer. III. Determination of Phosphorescence Efficiencies," *J. Chem. Phys.* 41, 3042 (1964).
2. A. C. Boccara, D. Fournier, W. Jackson and N. M. Amer, "Sensitive Photothermal Deflection Technique for Measuring Absorption in Optically Thin Media," *Opt. Lett.* 5, 377 (1980).
3. P. Avakian and R. E. Merrifield, "Experimental Determination of the Diffusion Length of Triplet Excitons in Anthracene Crystals," *Phys. Rev. Lett.* 13, 541 (1964).
4. R. G. Kepler and A. C. Switendick, "Diffusion of Triplet Excitons in Anthracene," *Phys. Rev. Lett.* 15, 56 (1965).
5. J. B. Birks, "Photophysics of Aromatic Molecules," Wiley-Interscience, 1970.
6. G. Vaubel and H. Baessler, "Diffusion of Singlet Excitons in Tetracene Crystals," *Mol. Cryst. Liq. Cryst.* 12, 47 (1970).
7. G. Vaubel and H. Kallmann, "Diffusion Length and Lifetime of Triplet Excitons and Crystal Absorption Coefficient in Tetracene Determined from Photo-current Measurements," *Phys. Stat. Sol.* 35, 789 (1969)
8. M. Pope, N. E. Geacintov and F. Vogel, "Singlet Exciton Fission and Triplet-Triplet Exciton Fusion in Crystalline Tetracene," *Mol. Cryst.* 6, 83 (1969).
9. R. R. Alfano, S. L. Shapiro and M. Pope, "Fission Rate of Singlet Excitons in a Tetracene Crystal Measured with Picosecond Laser Pulses," *Opt. Comm.* 9, 388 (1973).
10. B. Bouchriha, V. Ern, J. L. Fve, C. Guthmann, and M. Schott, "Magnetic Field Dependence of Singlet Exciton Fission and Fluorescence in Crystalline Tetracene at 300 K," *J. Phy.* 39, 257 (1978)
11. S. P. McGlynn, M. R. Padhye, and M. Kasha, "Lowest Triplet Levels of the Polyacenes," *J. Chem. Phys.* 23, 593 (1955).
12. A. N. Faidysh and V. L. Zima, "Influence of Impurity Concentration on the Quantum Efficiency of Luminescence as a Function of Anthracene Crystal Thickness," *Opt. Spectrosc.* 6, 568 (1959).
13. J. B. Birks, "The Fluorescence and Scintillation Decay Times of Crystalline Anthracene," *Proc. Phys. Soc.* 79, 494 (1962).
14. G. Vaubel and H. Baessler, "Diffusion of Singlet Excitons in Tetracene Crystals," *Mol. Cryst. Liq. Cryst.* 12, 47 (1970).

15. W. G. Herksroeter, A. A. Lamola and G. S. Hammond, "Mechanisms of Photochemical Reactions in Solution. XXVIII. Values of Triplet Excitation Energies of Selected Sensitizers," *J. Am. Chem. Soc.* 86, 4537 (1964).
16. Y. Maruyama and N. Iwasaki, "Absorption Spectra of Amorphous Organic Films," *Chem. Phys. Lett.* 24, 26 (1974).
17. W. Hofberger, "Structure and Optical Properties of Polycrystalline Evaporated Tetracene Films," *Phys. State. Sol.* 30, 271 (1975).
18. H. C. Wolf and H. Port, "Excitons in Aromatic Crystals: Trap States, Energy Transfer and Sensitized Emission," *J. Lumin.* 12, 33 (1976).
19. J. W. Weigl, "Spectroscopic Properties of Organic Photoconductors. I. Absorption Spectra of Cationic Dye Films," *J. Chem. Phys.* 24, 364 (1956).

#### **4.1 Introduction**

An understanding of the triplet decay kinetics of  $O_2^{1\Delta}$  is crucial to the evaluation of the singlet  $O_2$  generator. It has been shown in an earlier section that delayed fluorescence (DF) can be used to extract kinetics information of triplets. As already mentioned, DF is only observed for a few aromatic solid dyes, anthracene and tetracene, and cannot be used in the general case. The decay of triplet excitons is, however, predominantly nonradiative, and heat is the main product. It is therefore conceivable that triplet kinetics can be studied by measuring thermal signals. The method imposes a few requirements: (a) the measured signal must contain information about the amount of heat generated in the dye thin film and (b) the time evolution of the heat generation function can be extracted from the time dependence of the thermal signal. The second requirement implies that the detection must have a response time comparable to the anticipated triplet decay times, and a bandwidth as high as 20 MHz is contemplated.

There are several thermal detection schemes worth considering. A variety of spectroscopic techniques has been studied: thermal lensing,<sup>1</sup> photoacoustic detection,<sup>2</sup> photothermal deflection<sup>3-5</sup> and thin film pyroelectric detection.<sup>6-7</sup> A brief discussion and comparison of the mentioned techniques (except for pyroelectric detection) are given by Jackson et al.<sup>8</sup> Guided by that discussion, the technique of collinear Photothermal Deflection has been selected for the study of triplets. In an effort parallel to the mentioned study, a scheme of thin film pyroelectric detection has also been investigated. The theory of each technique will be briefly discussed and the results of the investigation will follow.

#### **4.2 Theory of Photothermal Deflection**

##### **4.2.1 Deflection vs. triplet decay**

The Photothermal Deflection (PD) technique requires two light beams: a pump beam which is absorbed in the sample and a probe beam which is deflected by the material perturbation of the former. Absorption of the pump beam changes the index of refraction of the region of the sample which is illuminated. Because the absorption causes a gradient of refractive index, a probe beam propagating through the heated region will be deflected by a corresponding angle. This is in contrast with thermal lensing wherein the propagation of the probe beam is changed by the refractive index curvature or interferometric methods where the thermally induced changes of  $n$  are directly measured. There are at least two methods of configuring the two pump and probe (laser) beams. One would configure the probe beam perpendicular to the pump beam (Transverse PD) or the two beams approximately collinear (Collinear PD). The collinear geometry is chosen for reasons which will be clear in the following discussion.

The transverse PD is not useful in our study for two main shortcomings: restricted spatial resolution and limited time resolution. In the transverse configuration the probe beam is perpendicular to the pump

beam and the probed region is in the thin layers adjacent to the heated surface. This mode of operation is not suitable for measuring intensity-dependent kinetics which are expected in this study. Because of the bimolecular decay kinetics in solid dyes, the triplet decay time presumably depends on the absorbed energy density and therefore on pump intensities. As far as spatial resolution is concerned, the transverse probe beam probes regions of different decay kinetics as long as the pump beam intensity profile is not uniform in the lateral direction. Another consequence of this geometry is that thermal deflection is delayed with respect to the actual heating of the sample by the time it takes heat to diffuse from the illuminated region to the region probed by the probe beam. The required time resolution, as discussed next, is readily attained using the Collinear PD configuration.

Figure 4.1 shows the collinear geometry of PD. The most straightforward way to measure the time-resolved thermal signal is to excite the sample film with a pulsed laser and record the time evolution of the thermal signal subsequent to the excitation (as long as the pulse duration is shorter than most relevant decay times and system response times.) The deflection of the probe beam depends on two separate factors. The first is the redistribution of absorbed energy in the sample/substrate medium, and the second is the propagation of a Gaussian beam in the inhomogeneous medium. The propagation of a Gaussian beam in an inhomogeneous medium has been treated by Casperson et al.<sup>9</sup> and is summarized here as follows

$$d\Phi = \frac{1}{n_0} \frac{dn(r,t)}{dr} ds \quad (4.1)$$

where

$d\Phi$	=	angular deflection of probe beam
$ds$	=	infinitesimal distance along the propagation axis
$dn/dr$	=	gradient of refractive index (in the radial direction)
$n_0$	=	refractive index of medium

The thermally induced inhomogeneity is assumed to be cylindrically symmetric about the pump beam axis (the gradient of refractive index is a function of the radial distance from the pump beam axis.) As shown in Eq. (4.1), the deflection,  $d\Phi$ , corresponds to the gradient of refractive index in the infinitesimal path length,  $ds$ . The expression is valid for probe beams which have a diameter much smaller than the gradient characteristic length of the inhomogeneity. When the lateral deflection of the probe is small compared to the dimension of the temperature distribution, the integration of  $d\Phi$  along the optical path can be expressed in a simple form. The above condition requires that the radial distance of the probe beam is practically unchanged over the region where measurable inhomogeneities are observed (which is always true in our system where  $\Phi$  is less than  $10^{-5}$  rad). With that approximation, the integrated deflection can be expressed as

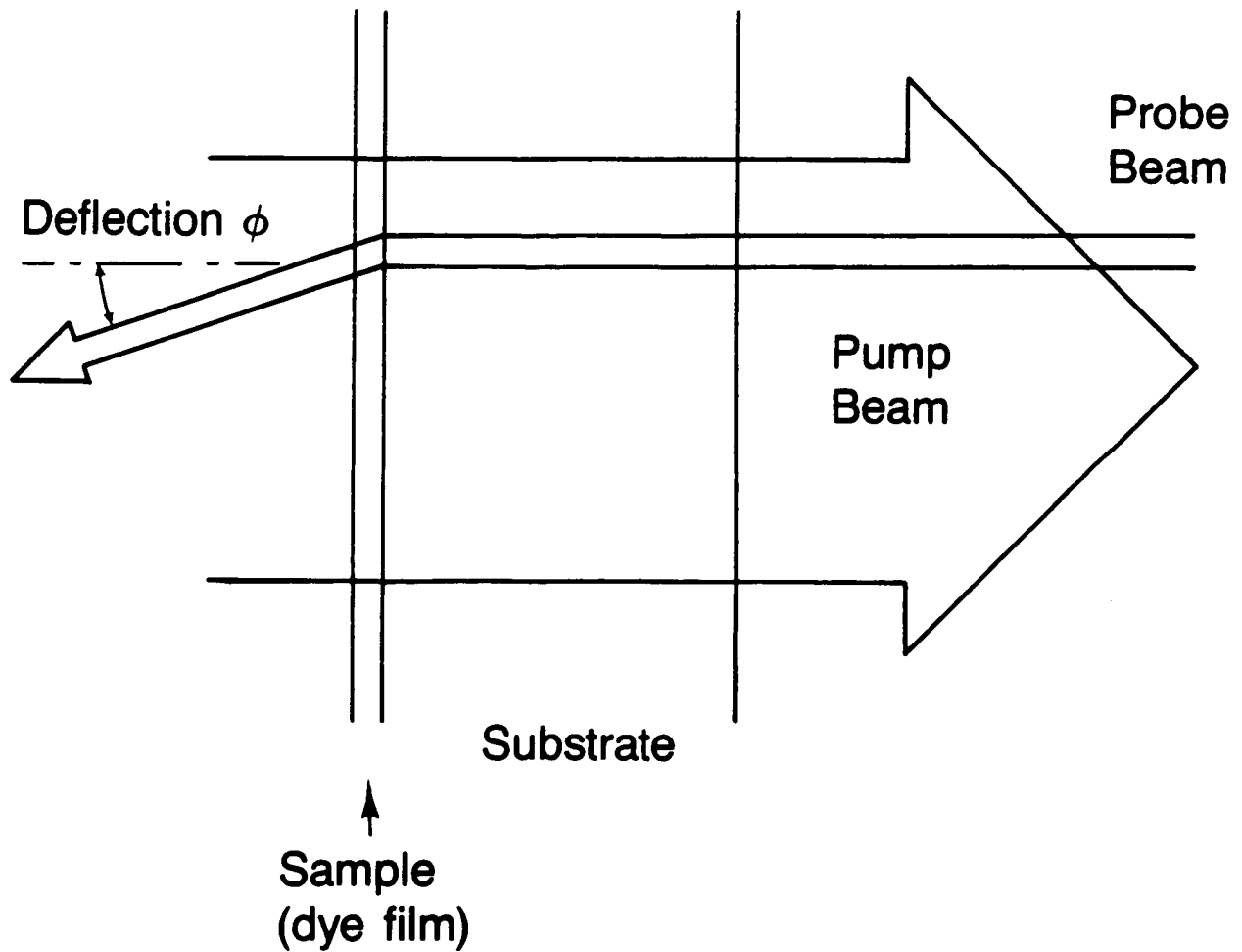


Figure 4.1 Collinear photothermal deflection.

$$\Phi = \frac{1}{n_0} \int_0^\infty ds \frac{dn(r,t)}{dr} \quad (4.2)$$

The change in refractive index can be caused by (1) the temperature dependence of  $n$  and (2) a change of  $n$  which is associated with the excited-state dye molecules. The second effect is localized to the dye film, and its time dependence is quite different from the first effect (if present it would easily be discriminated from the other signal.) For the rest of this study, only effect (1) is considered and one can write

$$\Phi = \frac{1}{n_0} \left( \frac{dn}{dT} \right) \frac{d}{dr} \left[ \int_0^\infty ds \frac{T(s,r,t)}{dr} \right] \quad (4.3)$$

The change in refractive index, as shown later, is not localized in the dye film, and the integral acquires contributions from the path length in the substrate itself (transparent glass or plastic). It should be noted that the sample film is in most cases ca. 1000 Å, and the corresponding thermal diffusion time is less than 10 ns. In the interval of time during which the probe deflection is measured, heat has effectively diffused out of the dye film.

The deflection also depends on the thermal redistribution in the sample/substrate. The treatment for heat diffusion is very simple if one limits oneself to the following practical conditions:

$$\omega_{\text{pump}} > \Delta T_{\max} \left( \frac{dT}{dr} \right)^{-1} \gg \omega_{\text{probe}} \quad (4.4-a)$$

$$\tau \ll \frac{\omega_{\text{probe}}^2}{\alpha} \ll \frac{\omega_{\text{pump}}^2}{\alpha} \quad (4.4-b)$$

These conditions insure that only one heat generation function needs to be considered. Condition (4.4-a) insures that temperature does not substantially change over the diameter of the probe beam. Condition (4.4-b) makes sure that in the time interval over which the measurement is made the lateral diffusion distance is still small compared to the diameter of the probe beam. These conditions guarantee that the path along the probe axis and adjacent to the dye film is heated by an infinite surface which is itself heated by a single arbitrary heat input function,  $f$ . The treatment of this problem of heat diffusion is well documented<sup>10</sup> and the result is given here as

$$T(s, r, t) = \frac{\alpha^{\frac{1}{2}}}{k\pi^{\frac{1}{2}}} \int_0^t d\tau f_r(t-\tau) \tau^{-\frac{1}{2}} e^{s^2/4\alpha\tau} \quad (4.5)$$

where

$\alpha$  = thermal diffusivity

$k$  = thermal conductivity

$f_r$  = heat input function at radial distance  $r$

The combination of (4.5) and (4.3) gives:

$$\Phi = \frac{1}{n_0} \left( \frac{dn}{dT} \right) \frac{\alpha}{k} \frac{d}{dr} \left[ \int_0^t d\tau f_r(t-\tau) \right] \quad (4.6)$$

where the integral at a given  $t$  represents the amount of heat generated in the dye film at point  $r$  and accumulated up to time  $t$ . To have a maximum angular deflection, the substrate must have a high  $dn/dT$  and a low thermal conductivity,  $k$ . Note that the dye film itself is thermally thin and does not contribute appreciably to the integrals shown in Eq. (4.2)-(4.6). This point will be demonstrated later in the next section. What has been learned here is that the generated heat can be expressed as a function of angular deflection  $\Phi$ . The deflection angle is related to triplet decay as follows. Because it is assumed that heat is the main product of triplet exciton decay, the triplet number density must be related to the deflection  $\Phi(t)$  as shown:

$$n(t) = \frac{E_{abs}}{hv} - \frac{\omega_{pump}}{2hv} \left[ \frac{1}{n_0} \left( \frac{dn}{dT} \right) \frac{\alpha}{k} \right]^{-1} |\Phi(t)| \quad (4.7)$$

When multiplied to  $hv$ , Eq. (4.7) states the conservation of energy: the left hand side is the electronic energy carried by triplet excitons, the first term of the right-hand side is the total input of energy and the last term is the thermal energy (see Eq. (4.6).) As a consequence of Eq. (4.7), it is expected that the thermal signal as described above would build up from baseline to a maximum deflection,  $\Phi_{max}$ . For times longer than those specified in (4.4-b), the heated dye film does not look like an infinite surface anymore, and heat loss in the lateral direction will decrease the measured deflection. In the time interval of interest (as determined by laser duration, detector response, triplet decay times and lateral heat loss) the time-resolved deflection can be analyzed to yield kinetics information. The analysis requires the spatial distribution of absorbed energy in the dye film to be well characterized and the actual absorbed energy density ( $J \text{ cm}^{-3}$ ), at the point where the dye film is probed, to be measured. The latter quantity is used to estimate the initial triplet number density at the probed region.

#### 4.2.2 $\Phi_{\max}$ and triplet decay

It will be shown how detection sensitivity depends on the pump beam dimensions. It follows from Eq. (4.1) that the maximum deflection is proportional to the temperature gradient and consequently

$$\Phi_{\max} \propto \frac{\Delta T}{w_{\text{pump}}} \quad (4.8)$$

where  $w_{\text{pump}}$  is the pump beam radius and  $\Delta T$  is the temperature change induced by the pump laser. If heat loss is neglected, the temperature is inversely proportional to the illuminated dye volume. With a fixed absorbed energy and a constant dye thickness, the temperature increase will have to change in inverse proportion with the area of the dye film illuminated by pump beam. In general,

$$\Phi_{\max} \propto (w_{\text{pump}})^{-3} \quad (4.9)$$

shows the dependence of the thermal deflection on pump beam radius. By focussing the pump beam to a tight spot, Jackson et al.<sup>8</sup> estimated a  $1 \times 10^{10}$  J energy sensitivity for a pulsed collinear PD detector. This mode of operation (tight focus), as discussed later, is not compatible with our application for the following reason. For a given dye film thickness, the triplet number density scales with the absorbed energy density and remains inversely proportional to  $w_{\text{pump}}^2$ . In solid dyes one expects bimolecular decay to be dominant (see Chapter 3) and the observed decay rate to be

$$k \approx \gamma n_T = \frac{\gamma E_{\text{abs}}}{h\nu (\pi w_{\text{pump}}^2)} \quad (4.10)$$

where	$\gamma$	=	annihilation rate ( $1 \times 10^{-11} \text{ cm}^3 \text{ s}^{-1}$ )
	$E_{\text{abs}}$	=	absorbed energy ( $1 \times 10^{-4} \text{ J}$ )
	$h\nu$	=	photon energy ( $3 \times 10^{-19} \text{ J}$ )
	$w_{\text{pump}}$	=	dye thickness ( $1 \times 10^{-5} \text{ cm}$ )
		=	pump beam radius (0.5 cm)

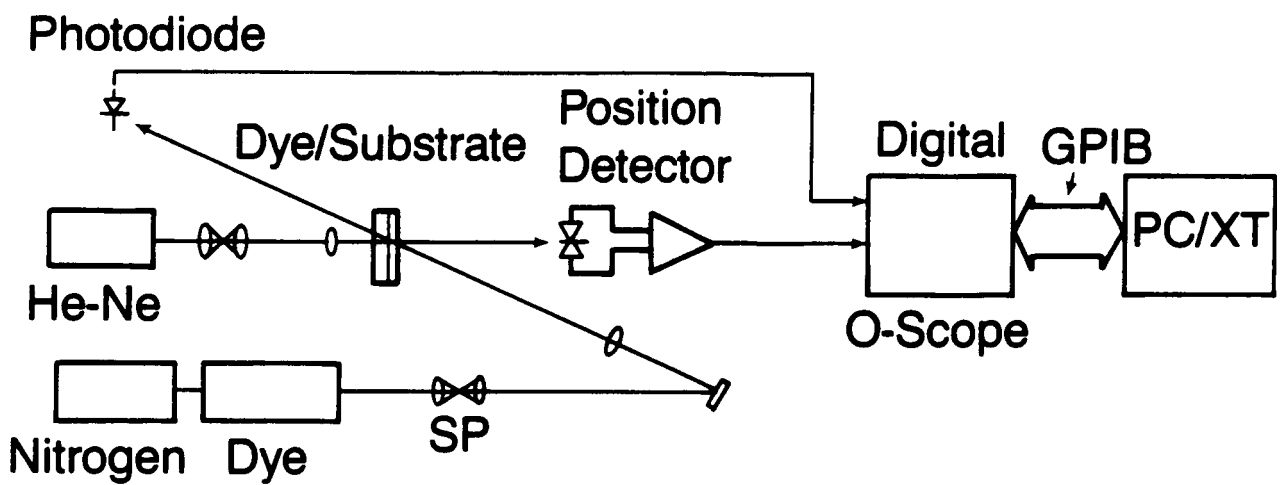
The following example shows how detector sensitivity parallels bandwidth requirement. As an example, typical values are used (shown in parentheses above). For this example the estimated rate (pseudo first order kinetics) is  $4 \times 10^8 \text{ s}^{-1}$ . To capture the time dependence of the thermal signal, the measurement would require a 200 MHz deflection detector. For position detectors which are now available, the operating bandwidth is typically one order of magnitude less than the requirement imposed by the above example. The complete evaluation of the technique will not be

possible without the knowledge of the signal-to-noise ratio at operating conditions and the detector bandwidth.

#### **4.3 Experimental Considerations in Photothermal Deflection Technique**

The experimental configuration is given in Figure 4.2. A pulsed laser (Molelectron UV-12 nitrogen and DL-II dye laser) is used as a pump beam. The pump beam is filtered with a spatial filter to remove high spatial frequency components. A He-Ne, (CW Radiation) probe beam is passed through a spatial filter/beam expander to obtain a clean Gaussian beam with diameter,  $2 \omega_{\text{HeNe}} = 2.4 \text{ mm}$ . The probe is refocused with a 200 mm f/l lens to a waist with diameter,  $2 \omega_0$  (see Figures 4.3 and 4.4). The diverging probe illuminates the "null" line of the segmented position detector. The segmented detector (Silicon Detector Corp. Bi-cell SD113-24-21-021) is chosen over lateral types for its wide bandwidth and will be discussed in more detail in a later section. The deflection signal is fed to a custom-designed preamplifier (discussed later) and then to a digital oscilloscope (Lecroy 9400.) Signal averaging is performed with a built-in function of the oscilloscope. The averaged waveform is then sent to a dedicated PC-XT for further analyses.

The alignment of the pump and probe beams deserves a detailed digression. A rectangular aperture is imaged onto the sample (dye) plane with a 500 mm focal length lens. It is required to know both the intensity profile of the pump beam and its intensity at the point where it overlaps the probe beam and intersects the sample plane. The irradiance profile is determined by a simple procedure which requires scanning an apertured photodiode across its cross section.<sup>12</sup> A second method of determining the beam profile involves measuring the deflection signal of a known sample as the pump beam is moved with respect to the probe. Since the deflection signal varies as the gradient of the temperature (laser intensity) profile, the deflection signal, when integrated over distance, will be proportional to the irradiance profile measured at the sample plane (see Figure 4.5). In Figure 4.5, the horizontal profile is displayed. Note that when the probe is positioned at the horizontal peak irradiance, the deflection is zero and remains close to zero as the probe vertical position varies over 80% of the height of the illuminated spot. This observation indicates that the irradiance is not a sensitive function of height, and the vertical profile can be approximated by a top hat distribution. As long as the horizontal irradiance profile and the position of the probe beam relative to the illuminated spot are known, the laser intensity in the probed region can be derived from the total energy reading. The latter value is given by a pyroelectric meter (Laser Precision RK3230). The accuracy of the method is discussed next. The motorized translational micropositioner used to position the pump beam relative to the probe is accurate to 2.5  $\mu\text{m}$ . In most operating situations both pump and probe beams are left intact even when the sample is changed. Routine checks show that the position repeatability is better than 5  $\mu\text{m}$ . With a typical pump beam width of 100  $\mu\text{m}$ , the relative laser intensity error which is introduced by alignment error is estimated to be less than 10 percent. The collinear PD configuration demands that the pump and probe beams are collinear (see Theory). The two beams are instead crossed at an angle of 10 degrees for convenience. Because the effective thickness of the



## Experimental setup and data flow

Figure 4.2 Experimental set-up.

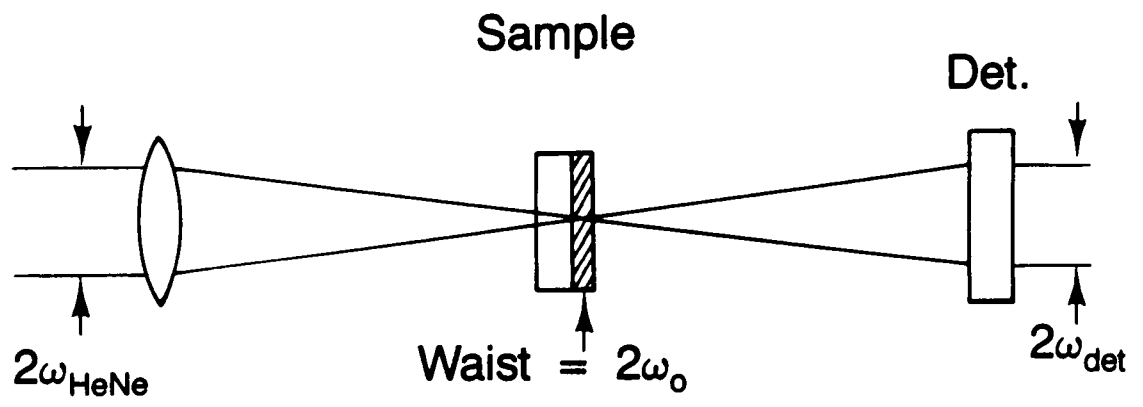


Figure 4.3 Probe beam. The HeNe probe is focused on the dye film with a 200 mm f.l. lens.

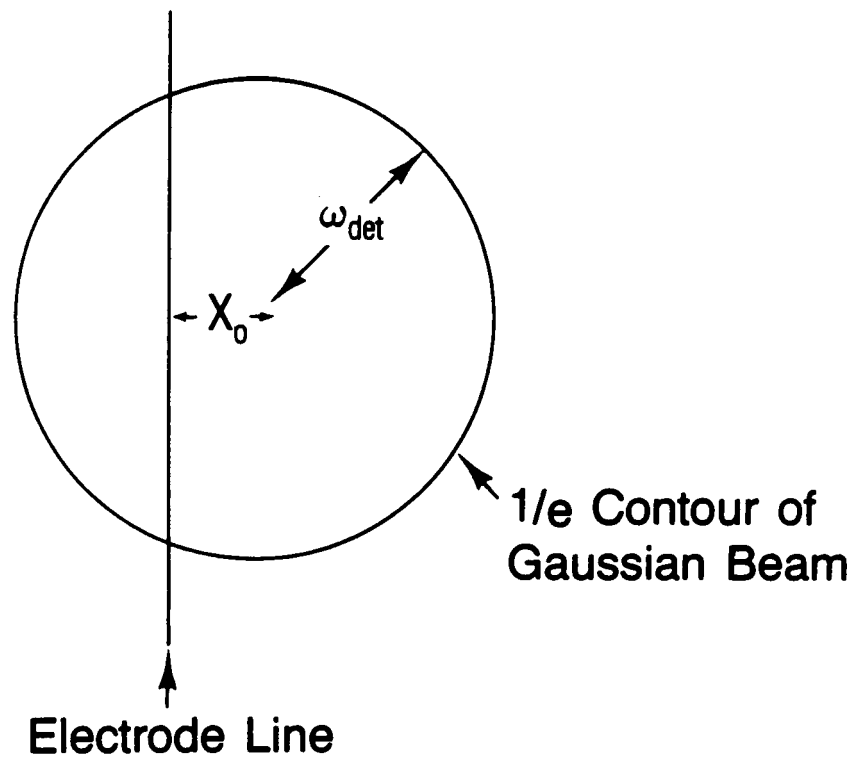


Figure 4.4 Illumination of position detector.

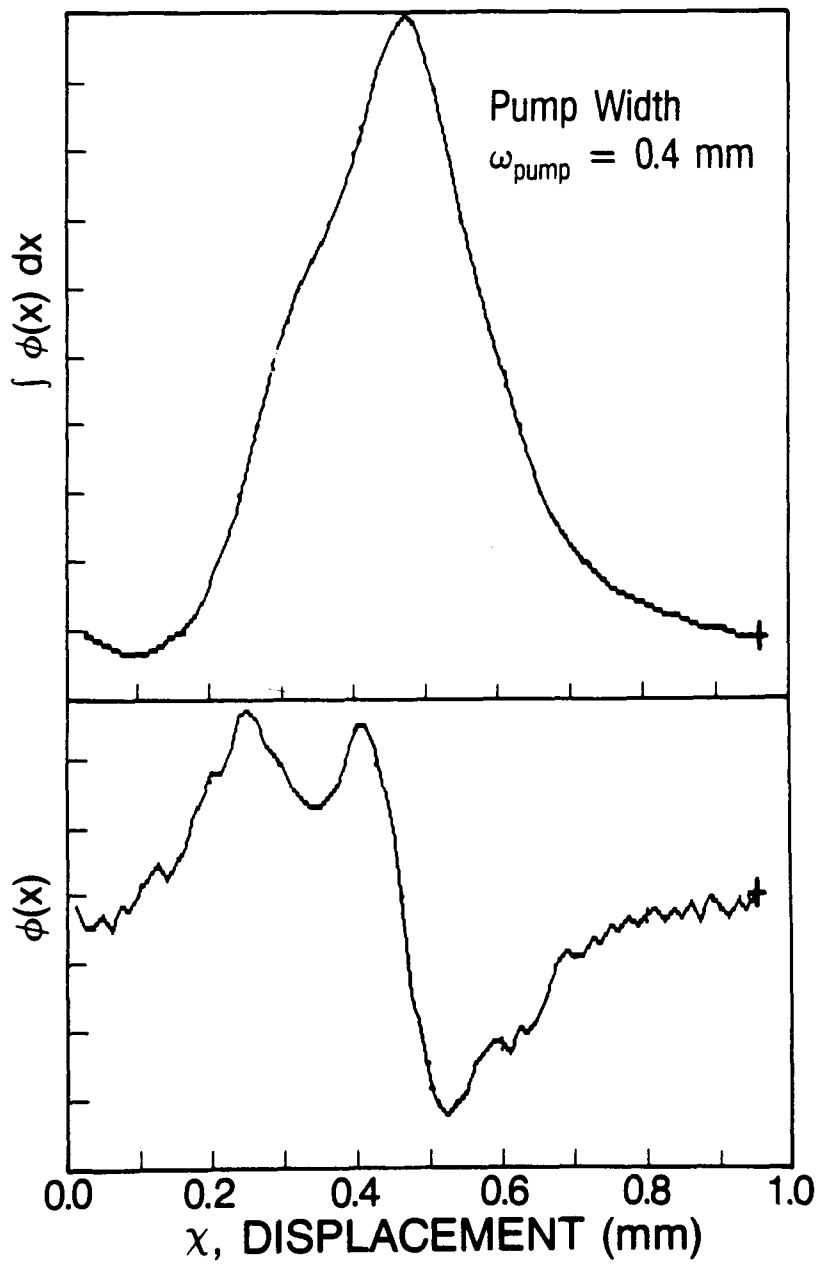


Figure 4.5 Deflection signal as a function of the pump probe overlap. The lower trace is the PD signal measured as the position of the probe is varied relative to the pumped spot. The upper trace is the PD signal integrated over the pump probe displacement.

heated layer is in most cases less than 5  $\mu\text{m}$ , the actual displacement of the probe beam ( $< 0.8 \mu\text{m}$ ) is negligible with regard to the pump cross section.

Sample alignment is straightforward. The sample consists of a thin layer of solid dye which is uniformly deposited on a transparent plate (thickness  $< 1 \mu\text{m}$ ). The plate is a 0.25 x 1 x 1 in. piece of glass or preferentially lucite (high  $d\text{n}/dT$  and low thermal conductivity; see Eq. (4.6)). The sample plate is perpendicular to the probe beam and the plane of dye film intersects the probe beam at the focal point. The sample plate is mounted on an x-y-z translator such that the position of the surface with dye is fixed with respect to the translator and therefore reproducible from sample to sample for reasons which will become apparent. Positioning the dye film plane along the probe axis so that it intersects the focal point is done by using a diffuse surface (on one side of a ground glass plate) instead of the dye film and observing its speckle patterns.<sup>13</sup> Once the proper position is found, the diffuser plate is removed and replaced by the sample plate. The plane of the dye layer will be at the very same position the diffuse surface had been.

#### 4.3.1 Deflection measurements

The detector is a segmented position detector. The detector operates as two photodiodes sharing a common electrode which is itself a thin linear boundary separating the two halves of the active region. The differential output current (difference of anode currents) is proportional to the difference in light flux falling on the two segments of the active region. With proper alignment, the output current can be made proportional to the angular deflection of the probe beam. The conditions of linearity are derived as shown next. A Gaussian beam is incident on the active region of the detector such that (a) its center is  $x_0$  from the null line (common electrode line) and (b) the 1/e radius of its intensity profile is  $\omega_{\text{det}}$ . The output current is proportional, as mentioned above, to

$$I_{\text{out}} \propto \int_0^{\infty} dx \int_{-\infty}^{\infty} dy \exp \left[ -2 \frac{(x-x_0)^2 + y^2}{\omega_{\text{det}}^2} \right] - \int_{-\infty}^0 dx \int_{-\infty}^0 dy \exp \left[ -2 \frac{(x-x_0)^2 + y^2}{\omega_{\text{det}}^2} \right] \quad (4.11)$$

and

$$I_{\text{out}} \propto 1 - \text{erf} \left( \frac{x_0 \sqrt{2}}{\omega_{\text{det}}} \right) \quad (4.12)$$

where  $\omega_{\text{det}}$  is just the probe beam spot at the detector plane. The current sensitivity is the derivative of  $I_{\text{out}}$  with respect to  $x_0$ :

$$\frac{dI_{\text{out}}}{dx_0} \propto e^{-\frac{-2x_0^2}{\omega_{\text{det}}^2}} = -\frac{\sqrt{2}}{\omega_{\text{det}}} + \frac{2\sqrt{2}}{\omega_{\text{det}}^3} x_0^2 + \dots \quad (4.13)$$

It follows from Eq. (4.13) that linear response (with respect to displacement) is attained whenever

$$x_0 \ll \frac{\omega_{\text{det}}}{\sqrt{2}} \quad (4.14)$$

Figure 4.6 shows the output current  $I_{\text{out}}$  as a function of displacement. The signal is measured as the detector is slowly moved with respect to the probe beam. Effectively the Gaussian probe beam (dia = .34 mm) is scanned across the null line. It turns out that the linearity is observed over a distance range comparable to the probe beam dimension. In other words, Eq. (4.14) is too conservative. In general the output current is composed of a drifting DC level, which is due to the offset between the probe and the null line, and a transient signal, which is caused by thermal deflection. The measured deflection current is typically much smaller than the displacement dynamic range (shown in Figure 4.6) and the ideal operating condition calls for a perfect null. Nulling the probe serves two purposes: (a) it ensures that the detector is operating in the linear regime and (b) it reduces shot noise associated with the DC level. The pointing characteristics of He-Ne are such that over a long period (a few minutes) the probe would drift off the null position by 10-20 percent of the dynamic range. It has been satisfactorily demonstrated that the detector can operate under conditions such that the measured output current is proportional to the probe displacement (and therefore proportional to angular deflection).

The focal point is shown in Figures 4.1 and 4.3 to be at the sample plane. The distance from the focal point to the detector plane is  $d$ , and the deflection angle is  $\Phi$ . The displacement measured at the detector is therefore

$$\Delta x = \Phi d \quad (4.15)$$

It seems at first that the signal would depend on  $d$  and that one can indeed gain sensitivity by placing the detector far away from the focal point. It turns out that the signal change above DC level is independent of  $d$ . That has been pointed out by Jackson et al.<sup>8</sup> and can be seen in this treatment by inspecting Eq. (4.13). Note that  $\omega_{\text{det}}$  is proportional to the distance,  $d$ , and the response goes as  $1/d$ . The diminished response, which is stated above, and the gain acquired by increasing  $d$  (Eq. (4.15)) will cancel each other. Using the responsivity given by SDC (0.55 A/W) and Eq. (29) in Ref. 8 one can express the voltage change as

$$\frac{\Delta V}{V} = \frac{4}{\sqrt{2\pi}} \frac{\Delta x}{\omega_{\text{det}}} \quad (4.16)$$

DEFLECTION SIGNAL

$$\omega_{\text{det}} = 1.2 \text{ mm}$$
$$1 \text{ mm}$$



$\chi$ , DISPLACEMENT

Figure 4.6 Bi-cell output vs. displacement of probe.

and the current change as

$$\Delta I_{\text{out}} [\text{A}] = 0.88 P_{\text{HeNe}} [\text{W}] \frac{\Delta x}{\omega_{\text{det}}} \quad (4.17)$$

where  $P_{\text{HeNe}}$  = power of Gaussian probe beam [W]. To determine the effective sensitivity of the detector in this application, it is now necessary to analyze the noise performance of the detector.

#### 4.3.2 Noise analysis

The total current noise is composed of the Johnson noise associated with the load resistor, the current and voltage noises of the preamplifier and the noise which is associated with the differential signal current. In conventional detection schemes, the last term includes fluctuations of the probe beam laser. The fluctuation can be statistical or non-statistical. It is, however, not a straightforward task to identify the source of the shot noise term in a segmented detector. It is argued in this report that the statistical noise associated with the differential signal does not depend on the total photocurrent generated by the probe beam but only on the difference of currents from the two segments of the diode. Before the defense of the argument can be undertaken, it is necessary to expand some more on the operation of the segmented position detector. The configuration of the segmented detector is shown in Figure 4.4. In principle, if a single wavefront is incident on the total active area of the segmented detector and the two photodiodes behave like identical perfect square-law detectors then the current measured at the anodes (the differential signal is measured with an ammeter connected to the anodes of the detector as in Figure 4.2; not the difference of anode currents) will be the difference of photo-currents. Furthermore, its noise is characteristic of the differential signal  $\Delta I$  not of the differences of two independent anode signals. On the other hand, if the wavefront incident on one half of the bi-cell is totally incoherent with the one on the other half, then the output current is again the difference of two photocurrents but its noise is caused by  $I_{\text{TOT}}$ . It is viable to operate the detector in the "coherent" mode because one can then "null" the output current and avoid laser power noise. In other words, the ideal segmented detector is not exposed to laser intensity noise: whether it is shot noise by origin or just non-statistical fluctuations in laser intensity.

In reality, the segmented detector probably can operate in a regime close to the "coherent" situation if the probe beam is (a) clean of components of high spatial frequency (use of spatial filter is required) and (b) free of pointing noise. The low-pass spatial filter is used in our experiment to improve the spatial coherence of the probe and satisfy the condition that a single wavefront is incident at the detector plane. For an operation which is almost "coherent," the differential signal can reject laser intensity fluctuation to 1 part in 1000 according to Jackson et al.<sup>8</sup> In the coherent mode, the noise of the differential output is due to the non-perfect nulling: good nulling ( $\Delta I_{\text{DC}} < .005 I_{\text{HeNe}}$ ) is difficult to maintain because the probe direction is slowly drifting

out of null level. A servo/feedback control operating at 100 Hz can conceivably maintain a null to better than 1 part in 1000 over long periods of time. In our experiment, the null position is adjusted just before measurements, and the maximum drift observed is still less than 1 part per 100. Even at that level, the detector is able to reject laser intensity noise to 1 percent, and the observed noise is already dominated by pointing noise.<sup>8</sup> The effect of pointing noise is to cause the partitioning of the wavefront on the active area to fluctuate with time. Pointing noise is typically  $5 \times 10^{-9}$  rad s<sup>1/2</sup> for most HeNe probes at frequencies close to DC.<sup>8</sup> Pointing noise is in general "pink" and with a 1 kHz RC high pass filter a large reduction in pointing fluctuation is expected. For most measurements, triplet decay information is at higher frequencies, and the filter does not throw away information. Our observed noise current is  $2.0 \times 10^{-11}$  A for a 1 MHz detection bandwidth and beam parameters as shown in Table 1. Table 1 summarizes the characteristic noise performance of the detector. Knowing that the deflection sensitivity is 0.00352 A/rad (this sensitivity is measured and reported later), one can derive a total pointing noise current of  $9.5 \times 10^{-9}$  rad (1 MHz) which is a dramatic improvement from the quoted noise level. Note that (a) the use of a spatial filter and a high pass RC filter markedly reduces noise current and (b) pointing noise is dominating over shot noise. From now on, only pointing noise is considered in our evaluation.

**Table 1. Noise in PD Detection ( $\Delta f = 1$  MHz)**

Pointing noise <sup>a</sup> ( $\Delta f = 1$ MHz), rad	$5 \times 10^{-6}$ rad
Observed noise <sup>b</sup> , A (mainly pointing noise)	$2.0 \times 10^{-11}$ A
Observed noise, rad <sup>c</sup>	$9.5 \times 10^{-9}$ rad
Estimated shot noise (null offset of 1% is assumed), A	$7 \times 10^{-12}$ A

<sup>a</sup> Reported pointing noise [Ref. 6]

<sup>b</sup> Measurement made with a 200 mm lens,  $2 \omega_{\text{HeNe}} = 2.4$  mm and  $P_{\text{HeNe}} = 0.04$  mW. Spatial filter for HeNe and 1 KHz high pass filter are used.

<sup>c</sup> Deflection sensitivity (see discussion on sensitivity) of 0.00352 A/rad is used.

### 4.3.3 Sensitivity: signal vs. displacement

Because the detector is not calibrated, it is important to establish that its response is linear (see Figure 4.6 and earlier discussion) and to determine its sensitivity. The overall sensitivity is composed of the angular and displacement sensitivities. The former is mainly determined by the sample and the pump beam as seen in Eq. (4.8). The latter is the electrical response of the position detector to a displacement of the probe beam. In general the displacement sensitivity is a function of the probe beam and the detector. For a Gaussian probe beam, Eq. (4.17) should hold. Since the actual sensitivity can deviate from (4.17) for a few reasons (responsitivity, beam profile, etc.) there is still a need to experimentally verify Eq. (4.17) with this apparatus. It is crucial to know the proportionality constant,  $a$ , in the expression:

$$\Delta I = a \Delta x \quad (4.18)$$

where  $\Delta I$  is the signal current induced by a displacement of the probe beam in the plane of the detector. Table 2 compares the measured and theoretical position sensitivities. Note that the theoretical sensitivity is calculated in Eq. (4.17) and the responsitivity is given by the manufacturer. The agreement is considered fairly good. The values in Table 2 are obtained for slow displacements of the probe beam (ca.  $1 \text{ mm s}^{-1}$ ). At high frequencies the overall sensitivity would be affected by the bandwidths of the detector and the amplifier. The overall bandwidth (3-dB) of the current detector is estimated to be 1 MHz for the reasons shown below. The latter is not limited by the detector which is reverse-biased at 10 VDC ( $\Delta f$  ca. 10 MHz, see Table 3). The differential preamplifier is built around an operational amplifier (NE5539) with a feedback resistor of  $4.1 \times 10^5 \Omega$ . Because the detector junction capacitance at 10 VDC is 15.6 pF (estimated from manufacturer's specifications), the overall bandwidth is estimated at ca. 1 MHz. The detector, which consists of Bi-cell SDC SD113-24-21-021 and the

**Table 2. Position Sensitivity of Detector #1**

	I(theoretical) <sup>a</sup>	I(measured)
$P_{\text{HeNe}} = 4 \times 10^{-5} \text{ W}$		
$\text{det} = 0.63 \text{ mm}$	$5.6 \times 10^{-8} \text{ A}/\mu\text{m}$	$3.2 \times 10^{-8} \text{ A}/\mu\text{m}$
$\omega_{\text{HeNe}} = 2.4 \text{ mm}$		
focal length = 200 mm		

<sup>a</sup> calculated with Eq. (4.17)

mentioned preamplifier, is referred to as detector #1 from now on. This set up is used mainly to characterize the noise performance of the system as well as to evaluate the technique. Its bandwidth and transconductance gain (ca.  $4 \times 10^5$  V/A) are too small in actual triplet decay measurements.

**Table 3. Specifications of Bi-Cell Detector at 23 C  
(Ref. Silicon Detector Corp. Brochure)**

PARAMETER	Bi Cell
	SD113-24-21-021
Typical Peak Responsivity (A/W)	.55
Maximum Nonuniformity of Response	$\pm 5\%$
Typical Position Sensitivity at Special Peak (A/cm)	.5P/R
Guaranteed Position Measurement Accuracy over Operating Range (cm)	$\pm .06R$ For Uniform Spot
Minimum Detectable Position Change (Angstroms)	$1.5 \sqrt{\Delta f/H}$
Typical Thermal Drift of Null Point ( $\mu\text{m}/^\circ\text{C}$ )	$R \times 10^{-5}$
Typical Parallel Output Capacitance-(pF)	
[ 0 Volts	50
[ 5 Volts	20
[ 50 Volts	7
Maximum Light Modulation Frequency - $\Delta f$	
[ 0 Volts	7 MHz
[ 5 Volts	16 MHz
[ 50 Volts	40 MHz
Maximum Total Light Power on Device @ Spectral Peak - P(mW)	.6
Maximum Light Power Density @ Spectral <Peak - H (mW/cm <sup>2</sup> )	25

#### **4.4 Photothermal Deflection: Testing and Evaluation**

There is one more test to be done before an evaluation can be initiated. It is required to prove that the deflection signal is (a) indeed caused by a thermally induced gradient of refractive index and (b) associated with triplet decay. (a) can be shown by testing the formalism that has been developed above. (b) can be resolved in measurements where the measured thermal signal is compared with a direct measurement of triplet decay.

##### **4.4.1 Test experiments**

The formalism (see section about Theory) predicts that the thermal signal will track the total amount of heat generated in the film (Eq. (4.6)). The maximum deflection signal is shown in Eq. (4.6) to be proportional to  $(dn/dT)$  and inversely proportional to the thermal conductivity of the substrate.<sup>14</sup> The material dependence is qualitatively shown in Figure 4.7 and Table 4. The three deflection signals are recorded for samples with 5000 Å of acridine orange dye film deposited on fused silica, pyrex and lucite (polymethylmethacrylate) substrates. The wavelength of the pump beam is at 580 nm, and the amount of heat absorbed is  $6 \times 10^{-6}$  J per pulse. The fused silica substrate, which has the smallest  $dn/dT$  (or linear expansion coefficient  $\alpha$ ), shows almost no deflection signal. The strongest signal is with lucite which has the highest coefficient of linear expansion (and  $dn/dT$ ) of the three materials.

**Table 4. Substrate parameters:<sup>a</sup> thermo-optical, thermal conductivity and linear expansion coefficients.**

	$dn/dT$ ( $K^{-1}$ )	$k$ ( $J cm^{-1}s^{-1} K^{-1}$ )	$\alpha (= \beta/3)$ ( $K^{-1}$ )
Fused Silica	$9.9 \times 10^{-6}$	0.014	$5.5 \times 10^{-7}$
Pyrex Glass		0.002	$3.2 \times 10^{-6}$
Lucite (PMMA)	$-1.1 \times 10^{-4}$	0.0019	$8.4 \times 10^{-5}$

<sup>a</sup> Melles Griot "Optics guide 2".

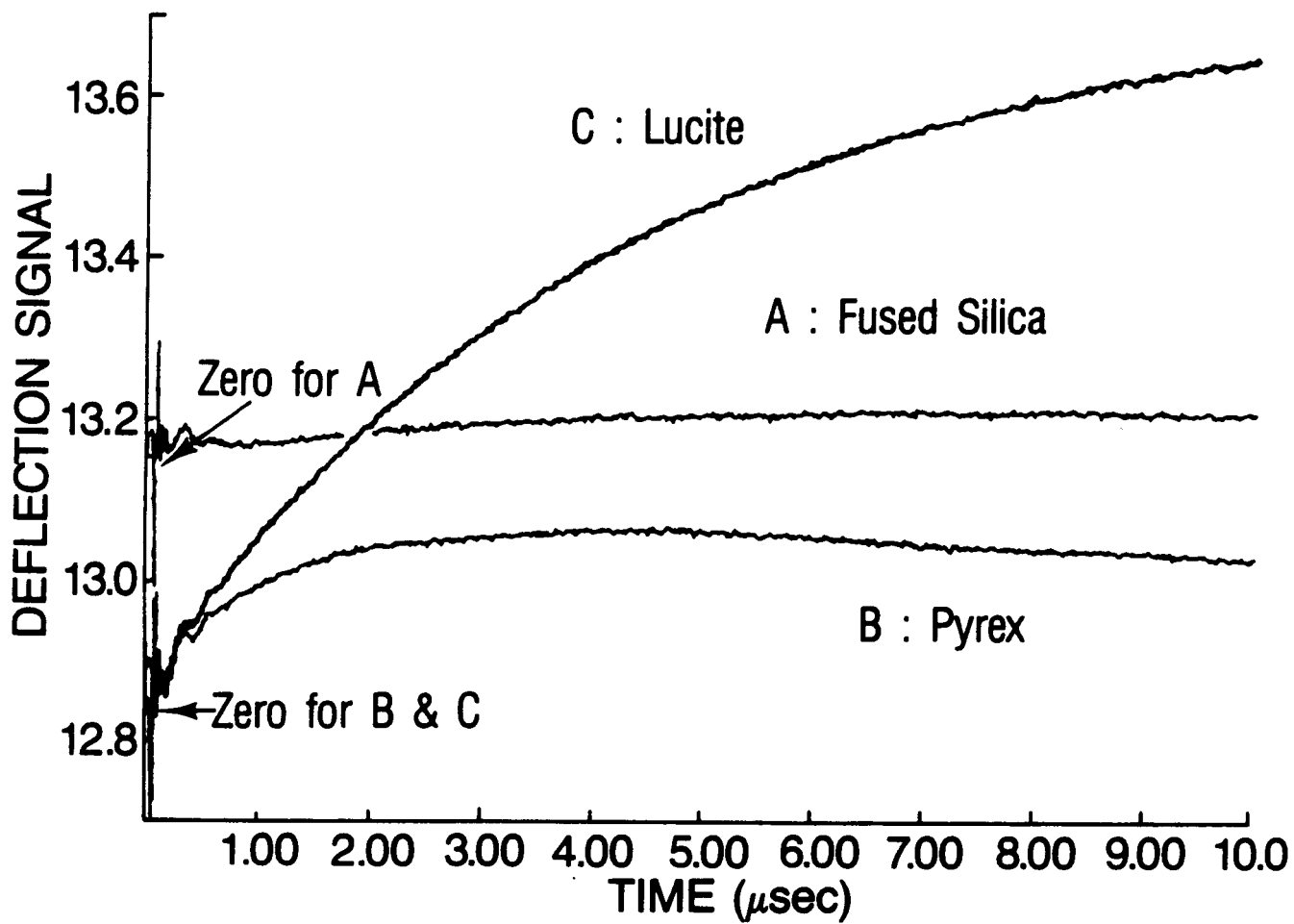


Figure 4.7 Material dependence of deflection signal. PD signal measured with 5000 Å of acridine orange deposited on fused silica (A), pyrex (B), and lucite (C).

It is also predicted in Eq. (4.1)-(4.6) that the deflection signal is bipolar and is a sensitive function of the probe relative to the pump beam position. The position dependence of the deflection signal again confirms the nature of the signal. In the study, the transverse position of the probe beam (with respect to the pump) is varied. Note that the magnitude of the deflection signal should be proportional to both the gradient  $dn/dx$  measured at the probed point and the signal polarity which is dependent on the sign of  $dn/dx$ . The lower trace in Figure 4.5 shows the deflection signal which is measured as a function of  $x$ . A 5000 Å thick film of acridine orange dye deposited on a lucite substrate is used in this measurement. To obtain the plot, the pump beam (wavelength = 580 nm) is moved such that the probed point is swept across the width of the pump intensity profile. The deflection signal is then numerically integrated to give an indirectly measured pump profile as shown in the upper trace of Figure 4.5. The pump beam width of the profile shown in Figure 4.5 has a FWHM of .4 mm which is in agreement with the width of the directly measured profile. It is crucial to point out that the bipolarity of the observed signal clearly shows that it is not caused by thermal lensing. The theory of photothermal deflection predicts that for a positive  $dn/dT$  the probe beam is deflected toward the center of the pump beam as indicated in Figure 4.1, and, in principle, one can determine the sign of the substrate thermo-optical constant  $dn/dT$  from the polarity of the PD signal. It is noted that the polarity of the deflection signal measured on lucite correlates correctly with its negative  $dn/dT$  constant (for lucite,  $-1.1 \times 10^{-4} \text{ K}^{-1}$ .) The observation clearly demonstrates that the probe beam is effectively deflected by a gradient of refractive index in the substrate. The approach taken in this work has been to test the technique by comparing the experimentally observed signal with theory. The fact that observations agree well with theory validates the use of the formalism to evaluate the PD technique. It is also realized that unless the measured heat is indeed related to triplet decay the technique would be of no real use in this study.

#### 4.4.2 Photothermal deflection vs. phosphorescence

The system to test the technique must not only be compatible with Collinear PD but furnish us with an independent measurement of triplet decay in addition to the PD signal. Solutions of erythrosin in glycerin are used for the following reasons: (a) erythrosin phosphorescence is at approximately 750 nm (determined with a spectrometer) and its quantum yield is high enough for phosphorescence to be observed<sup>15</sup> and (b) triplet decay rates measured in this system are well within the operation bandwidth of detector #1 (1Mhz.) Erythrosin dye (Kodak) is used as received and glycerin solutions are filtered with a fine Fritted disk filter. The pump wavelength is set in the range from 560 nm to 590 nm which is to the red side of the main absorption. The study calls for varying dye concentration, and the reason for changing the excitation wavelength is to make sure that the solution absorbance is kept below 0.5 while dye concentration changes from  $1 \times 10^{-2}$  to  $4 \times 10^{-5} \text{ mol/l}$ . Dye solution is contained in a spectroscopy cuvette having a 1 cm optical path. The solutions are optically thin at the HeNe wavelength, and filtering the solution prior to measurements is required to remove solid impurities which might scatter the light beams.

The system is of interest because it allows one to compare PD signals with directly measured triplet signals. On the other hand this configuration is not identical to the one required in thin film measurements. The overlap between the probe beam and the cylindrical volume of the optically pumped medium is 1 cm long consisting of a solution of dye in glycerin. In the overlap, the probe beam is deflected because of the change of refractive index which is associated with the excited-state dye molecules as well as the heating of the medium. Note that with thin film measurements which have been previously discussed the deflection of the probe is mainly due to thermal effects in the substrate. As mentioned earlier, signal caused by electronic transient has a different time behavior: it tracks the number density of excited molecules (triplet) instead of the generated heat density. In general one can expect that the thermal transient will be delayed with respect to the electronic transient and, if thermal relaxation is fast, its rise corresponds exactly to the decay of the electronic transient. In addition, the latter is opposite in sign to the thermal transient (polarizability of excited states is generally larger than ground state).

One should also note that in glycerin solutions with erythrosin concentrations  $< 2 \times 10^{-2}$  mol/l, the decay of erythrosin triplets is controlled by neither a Forster-type energy transfer nor by triplet-triplet quenching mechanism.<sup>15</sup> The observation implies that the decay time constant is not a function of laser fluxes and one does not have to know the point where the probe overlaps with the pump beam. This simplification is particularly helpful because the comparison between the PD signal and the directly measured triplet signal should be as straightforward as possible. The direct measurement of triplet number density is, in this case, the time-resolved phosphorescence of erythrosin molecules.

Figure 4.8 displays the deflection signal in the upper trace and the phosphorescence signal in the lower trace. The excitation wavelength is 560 nm which corresponds to the first excited singlet state of erythrosin. The pump beam is roughly Gaussian (4 mm dia), and the probe is focused to a midpoint between the cuvette walls with a 200 mm f.l. lens. The radial position of the overlap is adjusted to give maximum deflection. Except for the first 30 usec, the signal time dependencies are almost identical. Note that the deflection signal does not rise to its maximum within nanoseconds as it should (fast intersystem crossing) but appears distorted by the slow response of the detector (#1.) Plotting the decays on a semilogarithmic scale reveals that they are both single-exponential with 1/e time constant equal to 2.2 and  $2.3 \times 10^{-4}$  s, for the deflection and phosphorescence signals respectively (see Figure 4.9).

A quick study of dye concentration is performed next. The purpose of the study is not to understand the triplet decay per se but rather to vary the decay time constants over a wide range and check for agreement between the two methods. Figure 4.10 shows the comparison of time constants as measured by deflection and phosphorescence techniques. Triplet lifetimes increase with decreasing concentrations and at low limits ( $< 1 \times 10^{-4}$  mol/l) approach  $3.5 \times 10^{-4}$  s. The limit is in agreement with the value measured by time-resolved photoacoustic spectroscopy<sup>15</sup> which was reported at  $3.8 \pm 0.2 \times 10^{-4}$  s. The authors of this

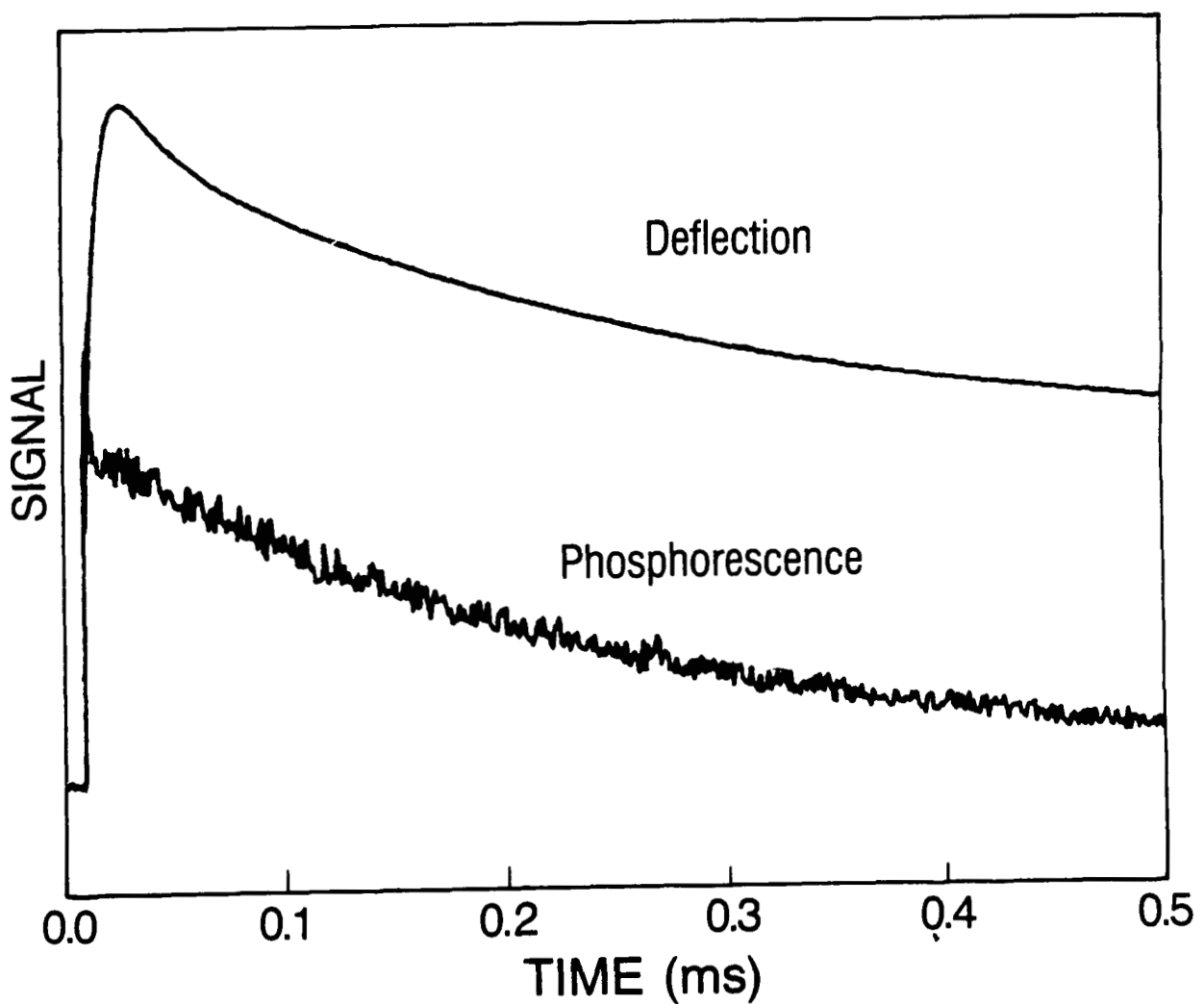


Figure 4.8 Comparison of PD signal and phosphorescence.

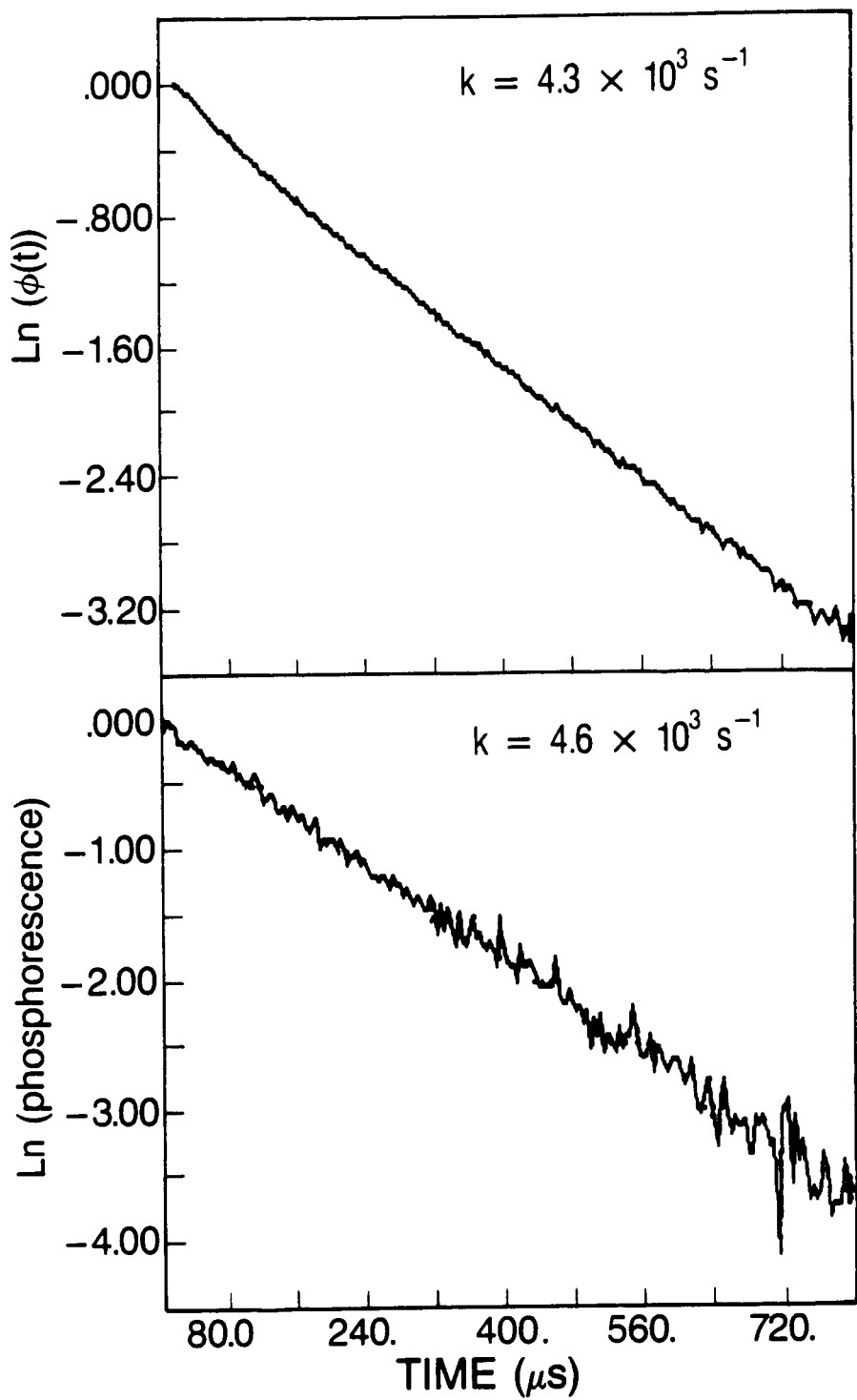


Figure 4.9 Time-resolved PD and phosphorescence signals on semi-logarithmic scale.

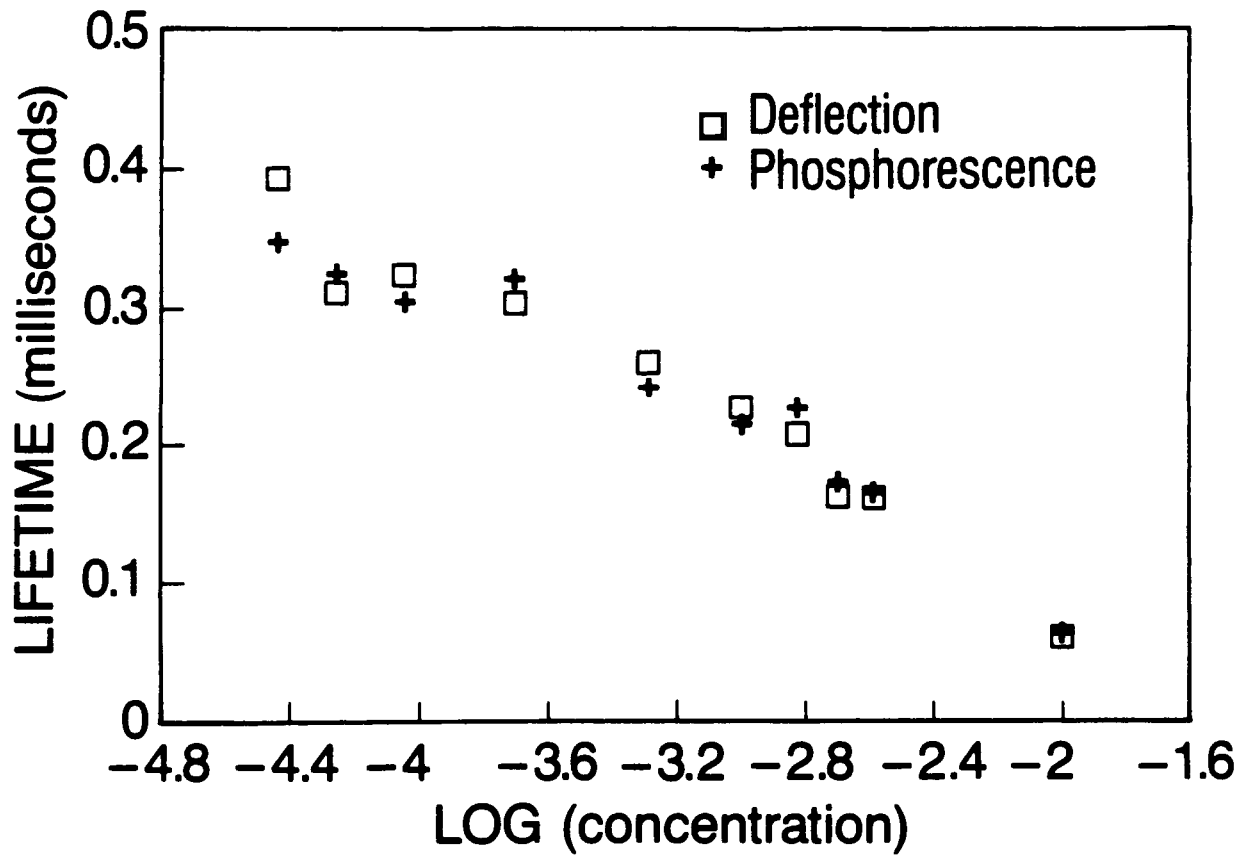


Figure 4.10 Lifetime of excitation as a function of dye concentration.

paper also reported single exponential decays.

Another comparison is made: deflection and phosphorescence signals are recorded as the temperature of the glycerin solution is varied from 10 C to 73 C.<sup>16</sup> The dye concentration used is  $1 \times 10^{-3}$  mol/l, and the excitation wavelength is 575 nm. Other experimental parameters are as mentioned in the last study. Figure 4.11 shows the combined result. The quenching of triplets in glycerin is speculated by Keller et al.<sup>15</sup> to be diffusion-limited. The presumption taken is that the quenching results from the binary collision of a triplet with another molecule (probably an impurity) and therefore is controlled by the mass diffusion in glycerin. The viscosity of glycerin can change by almost two orders of magnitude as the temperature is raised from 10 to 73 C. This is a convenient method of varying the decay rate constant of triplet quenching. Again, agreement is found for the two sets of rate constants.

The comparison of deflection and phosphorescence signals is the last test the technique is subjected to.

#### 4.4.3 Evaluation of PD technique

The photothermal deflection signal measures the change of optical phase which is induced by an optical pump source. What has been proposed in the thin film collinear PD measurement is a configuration which is particularly sensitive to the thermal contribution of the optical phase change. Furthermore, the proposed theoretical model has predicted that triplet decay kinetics can be derived from the deflection signal. The model is composed of two categorically different parts: heat diffusion in thin film/substrate systems and propagation of the probe beam in an inhomogeneous medium. The technique (and model) was proved useful by the following findings:

(a) The deflection is effectively caused by a gradient of refractive index in the substrate as indicated by the polarity and magnitude of the signal.

(b) There is agreement between (non-thermal) deflection signal and phosphorescence triplet signal. This test is, however, not conclusive as far as the thermal diffusion in thin film/substrate systems is concerned. This test nevertheless demonstrates that triplet decay information can be derived from optical phase change measurements.

It is obvious that the current detector (#1) has only limited applicability in the study of triplet decay. The displacement sensitivity attained with detector #1 is 60 percent of the theoretical value. Rewriting Eq. (4.17) to show the deflection sensitivity [A/rad] one obtains

$$\frac{\Delta I_{\text{out}}}{\Phi} = 0.88 P_{\text{HeNe}} [\text{W}] \frac{f}{\omega_{\text{HeNe}}} \frac{[\text{cm}]}{[\text{cm}]} \quad (4.19)$$

where  $f$  is the focal length and  $\omega_{\text{HeNe}}$  is the radius of the collimated HeNe beam before the lens. With optimized parameters ( $f = 500$  mm and  $\omega_{\text{HeNe}} = 1$  mm instead of those listed in Table 2) and the maximum input power allowed by SDC SD113-24-21-021 ( $P_{\text{HeNe}}(\text{max}) = 0.5$  mW), one can

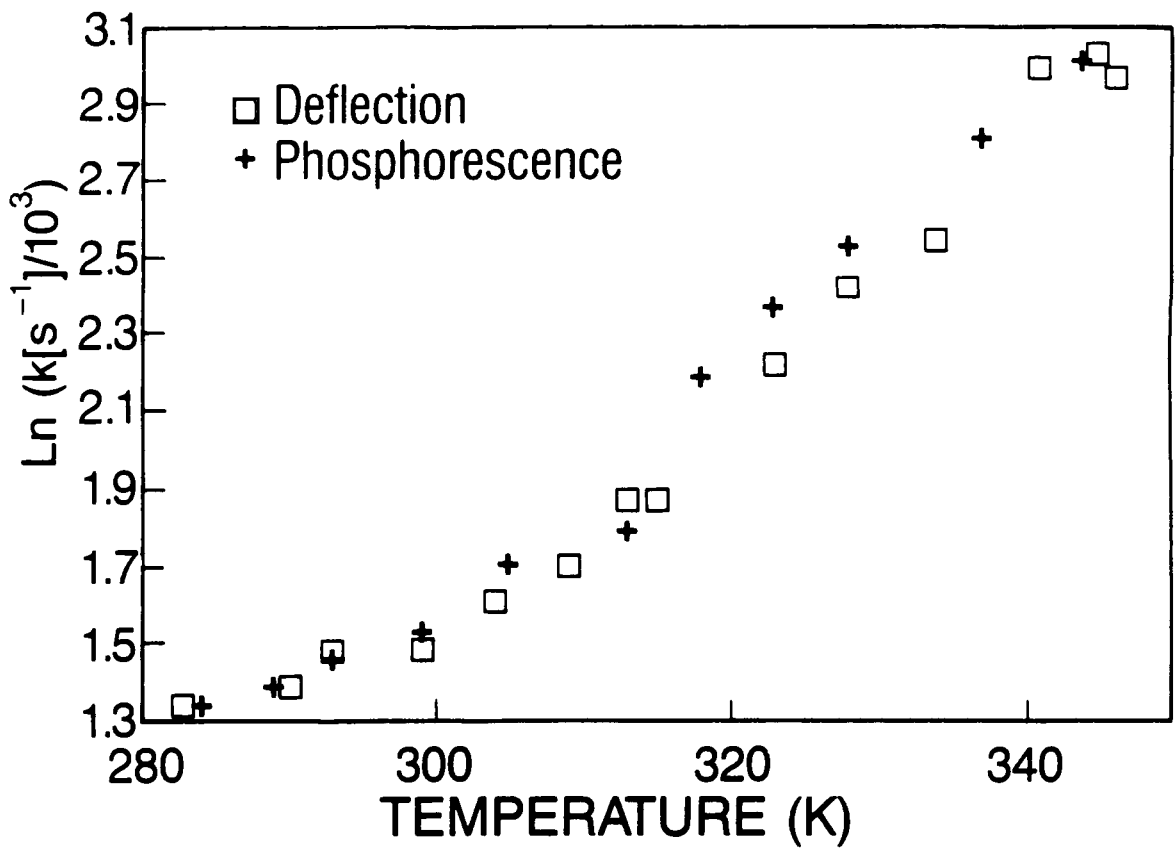


Figure 4.11 Lifetime of excitation as a function of glycerine temperature (viscosity).

attain a deflection sensitivity of .0264 A/rad. Table 5 summarizes the signal and noise levels which are expected of two sets of hypothetical experimental conditions. The first set of experimental conditions corresponds to a moderate pump fluence and the second set to a higher fluence. The moderate fluence case corresponds to a photoexcitation rate such that the initial triplet concentration is  $1 \times 10^{17} \text{ cm}^{-3}$ , and the effective decay constant is  $1 \times 10^6 \text{ s}^{-1}$  (a typical annihilation rate of  $1 \times 10^{-11} \text{ cm}^3 \text{ s}^{-1}$  and a slow unimolecular rate are assumed).<sup>14</sup> Using the same assumption, the case of high fluence corresponds to a  $1 \times 10^{19} \text{ cm}^{-3}$  triplet density and a  $1 \times 10^8 \text{ s}^{-1}$  decay rate. It is obvious that the noise level specified by the bi-cell's manufacturer is much too high compared to observations and is listed in Table 5 for the sake of completeness. Because detector #1 has a transconductance gain of ca.  $4 \times 10^5 \text{ V/A}$ , its use in the low fluence regime requires further amplification before the signal can be recorded by a typical oscilloscope. The kinetic study would require an amplifier with a gain 200 times higher than #1 and a bandwidth 10 times wider (10 MHz.). The building of device #2 was initiated but later discontinued because (a) there were difficulties with emi laser noise, (b) the would-be system is still severely limited by the detector response time (<50 MHz) and (c) it drops to a lower priority in the list of tasks.

All measurements indicate that this novel technique can be developed to the point where triplet kinetic measurement in thin films is feasible. The suitable system would benefit the most from a faster position detector. Fast photoconductive diodes which are now commercially available can easily work at 1 GHz. It is conceivable that future position detectors will be developed to approach that limit. With a 100 MHz bi-cell detector for example, the thermal deflection signal-to-noise ratio for a typical dye film measurement would be ca. 20 (using parameters listed in Ref. 17). A S/N of 100 is required for a reliable kinetics analysis. The single-event S/N can of course be improved by signal averaging.

It is understood that this technique requires dye films of good optical quality. The requirement is that the probe wave-front is not excessively broken up into beamlets by its propagation through the dye film. Polycrystalline films will present some difficulties if (a) the lateral width of the microcrystal is smaller than the probe beam waist (b) the orientation of microcrystals is random.

#### 4.5 Thin Film Pyroelectric Detection

Pyroelectric detection is one of several techniques, mentioned in Section 4.1, which can monitor heat generation in a thin film sample. The information of paramount importance to this research is time resolution (kinetics), and the ultimate worth of each method depends very much on its ability to provide kinetic information. Pyroelectric and piezoelectric (photoacoustic) techniques measure thermal and acoustic waves generated upon the absorption of light. The difference between the two techniques is that piezoelectric detection is known to yield excellent time resolution (10 ns according to Ref. 18) due to the high acoustic velocity in solids (ca.  $1 \times 10^5 \text{ cm s}^{-1}$ ) while pyroelectricity is not as well characterized. Pulsed pyroelectric detection has been recently investigated for measurements of thermal diffusivity.<sup>19</sup> In the reported

Table 5. Evaluation of PD Detector

	Moderate Fluence Case	Higher Fluence Case
Absorbed energy density (per pulse)	$4.3 \times 10^{-6} \text{ J cm}^{-2}$ a	$4.3 \times 10^{-4} \text{ J cm}^{-2}$ a
Maximum deflection, rad	$1.7 \times 10^{-9}$	$1.7 \times 10^{-7}$
Triplet decay time constant, s	$1 \times 10^{-6}$	$1 \times 10^{-8}$
Detector bandwidth, MHz	1	100
Deflection current, A		
according to Silicon Det. Corp. according to our measured sensitivity	$1.2 \times 10^{-10}$	$1.2 \times 10^{-8}$
theoretical (Gaussian probe beam)	$2.0 \times 10^{-10}$ $3.3 \times 10^{-10}$	$2.0 \times 10^{-8}$ $3.3 \times 10^{-8}$
Pointing noise reported in Jackson's work [Ref. 8], rad	$5 \times 10^{-6}$	
Corresponding noise current b, A ( $\Delta f = 1 \text{ MHz}$ )	$6.5 \times 10^{-7}$	
Observed pointing noise c, A ( $\Delta f = 1 \text{ MHz}$ )	$1.2 \times 10^{-9}$	$1.2 \times 10^{-8}$ ( $\Delta f = 100 \text{ MHz}$ )

a Parameters in Ref. 17 are used.

b Measured sensitivity of  $0.132 \text{ A/rad}$  is assumed.

c Spatial filter for probe beam and electrical high pass filter are used.

measurements, the film of material whose diffusivity is to be measured is sandwiched between a pyroelectric disk and an absorption layer. Heat generated by light absorption into the absorber will diffuse across the film of interest and be monitored by the detector. In this work, the proposed idea is to deposit the absorber directly on the detector and monitor the pyroelectric signal following the pulse excitation. With the proposed configuration, the thermal detection is expected to have faster response times (same order as piezoelectric detection) and can be useful in thin film experiments. Of the available pyroelectric materials, a ferroelectric polymer called polyvinylidene-difluoride (referred to as PVDF in this report) is of interest because fast response times have been reported for a thin (9  $\mu\text{m}$ ) PVDF detector.<sup>6-7</sup> Furthermore, the material is easy to handle and is compatible with the high vacuum environment required for thin film vacuum deposition.

#### 4.5.1 Principles of operation

Pyroelectric materials are characterized by a pyroelectric coefficient [ $\text{C cm}^{-2} \text{ K}^{-1}$ ] and other parameters which will be discussed next. Once heat is absorbed by the pyroelectric material, the temperature change induced is inversely proportional to the detector's heat capacity and is dependent upon heat losses. For a given change in temperature the induced charge is

$$C(t) = \int_{\text{detector}} d\vec{r} p(\vec{r}, t) \Delta t(\vec{r}, t) \quad (4.20)$$

The pyroelectric coefficient is written here as a function of position. The integral is taken over the volume occupied by the pyroelectric material. Depending on the electronic circuitry and especially the input impedance of the detector's preamplifier, the signal measured can be proportional to the induced charge (voltage signal) or its first derivative (current signal). In this work, the pyroelectric voltage signal is measured with a high impedance amplifier. It will be shown next that the detector measures heat in the same way a calorimeter measures heat.

The amount of heat change  $\Delta Q$  associated with the temperature change  $\Delta T$  is

$$\Delta Q(t) = \int c(\vec{r}, t) \rho(\vec{r}, T) \Delta T(\vec{r}, t) d\vec{r} \quad (4.21)$$

The specific heat capacity,  $c$ , and density,  $\rho$ , are shown as functions of position. If they are homogeneous within the pyroelectric volume and the temperature rise is small enough to neglect their temperature dependence, then Eq. (4.22) is valid.

$$\Delta Q(t) = cp \int d\vec{r} \Delta T(\vec{r}, t) \quad (4.22)$$

The above equation shows that the voltage signal is proportional to the average temperature in the pyroelectric detector. The detector is a disk with diameter ca. 1 cm and PVDF thickness ca. 9–100  $\mu\text{m}$ , and these dimensions have a number of implications. The thermal effects of the metallization (ca. 0.1  $\mu\text{m}$  of Al or Ni) are neglected for reasons which will become apparent. The aspect ratio of the disk is such that it can be treated as an infinite plate, and the only position coordinate of interest is in fact the distance measured along the normal to the disk plane. The latter is labelled the  $x$ -axis and its origin ( $x=0$ ) is chosen at the detector plane which is facing the light beam. Heat is generated at this plane. In any case, the integral can be taken from  $x = 0$  to  $x = L_D$  (PVDF thickness). The integral on the right-hand side of Eq. (4.20) can be similarly simplified by assuming that  $p$  is not position dependent in which case

$$C(t) = p \int d\vec{r} \Delta T(\vec{r}, t) \quad (4.23)$$

Comparing (4.22) and (4.23), one has

$$C(t) = \frac{p}{C_p} \Delta W(t) \quad (4.24)$$

Eq. (4.24) in fact describes the use of the pyroelectric detector as a calorimeter. It is obviously assumed that the temperature change and measurement are fast compared to the time scale of thermal and electrical losses, but slow compared to the inherent response time of the detection. The first assumption is easy to make because only the first time window, where heat is generated, is of concern. As seen later in actual signals, thermal loss is faster than electrical loss but still in the order of 1 msec or longer. The second assumption needs a thorough defense which is given next.

Figure 4.12 displays the relevant dimensions and components of the detection. Light is irradiating an absorbing layer which, together with the metal electrode represents an infinitely thin surface at  $x=0$ . The light beam is assumed to have a top-hat intensity distribution. The illuminated spot and the diameter of the detector disk are both infinitely larger than the thickness (10–100  $\mu\text{m}$ ). The problem of heat diffusion from a surface of an infinite semi-plane was treated by Carslaw et al.<sup>10</sup> and the temperature distribution  $T(x, t)$  is given in Eq. (4.5). The pyroelectric charge is now rewritten as

$$C(t) = p \frac{\alpha^{\frac{1}{2}}}{k\pi^{\frac{1}{2}}} \int_0^{L_D} dx \int_0^t d\tau f(t-\tau) e^{-\frac{(x^2/4\alpha\tau)^{\frac{1}{2}}}{\tau}} \quad (4.25)$$

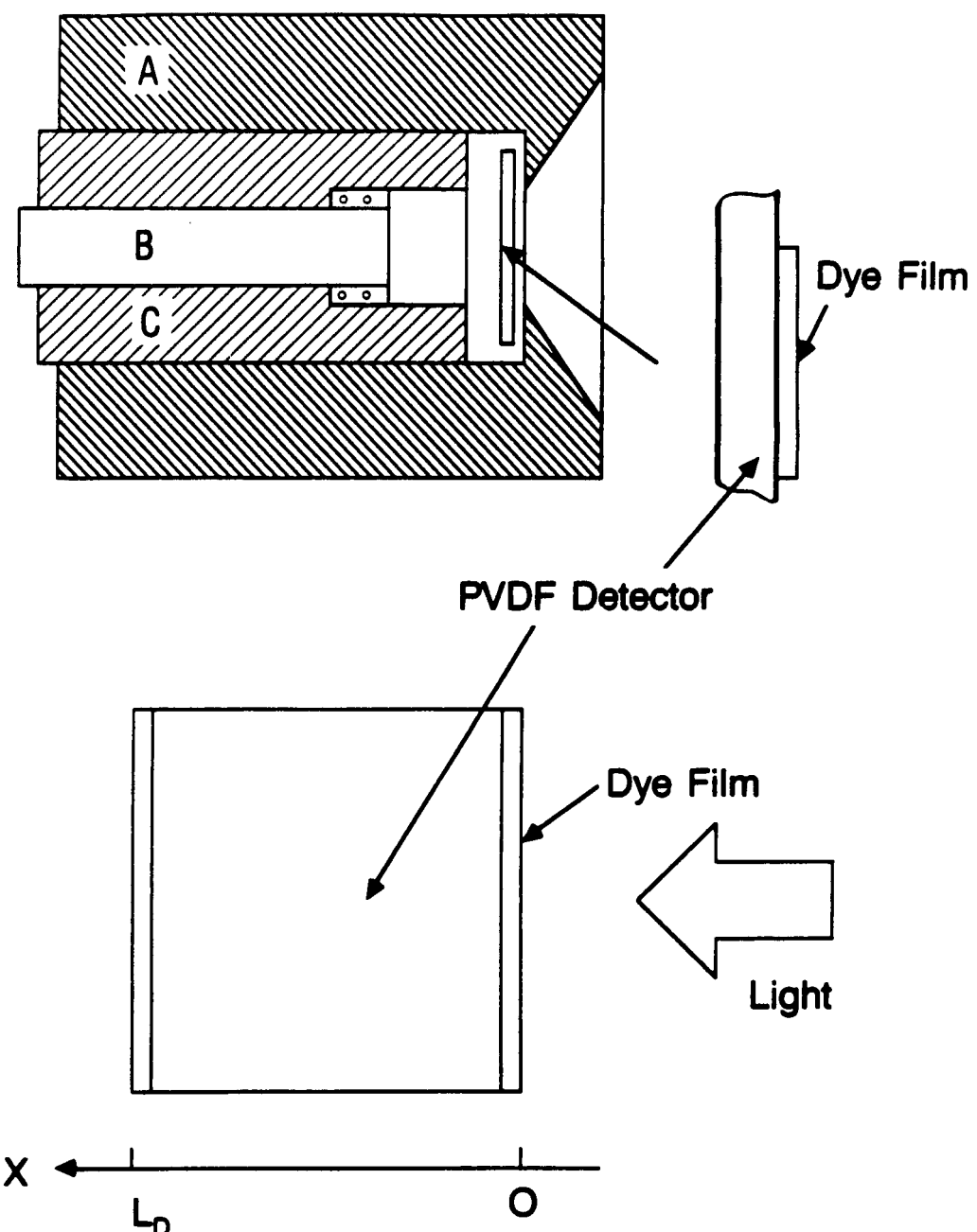


Figure 4.12 Thin-film ferroelectric detector.

where  $f(t-\tau)$  is the function depicting the heat generation at plane  $x=0$ ,  $\alpha$  the heat diffusivity and  $L_D$  the thickness of the PVDF film. Integration over the thickness gives

$$C(t) = p(c\rho)^{-1} \int_0^t d\tau f(t-\tau) \operatorname{erf} \left( \frac{L_D}{\sqrt{4\alpha\tau}} \right) \quad (4.26)$$

The time interval of observation is restricted to the limit:

$$\tau \ll \frac{L_D^2}{4\alpha}$$

In this limit, the value of the error function is approximated by 1. This limitation is not as severe as it may seem because the triplet kinetics of interest happen in times much smaller than the above interval. Numerically, the restriction means that for the thinnest PVDF (9  $\mu\text{m}$ ), any measurement at times longer than ca. 3 msec is not covered by this next approximation:

$$c(t) = p(c\rho)^{-1} \int_0^t d\tau f(t-\tau) \quad (4.27)$$

Eq. (4.27) is important because it assures that the charge which is measured at a given time,  $t$ , is proportional to the amount of heat generated at the surface up to time  $t$ . This amount is also related to the population of triplets in the film at that given time. The relation is as shown

$$n_T(t) = \frac{E_{\text{abs}} - c\rho p^{-1} C(t)}{V_{\text{dye}} h\nu} \quad (4.28)$$

where  $V_{\text{dye}}$  is the volume of the illuminated dye disk and  $h\nu$  is the triplet energy. The illumination is presumed to be uniform, and the triplet number density is not changing in the lateral dimension. There are several key assumptions made: (1) the pyroelectric coefficient,  $p$ , specific heat and density are constant in the PVDF volume, and (b) the time interval of observation is limited by the thermal diffusion time  $L_D^2/4\alpha$  and/or the heat loss time constant. Ferroelectric PVDF is produced by poling the polymer. The commercial process of poling involves subjecting the film to a high DC electric field and high temperatures, typically in the range of 80 to 120 C.<sup>20</sup> Depending on the process and the conditions of poling, the ferroelectric property of the

PVDF film can be more or less uniformly distributed throughout the volume. The spatial distribution of the piezoelectricity coefficient has been the subject of several studies.<sup>21</sup> The findings of these studies show that piezoelectricity is confined to a layer close to the positively biased electrode under certain conditions. It is also expected that pyroelectricity is correlated with piezoelectricity and therefore has a similar spatial distribution. The extent of this non-uniformity can affect the validity of the assumed approximation (Eq. (4.27)).

The PVDF is not only a thermal detector but, because of its piezoelectric property mentioned earlier, is also sensitive to acoustic waves. In this measurement, the pulsed heating of the sample layer can introduce an additional source of electrical signal. It is natural that the thermal gradient created by the heating also generates acoustic waves which may be picked up by the detector. The effects of this piezoelectric signal will also be discussed. Experimental measurements made with a PVDF detector and the implications need to be discussed.

#### 4.5.2 Experimental

In this study, ferroelectric PVDF (Pennwalt Kynar) foils are used. Foils with polymer thicknesses from 9 to 110  $\mu\text{m}$  are used. The metallization (metal coating used as electrodes) is Al or Ni and furnished by the manufacturer with a quoted thickness of approximately 0.1  $\mu\text{m}$ . This metal layer can be neglected with respect to the question of heat transport in the composite film. Figure 4.12 shows how the detector is mounted. A PVDF disk, 1.2 cm diameter, is positioned between the copper pieces A and B. The two pieces serve as electrical connections. The contact surface of the piston B is coated with a silver/polymer layer of paint. This conductive layer is there to absorb laser-induced acoustic waves. Its dampening effect is shown in Figure 4.13 where the PVDF signals of damped and undamped detectors are compared. The signals are definitely a mixture of a unipolar and a bipolar contribution. The bipolar ringing is attributed to echos of the acoustic disturbance because its occurrence correlates with the acoustic velocity in PVDF.<sup>22</sup> To emphasize the contribution of the acoustic ringing in this demonstration, a 110- $\mu\text{m}$ -thick PVDF foil is used instead of thinner films which do not generate as much acoustic ringing. With 9- $\mu\text{m}$ -thick foils, for example, the ringing is about one order of magnitude less than what is shown in Figure 4.14. It is worth noting that dampening the acoustic echos does not eliminate the acoustic contribution to the overall ferroelectric signal (the ringing observed with an undamped 9  $\mu\text{m}$  film is less than 10 % of the maximum signal). For the sake of generality, this combined signal will hereafter be referred to as the ferroelectric (FE) signal.

The pulsed heating is done by a nitrogen-pumped dye laser (Molelectron UV12 and DL-II). The laser beam is expanded so that the 1/e radius of the illuminated spot (at the detector) is 0.4 cm. The laser pulse energy is monitored with a pyroelectric detector (Laser Precision RK3230). The wavelength and the dye film thickness are chosen so that, for most experiments, the film optical density is higher than 1.0. Any light which transmits through the dye film will be absorbed in the metal layer. Light absorption at the metal layer results in a fast signal with a rise time less than 100 ns, observed here as well as by the

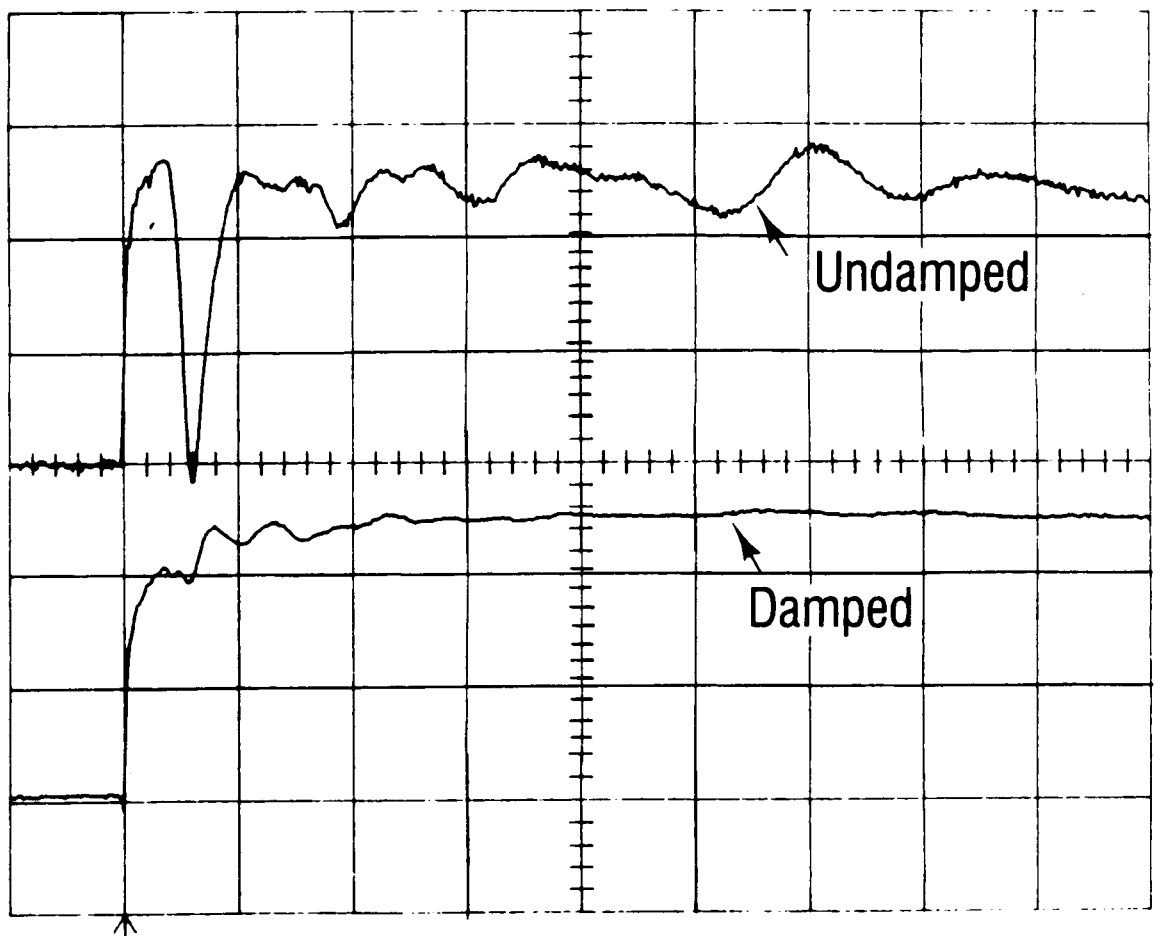


Figure 4.13 Ferroelectric signal. Time scale: 10  $\mu$ sec/div.

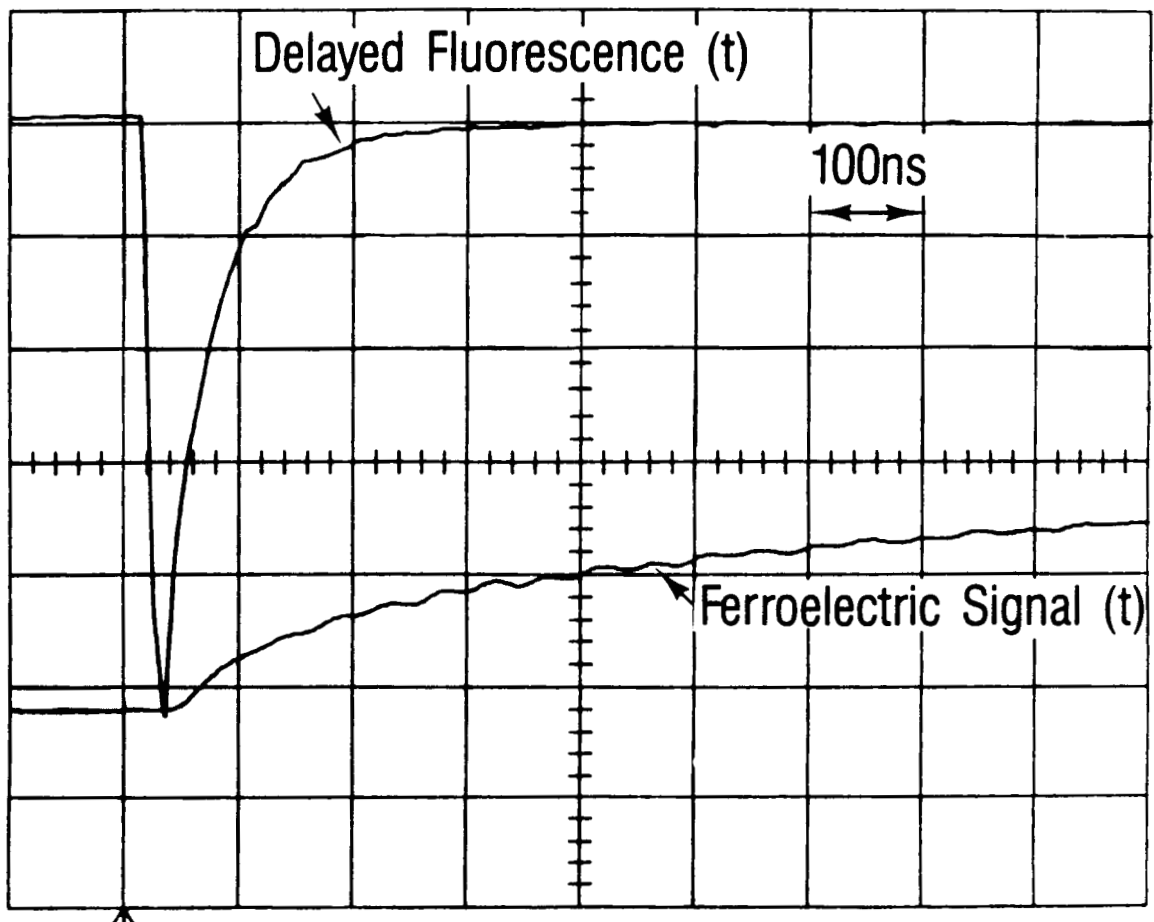


Figure 4.14 Comparison of ferroelectric and phosphorescence signal.

authors in Ref. 6 and 7. In any event, this noise is kept at minimum by controlling the dye film opacity.

The amplification and electrical configuration of the detector are worth a brief discussion. Emi problems are alleviated by putting the detector (as shown in Figure 4.12) and its amplifier in a metal casing. The amplifier is custom-built around two linear amplifiers (National Semiconductor LH0032 and LH0063) and proven to have a flat response from DC to 50 MHz. The overall bandwidth is probably limited by the PVDF detector itself. The input impedance of the amplifier is kept at  $1 \text{ M}\Omega$  which is ca. 1000 times the detector source impedance (for reasons, see earlier section). The signal is digitized by the digital oscilloscope. Averaged waveforms are transferred to a dedicated PC XT computer for data analysis.

#### 4.5.3 Results of tests

Because of the possibility of having both pyroelectric and piezoelectric (minor component in thin PVDF films; less than 10%) contributions in the signal, we hereafter refer to it as ferroelectric signal FE. Note that the combined FE signal still gives us the kinetics of triplet decay as long as the response times of both the pyroelectric and piezoelectric signals are fast enough for the measurement. To test the pyroelectric detector, films of tetracene are once more used. Delayed fluorescence signal DF (see Chapter 3) from tetracene will be compared to the ferroelectric signal. Figure 4.14 shows (1) DF(t) in the upper trace and (2) FE(t) signal in the lower trace. The DF signal should be proportional to the square of the triplet number density and decaying with time with a rate twice the triplet decay rate. On the other hand, FE is thermal and should increase with time as predicted by Eq. (4.28) (the build-up time should be the triplet decay time). To facilitate the comparison of the two signals, DF has been inverted in Figure 4.14. Furthermore, the scales of the two curves are adjusted such that the most negative data point of DF aligns with the baseline of FE signal, and the maximum value of FE which occurs  $7 \times 10^{-5}$  s after the laser (not included in oscillogram shown in Figure 4.14) is equal to the DF baseline. In principle, the decay rate observed with the inverted DF signal should be twice the one observed with FE. The agreement is not observed: 1  $\mu\text{sec}$  after the laser, DF is practically zero while FE has only reached 32 % of its maximum. At all times, the decay rate derived from the DF curve is much higher than that predicted by FE signal.

The above-stated discrepancy is probably caused by a sluggish ferroelectric response. Because the pyroelectric signal is the dominant component, it is safe to conclude that (a) the response time of the pyroelectric detection is inherently too long or (b) heat generation is delayed because electronic energy is trapped. If (b) is the main reason for the discrepancy in the decay rates, then pyroelectricity is still a valid method to measure triplet decay. The fact that excitons are trapped in low energy sites is common knowledge, and energy transport in tetracene films is no exception.

On the other hand, the discrepancy in the observed signals may be caused by an inherently slow detection. Because the bandwidth of the amplifier is not limiting the detector performance in this regime, the sluggishness is probably due to the breakdown of Eq. (4.27). The non-uniformity of ferroelectricity in the film volume can introduce a convo-

lution in the voltage signal. Inspection of Eqs. (4.26)-(4.27) hints that if the pyroelectric constant of an infinitesimal volume depends on its x-coordinate, the response to an impulse heat generation will not be a step function but a gradually rising function which is characteristic of the PVDF film. To measure the apparatus function one can do the following test. A 2000 Å thick layer of copper is deposited on the Ni electrode of a 9  $\mu\text{m}$  PVDF film. At 337 nm, the reflectance of evaporated copper is less than 0.5, and its optical density will be more than 1.0 for a 2000 Å Cu film. The output of the nitrogen laser produces pulses of duration less than 10 ns. Heat generation is expected instantly in metal. The response shown in Figure 4.15 is measured upon excitation of the copper film with the pulsed laser and represents the above-stated apparatus function. This is proof that the non-uniform spatial distribution of pyroelectricity has voided the validity of Eq. (4.27) and degraded the ultimate bandwidth of the detector.

#### 4.6 Conclusions

The report included the evaluation of two thermal techniques of studying triplet decay in dye thin films. The findings can be summarized as follows: (1) The Photothermal deflection technique looks promising because it can, in principle, monitor the generation of heat in sub-micron films. As to the application of this technique in thin films, the figure of merit has been identified as the product of detector sensitivity and detector bandwidth. Because of that relation, a position detector with faster response time might be the necessary and sufficient requirement. (2) The Ferroelectric detection has been shown to be limited in bandwidth. The observation contradicts the heat diffusion model (as indicated in Eq. (4.27)). The cause of this slow response is not understood yet. It is speculated that the nonuniform spatial distribution of ferroelectricity can cause the slow response and the deviation from Eq. (4.27).

The efforts invested in studying the thermal techniques which have been proposed as viable techniques to evaluate the singlet oxygen generator have been fruitful.

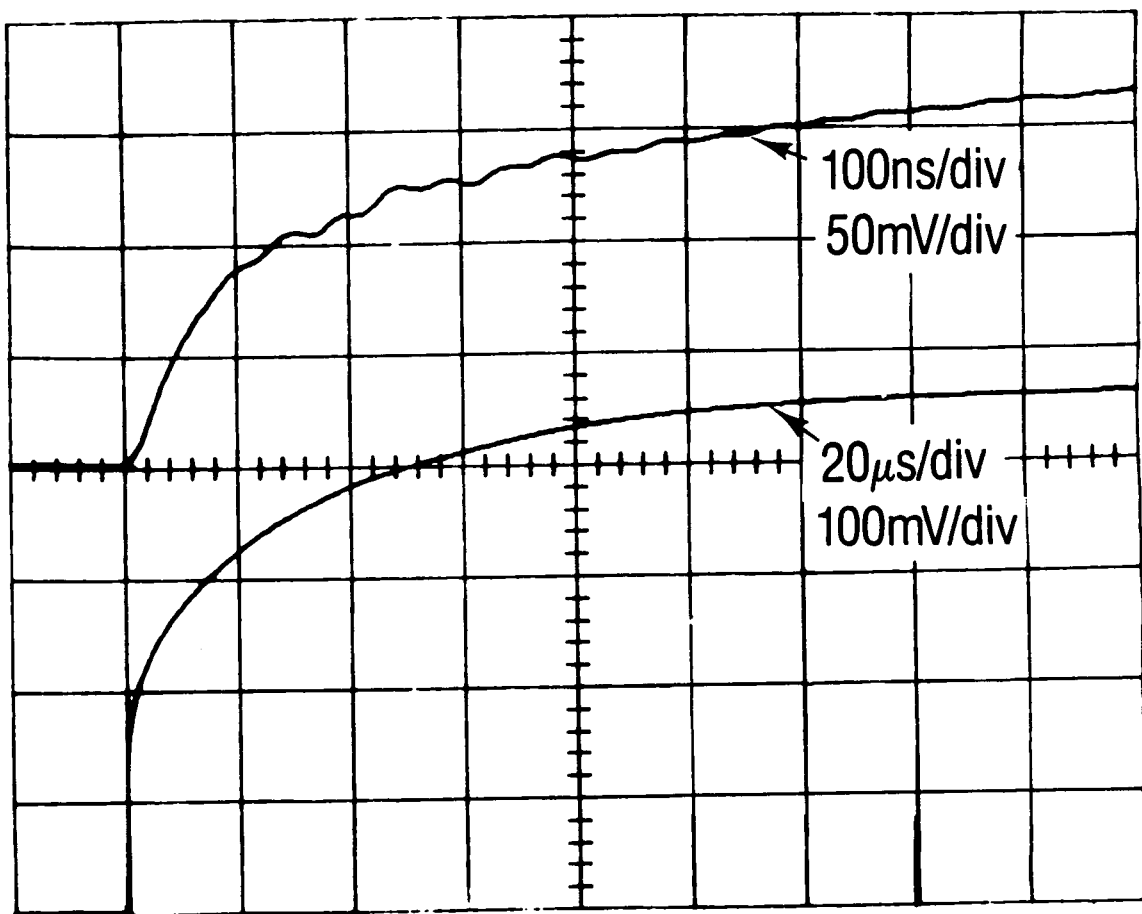


Figure 4.15 Response time of thin film ferroelectric detector.

#### **4.7 References and Notes**

1. J. R. Whinnery, "Laser Measurement of Optical Absorption in Liquids," Acc. Chem. Res. 7, 225 (1974).
2. Y. H. Pao, Ed., Optoacoustic Spectroscopy and Detection, Academic Press, New York (1977).
3. A. C. Boccara, D. Fournier, W. Jackson and N. M. Amer, "Sensitive Photothermal Deflection Technique for Measuring Absorption in Optically Thin Media," Opt. Lett. 5, 377 (1980).
4. D. Fournier, A. C. Boccara, N. M. Amer and R. Gerlach, "Sensitive In Situ Trace-gas Detection by Photothalermal Deflection Spectroscopy," Appl. Phys. Lett. 37, 519 (1980).
5. A. C. Boccara, D. Fournier and J. Badoz, "Thermo-optical Spectroscopy: Detection by the 'Mirage Effect'," Appl. Phys. Lett. 36, 130 (1980).
6. H. Coufal, "Photothalermal Spectroscopy Using a Pyroelectric Thin-Film Detector," Appl. Phys. Lett. 44, 59 (1984).
7. H. Coufal and P. Hefferle, "Thermal Diffusivity Measurements of Thin Films with a Pyroelectric Calorimeter," Appl. Phys. A 38, 213 (1985).
8. W. B. Jackson, N. M. Amer, A. C. Boccara and D. Fournier, "Photothalermal Deflection Spectroscopy and Detection," Appl. Opt. 20, 1333 (1981).
9. L. W. Casperson, "Gaussian Light Beams in Inhomogeneous Media," Appl. Opt. 12, 2434 (1973).
10. H. S. Carslaw and J. C. Jaeger, Conduction of Heat in Solids, Oxford University Press, New York, N.Y. (1986).
11. The refractive index change is composed of two components: (a) the change caused by a change in the molecular polarizability and (b) the change due to volume expansion. The first change is non-thermal and should have a time evolution different from change (b). Change (b) is thermally induced and expected to change the optical path length in two ways. It can directly change the refractive index ( $dn/dT$  is usually negative) or cause a lengthening of the sample. The latter change ( $n \propto, \alpha = \text{coefficient of linear thermal expansion}$ ) is typically positive and dominates over  $dn/dT$ .

12. The image of the aperture is approximately rectangular in shape with an aspect ratio of about 8 and with the larger side being vertical. The irradiance along the vertical can be approximated by a flat top distribution (for reasons mentioned in text). Vertical alignment can therefore be done by eye. The smaller dimension (horizontal width) of the rectangular image is typically .01 cm, and the irradiance profile along the horizontal is a sensitive function of position. To determine the horizontal irradiance profile a scanned apertured photodiode is used. A large ( $1 \text{ cm}^2$  active area) photodiode which is masked with a knife edge is scanned horizontally across the pump beam at the image plane. The dependence of the photocurrent on the detector position is related to the irradiance profile. The FWHM of the irradiance profile, measured by this method, agrees with the one obtained with the method described in text. Note that the method of scanning the apertured detector cannot determine the horizontal position of the probe beam.
13. Speckles are observed on a screen ca. 10 cm away from the rough surface and the sample translator is moved until the speckles look the sharpest.
14. At times where the maximum deflection is obtained, heat is effectively in the substrate itself because the dye film is only ca. 1000 Å.
15. W. W. A. Keller, W. Schubert, R. Germer and E. Strauss, "Time Resolved Photoacoustic Spectroscopy of Metastable Electronic States of Dye Molecules," *J. Phys. C6*, 397 (1983).
16. Data are interpolated from results shown in the following reference: J. B. Segur and H. E. Oberstar, "Viscosity of Glycerol and its Aqueous Solutions," *Ind. Eng. Chem.* 43 2117 (1951).
17. Typical parameters are used in this estimation:  
Quantum yield of producing triplet = 1  
Dye thickness = 1 micron  
Averaged photon energy =  $4.3 \times 10^{-19} \text{ J}$   
Annihilation rate,  $k_{TT} = 1 \times 10^{-11} \text{ cm}^{-3} \text{ s}^{-1}$ .
18. A. C. Tam and H. Coufal, "Photoacoustic Generation and Detection of 10-ns Acoustic Pulses in Solids," *Appl. Phys. Lett.* 42, 33 (1983).
19. S. D. Lang, "Theoretical Analysis of the Pulse Technique for Measuring Thermal Diffusivity Utilizing a Pyroelectric Detector," *Ferroelectrics* 11, 315 (1976).
20. M. A. Marcus, "Several Electric Polymers and their Application," paper presented at the 5th Int. Meeting on Ferroelectricity at Pennsylvania State University, (Aug. 17-21, 1981).

21. R. Gerhad, G. M. Sessler, J. E. West, K. Holdik, M. Haardt and W. Eisenmenger, "Investigation of Piezoelectricity Distributions in Poly(vinylidene fluoride) by Means of Quartz - or Laser-generated Pressure Pulses," *J. Appl. Phys.* 55, 2769 (1984); and references therein.
22. The acoustic velocity in PVDF is specified by the manufacturer to be  $1.5 - 2.2 \times 10^5 \text{ cm s}^{-1}$ . For a laser hitting the detector at its center, the acoustic disturbance can travel in the waveguide mode to the boundary and back with a round trip distance of ca. 1 cm. The travel time is 5  $\mu\text{sec}$  which is approximately the time at which the first (strongest) dip appears on the upper trace of Figure 4.12.

## CHAPTER 5: CONVERSTON OF 2PVN TO ENDOPEROXIDE

### 5.1 Introduction

In chapter 2 results were presented which showed that oxygen could diffuse into thin polymer films and quench the phosphorescence of porphyrin dye molecules dissolved in the polymer matrix. The assumption made in the isolated molecule studies was that quenching of dye luminescence by oxygen is a consequence of energy transfer from the triplet dye molecule to the oxygen molecule promoting the latter to the singlet delta state. If this energy transfer occurs in a 2PVN film one would expect that the singlet oxygen formed in the process would have a good chance of reacting with a naphthalene moiety to form the endoperoxide. In fact dye sensitized peroxidation of 2PVN does occur and experiments which quantify the reaction yield are reported below.

### 5.2 Experimental

Films of 2PVN, 84-nm-thick, which contain ZnTPP, PdTPP, or PtTPP were deposited on quartz substrates. A film with either 0.1 or 1.0 mole per cent of dye in 2PVN was prepared by spin coating from solutions with the same ratio of dye molecules to 2PVN monomeric units (each containing one naphthalene moiety). The films were heated in an oven at 80 to 100 C for 15 minutes prior to study in order to free the polymer film of any endoperoxide which may have formed during preparation.

The 2PVN film was exposed to light from an argon ion laser pumped dye laser. The wavelength of laser light which irradiated the polymer films doped with ZnTPP was 568 nm while the 514 nm argon ion line was used directly for irradiating the PdTPP or PtTPP doped 2PVN films. The optical path of the laser beam included a lens to expand the laser beam and an iris to aperture the beam to a 2-cm-diameter spot on the substrate. The polymer film doped with either 0.1 or 1.0 mole per cent porphyrin was illuminated for a measured period of time with 44 or 4.4 milliwatts of energy, respectively. The power level of the laser beam incident on the sample was measured with a calibrated power meter.

The experiments were performed with the polymer films exposed to ambient air which has a partial pressure of oxygen of roughly 150 Torr. Under these conditions most of the phosphorescence from the dye molecules is quenched, presumably by energy transfer to oxygen. After illumination of the porphyrin-doped 2PVN film for a measured interval of time, the absorbance of the film at 294 nm was measured with an IBM 9430 spectrophotometer. The kinetics of the conversion of 2PVN to the corresponding endoperoxide were determined by the change in absorbance of the polymer film at 294 nm as a function of irradiation time (and thus number of incident photons).

### 5.3 Results

The irradiation of ZnTPP doped 2PVN in the presence of air results in the conversion of naphthalene units in the polymer to endoperoxide.

In Figure 5.1 this conversion is demonstrated by the decrease in absorbance in the spectral band peaking at 294 nm following laser irradiation. This spectral feature is assigned to the pi electron system of the naphthalene group and disappears upon peroxidation. The decrease in absorbance at 294 nm is directly proportional to the fraction of naphthalene units which have been converted to endoperoxide. The absorbance at 294 nm is found to fully recover to its pre-irradiated value after heating the polymer film to 80°C for 15 minutes, indicating the complete reversibility of the endoperoxide formation reaction.

The kinetics of the conversion of 2PVN to the corresponding endoperoxide were determined by measuring the absorbance of the polymer film at 294 nm as a function of the number of photons per  $\text{cm}^2$  absorbed by the film. The fractional conversion to 2PVNE was computed from  $1 - A(p)/A(0)$ , where  $A(p)$  is the absorbance after the film has absorbed  $p$  photons/ $\text{cm}^2$ . Figures 5.2 through 5.4 show the fractional conversion of naphthalene units to endoperoxide in 2PVN films doped with 0.1 and 1.0 per cent ZnTPP, PdTPP and PtTPP as a function of  $p$ , calculated from the product of the incident fluence ( $\text{J}/\text{cm}^2$ ), the number of photons per Joule at the laser wavelength, and the fraction of incident photons absorbed by the sample. The latter quantity was determined directly from absorbance measurements of pre-irradiated 1% porphin doped 2PVNE films and assumed to be a factor of 10 less for 0.1% porphin doped films.

From Figures 5.2-5.4 it appears that the rate of conversion (the slope of the curves) decreases as the number of photons absorbed by the polymer film increases. If dye molecules are bleached (lose absorbance in the visible) by reaction with oxygen or the polymer as a consequence of the sensitization process, the observed conversion rate decrease may be a direct result of the decreasing fraction of light absorbed by the film which was not accounted for in Figures 5.2-5.4 (it was assumed in the calculations for the number of absorbed photons that the absorbance of the film at the laser wavelength was constant in time). In fact it is found that the absorbance of the film at the laser wavelength does fall off over the course of a series of measurements of conversion rate; however, the actual decrease in dye absorbance can not fully account for the reduction in conversion rate observed in Figures 5.2-5.4.

The loss of absorbance of ZnTPP in 2PVNE over the course of a conversion experiment was measured in one experiment. A 1.0 per cent ZnTPP doped 2PVN film was irradiated at 568 nm and at selected intervals the absorbance spectrum of the film was measured, both in the neighborhood of the naphthalene absorption peak at 294 nm and at 405 nm in the Soret band of the porphin dye (this absorption band is more prominent in the spectrum than the band further to the red at the irradiation wavelength and more amenable to quantitative work). At the completion of the experiment 11 per cent of the naphthalene units in the polymer film were converted to endoperoxide units while the dye absorbance had only suffered a 12 per cent decrease. Figure 5.5 shows two plots of fractional conversion versus number of absorbed photons. The two plots are derived from the same data, but in one case the data have not been corrected for bleaching of the ZnTPP dye. It is clear from Figure 5.5 that the small amount of bleaching of the dye which does occur can not fully explain the decrease in the rate of fractional conversion with irradiation.

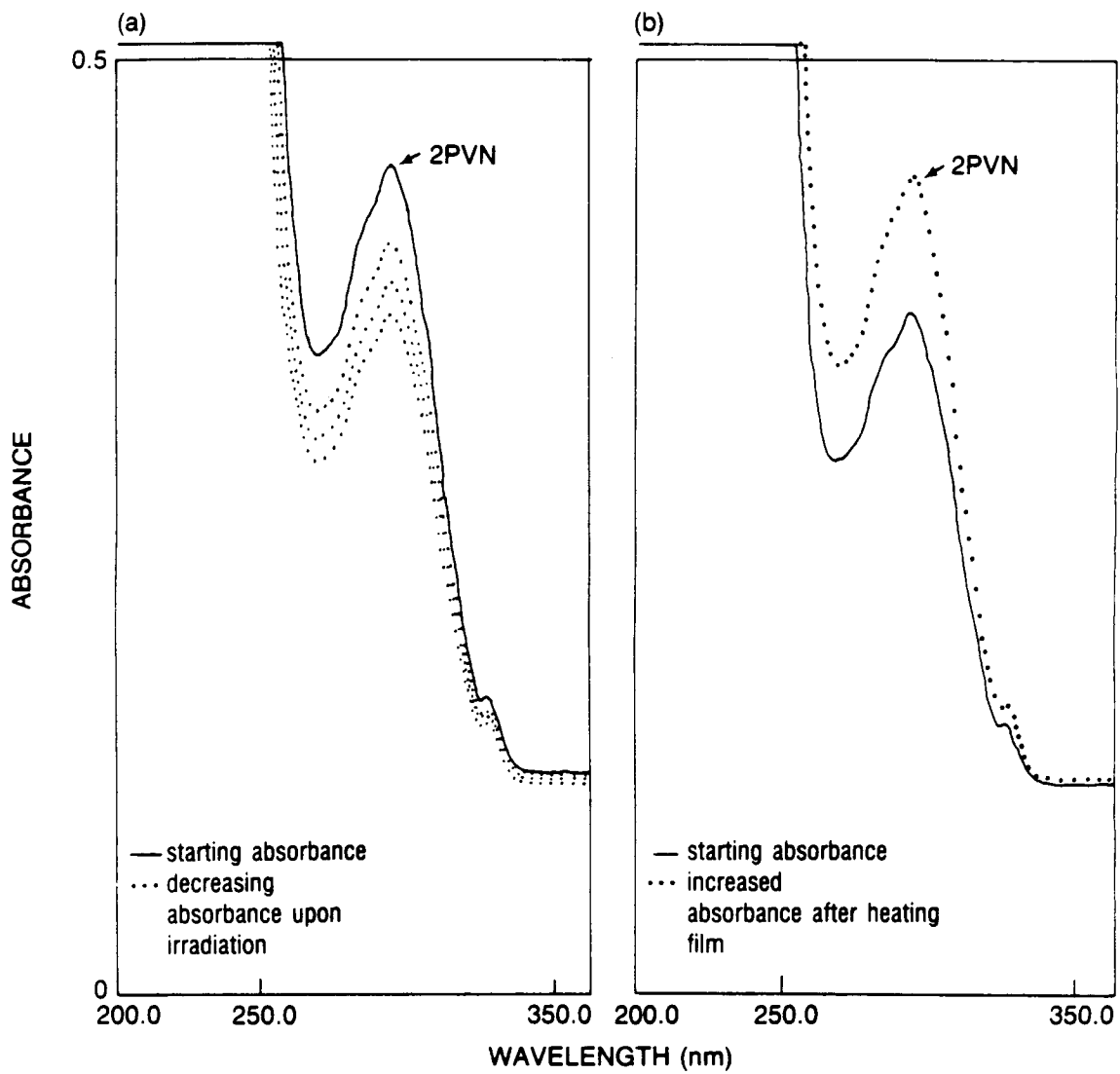


**Figure 5.1** Absorption spectrum of 2PVN showing a) the decrease in absorbance of the 294 nm band upon irradiation of the ZnTPP/2PVN film with light b) the increase in absorbance in the same absorption band with heating of polymer at 80° C for 15 min.

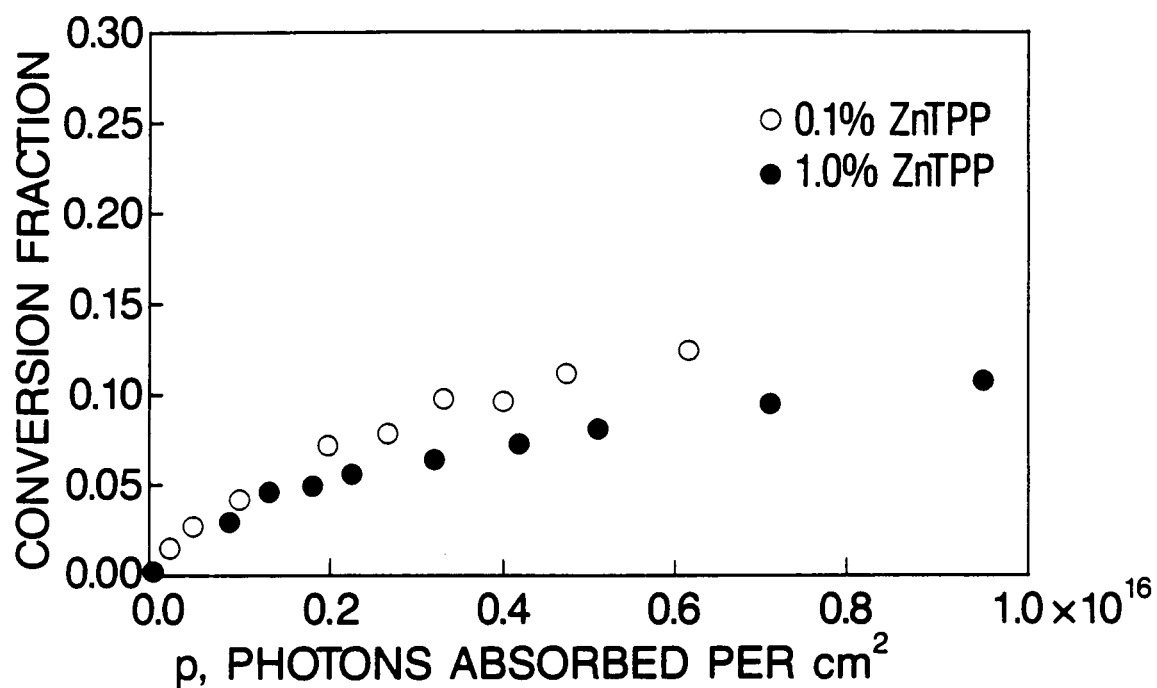


Figure 5.2 The fraction of naphthalene units converted to endoperoxide as a function of the number of absorbed photons.  
 ○, 2PVN film 0.1 mole per cent ZnTPP.  
 ●, 2PVN film with 1.0 mole per cent ZnTPP.

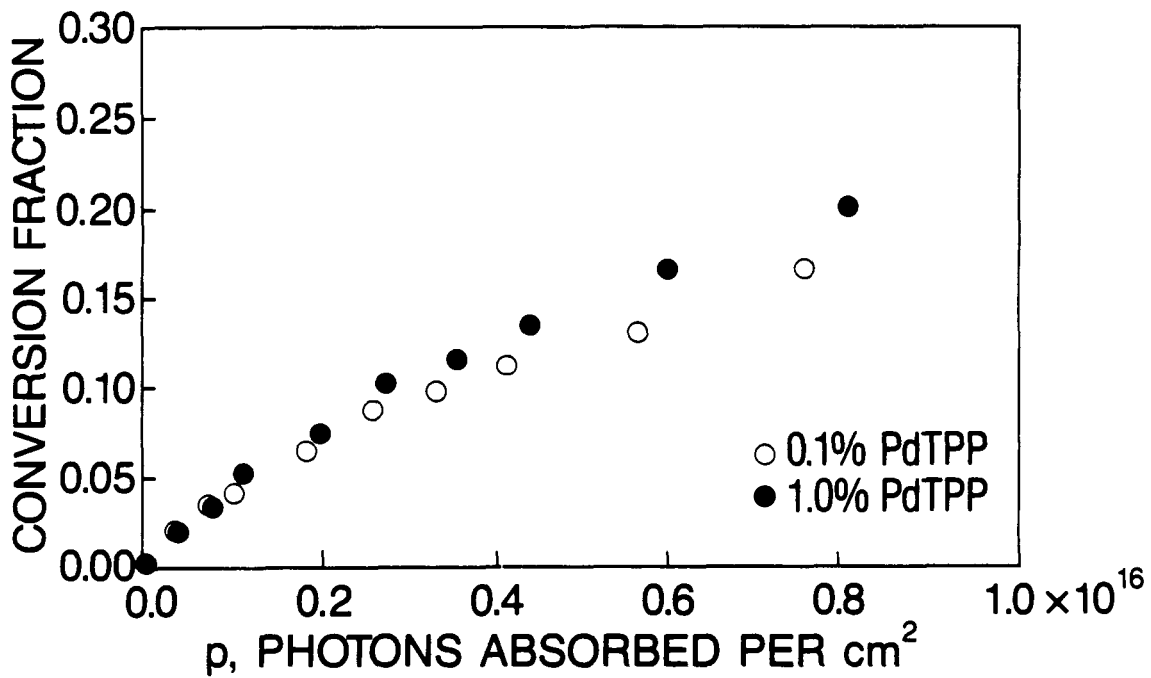
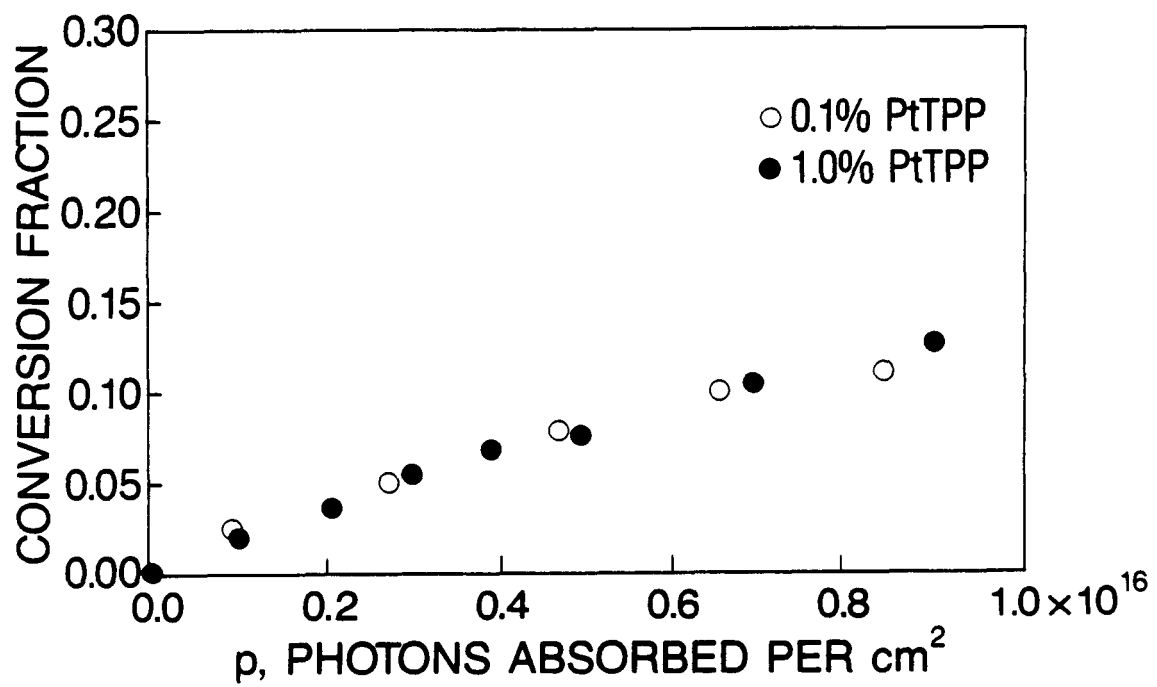


Figure 5.3 The fraction of naphthalene units converted to endoperoxide as a function of the number of absorbed photons.  
 ○, 2PVN film 0.1 mole per cent PdTPP.  
 ●, 2PVN film with 1.0 mole per cent PdTPP.



**Figure 5.4** The fraction of naphthalene units converted to endoperoxide as a function of the number of absorbed photons.  
 ○, 2PVN film 0.1 mole per cent PtTPP  
 ●, 2PVN film with 1.0 mole per cent PtTPP

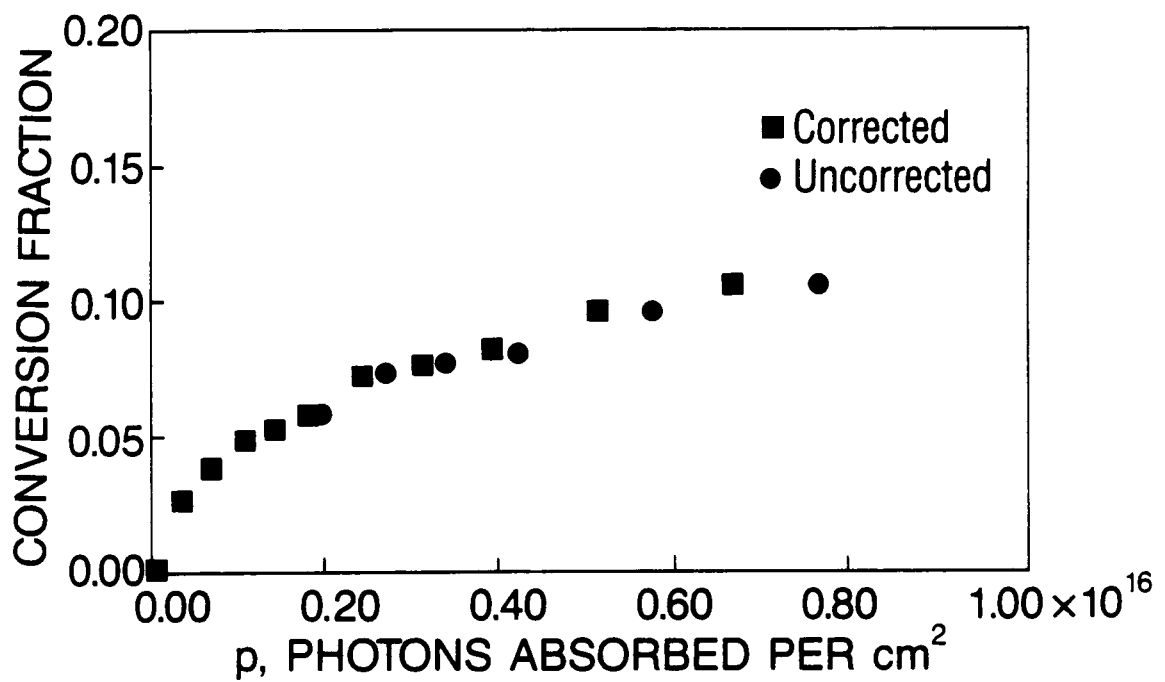


Figure 5.5 The fraction of naphthalene units converted to endoperoxide as a function of the number of photons absorbed by ZnTPP  
●, uncorrected data  
■, corrected data (see text)

The performance of a solar powered oxygen-iodine laser is greatly affected by the efficiency with which solar energy can be harvested and converted into electronic excitation of the oxygen molecule. In Figures 5.6-5.8 the data presented in Figures 5.2-5.4 are replotted to show how the integrated conversion quantum yield (the fraction of absorbed quanta which convert naphthalene to endoperoxide) changes as the fraction of the bulk polymer which is converted increases. The quantum yield is calculated by dividing the number of naphthalene units converted to endoperoxide by the number of absorbed photons. The number of endoperoxide units is given by the product of the number of naphthalene units initially available and the conversion fraction. The initial number of naphthalene units available for reaction can be easily estimated from the mass density (approximately 1 g/cm<sup>3</sup>), the molecular weight of 2PVN (182 g/mole) and an estimate of the film thickness (84 nm, obtained from the correlation described in reference which is actually for films of 2PVN which is 70 per cent converted to endoperoxide).

In Figures 5.6-5.8 the quantum yield is initially large and decreases as naphthalene is converted to endoperoxide for all three porphins. While in some of the plots the quantum yield exceeds unity at very low conversion fraction, the uncertainty in the measurements is large. The error bars attached to the quantum yield data in these figures were calculated assuming that the only significant statistical error in the quantum yield data came from the measurement of absorbance of the film at 294 nm. This uncertainty was estimated to be 0.001 absorbance units which probably results in a good estimate of the standard deviation at low conversion fraction but results in an underestimate of the standard deviation at larger conversion fraction as the scatter in the data points suggests.

A difference between the behavior of the 0.1% porphin doped 2PVN and the 1% doped samples can not be inferred from the data for the series of three porphins. A difference would not be expected if a higher doping fraction only results in larger aggregates of dye included in the polymer matrix.

#### 5.4 Discussion

The initial quantum yield of endoperoxide formation is close to unity for all three porphins. This can only occur if 1) energy is transferred from the excited dye molecules to oxygen with a quantum yield close to unity and 2) the singlet oxygen so formed reacts to give endoperoxide with near unity quantum efficiency.

Under the conditions of our experiments the first condition appears to be satisfied. The rate constants for decay of ZnTPP, PdTPP and PtTPP in a polymer matrix (nylon) are 33 s<sup>-1</sup>, 1000 s<sup>-1</sup>, and 13000 s<sup>-1</sup> respectively (the decay constants for all three porphins have not been measured in 2PVN so we have used the values obtained in nylon). A quenching rate constant of 350 Torr<sup>-1</sup>s<sup>-1</sup> has been measured for ZnTPP in 2PVN and it will be assumed that this value is independent of the particular porphin used (this has been shown to be the case for porphins in nylon - see chapter 2 section 2.3.4). With the 2PVNE film exposed to atmosphere (150 Torr of oxygen) a rate constant of 53000 s<sup>-1</sup> is calculated for the quenching of porphin excitation by oxygen. Only for PtTPP which has a

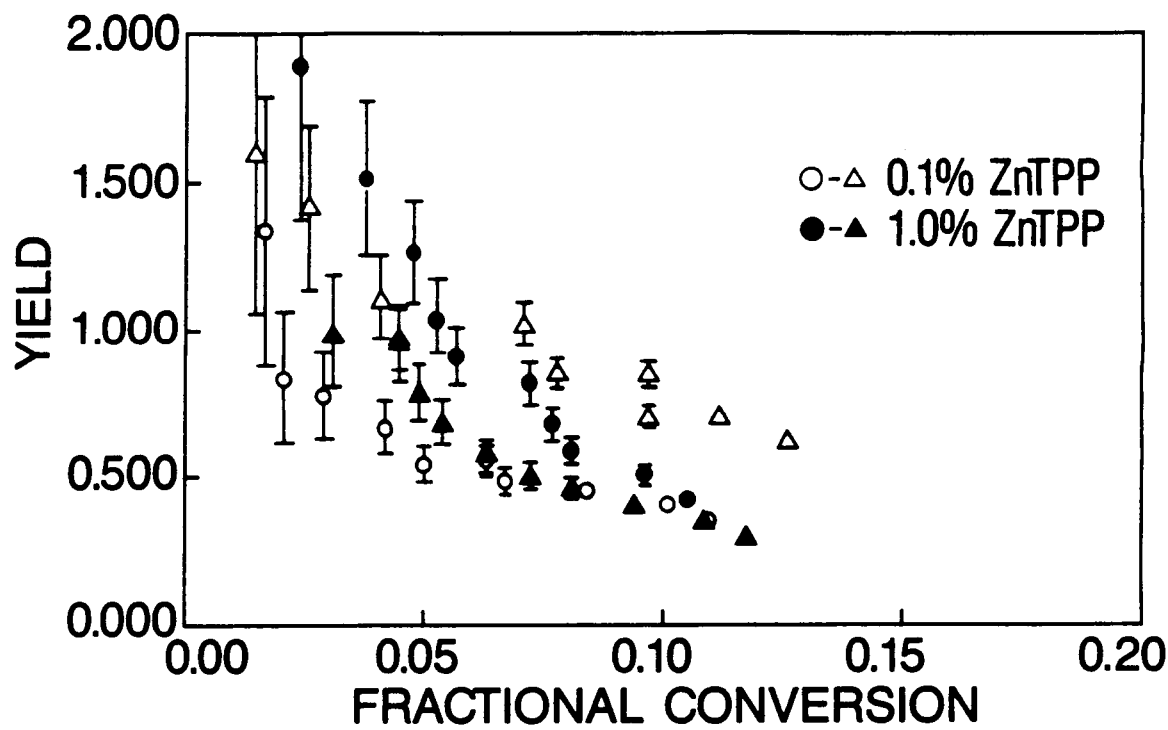


**Figure 5.6** The quantum yield of endoperoxide formation as a function of the fraction of naphthalenes converted to endoperoxide.  
 ZnTPP data:

○, △-0.1 mole per cent ZnTPP  
 ●, ▲-1.0 mole per cent ZnTPP

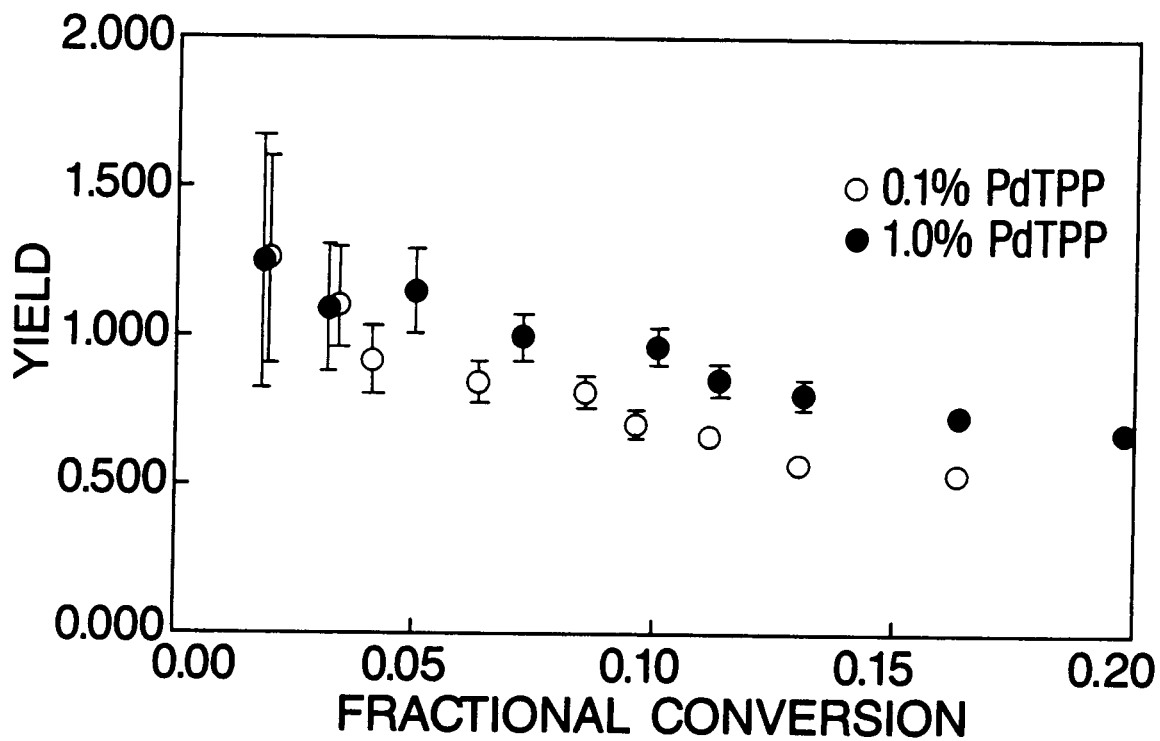


**Figure 5.7** The quantum yield of endoperoxide formation as a function of the fraction of naphthalenes converted to endoperoxide.  
PdTPP data;

○-0.1 mole per cent PdTPP  
●-1.0 mole per cent PdTPP

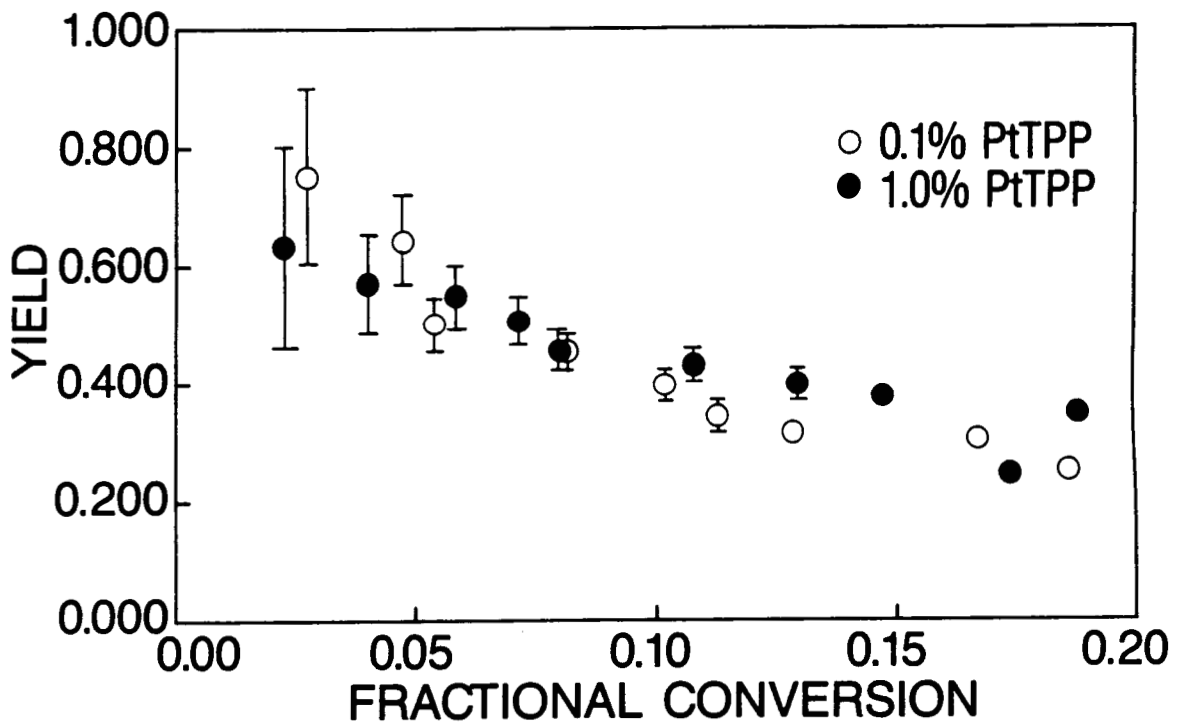


Figure 5.8 The quantum yield of endoperoxide formation as a function of the fraction of naphthalenes converted to endoperoxide.  
PtTPP data;

○—0.1 mole per cent PtTPP  
●—1.0 mole per cent PtTPP

short triplet lifetime will the natural decay of the dye molecule compete at all with the rate of quenching. However, even for this porphin, quenching of the triplet state by oxygen (leading to singlet oxygen production) is expected to take place with approximately 80 per cent quantum efficiency.

The second condition needed to ensure near unity quantum yield for the initial endoperoxide formation reaction is satisfied if the rate of quenching of singlet oxygen excitation by the polymer matrix is slower than the reaction of singlet oxygen with the naphthalene units. Because the experimental data presented in Figures 5.6-5.8 show a limiting quantum yield of close to unity, one can infer that the endoperoxide formation rate must be more rapid than the rate of quenching.

A decrease in the rate of conversion of 2PVN to its endoperoxide form is expected to occur as the reaction proceeds and fewer naphthalenes become available for reaction. In a series of experiments which measured the fraction of oxygen released into the gas phase upon thermolysis of a thin film of 2PVN it was found that oxygen can diffuse distances on the order of 10 nm without experiencing much quenching by the polymer. If this distance is taken as the radius of a sphere surrounding each dye molecule, the sphere will occupy a volume,  $V$ , of about  $4 \times 10^{-18} \text{ cm}^3$ . The number of naphthalene units present in this volume is approximately given by  $N_a V / M d$  where  $N_a$  is Avogadro's number,  $d$  is the mass density of 2PVN, and  $M$  is the monomeric molecular weight of the polymer. The number of naphthalene units which are well within the diffusion distance of each dye molecule is the order of  $10^4$ . Even as little as 0.1% molar density of porphin dye only requires that each dye molecule service  $10^3$  naphthalene units. From this line of reasoning one can infer that the quantum yield for endoperoxide formation should not decrease significantly until most of the film has been converted to endoperoxide, in contradiction to the experimental evidence which shows a fall off in the endoperoxide formation rate at low conversion fraction (10 to 20 per cent) even for 1% loading of porphin in polymer.

The drop in the quantum yield of endoperoxide formation at unexpectedly low conversion fraction may be a consequence of dye aggregation in the polymer film. In the calculation described above for the number of naphthalene units in the sphere of influence of each dye molecule, it was assumed that the dye molecules were distributed homogeneously throughout the polymer. A singlet oxygen molecule can diffuse from the dye production site a distance long enough to reach  $10^4$  naphthalene units without suffering a high probability of being quenched. However, if the dye molecules cluster into aggregates of 1000, even a 1% overall molar density of porphin must service a volume in the polymer film which includes 105 naphthalene units. Under these conditions, the quantum yield may decrease at a relatively low fractional conversion as is observed.

The efficiency of solar collection and utilization in a solar pumped oxygen-iodine laser will be determined by several factors. Of obvious importance is the fraction of light in the solar spectrum which can be absorbed by dye molecules. A practical upper limit on the energy collection efficiency is set at 0.82 by the fraction of solar energy available with a wavelength shorter than 1300 nm, the wavelength corresponding to the energy of singlet delta oxygen. With three dyes, methylene blue, rose bengal, and acridine orange, light with wavelength

between 450 and 650 nm can be harvested. The fraction of solar energy which can be absorbed in this spectral region is 0.26. Because over one half of this energy does not end up as electronic excitation of oxygen but is degraded into heat energy, the real efficiency of energy utilization is less than 0.13 for photons absorbed in the 450 to 650 nm spectral region. Another 11 per cent of the solar energy is available in the wavelength region from 450 nm to 350 nm, but would add only another 3 per cent to the overall efficiency of the energy conversion process. A much larger fraction of usable energy lies in the spectral region between 650 and 1300 nm, and use of cyanine dyes which absorb in the near infrared spectral region may provide substantial improvements in the yield of solar energy harvested.

Once a photon has been absorbed by a dye molecule, it must be transferred to molecular oxygen before the dye is deactivated and all the energy is lost to heat. This fraction can be controlled by the partial pressure of oxygen in contact with the polymer. The porphins which we have investigated apparently have a quantum efficiency for energy transfer to oxygen of close to unity at 150 Torr of oxygen. Dye molecules with long triplet decay times such as ZnTPP require a partial pressure of oxygen considerably less than 150 Torr to efficiently harvest solar energy.

The singlet oxygen which is produced by dye sensitization must be stored for eventual use as a laser fuel. The reaction of singlet oxygen with 2PVN to make the endoperoxide achieves this purpose. The results with porphin doped 2PVN demonstrate that quantum yields as high as 1 are possible; however, the yield decreases substantially after only a moderate fraction (about 20 per cent) of the naphthalene units are converted to endoperoxide. Here large improvements may be realized. A significant increase in endoperoxide conversion efficiency will almost certainly be achieved if the 2PVN polymer can be deuterated. Replacing all the C-H bonds in the polymer by C-D bonds should decrease the rate of deactivation of singlet oxygen as it diffuses through the polymer by at least an order of magnitude allowing a longer time for the excited oxygen to seek out and react with a naphthalene unit.

Large improvement in performance is also possible if a lack of homogeneity in the dye distribution as it is now incorporated in the polymer film is the reason for a decrease in the yield at modest conversion fractions. Copolymerization of a vinyl substituted dye molecule with the vinyl naphthalene monomer should provide a near random distribution of dye in the polymer even at substantial loading of dye in polymer. The copolymerized dye/2PVN is expected to regenerate the polymer-bound endoperoxide with near unity quantum yield and do so until most (say 90 per cent) of the initially available naphthalene units have been reacted.

## CHAPTER 6: EXECUTIVE SUMMARY

The objective of the work reported in this document was to evaluate several technical steps in the conceptual design of a solar powered oxygen-iodine laser. The major obstacles to the realization of this goal are the efficient production of singlet delta oxygen using solar radiation and the concentration and storage of this excited molecule. The efficient production of singlet oxygen was conceived as taking place through absorption of solar radiation by thin polycrystalline films of dye molecules and the transference of part of this energy to the dye film surface by exciton migration. The energy of the exciton is trapped at the surface of the dye film by other dye molecules chosen explicitly for this function. The trapped exciton transfers its energy to a colliding oxygen molecule forming the singlet delta state of the latter.

The singlet oxygen molecule can be used directly as the chemical fuel for an oxygen-iodine laser, but it is advantageous to preferentially remove the singlet oxygen from the oxygen gas thereby concentrating the laser fuel and storing it for future use. Reaction of singlet oxygen with a substituted aromatic hydrocarbon such as 1,4-dimethylnaphthalene produces an endoperoxide which is stable at reduced temperature for years. The heating of endoperoxide results in the reverse reaction, production of singlet delta oxygen and the parent aromatic hydrocarbon.

The two steps which were the primary concern of this investigation are the trapping of exciton energy at a surface site on the dye film and the transfer of energy from an excited dye molecule isolated on a surface to gaseous molecular oxygen.

### **6.1 Transfer of energy from isolated dye molecules**

The rate at which energy can be transferred from a dye molecule adsorbed on the surface of an organic crystal to an oxygen molecule which collides with it from the gas phase will depend on the temperature and partial pressure of oxygen as well as the probability of energy transfer per collision. The latter quantity is intrinsic to the dye molecule and is the parameter which was sought in our studies of dye molecules supported on various solid substrates. Three categories of substrate were investigated: silica gel, NaCl crystals, and polymers. All of these substrates provide, in varying degrees, a high surface area allowing the study of a large population of excited dye molecules while still insuring that the molecules are sufficiently separated from each other so that energy migration among molecules does not dominate the photokinetics of the system. However, all three types of substrate behave differently.

Silica gel has been used extensively as a dye molecule support for the sensitized production of gas phase singlet delta oxygen. Several research groups have reported the fabrication of heterogeneous singlet oxygen generators using a dye sensitizer supported on silica gel. The efficiency of these generators is not reported; however, in cases where enough information is provided, the efficiency can be estimated and is always low. Originally we supposed that the low efficiency of these systems occurred because the dye molecules were present on the silica gel surface in low density and therefore the total fraction of incident

light absorbed was very low. The silica gel substrate could nevertheless serve as a dye substrate for measuring the kinetics of energy transfer from triplet dye molecule to gas phase oxygen. This point of view has proved to be somewhat in error. As we have shown, it now appears that quenching of dye luminescence on silica gel involves oxygen adsorbed to the silica gel surface rather than gas phase oxygen.

The lack of change in the magnitude of the slow decay phosphorescence of silica gel adsorbed ZnTPP over a pressure range in which the pre-exponential factor changes by an order of magnitude is evidence of static quenching. Oxygen is apparently affecting the initial triplet population (proportional to the pre-exponential) but not the decay rate constant. This behavior can be understood if it is presumed that quenching occurs by action of oxygen adsorbed on the silica gel rather than by collisions of gas phase oxygen molecules with ZnTPP. If oxygen is strongly bound to silica gel, only those ZnTPP molecules which are very close to adsorbed oxygen when photoexcited will be quenched. ZnTPP molecules which do not have neighboring oxygen molecules at the time of photoexcitation will phosphoresce with very little probability of being quenched (assuming the mobility of both oxygen and of ZnTPP on the silica gel surface is low). As the oxygen pressure is increased, the fraction of the silica gel surface covered by adsorbed oxygen increases thus increasing the probability of ZnTPP phosphorescence quenching.

It is expected that this mechanism of phosphorescence quenching by oxygen is general for dyes adsorbed on a silica gel surface. If so the production of gas phase singlet delta oxygen requires not only energy transfer from the dye molecule to adsorbed oxygen but also desorption of the excited oxygen. The latter step will compete with the quenching of singlet delta oxygen excitation by the silica gel surface.

In an effort to find a substrate surface which is passive (it only supports the dye molecule but does not interact with the dye except through weak van der Wall's forces or does not adsorb oxygen), we investigated dye deposited on a nylon mesh used in industry as a filtering material. The quenching behavior of dye molecules on this high surface area substrate was consistent with expectations of a collisional quenching model. However, further research has convinced us that during the process of depositing the dye on the nylon surface, much of the dye becomes embedded in the nylon polymer. Quenching takes places when dissolved oxygen diffuses through the polymer to the excited dye molecule. While the nylon mesh studies did not provide the information which we were seeking, they motivated the study of endoperoxide formation in dye doped 2PVN. These studies opened up a new direction for the efficient sensitized production and trapping of singlet delta oxygen (*vide infra*).

Initially it was thought that dye coated on nylon mesh by deposition from solution was adsorbed to surface sites on the nylon fibers. However, the luminescence quenching rates measured for this system are markedly smaller than that for dye deposited on NaCl. Furthermore, the magnitude of these quenching rates can be explained if it is assumed that the dye has become incorporated inside the nylon polymer solid.

A solution phase quenching model is consistent with all of our observations for the quenching of polymer supported dyes (we have studied several polymer substrates) and provides a means of comparing the apparent rate constant for quenching with data determined in other experiments. The dye molecules are presumed to be incorporated in the

polymer substrate. Dissolved oxygen diffuses throughout the polymer and upon encountering an excited dye molecule, quenches its luminescence. The apparent quenching rate constant is a product of a diffusion controlled reaction rate constant, a probability factor, and a solubility coefficient. Further analysis shows that the apparent rate constant for luminescence quenching is proportional to the product of the oxygen diffusion coefficient and the solubility coefficient. This product is termed the permeability of the polymer for oxygen and has been measured by other methods and reported in the literature. Comparison of the permeabilities which are determined from the phosphorescence quenching data with literature values shows:

1. The permeability values determined from phosphorescence quenching data are of the correct order of magnitude.
2. The ordering of permeability values which was determined from phosphorescence quenching data is the same ordering determined from literature values of this quantity.

Given the nature of the assumptions which enter our determination of the value of the permeability as derived from the apparent rate constant for quenching and the fact that it is not at all clear that polymers of the same molecular weight and branching structure are being compared, the agreement found between literature values of the permeability and our values is considered very satisfactory.

Finally, we examined dyes deposited on NaCl crystals. The choice of this substrate material was motivated by the lack of success experienced with the nylon substrate. The NaCl crystal is not permeable to organic solvents and the ionic lattice structure of the crystal does not provide a good environment for a large neutral organic dye molecule, so that deposition of a dye on NaCl from an organic solvent will not likely lead to incorporation of the dye molecule in the interior of the NaCl crystal. Our quenching data support the supposition that the dye remains on the NaCl surface and is quenched by collisions of gas phase oxygen with the dye molecule.

On the NaCl substrate the quenching of dye phosphorescence is accompanied by the increase in the phosphorescence decay rate. The integrated phosphorescence signal obeys Stern-Volmer kinetics when the gas phase pressure of oxygen is chosen as the independent variable. We conclude from this behavior that dye molecules are quenched on this surface by collisions of gas phase oxygen with the dye molecules. Using a value of  $10^{-18} \text{ m}^2$  for the cross sectional area of the ZnTPP molecule, the number of collisions per second per Torr of oxygen experienced by this dye molecule is  $4 \times 10^6$ , calculated from gas kinetic theory. At room temperature the rate constant for phosphorescence quenching of a single ZnTPP molecule is  $1100 \text{ s}^{-1} \text{ Torr}^{-1}$  (from the least squares fit to the data presented in Figure 2.7). The probability of quenching per collision, given by the ratio of these numbers, is  $3 \times 10^{-4}$ . While only a small fraction of collisions lead to energy transfer, it should be noted that at 100 Torr of oxygen the energy transfer rate is about  $10^5 \text{ s}^{-1}$ , a value which is large enough for consideration as an exciton trap and energy transfer site.

## **6.2 The photophysics of excitons in dye solids**

Single crystals of tetracene were examined for purposes of comparison with polycrystalline dye films. Tetracene is a convenient dye because the fusion of two triplet excitons in the crystal results in the creation of one singlet exciton which has a small but finite probability of fluorescing. This delayed fluorescence can be used to monitor the triplet exciton density.

In clean single crystals of tetracene under conditions of bulk excitation (excitation of tetracene molecules in the interior of the crystal as opposed to near the crystal surface), the unimolecular decay rate constant of triplet excitons was measured to be  $1.2 \times 10^5 \text{ s}^{-1}$ . The bimolecular decay rate constant resulting from triplet-triplet annihilation was also measured and found to be  $1 \times 10^{-11} \text{ cm}^3 \text{s}^{-1}$ , a value which is a factor of 4 lower than the literature value. An experiment was performed which measured the unimolecular decay rate as a function of the average distance the exciton was born to the crystal surface. The latter was controlled by varying the excitation wavelength and thus the absorption length. The unimolecular rate constant varies from about  $6 \times 10^5 \text{ s}^{-1}$  at an absorption length of 30 micrometers to greater than  $2 \times 10^6 \text{ s}^{-1}$  at an absorption length of less than 0.4 micrometers. This is a direct observation of lifetime shortening which occurs upon trapping or quenching of triplet excitation at sites near the crystal surface.

The rate of decay of delayed fluorescence in polycrystalline tetracene films about 100 nm thick was examined using the same signal analysis techniques as were used for the single crystal data. The unimolecular decay constant in the polycrystalline films was found to be  $1 \times 10^7 \text{ s}^{-1}$  which is about two orders of magnitude larger than the single crystal value. This is qualitatively consistent with the increase in unimolecular decay constant observed in single crystal work when excitons were generated close to the crystal surface; an exciton created in a 100 nm film is always close to a crystal surface. The bimolecular triplet exciton annihilation rate constant was in reasonably good agreement ( $1.5 \times 10^{-11} \text{ cm}^3 \text{s}^{-1}$ ) with the single crystal result.

The increase in the unimolecular decay rate of triplet excitons born close to a tetracene crystal surface may be the result of oxygen which has diffused into the crystal lattice. Our experiments were done in atmosphere, and even several experiments which were performed in an inert atmosphere did not protect the crystals from pre-exposure to oxygen and possible slow incorporation of oxygen. Once in the crystal lattice, the oxygen molecule may serve as an energy transfer site and thus effectively shorten the exciton lifetime. Oxidation of surface molecules of tetracene crystals to a tetraquinone has been reported, and while it is probably not energetically possible for these molecules to act as triplet exciton traps, nevertheless, charge transfer interactions between triplet tetracene molecules and tetraquinone may occur and may also cause the premature decay of the triplet exciton.

An attempt was made to develop a technique which could monitor the decay of excitons in polycrystalline films of dyes other than tetracene by measuring the heat released in the exciton decay process. This approach would be a more universally applicable technique and allow a large number of dye solids which do not show delayed fluorescence to be examined.

Two thermal techniques for studying triplet decay in dye thin films were examined. A photothermal deflection technique was developed which proved to be very sensitive for the measurement of the decay of small amounts of energy absorbed by a dye film. In principle this technique can monitor the generation of heat in sub-micron dye layers. However, it was found that the bandwidth of present commercially available position detectors is not large enough to measure the very fast decay kinetics of the dye films which were tested. Future work in this area might progress quickly if faster position sensors become available.

Detection of triplet exciton decay was also attempted by monitoring the signal created in a ferroelectric material upon heat released by an adjacent dye layer. The response time of this material was found to be quite slow. We did not have time to investigate the direct cause of the slow response (the diffusion of heat into the ferroelectric material should be sufficiently rapid), but it is probable that a nonuniform spatial distribution of ferroelectricity is the cause for a complex and sluggish response.

### **6.3 A system which combines singlet oxygen generation and storage**

During the process of evaluating the energy transfer characteristics of dye molecules adsorbed to polymer substrates, it became clear that the process which we were using for depositing the dye molecules led to inclusion of the dye in the polymer matrix. Thereafter, we deliberately incorporated porphin dyes in films of 2PVN, a polymer which is the precursor for an endoperoxide. The endoperoxide of 2PVN is routinely prepared at KMS in the solution phase, and films of this solid polymeric endoperoxide are prepared by spin coating from the solution. However, the observation of efficient quenching of porphins which were doped in 2PVN by oxygen diffusing into the polymer film from the gas phase led to the speculation that if singlet oxygen were being generated in the 2PVN solid, it should be reacting with the naphthalene units to form endoperoxide. If this process is efficient, the generation of singlet oxygen using solar energy and the concentration and storage of singlet oxygen can be accomplished in one step.

The irradiation of porphin-doped 2PVN in the presence of air does result in the conversion of naphthalene units in the polymer to endoperoxide. The initial quantum yield of endoperoxide formation is close to unity for the three porphins studies (ZnTPP, PdTPP, and PtTPP). This can only occur if 1) energy is transferred from the excited dye molecules to oxygen with a quantum yield close to unity and 2) the singlet oxygen so formed reacts to give endoperoxide with near unity quantum efficiency.

A decrease in the rate of conversion of 2PVN to its endoperoxide form may be expected to occur as the reaction proceeds and fewer naphthalenes are available for reaction. However, in a series of experiments which measured the fraction of oxygen released into the gas phase upon thermolysis of a thin film of 2PVN, it was found that oxygen can diffuse distances on the order of 10 nm without experiencing much quenching by the polymer. If this distance is taken as the radius of a sphere surrounding each dye molecule dissolved in 2PVN, the sphere will occupy a volume, V, of about  $4 \times 10^{-10} \text{ cm}^3$ . Using this volume the number of naphthalene units which are calculated to be well within the diffusion distance of each dye molecule is the order of  $10^4$ . Even as

little as 0.1% molar density of porphin dye only requires that each dye molecule service  $10^3$  naphthalene units. From this line of reasoning, we can infer that the quantum yield for endoperoxide formation should not decrease significantly until most of the film has been converted to endoperoxide, in contradiction to the experimental evidence which shows a fall off in the endoperoxide formation rate at low conversion fraction (10 to 20 per cent) even for 1% loading of porphin in polymer.

The drop in the quantum yield of endoperoxide formation at unexpectedly low conversion fraction may be a consequence of dye aggregation in the polymer film. In the calculation described above for the number of naphthalene units in the sphere of influence of each dye molecule, it was assumed that the dye molecules were distributed homogeneously throughout the polymer. Extensive dye aggregation would leave each dye aggregate with considerably more naphthalene units at larger distances from the singlet oxygen generation site. Under these conditions, the quantum yield may decrease at relatively low fractional conversion.

#### **6.4 Directions of future work**

The direct incorporation of dye molecules in 2PVN solids may provide a convenient material for singlet oxygen generation, concentration, and storage. The *in situ* generation of singlet oxygen in 2PVN and its subsequent reaction with the naphthalene units in this polymer to form endoperoxide has been demonstrated, and future work in this area could easily increase the efficiency with which this process utilizes solar radiation for the conversion process.

The efficiency of solar collection and utilization in a solar pumped oxygen-iodine laser will be determined by several factors. Of obvious importance is the fraction of light in the solar spectrum which can be absorbed by dye molecules. A practical upper limit on the energy collection efficiency is set at 0.82 by the fraction of solar energy available with a wavelength shorter than 1300 nm, the wavelength corresponding to the energy of singlet delta oxygen. With three dyes, methylene blue, rose bengal, and acridine orange, light with wavelength between 450 and 650 nm can be harvested. The fraction of solar energy which can be absorbed in this spectral region is 0.26. Because over one-half of this energy does not end up as electronic excitation of oxygen but is degraded into heat energy, the real efficiency of energy utilization is less than 0.13 for photons absorbed in the 450 to 650 nm spectral region. Another 11 per cent of the solar energy is available in the wavelength region from 450 nm to 350 nm, but would add only another 3 per cent to the overall efficiency of the energy conversion process. A much larger fraction of usable energy lies in the spectral region between 650 and 1300 nm, and use of cyanine dyes which absorb in the near infrared spectral region may provide substantial improvements in the yield of solar energy harvested.

Once a photon has been absorbed by a dye molecule, it must be transferred to molecular oxygen before the dye is deactivated and all the energy is lost to heat. This fraction can be controlled by the partial pressure of oxygen in contact with the polymer. The porphins which we have investigated apparently have a quantum efficiency for energy transfer to oxygen of close to unity at 150 Torr of oxygen. Dye molecules with long triplet decay times such as ZnTPP require a partial

pressure of oxygen considerably less than 150 Torr to efficiently use solar energy.

The singlet oxygen which is produced by dye sensitization must be stored for eventual use as a laser fuel. The reaction of singlet oxygen with 2PVN to make the endoperoxide achieves this purpose. The results with porphin-doped 2PVN demonstrate that quantum yields as high as 1 are possible; however, the yield decreases substantially after only a moderate fraction (about 20 per cent) of the naphthalene units are converted to endoperoxide. Here large improvements may be realized. A significant increase in endoperoxide conversion efficiency will almost certainly be achieved if the 2PVN polymer can be deuterated. Replacing all the C-H bonds in the polymer by C-D bonds should decrease the rate of deactivation of singlet oxygen as it diffuses through the polymer by at least an order of magnitude, allowing a longer time for the excited oxygen to seek out and react with a naphthalene unit.

Large improvement in performance is also possible if a lack of homogeneity in the spatial distribution of dye molecules in the polymer film is the reason for a decrease in conversion yield at modest conversion fractions observed in our past experiments. Copolymerization of a vinyl substituted dye molecule with the vinyl naphthalene monomer should easily provide a near random distribution of dye in the polymer even at substantial loading of dye in polymer. The copolymerized dye-2PVN is expected to regenerate the polymer-bound endoperoxide with near unity quantum yield and do so until most (say 90 per cent) of the initially available naphthalene units have been reacted. This dye impregnated polymer material should provide a key component for the future development of a solar powered oxygen-iodine laser.



# Report Documentation Page

1. Report No.  NASA CR-4127	2. Government Accession No.	3. Recipient's Catalog No.	
4. Title and Subtitle  Solar Generation and Storage of O <sub>2</sub> (a <sup>1</sup> Δ <sub>g</sub> )		5. Report Date  March 1988	
		6. Performing Organization Code	
7. Author(s)  Allen J. Twarowski, Phan Dao, and Lisa A. Good		8. Performing Organization Report No.  KMSF-U1947	
9. Performing Organization Name and Address  KMS Fusion, Inc. P.O. Box 1567 Ann Arbor, MI 48106		10. Work Unit No.  506-41-41-01	
12. Sponsoring Agency Name and Address  National Aeronautics and Space Administration Langley Research Center Hampton, VA 23665-5225		11. Contract or Grant No.  NAS1-17988	
15. Supplementary Notes  Langley Technical Monitor: Dr. Nelson W. Jalufka Final Report		13. Type of Report and Period Covered  Contractor Report	
16. Abstract  An investigation of the technical steps required to design a solar powered oxygen-iodine laser was performed under this contract. Singlet delta oxygen is formed upon transfer of energy from selected photo-excited dye molecules to ground state molecular oxygen and then is concentrated and stored as an endoperoxide by reaction with an aromatic hydrocarbon. The endoperoxide, when heated, releases singlet oxygen in high yield thus providing a regenerable source of laser fuel.  Energy transfer from dye molecules to molecular oxygen was investigated. When dye molecules were adsorbed to polymer substrates it was observed that the dye became embedded in the polymer matrix. Porphin dyes were incorporated into films of 1,4-dimethyl-2-poly(vinyl naphalene), 2PVN. An endoperoxide was formed when porphin-doped 2PVN was exposed to visible radiation. This demonstrates the possibility of generating singlet oxygen using solar energy and concentrating and storing it in one simple step.  Transport of energy by exciton migration in polycrystalline dye films was also examined.		14. Sponsoring Agency Code	
17. Key Words (Suggested by Author(s))  endoperoxide, singlet oxygen, solar energy, laser, exciton, kinetics	18. Distribution Statement  Unclassified - Unlimited	Subject Category 36	
19. Security Classif. (of this report)  Unclassified	20. Security Classif. (of this page)  Unclassified	21. No. of pages  164	22. Price  A08